université de BORDEAUX

TECHNISCHE UNIVERSITÄT DARMSTADT

Joint Thesis (EJD-FunMat)

Approved by:

The Department of Material and Geosciences of the Technical University of Darmstadt in Fulfillment of the Requirements for the Degree of Doctor Rerum Naturalium (Dr. Rer. Nat.)

The Doctoral School of Chemical Sciences of the University of Bordeaux in Fulfillment of the Requirements for the Degree of Doctor with Specialty Physical Chemistry of Condensed Matter

Interface analysis and development of $BiVO_4$ and $CuFeO_2$ heterostructures for photochemical water splitting

Yannick Hermans

Born in Brasschaat, Belgium

Scheduled defense at 06/05/2019 before a jury composed of :

PhD supervisor	**Prof. Dr. Jaegermann, Wolfram**	(TU Darmstadt)
PhD supervisor	**Prof. Dr. Toupance, Thierry**	(UBordeaux)
Reviewer	**Prof. Dr. Cassaignon, Sophie**	(Sorbonne Université)
Reviewer	**Dr. Robert, Didier**	(Université de Lorraine)
Examiner	**Jun. Prof. Dr. Kramm, Ulrike**	(TU Darmstadt)
Examiner	**Prof. Dr. Weidenkaff, Anke**	(TU Darmstadt)
Examiner	**Prof. Dr. Cloots, Rudi**	(ULiège)

Interface Analysis and Development of $BiVO_4$ and $CuFeO_2$ Heterostructures for Photochemical Water Splitting

Genehmigte Dissertation von Yannick Hermans aus Brasschaat, Belgien

1. Gutachten: Prof. Dr. W. Jaegermann

2. Gutachten: Prof. Dr. T. Toupance

Tag der Einreichung: 27/03/19

Tag der Prüfung: 06/05/19

Darmstadt — D 17

Statement regarding the thesis

I, hereby, confirm that I have written the present thesis independently and without illicit aid from third parties, using solely the aids mentioned. All passages from other sources are marked as such. This work has not been presented to an examination office before in this or a similar form.

Déclaration sur la dissertation

Je déclare par la présente que la thèse a été rédigée sans l'aide d'un tiers et que toutes les aides et supports ont été mentionnés. Toutes les sources ont été indiquées. Ce travail n'a pas été présenté antérieurement devant un comité d'examen, que ce soit en totalité ou en partie.

Erklärung zur Dissertation

Hiermit versichere ich, die vorliegende Dissertation ohne Hilfe Dritter nur mit den angegebenen Quellen und Hilfsmitteln angefertigt zu haben. Alle Stellen, die aus Quellen entnommen wurden, sind als solche kenntlich gemacht. Diese Arbeit hat in gleicher oder ähnlicher Form noch keiner Prüfungsbehörde vorgelegen.

Darmstadt, den 27 März 2019 _____

(Yannick Hermans)

”It does not matter how slowly you go as long as you do not stop.”
—Confucius—

Zusammenfassung

Die photo(elektro)chemische (PEC) Wasserspaltung ist ein vielversprechender Weg zur Erzeugung von Wasserstoff aus erneuerbaren Energiequellen. Insbesondere PEC-Systeme vom Typ 2, bei denen die erforderliche Energie zum spalten von Wasser von zwei komplementären Photoabsorbern bereitgestellt werden kann, haben das Potenzial wirtschaftlich zu konkurrieren mit der Dampfreformierung von Methan, dem herkömmlichen Verfahren zur Wasserstoffherstellung. In dieser Arbeit wurden $BiVO_4$ und $CuFeO_2$ ausgewählt, um die Wasseroxidation beziehungsweise Wasserreduktion durchzuführen. Laut Literatur sind jedoch zusätzliche Kontaktmaterialien erforderlich um eine angemessene Wasserspaltleistung zu erreichen.

Die genauen Vorteile dieser Kontaktmaterialien sind noch nicht vollständig geklärt. Deshalb wurde sich in dieser Arbeit da zu entschieden, die Heteroübergangseigenschaften bestimmter $BiVO_4$- und $CuFeO_2$-basierter Heterostrukturen durch sogenannte Grenzflächenexperimente zu untersuchen. Innerhalb dieser Grenzflächenexperiment wurde ein bestimmtes Kontaktmaterial schrittweise auf ein $BiVO_4$- oder $CuFeO_2$-Substrat gesputtert und photoelektronenspektroskopische Messungen zwischen jedem Abscheidungsschritt durchgeführt. Auf diese Weise könnte die Bandanpassung zwischen dem Substrat und dem Kontaktmaterial sowie die maximal mögliche Variierung des Fermi-Niveaus für die untersuchten Photoabsorbern bestimmt werden.

Ein weiterer Teil dieser Arbeit umfasst die Herstellung von neuen anisotropen heterostrukturierten $CuFeO_2$-und $BiVO_4$-Pulvern durch Photodeposition. Insbesondere wurde Silber, Platin, Cobalt(oxy)(hydr)oxid und Nickel(oxy)(hydr)oxid auf anisotrop geformten $BiVO_4$- und $CuFeO_2$-Pulvern abgeschieden. Diese Pulver wurden auf ihre Leistung bei der photochemischen Wasserspaltung getestet.

Stichwörter:

photo(elektro)chemische Wasserspaltung, Anisotropie, $BiVO_4$, $CuFeO_2$, Heterostrukturen, Photoelektronenspektroskopie, Grenzflächenexperiment, Photodeposition, Bandanpassung.

Résumé

Le craquage photo(électro)chimique (PEC) de l'eau par l'énergie solaire est considéré comme une méthode prometteuse de production renouvelable d'hydrogène. En particulier, les systèmes PEC de type 2, dans lesquels la phototension nécessaire de 1.23 V peut être fourni par deux matériaux absorbeurs complémentaires, peuvent potentiellement rivaliser économiquement avec le vaporeformage du méthane, la méthode de production conventionnelle d'hydrogène. Dans ce travail, $BiVO_4$ et $CuFeO_2$ ont été choisis pour effectuer la réaction d'oxydation et de réduction de l'eau, respectivement. Cependant, selon la littérature, des matériaux supplémentaires sont nécessaires pour atteindre des efficacités de craquage de l'eau raisonnable.

Les avantages exacts de ces matériaux supplémentaires n'ayant pas encore été complètement élucidés, ce travail a eu tout d'abord pour objectif d'examiner les propriétés de certaines hétérojonctions à base de $BiVO_4$ et de $CuFeO_2$ par des expériences d'interface. Dans ce but, un certain matériau a été pulvérisé sur un substrat de $BiVO_4$ ou de $CuFeO_2$ et des mesures de spectroscopie de photoélectrons ont été effectuées à chaque étape du dépôt. Nous avons ainsi pu interpréter l'alignement des bandes entre le substrat et le matériau pulvérisé, et déterminer l'accordabilité du niveau de Fermi pour les absorbeurs étudiés.

Par ailleurs, des hétérostructures à base de particules de $CuFeO_2$ et de $BiVO_4$ anisotropes sont été élaborées par photodéposition. En particulier, le dépôt d'argent, de platine, de l'(oxy)(hydr)oxyde de cobalt et de l'(oxy)(hydr)oxyde de nickel a été réalisé avec succès sur des particules anisotropes de $BiVO_4$ et $CuFeO_2$. Les performances de ces poudres dans des expériences de craquage photochimique de l'eau ont ensuite été déterminées.

Mots-clé:

Craquage photo(électro)chimique de l'eau, anisotropie, $BiVO_4$, $CuFeO_2$, hétérostructures, spectroscopie de photoélectrons, expérience d'interface, photodéposition, l'alignement des bandes.

Samenvatting

Foto-elektrochemische (PEC) ontleding van water wordt beschouwd als een veelbelovende hernieuwbare manier om waterstofgas te produceren. Vooral PEC-systemen van type 2, waarin de benodigde energie voor de ontleding van water kan worden geleverd door twee complementaire lichtabsorberende materialen, zouden economisch kunnen concurreren met de stoomreforming van methaan, de conventiële industriële waterstofproductiemethode. In dit werk werden $BiVO_4$ en $CuFeO_2$ gekozen om respectievelijk wateroxidatie en waterreductie uit te voeren. Volgens de literatuur zijn extra contactmaterialen vereist om een behoorlijke waterontledingsprestatie te bereiken.

De exacte voordelen van deze contactmaterialen zijn echter nog niet volledig opgehelderd. Om die reden hebben we in dit werk gekozen om de junctie-eigenschappen van bepaalde $BiVO_4$ en $CuFeO_2$ gebaseerde heterostructuren te onderzoeken via zogenaamde grensvlakexperimenten, waarbij een bepaald contactmateriaal stapsgewijs werd gesputterd op een $BiVO_4$- of $CuFeO_2$-substraat, waarbij foto-elektronen spectroscopie metingen werden uitgevoerd tussen elke depositiestap. Op deze manier werd de elektronische bandstructuur tussen het substraat en het contactmateriaal evenals de maximaal magelijke variatie van het Fermi-niveau voor de bestudeerde lichtabsorberende materialen bepaalt.

Een ander deel van dit werk betrof het creëren van nieuwe heterogestructureerde anisotrope $CuFeO_2$ en $BiVO_4$ poeders door middel van fotodepositie. In het bijzonder deponeerden we zilver, platina, kobalt(oxy)(hydr)oxide en nikkel(oxy)(hydr)oxide op anisotropisch gevormde $BiVO_4$ en $CuFeO_2$ poeders. De prestatie van de poeders voor de fotochemische ontleding van water werd evenzeer getest.

Trefwoorden:

Foto-elektrochemische ontleding van water, anisotropie, $BiVO_4$, $CuFeO_2$, heterostructuren, foto-elektronen spectroscopie, grensvlakexperiment, photodepositie, elektronische bandstructuur.

Abstract

Solar photo(electro)chemical (PEC) water splitting is regarded as a promising ways of renewable hydrogen production. Especially, type 2 PEC systems, in which the necessary energy needed to split water can be supplied by two complimentary photoabsorbers, have the potential to economically compete with steam methane reforming, the conventional hydrogen production method. In this work, $BiVO_4$ and $CuFeO_2$ were chosen to perform the water oxidation and water reduction reaction, respectively. However, according to literature additional contact materials are required to achieve a reasonable water splitting performance.

The exact benefits of these contact materials have not yet been completely elucidated. Therefore, we opted in this work to investigate the junction properties of certain $BiVO_4$ and $CuFeO_2$ based heterostructures through so called interface experiments, whereby a certain contact material was stepwise sputtered onto a $BiVO_4$ or $CuFeO_2$ substrate, performing photoelectron spectroscopy measurements in between each deposition step. In this way we could interpret the band alignment between the substrate and the contact material, as well as determine the Fermi level tunability for the studied photoabsorbers.

In parallel, new anisotropic $CuFeO_2$ and $BiVO_4$ based heterostructured powders were created through photodeposition. In particular, silver, platinum, cobalt(oxy)(hydr)oxide and nickel(oxy)(hydr)oxide were successfully deposited onto anisotropically shaped $BiVO_4$ and $CuFeO_2$ powders. These powders were tested as well for their performance in photochemical water splitting.

Keywords:

Photo(electro)chemical water splitting, anisotropy, $BiVO_4$, $CuFeO_2$, heterostructures, photoelectron spectroscopy, interface experiment, photodeposition, band alignment.

Acknowledgements

First, I would like to thank Prof. **Wolfram Jaegermann** and Prof. **Thierry Toupance** to provide me with the amazing opportunity to work in their research groups towards the preparation of my PhD. I am extremely grateful for all the assistance you provided, to help me keep track of my research project and to challenge my mind with the thorough scientific discussions we held. Working in your groups was a real pleasure.

Second, many thanks to prof. **Andreas Klein**. I would not have been able to write this work without you providing me with your knowledge on fundamental solid state physics, electronic structure of materials and semiconductor oxides. Your scientific curiosity, openness and ability to create new ideas inspired me greatly.

Furthermore, I would like to thank all our scientific collaborators. I would like to thank Dr. **Sebastián Murcia-López** and Dr. **Klaus Ellmer** for providing me with $BiVO_4$ thin films. I would like to thank Prof. **Roel van de Krol** and Prof. **Joan Ramón Morante** for their contributions to the two published articles on $BiVO_4$ solid state interface analysis.

Thanks to **Marc Birot**, **Marie-Anne Dourges** and **Odille Babot** for introducing me to the measurement equipment at C2M. Special thanks are due to Dr. **Joachim Brötz** and Dr. **Eric Lebraud** for measuring some of my samples with XRD. I would also like to thank **Jean-Christophe Jaud** for carrying out a few Rietveld analyses. I thank Dr. **Matthias Fingerle** for assisting me in performing the water desorption experiments on $BiVO_4$.

Off course I also want to acknowledge the great and open work atmosphere that my **fellow colleagues** contributed to the **C2M group** in Bordeaux and the Surface Science group of prof. Jaegermann at TU Darmstadt, especially my close colleagues from the **oxide group**. I will miss playing sports with you as well as sharing a coffee (or rather tea) with some cookies/cake after lunch or at 4pm.

Also a special thanks to all of my **old friends** in Belgium and my **new friends** in Bordeaux and Darmstadt to take my mind off work from time to time. I have especially good memories from my time in the house in **Pierre Romain 16**; thank you fellow **housemates** for sharing in all the adventures at Kim's house.

Last but not least I acknowledge my parents, **Marijke Stessels and Peter Hermans**, for aiding me in any way possible at any time possible, my sister, **Silke Hermans**, for support but also to accompany me in some travelling and going to music concerts and the rest of **my family** for their encouragement and support.

Contents

List of Figures

List of Tables

List of abbreviations

acac: acetylacetonate

AES: Auger electron spectroscopy

AFM: Atomic force microscopy

ALD: Atomic layer deposition

BE: Binding energy

BoS: Balance of system

BSE: Backscattered electrons

CB: Conduction band

CBM: Conduction band minimum

CCD: Charge-coupled device

CCS: Carbon capture and sequestration

CoPi: Cobalt phosphate

DAISY-MAT: Darmstadt integrated system for materials analysis

DFT: Density functional theory

DWE: Dual-working-electrode

EDS: Energy-dispersive X-ray spectroscopy

EDTA: Ethylenediaminetetraacetic acid

EELS: Energy electron loss spectrum

FEG: Field emission gun

FESEM: Field emission secondary electron microscope

FTO: Fluorine-doped tin oxide

GC: Gas chromatograph

GSPV-E: Grid supplemented photovoltaic-electrolysis

HAADF: High-angle annular dark-field

HER: Hydrogen evolution reaction

ICSD: Inorganic crystal structure database

IREC: Institut de recerca en energia de catalunya

ITO: Tin-doped In_2O_3

IUPAC: International union of pure and applied chemistry

JCPDS: Joint committee on powder diffraction standards

KBi: Potassium borate

LCAO: Linear combination of atomic orbitals

LCH: Levelised cost of hydrogen production

LCOE: Levelised cost of electricity

MeOH: Methanol

NHE: Normal hydrogen electrode

NIST: National institute of standards and technology

OER: Oxygen evolution reaction

PEC: Photoelectrochemical

PEM: Polymer electrolyte membrane

PES: Photoelectron spectroscopy

PLD: Pulsed laser deposition

PV: Photovoltaic

PV-E: Photovoltaic-electrolysis

PXRD: Powder X-ray diffraction

Rhd B: Rhodamine B

RHE: Reversible hydrogen electrode

SAED: Selected area electron diffraction

SAM: Scanning Auger microscopy

SDS: Sodium dodecyl sulphate

SEC: Secondary electron cut-off

SEI: Secondary electron imaging

SEM: Secondary electron microscope

SHE: Standard hydrogen electrode

SMR: Steam methane reforming

SPS: Surface photovoltage spectroscopy

STEM: Scanning transmission electron microscope

STH: Solar to hydrogen conversion efficiency

TAS: Transient absorption spectroscopy

TCD: Thermal conductivity detector

TEM: Transmission electron microscope

THF: Tetrahydrofuran

TRMC: Time-resolved microwave conductivity

UHV: Ultra-high vacuum

UP: Ultraviolet photoelectron

UPS: Ultraviolet photoelectron spectroscopy

UV-Vis: UV visible

UV-Vis-NIR: UV-visible-near infrared

VB: Valence band

VBM: Valence band maximum

vol%: Volume percentage

WF: Work function

wt%: Weight percentage

XP: X-ray photoelectron

XPS: X-ray photoelectron spectroscopy

ZPC: Zero point charge

Chapter 1

Preface

1.1 Motivation

At the moment we are still living in a hydrocarbon based economy, in the sense that we are mostly dependent on coal, natural gas and oil for transportation, food production, electricity and heating. The reliance on fossil fuels, however, poses several problems. Fossil fuels are unevenly distributed over the globe, creating often geopolitic tensions and giving some states, such as the Gulf Arab states or Russia, tremendous power. Fossil fuel burning has also led to a plethora of environmental problems, being regarded as a main cause of climate change due to it being the largest source of greenhouse gas emissions and a major cause of air pollution due to the undesired release of nitrogen oxides, sulphur dioxide, volatile organic compounds and heavy metals. Potentially, these problems can be overcome by shifting from a fossil fuel based economy towards a hydrogen based economy with hydrogen as predominant energy carrier. Actually, approximately 65 Mt hydrogen is produced yearly,[1] for the production of ammonia (49% of global H_2 production), cracking of heavy petroleum derivatives into lighter fractions (37%), for methanol production (8%) and for a few niche uses (6%).[2] These niche uses include energy storage, fuel cell conversion, agent in speciality chemical production and agent in carbon based fuel production. In a hydrogen based economy these niche uses would grow in importance. There are a few ways of producing hydrogen; some which are existing mature technologies: steam methane reforming (SMR) and coal gasification (96% of total hydrogen production), and water electrolysis (4%); while others are still at the lab scale such as photo(electro)chemical water splitting. Lab scale methods with reduced CO_2 emissions need to be further developed and adaptations to the existing technologies need to be implemented to realise a renewable hydrogen economy with a limited environmental impact. Figure 1.1 shows how a renewable hydrogen economy could look like.[3]

The main reason why there is now such a strong discrepancy between the amount of hydrogen produced from water electrolysis and from fossil fuels is due to the extremely low cost to produce hydrogen from fossil fuels. For instance, the current levelised cost (including capital and

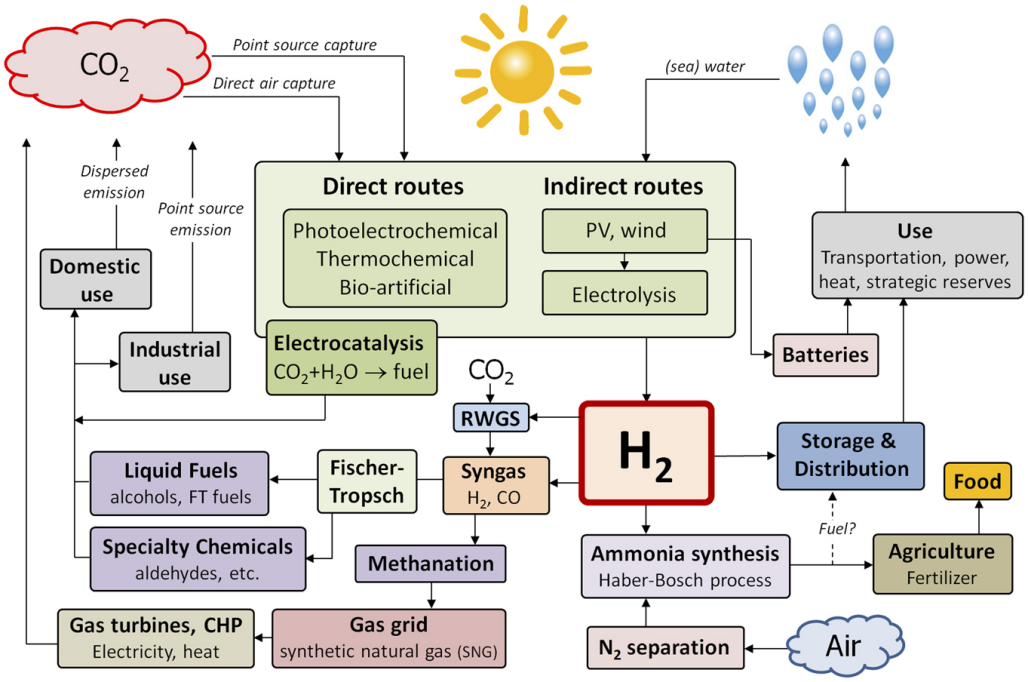

Figure 1.1: Scheme of a future energy infrastructure based on the hydrogen economy idea. Central in this scheme is the production of hydrogen through direct and indirect water splitting, using wind and sun as renewable and fossil-free energy sources. The hydrogen can then be used to produce carbon-, nitrogen-, and hydrogen-based chemical fuels through already existing large-scale infrastructure for methanation and Fischer–Tropsch syntheses or used in the Haber-Bosch process to produce ammonia.[3]

operating costs) of hydrogen production (LCH) through steam methane reforming is estimated at around \$1.25 per kg H_2 based on the linear relationship between natural gas prices and hydrogen production cost with natural gas prices lying around \$3.50 per GJ.[4] On the other hand, water electrolysis driven by the industrial coal-powered electricity price of \$0.05 per kWh^{-1} has an approximate cost of \$4.09 per kg H_2, which was calculated through an H2A[i] type analysis.[5] Another study showed a levelised cost of hydrogen produced through grid electrolysis to be \$5.5 per kg H_2, assuming an electrolysis system efficiency of 61% and a grid electricity cost of \$0.07 per kWh^{-1}.[6]

Reducing greenhouse gas emissions is one argument for switching towards a hydrogen economy. However, hydrogen should then be produced in another way as both SMR and electrolysis based on electricity from coal power plants emit more CO_2 (Figure 1.2) than if fossil fuels were to be used directly. A few greenhouse gas emission reduction strategies have been suggested, which, however, all come with a cost compared to the base cost of SMR. Carbon capture and sequestration (CCS) has been frequently proposed as a ways to reduce the CO_2 emissions originating from

[i] The H2A (hydrogen analysis) project was established at the initiative of the Department of Energy of the United States and provides modelling tools which enable users to assess the cost of producing and delivering hydrogen. More information can be found on https://www.hydrogen.energy.gov/h2a_analysis.html

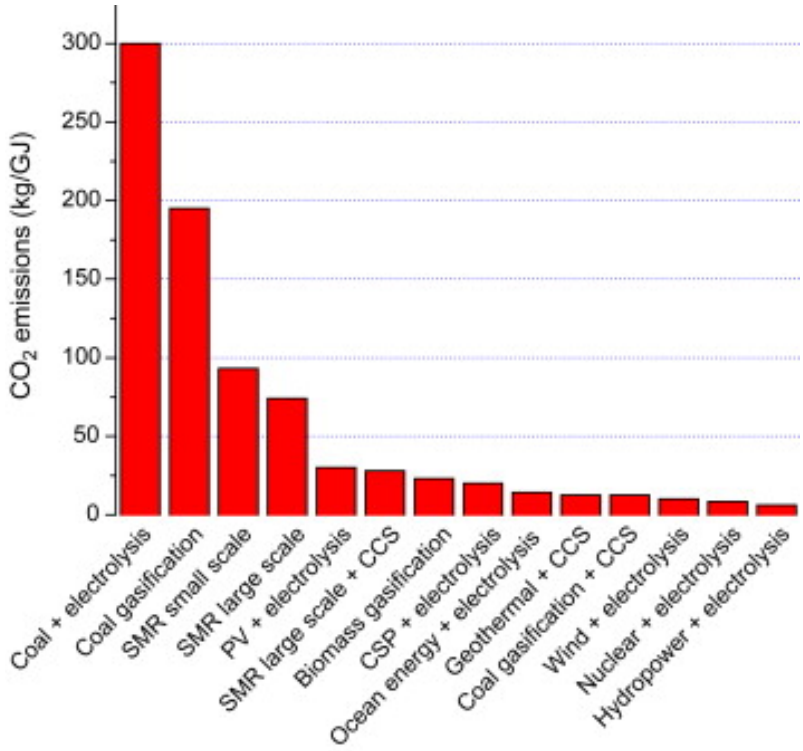

Figure 1.2: CO_2 emissions for different hydrogen production technologies.[4]

the reforming of fossil fuel feedstocks. Alternatively, methane pyrolysis, whereby hydrocarbons are decomposed at high temperatures in the absence of oxygen, yield lower greenhouse gas emissions, due to carbon being transformed into solid carbon black. Hydrogen can eventually also be produced through biomass gasification, which, when coupled to CCS, potentially yield negative CO_2 emissions, due to CO_2 being fixated by photosynthesis during growing processes. A promising but immature hydrogen production technology involves the direct conversion of nuclear heat through thermochemical cycles,[7] whereby the sulphur-iodine and copper chloride cycles have been identified as being most performant.[8] Although, the direct emissions from water electrolysis are very low, the indirect emissions related to power generation and electrolyser systems have to be considered, whereby renewable (solar, wind, hydro, geothermal) and nuclear power generation yield the lowest CO_2 emissions (Figure 1.2). Recently, Parkinson et al. made a life cycle assessment of all the above listed hydrogen production techniques in their current state, comparing the cost of mitigation and the proportion of decarbonization (Figure 1.3).[9] Herein, the decarbonization of fossil fuel based hydrogen production methods was regarded as being most cost-effective with, however, only middling decarbonization levels. Also, methane pyrolysis links high cost-effectiveness to moderate decarbonization levels, which, unfortunately suffers from cost variability, due to the dependence on the carbon black price. The use of nuclear energy is promising due to the high cost-effectiveness and significant carbon emission reductions, but its implementation could be complicated due to concerns with regards to proliferation and percep-

tions of safety together with the required high capital investment costs. Additionally, according to the authors, the studies regarding the conversion of nuclear heat through thermochemical cycles exhibited limited depth, transparency and reliability. Renewable water electrolysis also provides hydrogen with strongly reduced CO_2 emissions, which, can, however, not be implemented yet on a large scale due to the high production costs. Reducing the hydrogen production costs of electrolysis requires higher capacity factors, lower electrolyser costs and/or a low cost electricity supply.

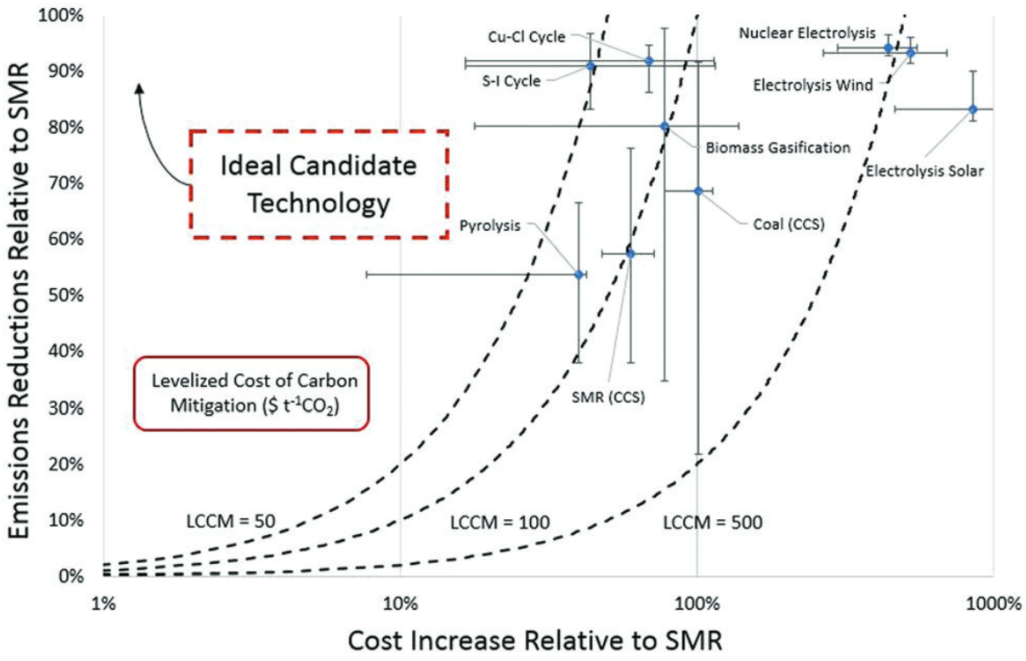

Figure 1.3: Proportional CO_2 emission reduction versus the percentual cost increase relative to steam methane reforming (SMR). LCCM corresponds to the levelised cost of carbon mitigation and is a measure for the extra cost related to emission reduction from hydrogen production per ton of CO_2 emitted compared to the emissions of hydrogen production through SMR.[9]

To assess the economics of solar hydrogen production and to provide an incentive to focus on certain research goals Shaner et al. made an extensive technoeconomic analysis of photovoltaic-electrolytic (PV-E) and photoelectrochemical (PEC) water splitting.[10] Herein, base-case PV-E with an electrolyser efficiency of 61%, a photovoltaic efficiency of 16%, a photovoltaic/electrolyser capacity factor of 0.204 and a photovoltaic area of 0.75 km^2 with current balance of system (BoS), electrolyser and PV costs would yield an LCH of \$12.1 per kg H_2 with the overall plant efficiency having the largest impact on the LCH.[10] Because of the high BoS costs, halving the PV module and electrolyser cost would only result in a reduced LCH of \$10 per kg H_2 whereas doubling the plant efficiency by increasing the capacity or using more efficient photovoltaics (PV) could reduce the LCH to \$6 per kg H_2 (Figure 1.4a). The authors further specified the effect of the elec-

trolyser and PV module cost on the LCH (Figure 1.4b). When the PV levelised cost of electricity (LCOE) would drop to about $0.02, which can be expected by 2050 in some regions in the EU, a drop in PV capital cost to about $0.50 per watt was calculated, assuming a PV lifetime of 25 years and a capacity factor of 30%. Moreover, by augmenting PV-E with wind energy, an electrolyser capacity up to 75% can be obtained, so that only an electrolyser capital cost reduction to $0.6 per watt is needed to obtain an LCH of $3 per kg H_2 (Figure 1.4b). Another option to reduce the LCH of PV-E is to allow the electrolysis installation to run on grid electricity during low solar power output, a technique which is called grid supplemented photovoltaic electrolysis (GSPV-E). Although, GSPV-E requires a higher BoS cost due to the implementation of additional power electronics such as AC-DC converters, a remarkably lower LCH, $6.1 per kg H_2, was calculated with respect to PV-E, because of an increased electrolyser capacity of 97%.[10]

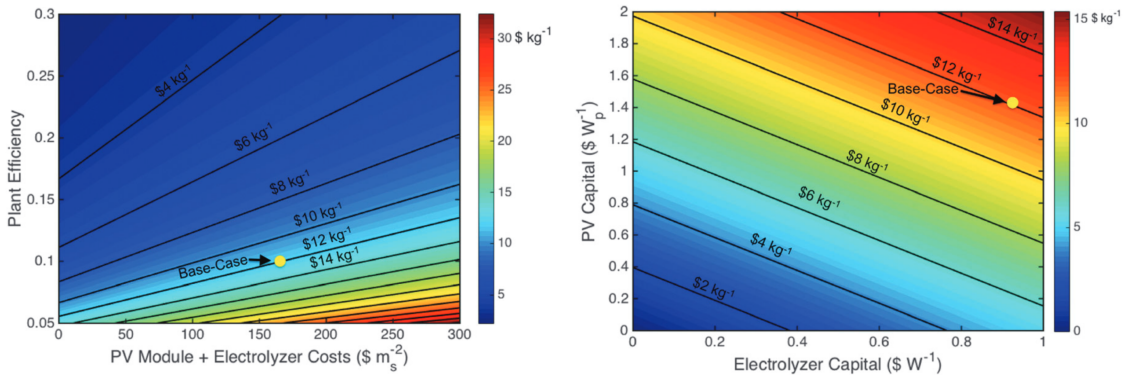

(a) (b)

Figure 1.4: Contour plot of LCH ($ per kg H_2) for the PV-E case (a) as a function of the plant efficiency and the areal capital expense of PV modules and electrolysers normalised by the necessary solar collection area ($ per square meter) and (b) as a function of the electrolyser and PV capital expenses ($ per watt). The yellow circle indicates the base case.[10]

The combination of PV and/or wind facilities with electrolysers is an indirect way of water splitting. Alternatively, water splitting could be done directly through a process called photoelectrochemical (PEC) water splitting, which basically integrates light absorbers with electrocatalysts into one monolithic device, or through a particle suspension, which is designed for overall water splitting or for hydrogen/oxygen evolution using a redox mediator for charge transfer between particles. Pinaud et al. described how these direct water splitting processes could be integrated into large scale centralised reactors and calculated the LCH of each of these reactors through the H2A model by considering the current lab scale performance of the direct water splitting techniques, and the capital and operating costs of the reactors and auxiliaries.[11] The authors came up with 4 different realistic reactor types (Figure 1.5), making the distinction between particulate and photoelectrochemical water splitting. They calculated that a simple PEC array (type 3 reactor) operating at a solar-to-hydrogen conversion efficiency (STH) of 10% would have an LCH of

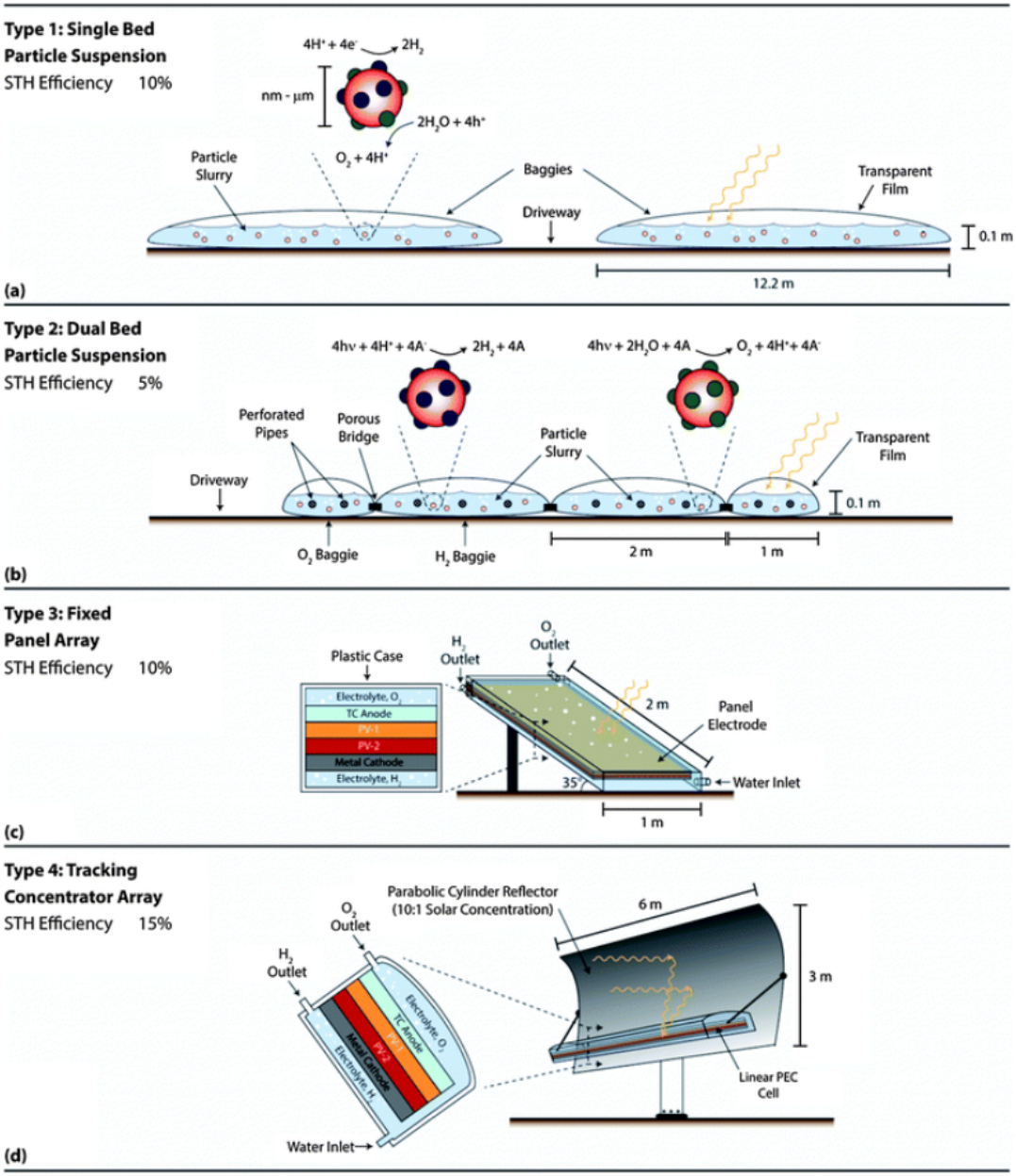

Figure 1.5: Four different direct water splitting reactor types: (a) baggies containing a particle slurry which directly converts sunlight and water into hydrogen and oxygen, (b) an alternating series of two different baggies each containing a particle slurry which is responsible for oxygen or hydrogen evolution, (c) A PEC panel containing several photoactive layers sandwiched between a cathode for hydrogen evolution and an anode for oxygen evolution, (d) a linear PEC panel in combination with a parabolic solar concentrator.[11]

\$10.40 per kg H_2, while supplementing the PEC array with a solar concentrator (type 4 reactor) now operating at 15% STH would lower the cost to \$4.10 per kg H_2 due to the tenfold increase in solar concentration. Meanwhile, Shaner et al. calculated an LCH of \$11.4 per kg H_2 for a type 3 PEC system (15% STH) and an LCH of \$9.2 per kg H_2 for a type 4 PEC cell working at an STH of 20%.[10] Type 3 and type 4 PEC reactors have only a slightly lower estimated LCH than what was estimated for PV-E (see above), assuming a 10% STH for both cases. The lower LCH for PEC mainly stems from the approximate 2x lower BoS costs of a PEC device due to a more cost efficient energy transmission and because they have only 1 set of hard BoS costs compared to the two sets of BoS costs of a photovoltaics-electrolyser combination. However, the base case PEC assumptions, an STH of 10% and 10 year lifetime, have not yet been demonstrated on a lab scale, whereas PV panels and electrolysers, which together can operate at the same base assumptions, can already be produced on an industrial scale.[6,12,13] Thus, PV-E is a technology which is much more mature with proven electrolyser and photovoltaics industries. PV-E has the advantage that the systems for light absorption and water electrolysis can be separately optimized, which is less complicated than to design one device which can do both in a stable, safe and efficient way. For instance, the light absorber in PEC devices has to be stable in an electrolyte during operation for a prolonged period of time, the amount of electrocatalysts need to be limited to avoid parasitic light absorption and the extra interfaces need to be optimised for charge extraction without generating surface state induced charge carrier recombination. Therefore, critics assume that PEC devices which are cosmetically similar (type 3 and type 4) to PV-E systems will not be able to compete with PV-E on a mid to long term.[14,15] More so, because advancements in PEC design which originate from electrolyser or PV technology such as buried junctions or usage of earth-abundant electrocatalysts would not give PEC systems a competitive edge over PV-E, because PV-E would also benefit from these advancements.[16,17]

Due to the higher simplicity, and thus a lower BoS cost, of particulate based water splitting reactors lower LCHs could potentially be reached. In the technoeconomic analysis of Pinaud et al. an LCH of \$1.60 per kg H_2 was calculated for a single bed particle suspension operating at an STH of 10% and an LCH of \$3.20 per kg H_2 was calculated for a dual bed particle slurry with an STH of 5%, thus indicating that such reactor designs (Figure 1.5) could be competitive to PV-E water splitting or even steam methane reforming.[11] In the calculations a strong sensitivity of the LCH on the efficiency was established, so that research efforts into particulate based water splitting should focus on improving the efficiency. However, on a lab scale, the state of the art particulate based water splitting system could only reach an STH of around 1%[18,19] and for a real device, a flat panel reactor of 1 m^2 operating under direct sunlight, an even lower efficiency, STH of 0.4%, was measured.[20] Possible technological limitations for type 1 and type 2 PEC reactor types are the safe operation of a single bed particle suspension system due to mixing of O_2 and H_2 and the long distances redox shuttles need to travel between the two different particles in a type 2 reactor, respectively.

All in all, renewable ways of water splitting could be viable in the foreseeable future if fur-

ther efficiency improvements, capacity increases and cost reductions can be realised in PV and electrolysers, a breakthrough in PEC or particulate water splitting is achieved or a large enough tax on CO_2 emissions is implemented. The strong reliance of the LCH on the efficiency of PV-E, PEC and particulate based water splitting is an invitation to further the applied and fundamental research into these aspiring technologies.

1.2 Thesis overview and structure

As outlined above, particulate water splitting has the potential to become a cost competitive and green hydrogen production alternative to steam methane reforming, if the above listed base conditions, 10% STH + 5 years lifetime for Type 1 and 5% STH + 5 years lifetime for Type 2,[11] are fulfilled. Therefore, we opted to prepare new heterostructured particulate powders for water splitting as well as to improve the understanding of the junction properties of the solid state interfaces inherent to heterostructures. The ultimate goal was to come up with a working type 2 particulate water splitting system. Hence, we selected two semiconducting oxides, one which is appropriate for water oxidation, $BiVO_4$,[21] and one which should be suitable for water reduction, $CuFeO_2$.[22] These oxides have, however, a few shortcomings, such as charge carrier recombination and unfavourable water redox kinetics, which prevent them from reaching their theoretically predicted water splitting capacities.[22–25] A recognized solution is the creation of heterostructures by attaching additional contact materials onto the main photoabsorber.[26] However, in most cases the precise effects of those heterostructures are not fully understood yet, as many characteristics of the main photoabsorber, including surface passivation,[27] charge carrier separation[28] and surface redox kinetics,[25] can be altered through the incorporation of an additional contact material. Special mention goes to the remarkable finding that for $\{010\}/\{011\}$ dual facet exposed $BiVO_4$ truncated bipyramidal shaped particles, anisotropic charge carrier separation and accumulation takes place.[29] Due to the anisotropic charge accumulation, anisotropic heterostructures, with an oxidation cocatalyst on one facet and a reduction cocatalyst on the other, could be created through facet-selective photoreduction and photo-oxidation reactions.[30] Dual cocatalyst coated $BiVO_4$ heterostructures demonstrated an up to two orders of magnitude increased water oxidation performance compared to bare $\{010\}/\{110\}$ dual facet exposed $BiVO_4$ particles, due to a simultaneous optimization of charge carrier separation and synergistic surface redox kinetics.[25] Given this landmark finding, we wanted to develop novel anisotropic heterostructures based on anisotropically shaped $BiVO_4$ and $CuFeO_2$. Additionally, due to the current open questions regarding the effects of heterostructures, we analysed the interfacial characteristics of selected $BiVO_4$ and $CuFeO_2$ heterostructures through in situ photoelectron spectroscopy and discussed how the results could improve the understanding of oxide heterostructure interfaces with respect to charge carrier separation and interfacial electronic structure.

Chapter 2 gives an introduction to the broad topic of photocatalysis, photochemical water splitting and interface analysis. The emphasis is laid on fundamental principles and on the state of

the art heterostructured particulate water splitting systems. Furthermore, the specific evolution of $BiVO_4$ and $CuFeO_2$ based systems is detailed.

Chapter 3 encloses the experimental details of all synthesis and analysis techniques used during this work. Where relevant a short introduction to the used apparatuses is given. Also, all recipes are denoted in detail.

In Chapter 4 the results regarding the development of anisotropic $BiVO_4$ heterostructures will be given and discussed. First, the upscaling of the $\{010\}/\{110\}$ dual facet exposed $BiVO_4$ powder synthesis is detailed. Afterwards, the preparation of heterostructured $BiVO_4/NiO_xOH_y$, $BiVO_4/CoO_xOH_y$, $BiVO_4$/Ag and $BiVO_4$/Pt through photodeposition is reviewed and the regioselectivity of the deposits is described through electron microscopy. Subsequently, the dye degradation and water oxidation performance of the heterostructured $BiVO_4$ powders are discussed.

Chapter 5 presents an overview of the $BiVO_4$ based interface experiments, carried out through a combination of thin film sputtering and photoelectron spectroscopy. This Chapter is opened with an overview of the surface and bulk characteristics of the two $BiVO_4$ thin film substrates, which were used to perform the interface experiments, denoted as gradient $BiVO_4$ and PLD $BiVO_4$. Next, the results of the interface experiments of $BiVO_4$ with the high work function (WF) materials, NiO, CoO_x and RuO_2, and the low work function material tin-doped In_2O_3 (ITO) are described. Subsequently, the results of the interface experiments are thoroughly discussed to evaluate the interfacial properties of the analysed heterostructures, bulk Fermi level pinning phenomena and solid state band alignment.

The techniques and knowledge acquired in Chapter 4 and 5 were used to develop and study novel $CuFeO_2$ heterostructures, which is the topic of Chapter 6. The Chapter starts with a description of the upscaling of the synthesis of 2H-$CuFeO_2$ hexagonal nanoplatelets, which were used as the anisotropic substrates during the photodeposition experiments. Specifically, Pt, Ag and NiO_xOH_y were deposited, whereby the regioselectivity of the deposits was examined through electron microscopy. Thereafter, the sacrificial water reduction efficiency of the heterostructures was tested. Finally, interface experiments were performed with $CuFeO_2$ pellets, prepared by pressing $CuFeO_2$ powder, as substrates, and ITO and water as contacts.

References

(1) Simbollotti, G. *IEA Energy Technology Essentials: Hydrogen Production & Distribution*; tech. rep.; 2017.

(2) Stiegel, G. J.; Ramezan, M. Hydrogen from coal gasification: An economical pathway to a sustainable energy future. *Int. J. Coal Geol.* **2006**, *65*, 173–190.

(3) van de Krol, R.; Parkinson, B. A. Perspectives on the photoelectrochemical storage of solar energy. *MRS Energy Sustain.* **2017**, *4*, E13.

(4) Lemus, R. G.; Martínez Duart, J. M. Updated hydrogen production costs and parities for conventional and renewable technologies. *Int. J. Hydrogen Energy* **2010**, *35*, 3929–3936.

(5) Kroposki, B.; Levene, J.; Harrison, K.; Sen, P.; Novachek, F. *Electrolysis: Information and Opportunities for Electric Power Utilities*; tech. rep.; Golden, CO: National Renewable Energy Laboratory (NREL), 2006.

(6) Colella, W. G.; James, B. D.; Moton, J. M. *Hydrogen Pathways Analysis for Polymer Electrolyte Membrane (PEM) Electrolysis*; tech. rep.; Strategic Analysis Inc., 2014.

(7) Bartels, J. R.; Pate, M. B.; Olson, N. K. An economic survey of hydrogen production from conventional and alternative energy sources. *Int. J. Hydrogen Energy* **2010**, *35*, 8371–8384.

(8) Tolga Balta, M.; Dincer, I.; Hepbasli, A. Thermodynamic assessment of geothermal energy use in hydrogen production. *Int. J. Hydrogen Energy* **2009**, *34*, 2925–2939.

(9) Parkinson, B.; Balcombe, P.; Speirs, J. F.; Hawkes, A. D.; Hellgardt, K. Levelized cost of CO_2 mitigation from hydrogen production routes. *Energy Environ. Sci.* **2019**, *12*, 19–40.

(10) Shaner, M. R.; Atwater, H. A.; Lewis, N. S.; McFarland, E. W. A comparative technoeconomic analysis of renewable hydrogen production using solar energy. *Energy Environ. Sci.* **2016**, *9*, 2354–2371.

(11) Pinaud, B. A.; Benck, J. D.; Seitz, L. C.; Forman, A. J.; Chen, Z.; Deutsch, T. G.; James, B. D.; Baum, K. N.; Baum, G. N.; Ardo, S.; Wang, H.; Miller, E.; Jaramillo, T. F. Technical and economic feasibility of centralized facilities for solar hydrogen production via photocatalysis and photoelectrochemistry. *Energy Environ. Sci.* **2013**, *6*, 1983–2002.

(12) Feldman, D.; Margolis, R.; Bof. Daniel *Q2/Q3 '14 Solar Industry Update*; tech. rep.; U.S. Department of Energy: SunShot, 2014.

(13) Honeyman, C.; Litvak, N.; Kann, S.; Mehta, S.; Shiao, M.; Jones, J.; Kimbis, T.; Baca, J.; Rumery, S.; Holm, A. *Q2 2014 U.S. Solar Market Insight*; tech. rep.; Greentech Media Inc. and Solar Energy Industries Association, 2014.

(14) Ardo, S. et al. Pathways to electrochemical solar-hydrogen technologies. *Energy Environ. Sci.* **2018**, *11*, 2768–2783.

(15) Jacobsson, T. J. Photoelectrochemical water splitting: an idea heading towards obsolescence? *Energy Environ. Sci.* **2018**, *11*, 1977–1979.

(16) Jacobsson, T. J.; Fjällström, V.; Edoff, M.; Edvinsson, T. Sustainable solar hydrogen production: from photoelectrochemical cells to PV-electrolyzers and back again. *Energy Environ. Sci.* **2014**, *7*, 2056–2070.

(17) Liu, X.; Wang, X.; Yuan, X.; Dong, W.; Huang, F. Rational composition and structural design of in situ grown nickel-based electrocatalysts for efficient water electrolysis. *J. Mater. Chem. A* **2016**, *4*, 167–172.

(18) Wang, Q.; Hisatomi, T.; Jia, Q.; Tokudome, H.; Zhong, M.; Wang, C.; Pan, Z.; Takata, T.; Nakabayashi, M.; Shibata, N.; Li, Y.; Sharp, I. D.; Kudo, A.; Yamada, T.; Domen, K. Scalable water splitting on particulate photocatalyst sheets with a solar-to-hydrogen energy conversion efficiency exceeding 1%. *Nat. Mater.* **2016**, *15*, 611–615.

(19) Kibria, M. G.; Chowdhury, F. A.; Zhao, S.; AlOtaibi, B.; Trudeau, M. L.; Guo, H.; Mi, Z. Visible light-driven efficient overall water splitting using p-type metal-nitride nanowire arrays. *Nat. Commun.* **2015**, *6*, 6797.

(20) Goto, Y.; Hisatomi, T.; Wang, Q.; Higashi, T.; Ishikiriyama, K.; Maeda, T.; Sakata, Y.; Okunaka, S.; Tokudome, H.; Katayama, M.; Akiyama, S.; Nishiyama, H.; Inoue, Y.; Takewaki, T.; Setoyama, T.; Minegishi, T.; Takata, T.; Yamada, T.; Domen, K. A Particulate Photocatalyst Water-Splitting Panel for Large-Scale Solar Hydrogen Generation. *Joule* **2018**, *2*, 509–520.

(21) Cooper, J. K.; Gul, S.; Toma, F. M.; Chen, L.; Glans, P. A.; Guo, J.; Ager, J. W.; Yano, J.; Sharp, I. D. Electronic structure of monoclinic $BiVO_4$. *Chem. Mater.* **2014**, *26*, 5365–5373.

(22) Oh, Y.; Yang, W.; Tan, J.; Lee, H.; Park, J.; Moon, J. Photoelectrodes based on 2D opals assembled from Cu-delafossite double-shelled microspheres for an enhanced photoelectrochemical response. *Nanoscale* **2018**, *10*, 3720–3729.

(23) Xie, M.; Fu, X.; Jing, L.; Luan, P.; Feng, Y.; Fu, H. Long-Lived, Visible-Light-Excited Charge Carriers of TiO_2/$BiVO_4$ Nanocomposites and their Unexpected Photoactivity for Water Splitting. *Adv. Energy Mater.* **2014**, *4*, 1300995.

(24) Prévot, M. S.; Jeanbourquin, X. A.; Bourée, W. S.; Abdi, F.; Friedrich, D.; van de Krol, R.; Guijarro, N.; Le Formal, F.; Sivula, K. Evaluating Charge Carrier Transport and Surface States in $CuFeO_2$ Photocathodes. *Chem. Mater.* **2017**, *29*, 4952–4962.

(25) Li, R.; Han, H.; Zhang, F.; Wang, D.; Li, C. Highly efficient photocatalysts constructed by rational assembly of dual-cocatalysts separately on different facets of $BiVO_4$. *Energy Environ. Sci.* **2014**, *7*, 1369–1376.

(26) Kudo, A.; Miseki, Y. Heterogeneous photocatalyst materials for water splitting. *Chem. Soc. Rev.* **2009**, *38*, 253–278.

(27) Zachäus, C.; Abdi, F. F.; Peter, L. M.; Van De Krol, R. Photocurrent of $BiVO_4$ is limited by surface recombination, not surface catalysis. *Chem. Sci.* **2017**, *8*, 3712–3719.

(28) Barroso, M.; Cowan, A. J.; Pendlebury, S. R.; Grätzel, M.; Klug, D. R.; Durrant, J. R. The role of cobalt phosphate in enhancing the photocatalytic activity of α-Fe_2O_3 toward water oxidation. *J. Am. Chem. Soc.* **2011**, *133*, 14868–14871.

(29) Wang, D.; Jiang, H.; Zong, X.; Xu, Q.; Ma, Y.; Li, G.; Li, C. Crystal Facet Dependence of Water Oxidation on $BiVO_4$ Sheets under Visible Light Irradiation. *Chem. - A Eur. J.* **2011**, *17*, 1275–1282.

(30) Li, R.; Zhang, F.; Wang, D.; Yang, J.; Li, M.; Zhu, J.; Zhou, X.; Han, H.; Li, C. Spatial separation of photogenerated electrons and holes among $\{010\}$ and $\{110\}$ crystal facets of $BiVO_4$. *Nat. Commun.* **2013**, *4*, 1432.

Chapter 2

Introduction

The fundamental concepts presented in this chapter have been deduced from the following main references, according to topic: General solid state physics,[1] semiconductor device physics,[2,3] semiconductor physics and interfaces,[4] photocatalysis,[5] photoelectrochemical water splitting[6] and photoelectron spectroscopy.[7]

2.1 Photo(electro)chemical water splitting

2.1.1 Fundamentals of semiconductors

Photo(electro)chemical water splitting is a photocatalytic process, wherein semiconductors utilize the energy obtained from light absorption to split water into hydrogen and oxygen. Although, molecular water splitting exists as well and hybrid molecular/inorganic water splitting is on the rise, photo(electro)chemical water splitting in this work refers exclusively to the process performed with inorganic semiconductors. Semiconductors distinguish themselves from conductors and insulators through their intermediate electrical conductivity, for which an explanation can be found in the energy band model. The energy band model can be seen as an extension to the LCAO (linear combination of atomic orbitals) model, whereby molecular orbitals of a molecule are considered to be the result of linear combinations of the atomic orbitals of the atoms constituting the molecule. Semiconductors have, just like many other solid state materials, a crystalline structure, which is built-up through a repetitive three-dimensional translation of unit cells. The unit cells are the smallest grouping of atoms, which constitute the repeating pattern. In contrast to a molecule, which in most cases only consist of a few to a few 100s of atoms, macromolecules not included, a crystalline structure contains around 10^{22} unit cells per cm^3. Now, when such a large number of atomic orbitals overlap, the resulting ”molecular” orbitals of similar nature (e.g. combination of 1s atomic orbitals) will be so closely spaced in energy that they are considered to form a continuum of electronic states, also called an energy band (e.g. the 1s atomic orbitals form a 1s band). For semiconductors, a series of bands will be completely filled with electrons,

whereby the band containing the electrons with the highest energies is denoted as the valence band (VB),[i] and the empty band closest in energy to the valence band is considered to be the conduction band (CB). In between those bands there is a "gap", generally denoted as band gap, where no electronic states exist. Band gaps vary in the range of 0.1 eV — 4.0 eV, thus in the UV-Vis-NIR (ultraviolet-visible-near infrared) spectral region. Figure 2.1 shows, for instance, that the valence band (VB) and conduction band (CB) of silicon result from the overlapping of $3sp^3$ hybrid atomic orbitals of silicon atoms periodically ordered in a crystalline lattice.

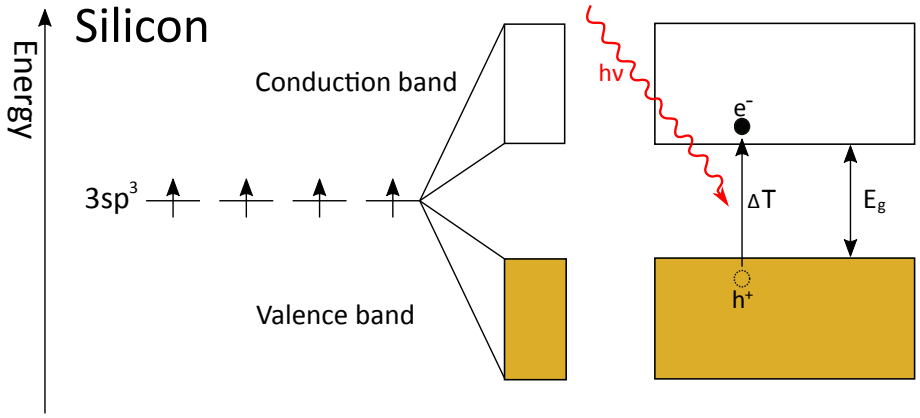

Figure 2.1: Scheme showing how the $3sp^3$ hybrid atomic orbitals of silicon combine into bands separated by a band gap.

Electrical conductivity depends on the number of mobile charge carriers and to be considered mobile, charge carriers should have access to empty states, which are close in energy. Due to semiconductors having a band gap, which do not contain any electronic states, a considerable amount of energy, be it thermal or light, is required to allow the electrons to cross the band gap and reach the conduction band where the electrons have access to empty states. The electrons that are excited to the conduction band leave behind empty states or "holes" in the valence band, which are also considered to be mobile charge carriers, as electrons at the top of the valence band can move into these empty states. In the absence of light, the probability that a state of energy E is filled with an electron, f(E), is governed by the Fermi-Dirac distribution, which takes into account the Pauli exclusion principle which states that two or more identical fermions, electrons being fermions, cannot occupy the same electronic state:

$$f(E) = \frac{1}{1 + e^{(E-\mu)/k_B T}} \tag{2.1}$$

where $k_B T$ is the product of the temperature and the Boltzmann constant, and μ stands for the total chemical potential of the electrons, which in semiconductor physics is also commonly denoted as the Fermi level (E_F). The mobile charge carrier concentration, for electrons n and

[i] Within this thesis the denotion of the band energies is in relation to the band position in the used energy diagrams: higher (lower) lying bands have a lower (higher) distance to the vacuum level with increased (reduced) electron energy.

for holes p, can then be obtained by multiplying the Fermi-Dirac distribution with the density of states D(E). Figure 2.2 shows the Fermi-Dirac distribution, the density of states distribution, and the resulting hole and electron charge carrier concentration for an intrinsic, an n-type and a p-type semiconductor. n-type and p-type semiconductors distinguish themselves from intrinsic semiconductors through their higher electron and hole charge carrier concentration, respectively. A higher charge carrier concentration may be caused by intrinsic defects or due to the presence of impurities. A distinction is made between acceptor and donor impurities which may increase the electron and hole charge carrier concentration, relatively, as these impurities, associated with inter-gap states, tend to ionize and introduce additional charge carriers into the bands. The controlled incorporation of impurities is called doping. In this way, p-type silicon can be obtained by doping with a lower valence element (acceptor), such as boron, and n-type silicon can be obtained by doping with a higher valence element (donor), such as phosphorus.

The distinction between direct and indirect semiconductors is another semiconductor property that has to be considered with regards to photocatalysis (Figure 2.3). For all interactions between elementary particles, including electrons, holes, photons and phonons (lattice vibrations) the requirement of conservation of energy and conservation of crystal momentum (k-vector)[ii] has to be fulfilled. Now, semiconductors are called direct when their valence band maximum (VBM) and conduction band minimum are associated with the same crystal momentum, as is the case for some III-V semiconductors like GaAs and InP. When the crystal momentum is different, a semiconductor is considered to be indirect, which is the case, for instance, for Ge and Si. A process which one tries to avoid in photocatalysis is charge carrier recombination, whereby light-induced holes and electrons annihilate each other with the release of energy in the form of phonons or photons. Recombination is in direct competition with photocatalysis, due to the electrons and holes not being involved in chemical redox reactions; the actual goal of photocatalysis. In direct semiconductors radiative recombination with the release of photons can easily take place, because the electron-hole annihilation preserves the crystal momentum and photons with energies of a few eV have almost zero momentum. In contrast, radiative recombination in indirect semiconductors necessitate the emission or absorption of a phonon to compensate for the momentum difference between the hole and the electron. The indirect photon-phonon recombination process in indirect semiconductors has a lower probability than the direct radiative recombination in direct semiconductors. Therefore, indirect semiconductors are more suitable for photocatalysis.

In this Section, the energy band model concept has only been described briefly. If one would like to have a more complete derivation of the theory and to gain a better understanding on

[ii] The crystal momentum $P_{crystal}$ is defined as $P_{crystal} \equiv \hbar k$ with $\hbar$ being the reduced Planck constant and k the wave vector. The wave vector is a consequence of Bloch's theorem, wherein the motion of electrons in a crystal lattice are considered to be subjected to an infinite periodic potential. According to Bloch's theorem, the single particle wavefunction (ψ_n) of an electron in a crystalline lattice can be written as: $\psi_n = e^{ikx} u_{nk}(x)$, $u_{nk}(x+a) = u_{nk}(x)$. Hence, the single particle wave function finds its stationary state solutions in terms of a periodic function u(x) multiplied by a plane wave, whereby the wave vector k can be seen as a representation of the stationary state solutions.

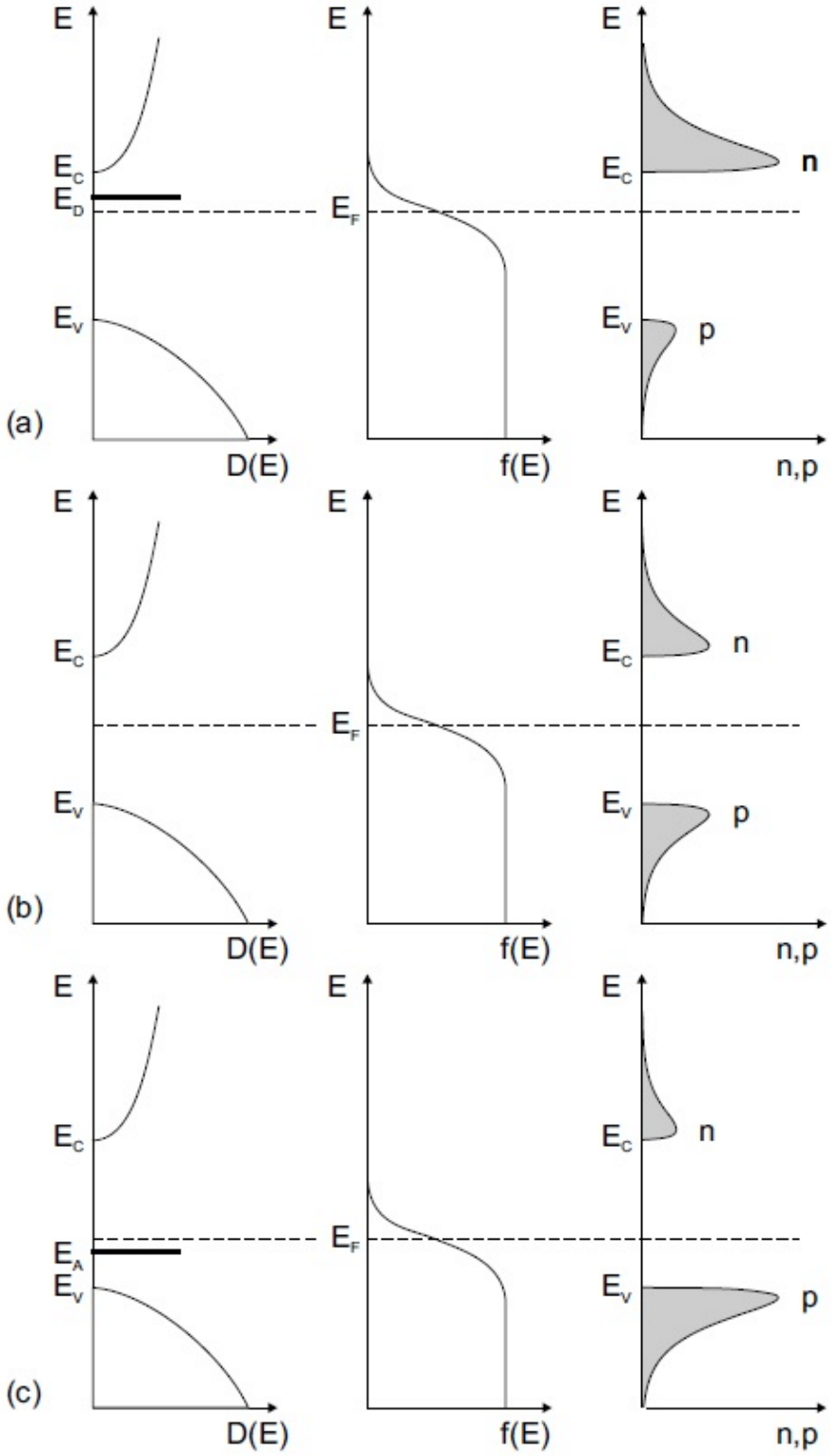

Figure 2.2: (a) n-type semiconductor, (b) intrinsic semiconductor, (c) p-type semiconductor. Left column: density of states D(E); Middle column: Fermi distribution f(E); Right column: carrier concentration (n,p). n and p are the concentrations of electrons and holes in the conduction and valence bands. E_C: conduction band minimum, E_V: valence band maximum, E_F: Fermi energy level, E_D: donor ionization energy, E_A: acceptor ionization energy.[8]

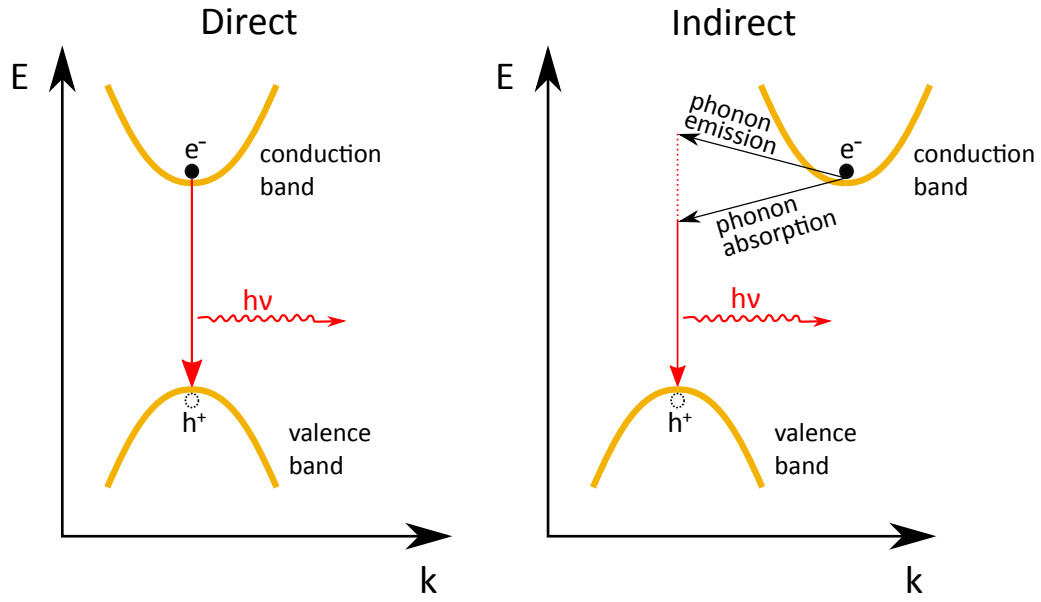

Figure 2.3: Schematic that shows the radiative recombination mechanism for direct and indirect semiconductors.

semiconductor properties, I would recommend the reader to read through "Band Theory and Electronic Properties of Solids" by John Singleton.[9] In addition, readers are invited to read "Physics and Technology of Semiconductor Devices" by Andy Grove[3] or "Physics of Semiconductor Devices" by Sze[2] to learn how semiconductor physics play a role in the design of semiconductor-based devices.

2.1.2 Photocatalysis

As defined by the International Union of Pure and Applied Chemistry (IUPAC), photocatalysis is the initiation or the change in rate of a chemical reaction under the action of infrared, visible or ultraviolet radiation in the presence of a substance, the photocatalyst, which absorbs the light and is involved in the chemical transformation of the reaction partners.[10] According to this definition, a semiconductor based photocatalytic process follows three steps (Figure 2.4): 1) photons with an energy larger than the band gap are absorbed, leading to the creation of electron-hole pairs, 2) the electron-hole pairs are separated from each other, followed by charge carrier flow towards the semiconductor surface, 3) adsorbed reactants participate in redox reactions and consume the surface accumulated charge carriers.

However, several other processes compete with photocatalysis (Figure 2.5). As explained in the previous Section, the light induced electron-hole pairs can recombine again, whereby a distinction is made between surface and bulk recombination. Bulk recombination in indirect semiconductors mainly take place because of improper charge carrier separation and limited diffusion lengths. The charge carrier diffusion length L depends on the charge carrier lifetime τ_{lt}

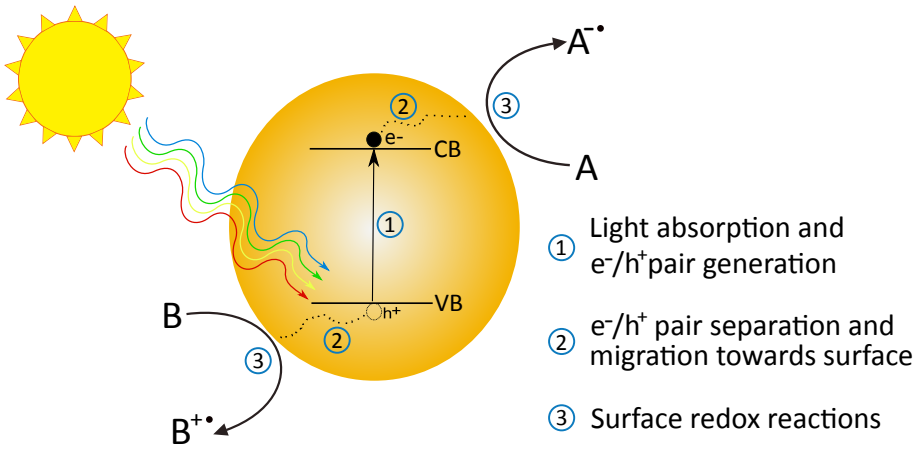

Figure 2.4: Photocatalysis scheme showing how light can be used by a semiconductor to initiate redox reactions at the semiconductor surface. e^-: electron, h^+: hole, VB: valence band, CB: conduction band.

and on the diffusion coefficient D according to:

$$L = \sqrt{D.\tau_{lt}} \tag{2.2}$$

whereby the diffusion coefficient according to the Einstein relation can be written as:

$$D = \mu.\frac{k_B T}{e} \tag{2.3}$$

with e being the elementary charge and μ being the mobility of the charge carriers. Charge carrier mobility is defined as the proportional constant which relates the velocity of a charge carrier (v_D) moving through a particular semiconductor under the influence of an electric field E:

$$v_D = \mu.E \tag{2.4}$$

In a simple model, where charge carriers are considered to be delocalized, i.e. not attached to individual atoms, mobility depends mostly on the scattering time τ_{sc}, which is the average time between scattering events. A scattering event namely negatively impacts the drift velocity, as the acceleration of the charge carrier by the electric field is stopped and the energy and/or direction of the charge carrier is changed. Several bulk scattering events have been identified, including ionized impurity scattering, defect scattering, phonon scattering, inelastic scattering, electron-electron scattering and some other minor scattering events. The exact relation between μ and τ_{sc}, for delocalized electrons, becomes:

$$\mu = \frac{e.\tau_{sc}}{m^*} \tag{2.5}$$

with m^* being the effective mass of the charge carriers. The notion of an effective mass is a repercussion of the above-discussed band theory and originates from the different motion of charge carriers in a periodic potential, as found in crystalline solids, with respect to the motion of an electron in a vacuum. The effective mass is material dependent and describes the mass a charge carrier seems to have in response to a certain force. The effective mass of electrons m_e^* and holes m_h^* differs in most cases from each other and is related to the density of states near the conduction band minimum N_C and valence band maximum N_V, relatively. For an ideal semiconductor with parabolic valence and conduction band structures near the band edges:

$$N_C = 2\left(\frac{2\pi m_e^* k_B T}{h^2}\right)^{\frac{3}{2}} \tag{2.6}$$

$$N_V = 2\left(\frac{2\pi m_h^* k_B T}{h^2}\right)^{\frac{3}{2}} \tag{2.7}$$

The assumption of a parabolic band structure is valid for many semiconductor valence bands, such as for Ge, Si and GaAs, and for some semiconductor conduction bands, such as for GaAs. For asymmetric bands, such as the conduction band of Si, the effective mass also depends slightly on temperature. For the semiconductors analysed in this work, $BiVO_4$ and $CuFeO_2$, charge carrier mobility is slightly more complicated as electrons and holes in these semiconductors are assumed to form polarons, which have considerably higher effective masses, as will be explained further in Section 2.3. In summary, the diffusion length depends on the charge carrier lifetime and the charge carrier mobility, whereby mobility is governed by scattering events and the effective masses of the charge carriers.

For indirect semiconductors, which contain bulk defects, charge carrier lifetime and mobility are strongly dependent on the number of defects. These defects can, namely, act as recombination centres and scattering centres, which reduce charge carrier lifetime and charge carrier mobility, respectively. Recombination at bulk defects, which act as deep level traps, whereby the energy is exchanged in the form of lattice vibration is also called Shockley-Read-Hall recombination.[11,12] Bulk defects intrinsic to a certain material cannot be overcome. However, structure related bulk defects such as dislocations, point defects and grain boundaries can be reduced by synthesizing the semiconductor under the ”right” conditions. For instance, monocrystalline silicon has a strongly reduced number of defects compared to polycrystalline silicon, which is why monocrystalline silicon photovoltaics generally outperform polycrystalline silicon photovoltaics.

Besides trying to optimize the charge carrier diffusion length, bulk recombination can be prevented through more efficient charge carrier separation. Charge carrier separation can be re-

alised through the introduction of an internal electric field and/or the implementation of charge selective contacts. Herein, interfaces play an important role. How semiconductor surfaces and interfaces influence charge carrier separation will be explained in greater detail in Section 2.2, wherein the physics and effects of semiconductor surfaces and interfaces are described. Another way to reduce bulk recombination is through nanostructuring, because then the distance between the point of light-induced electron-hole generation and the surface is reduced, which especially benefits semiconductors with limited diffusion lengths. Furthermore, nanostructuring leads to a decrease in the bulk-to-surface ratio, which has the advantage that the number of potential surface reaction sites is increased, but which may also increase the number of surface recombination centres. Additionally, light absorption may be negatively impacted, because semiconductor UV-Vis absorption lengths are on the scale of 100 — 1000 nm.

Although, intergap states are, just like for bulk recombination, the main cause for surface recombination, their origin in most cases is different and is related to the surface/interface structure of the semiconductor. Surface states are inherent to crystalline structures and originate from the sudden disruption of the crystalline lattice, with atoms at the surface having fewer bonding partners. Hence, some electrons at the surface do not engage in bonding, but form so-called dangling bonds, whereby the electrons are unpaired and reside in electronic energy levels inside the normally forbidden band gap. Strategies to reduce surface recombination are commonly referred to as surface passivation strategies and mainly try to reduce the number of dangling bonds or attempt to reduce the concentration of a particular carrier at the surface.

Instead of participating in the desired redox reactions or recombining at surface states, charge carriers arriving at the surface can also engage in corrosion processes, leading to a gradual dissolution of the semiconductor. In this case, the semiconductor should be coated by a protection layer, which shield the semiconductor surface from the electrolyte. Applying a conformal protection layer is relatively easily done for thin films, but can be cumbersome for particulate based systems.

All in all, photocatalytic systems can be plagued by a series of problems, which all necessitate tailor-made solutions depending on the semiconductor bulk and surface properties, and the desired application. At the moment, the optimization and implementation of photocatalysts is mainly studied with regards to the decomposition of air and water borne substances and photo(electro)chemical water splitting.

2.1.3 Fundamentals of photo(electro)chemical water splitting

Basically, water splitting processes focus on the dissociation of water into hydrogen and oxygen. The overall reaction is as follows:

$$2\,H_2O \rightleftharpoons 2\,H_2 + O_2$$

and can also be written in terms of two standard reduction reactions:

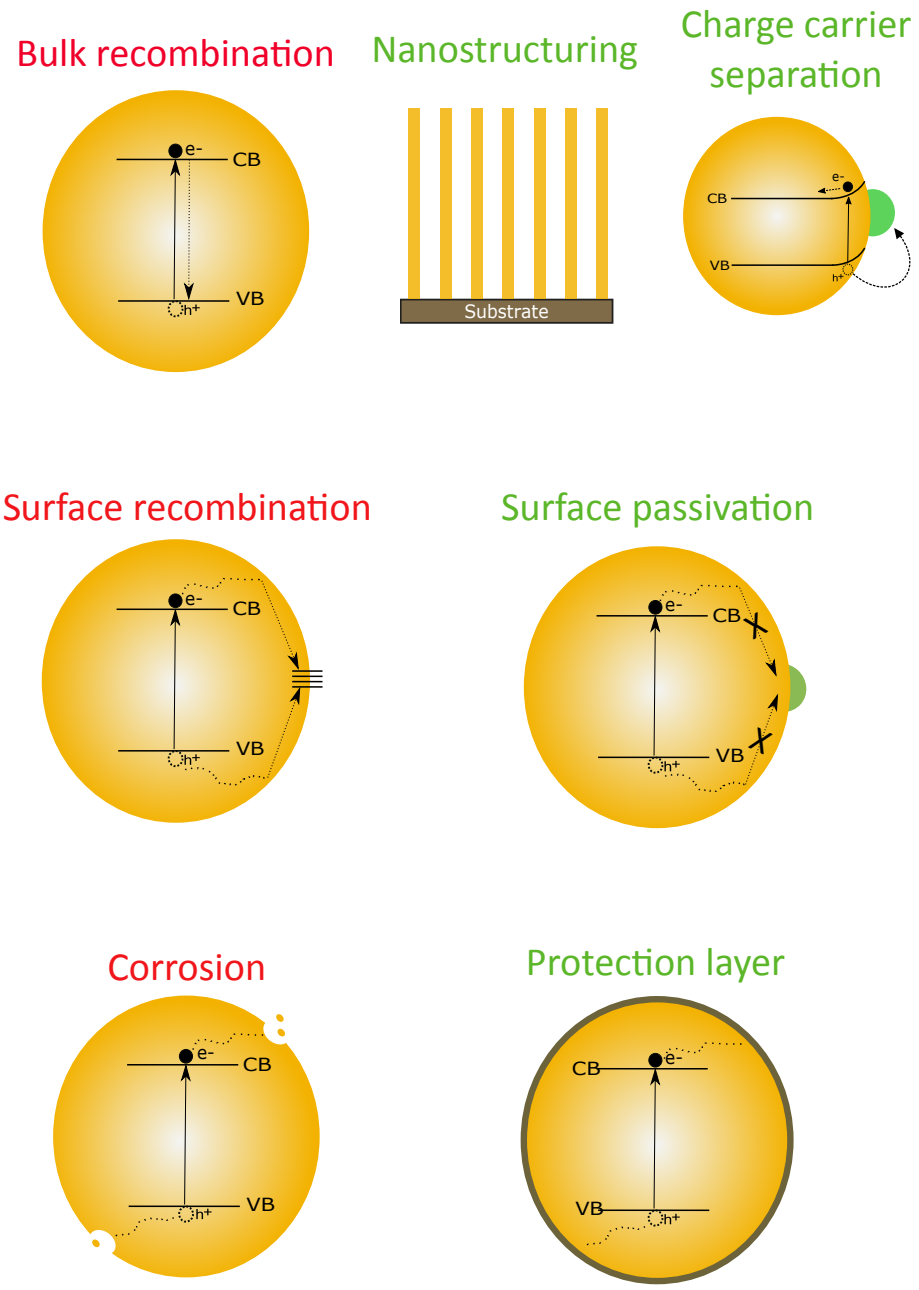

Figure 2.5: Common problems that may limit the efficiency of a photocatalytic material and solutions to overcome those problems.

$$2\,H^+ + 2\,e^- \rightleftharpoons H_2$$

$$O_2 + 4\,H^+ + 4\,e^- \rightleftharpoons 2\,H_2O$$

with H^+/H_2 and O_2/H_2O reactions yielding standard (pH = 0, 25 °C, 1 bar) reduction potentials of 0 V and 1.23 V relative to the standard hydrogen electrode (SHE), respectively. Hence, the total cell potential (E^0) amounts to -1.23 V and is associated with a strongly positive standard Gibbs free energy according to:

$$\Delta G^0 = -nFE^0 \tag{2.8}$$

with n being the number of electrons involved in the overall reaction and F being the Faraday constant. Herein, ΔG^0 amounts to 237.13 kJ mol^{-1}, meaning that the overall water splitting reaction is thermodynamically uphill, thus not spontaneous, for which a minimal potential difference of 1.23 V needs to be supplied. This potential difference can be supplied by an external bias and/or through the absorption of light, which leads to the concept of photo(electro)chemical water splitting.

According to the aforementioned IUPAC definition of photocatalysis, photo(electro)chemical water splitting can be understood as a photocatalytic process, because light allows the initiation of the energetically uphill water splitting reaction in the presence of an appropriate photocatalyst. Therefore, authors also commonly refer to photocatalytic water splitting instead of photo(electro)chemical water splitting, which is used primarily in this work.

To overcome the 1.23 V potential difference with light alone, a semiconductor has to be found with a band gap of at least 1.23 eV and with band positions that straddle the H^+/H_2 and O_2/H_2O reduction potentials. Figure 2.6 shows which binary semiconductors could be suitable for overall water splitting according to their band gap and band positions.[13] Herein, the band gap requirement of 2.2 eV is more strict than the minimal 1.23 eV to accommodate the need of overpotentials, due to activation barriers, shunt losses and resistances. As can be observed, not many binary semiconductors are suitable for overall water splitting and the ones that are, are normally wide-band gap semiconductors such as, TiO_2, ZnO and ZnS. Because their band gaps are above 3 eV, wide-band gap semiconductors are only able to absorb UV radiation, which makes them rather inefficient for solar water splitting, due to the small fraction of UV light in the solar spectrum (Figure 2.7). The main reason why mostly only wide-band gap oxides are suitable for water splitting is because of their valence band maxima, which lie in most cases far below the water oxidation potential (see Section 2.2.1.3 for a description on band edge position determination). The relatively low VBMs of oxides are mainly due to the low lying O2p states which make up most of the oxide valence band maxima. Binary II-VI and III-V semiconductors have generally higher valence band maxima, but they are often highly susceptible to photocorrosion.[14–16]

Due to the unsuitability of binary semiconductors for overall solar photochemical water splitting, one could select suitable ternary and quaternary semiconductors (Section 2.3) and/or select

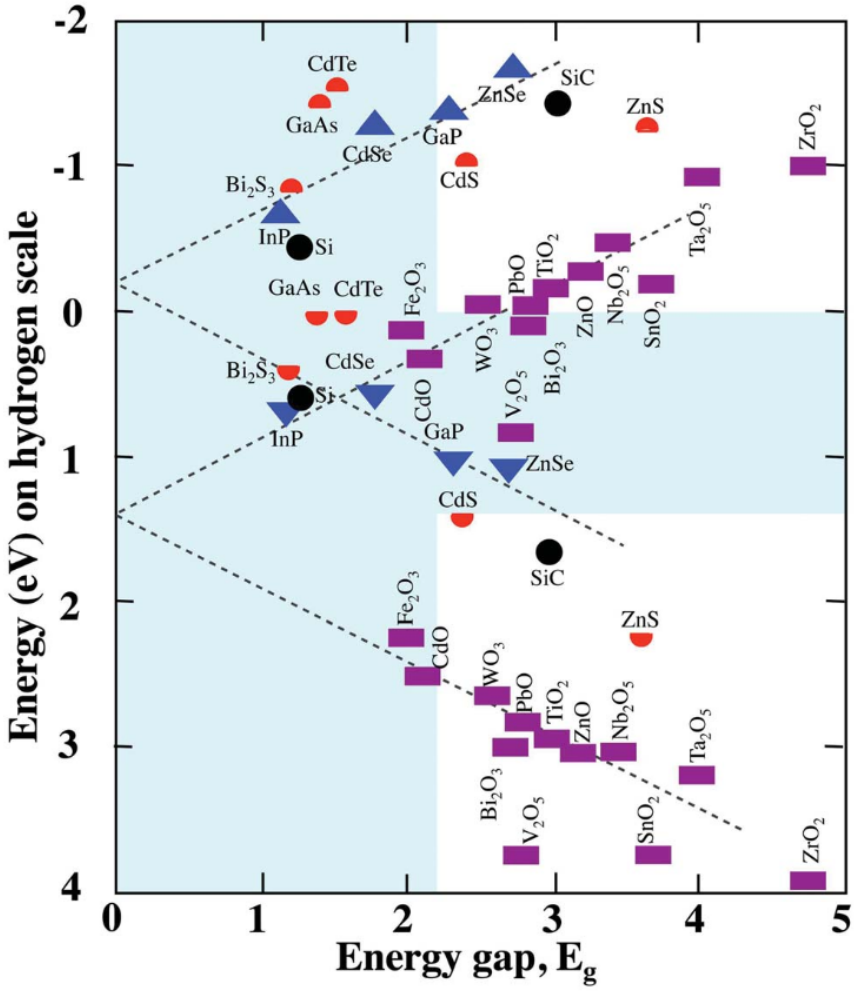

Figure 2.6: Scheme of binary semiconductor band positions according to their band gaps. The blue zone indicates the band positions and/or band gaps that are unsuitable for overall water splitting.[13]

multiple semiconductors with complementary band positions and/or supply electric energy to achieve enough voltage to realize the water splitting reactions. The strong advantage of using a combination of photoabsorbers is that semiconductors with band gaps below 2.2 eV become useful, meaning that a larger fraction of sunlight may be captured. Figure 2.8 shows a scheme of how two semiconductors could be combined to achieve overall photo(electro)chemical water splitting. Herein, one semiconductor should be an n-type semiconductor with a relatively wide band gap and a VBM suitable for water oxidation which preferably exhibits upwards band bending, while the other semiconductor should be a p-type semiconductor with a more narrow band gap and a conduction band minimum (CBM) suitable for water reduction which preferably exhibits downwards band bending. The two semiconductors should be able to shuttle charge carriers through an external circuit, with which the semiconductors should form ohmic contacts,

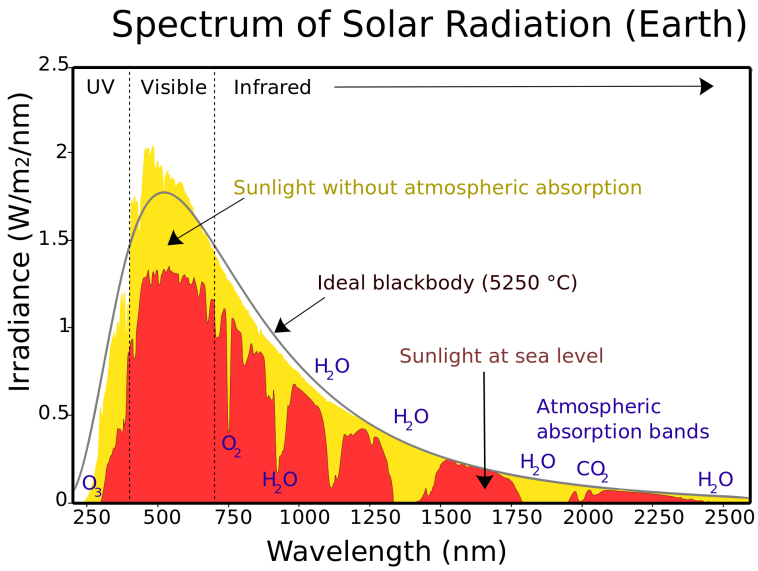

Figure 2.7: Solar radiation spectrum at sea level and at the top of the atmosphere.[17]

or through a redox mediator, which is often a dissolved compound with multiple valence states such as iron.[18]

Essentially, two semiconductors can be combined according to two different geometries: 1) a stack can be formed by placing one semiconductor on top of the other, so that the top semiconductor is irradiated by the full solar spectrum, while the bottom photoabsorber only receives the photons with energies below the band gap of the top photoabsorber or 2) the two light absorbers can be placed "side-by-side", so that they both receive the full solar spectrum, which is, for instance, the only possibility in particulate photochemical water splitting. Pinaud et al. calculated, for both geometries, the maximally attainable solar-to-hydrogen (STH) efficiency for a set of band gaps, taking into account entropic losses and reaction overpotentials (Figure 2.9).[19] For a dual side-by-side geometry, a maximum STH efficiency of merely 15.5% could potentially be reached through the combination of two semiconductors with an identical band gap of 1.59 eV. In contrast, a dual stacked geometry would allow for a considerably higher maximum STH efficiency of 22.8% through the combination of a top and bottom light absorber with band gaps of 1.84 eV and 1.23 eV, respectively. Practically, Young et al. was able to realize semiconductors with nearly optimal band gaps through the combination of a precisely alloyed GaInP(1.8 eV)/GaInAs(1.2 eV) top/bottom stack, for which the authors demonstrated a state of the art STH efficiency of 16.2% under direct sun light.[20] Adding additional absorbers in a stacked geometry could potentially lead to even higher attainable STH efficiencies. However, Fountaine et al. calculated that by adding a third absorber to the stack only a potential increase of $1 - 2\%$ in STH efficiency could be obtained compared to a dual stack.[21]

Engineering the band gap of oxide semiconductors is more complicated than it is for III-V

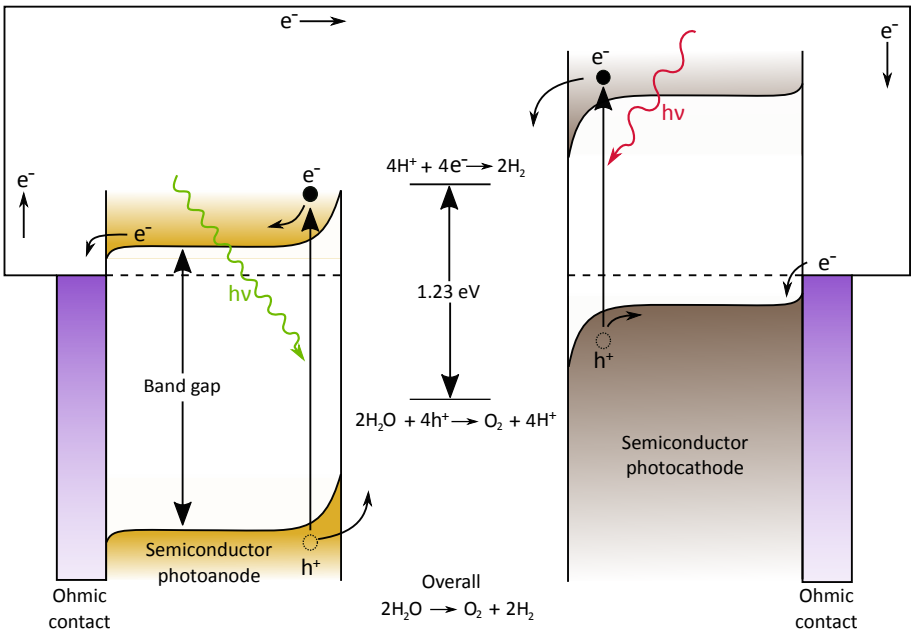

Figure 2.8: Band diagrams of two semiconductors with suitable band gaps, band positions and interface alignment for overall water splitting. The external circuit connecting the two semiconductors could also be replaced by a redox mediator to shuttle charges between the two semiconductors. Adapted from [19].

semiconductors, because of the higher compositional freedom of III-V semiconductors, and because of the O2p states giving rise to relatively low VBMs. Hence, finding an oxide semiconductor able to reduce water with a band gap below 3.0 eV is not straightforward (Figure 2.6). However, for certain oxides the VBM is not only governed by the O2p states but also by the valence states of other elements, as is the case for bismuth, copper and iron containing oxides (Figure 2.10).[22] These kind of oxides are, thus, promising for (partial) photo(electro)chemical water splitting. Additionally, higher VBMs can be obtained with oxide semiconductors through the addition of nitrogen, forming oxynitrides. Oxynitride compounds pose, however, new challenges such as a lower stability against photocorrosion.[23] To learn more about oxynitrides I refer the reader to a recently published review by Takata et al.[24]

In this work, $BiVO_4$ and $CuFeO_2$ were chosen for the photochemical water oxidation and water reduction reaction, respectively (Figure 2.11). Although, $BiVO_4$ may not have the optimal optical band gap, 2.4 eV,[25] it is at the moment the state of the art oxide photoanode having demonstrated an STH efficiency of 4.9% in combination with a double junction amorphous Si solar cell[26] or having shown a photocurrent of 6.72 mA cm^{-2} vs 1.23 V_{RHE} when combined with WO_3 into a core-shell nanostructured photoanode.[27] $CuFeO_2$, in contrast, has a band gap, 1.5 eV,[28] which is very close to the optimal band gap and has suitable band positions for water reduction, however its efficiencies so far have been rather poor. The $BiVO_4$ and $CuFeO_2$ state of the art is further described in this Chapter in Section 2.3.

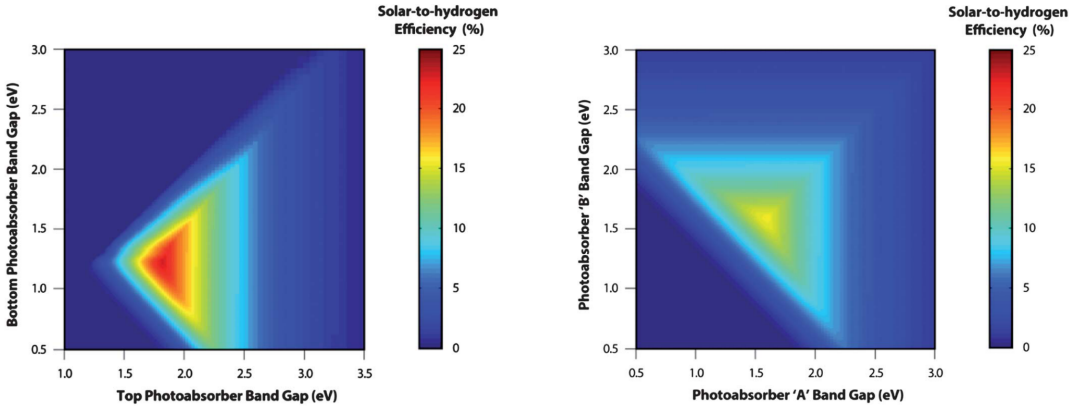

(a) (b)

Figure 2.9: Maximum theoretical STH efficiency for a dual absorber in (a) a tandem configuration and (b) a side-by-side configuration as a function of both photoabsorber band gaps. For the tandem configuration the top photoabsorber is illuminated by the whole solar spectrum, whereas the bottom photoabsorber only receives the photons transmitted by the top photoabsorber. For the side-by-side configuration both photoabsorbers are illuminated by the complete solar spectrum.[19]

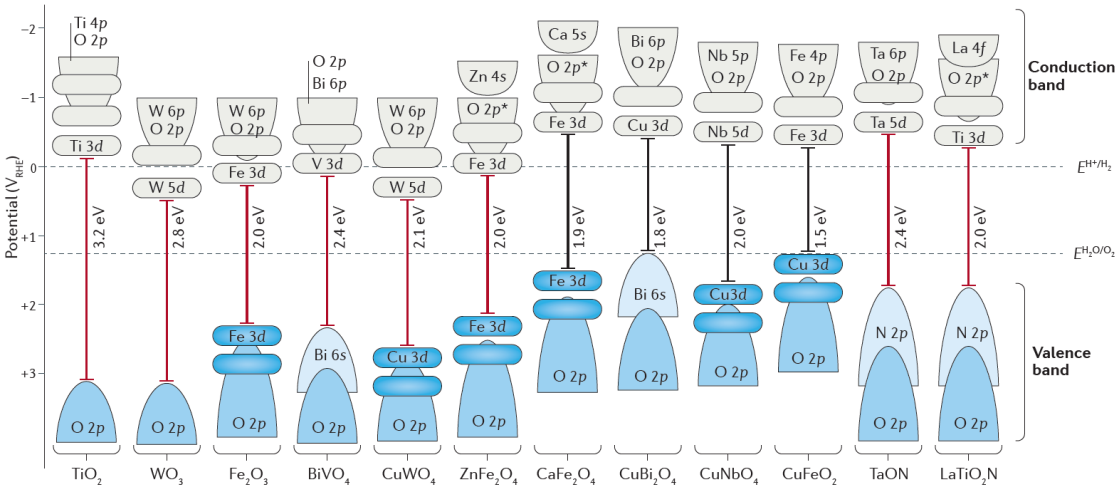

Figure 2.10: Band gaps and band positions of some promising oxide semiconductors for photo(electro)chemical water splitting, whereby the contribution of the metal, oxygen and nitrogen atomic orbitals to the valence band and conduction band are indicated.[22]

On a side note, several efficiency parameters have been used throughout literature to assess photo(electro)chemical systems, whereby the STH efficiency is considered to be the central benchmark. I refer the reader to the article of Qureshi et al. for a complete overview of the efficiency parameters and how to appropriately measure those efficiencies,[29] because efficiency parameters other than the STH efficiency will be mentioned occasionally throughout this work.

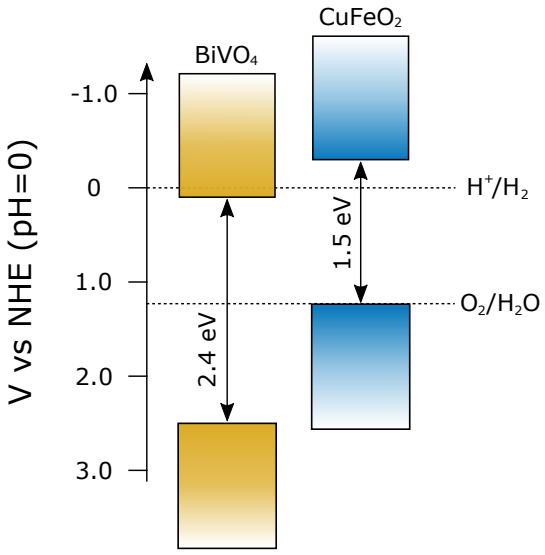

Figure 2.11: Band gaps and band positions of $BiVO_4$ and $CuFeO_2$ with respect to the H^+/H_2 and O_2/H_2O standard reduction potentials on the NHE scale.

2.1.4 Particulate water splitting

As mentioned in the Preface, four types of photo(electro)chemical water splitting reactors can be distinguished (Figure 1.5), whereby type 3 and type 4 are based on PEC stacks and type 1 and type 2 on baggies containing particle slurries. Due to the high BoS costs and the high resemblance to PV-E, questions arise whether PEC stacks will be able to compete with PV-E and SMR in the near to far future.[19,30] In contrast, type 1 and type 2 particulate water splitting systems could be economically viable, with computed levelised hydrogen production costs of $1.60 and $3.20 per kg H_2, respectively, if the baseline conditions are fulfilled, i.e. 5% STH efficiency + 5 years lifetime and 10% STH efficiency + 5 years lifetime, respectively.[19] Nonetheless, is the research into PEC water splitting ongoing, because the knowledge gained on PEC systems can be used for the development of photovoltaics and/or particulate water splitting systems. Therefore, literature references to photo(electro)chemical systems have been mainly included in this work to highlight certain structural modifications which improved upon the water splitting performance or to provide insight into certain photo(electro)chemical water splitting mechanics.

Particulate water splitting can be realised in the absence or in the presence of a redox mediator, which transfers the electrons from the water reduction photoabsorber to the water oxidation photoabsorber. In the presence of a redox mediator the particulate water splitting system is referred to as a Z-scheme type system (Figure 2.12), which name is derived from the ”Z-scheme” natural photosynthesis process in green plants.[18] The redox mediator can be an aqueous redox mediator such as Fe^{2+}/Fe^{3+},[31] IO_3^-/I^-[32] and I^{3-}/I^-[33] or a solid state redox mediator like reduced graphene oxide[34] or gold.[35] The redox mediator can also be a conductive film onto which the particulate photoabsorbers have been immobilized. Remarkably, these kind of integrated par-

ticulate systems have demonstrated state of the art particulate-based unassisted lab-scale STH efficiencies ranging from 1.0 to 1.2%.[36,37] At a larger scale, a state of the art particulate-based STH efficiency of 0.4% was recently achieved under direct sunlight with a 1 m^2-sized photocatalytic water splitting panel, consisting of immobilized Al-doped $SrTiO_3$/$RhCrO_x$ particles.[38]

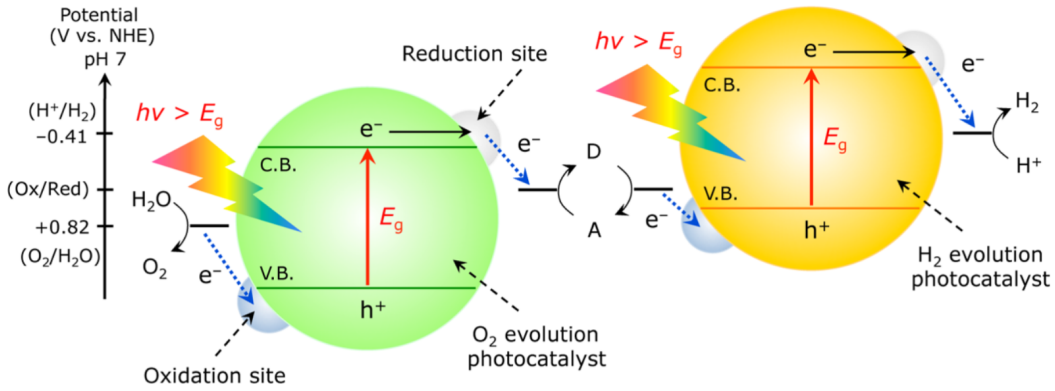

Figure 2.12: Schematic of a Z-scheme type photochemical water splitting system.[18]

In the following Section, fundamental semiconductor surface and interface properties will be described as well as their relevance to photo(electro)chemical water splitting.

2.2 Semiconductor interfaces

2.2.1 Interfacial band structure

2.2.1.1 Solid state junctions

As was discussed in Subsection 2.1.2, heterostructures, whereby the photoabsorber is contacted with another material, may help to overcome certain intrinsic semiconductor deficiencies. Besides the chemical and electronic properties of the contact material, the resulting interface structure may play an important role in the overall device performance. A first junction which one may come across in photo(electro)chemical devices are semiconductor/metal junctions, also called Schottky barriers. For instance, platinum has been added occasionally to the main photoabsorber to act as water reduction "cocatalyst".[39,40] The alignment between two solid state compounds is often represented through an energy band diagram, whereby certain energy levels of the compounds are plotted as a function of a spatial dimension using the Fermi level or vacuum level as energy reference. The vacuum level, herein, is defined as the energy level of a free stationary electron outside the material but near the surface. In Figure 2.13 a band diagram for the semiconductor/metal junction is shown. In this band diagram, the indicated semiconductor electron affinity, work function and ionization potential are defined as the energy difference between the vacuum level on the one side and the conduction band, Fermi level and valence

band, respectively, on the other side. The work function, herein, represents the minimum energy needed to bring the electron from the solid to a point in vacuum near the solid surface. Due to the metal having no band gap, the electron affinity, ionization potential and work function are identical for a metal. When the metal and semiconductor are brought into contact, the Fermi level is used as a reference instead, due to the equilibration of the electron electrochemical potential in both materials. The semiconductor/metal band alignment can be estimated through the Mott-Schottky rule, which state that the energy transfer between the metal and the semiconductor is proportional to the difference between the semiconductor electron affinity and metal work function. However, for many semiconductors the Mott-Schottky rule is not applicable, as the created interface gives rise to surface states within the band gap, which reduces the expected amount of charge transfer, a phenomenon called Fermi level pinning. These surface states are often called metal-induced gap states due to tails of the metal wave functions spilling into the semiconductor, creating inter-gap states.[41,42] Inter-gap surface states may also arise from dangling bonds and from structural defects at the semiconductor surface.[43] Fermi level pinning may even be caused through bulk semiconductor defects in a process called "self-compensation".[44] The amount of Fermi level pinning at the semiconductor/metal contact has also been found to depend largely on the chemical nature of the semiconductor, whereby covalent semiconductors such as Si have shown strong Fermi level pining, whereas ionic semiconductors such as oxides have generally demonstrated weak Fermi level pinning.[45,46]

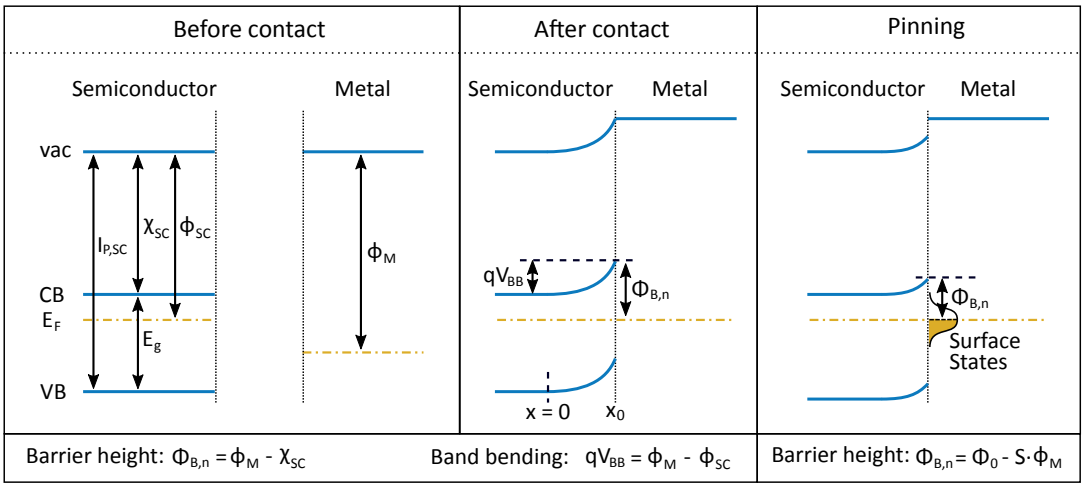

Figure 2.13: Scheme illustrating the band alignment of an n-type semiconductor with a metal before and after contact, and with/without Fermi level pinning at surface states. $I_{P,SC}$: ionisation potential of semiconductor, χ_{SC}: electron affinity of semiconductor, ϕ_{SC}: work function of semiconductor, ϕ_M: work function of metal, $\Phi_{B,n}$: barrier height between Fermi level and CB, qV_{BB}: band bending.

The transfer of mobile charge carriers between semiconductor and metal may induce a space charge region in the semiconductor, due to inefficient screening of the excess charge in the semiconductor near the semiconductor/metal interface. The inefficient screening of the excess charge

may lead to a decrease, increase or inversion, of the number of native mobile charge carriers near the semiconductor/metal interface at the semiconductor side, so that the space charge region can be further specified as a depletion, accumulation or inversion region (Figure 2.14). For instance, a depletion region in an n-type semiconductor has a lower electron density near the semiconductor/metal interface compared to the bulk of the semiconductor. A depletion region will, thus, exhibit insulating behaviour. Through the application of an external bias, one can switch between depletion, accumulation and inversion, and thus between the conductive and resistive behaviour of the Schottky barrier, which is, therefore, also called a Schottky diode.

The space charge region width can be calculated with Poisson's equation and depends strongly on the doping concentration. Below, the calculation is made for the depletion region width of an n-type semiconductor. In one dimension, Poisson's equation equates to:

$$\frac{d^2V}{dx^2} = -\frac{\rho}{\epsilon\epsilon_0} \tag{2.9}$$

with V being the potential, ϵ the dielectric constant, ϵ_0 the vacuum dielectric constant and ρ the charge density, whereby for an n-type depletion region:

$$\rho = N_d e \tag{2.10}$$

with N_d the ionized donor density. The potential V can be replaced by the electron energy ϕ:

$$\frac{d^2\phi}{dx^2} = \frac{N_d e^2}{\epsilon\epsilon_0} \tag{2.11}$$

In the absence of Fermi level pinning, following boundary conditions can be defined:

$$\phi = (\frac{d\phi}{dx}) = 0 \qquad \text{at } x = 0 \tag{2.12}$$

$$\phi = \phi_M - \phi_{SC} \qquad \text{at } x = x_0 \tag{2.13}$$

whereby x = 0 corresponds to the beginning of the depletion region and x_0 is the position of the semiconductor/metal contact. By integrating Poisson's equation according to the boundary conditions, following solution can be obtained:

$$\phi_M - \phi_{SC} = \frac{N_d x_0^2 e^2}{2\epsilon\epsilon_0} \tag{2.14}$$

The depletion region width x_0, thus, scales with $N_d^{-\frac{1}{2}}$. Depletion region widths between 10 nm and 100 nm are typical. In photocatalysis the depletion region width plays an important role, as it is the parameter which state how far from the interface a photon-induced charge carrier is under the influence of the interface-induced internal electric field, which helps to separate the

charge carriers. In a band diagram the internal electric field is commonly visualised through band bending, which results from the electron electrochemical potential changing with respect to the band edges due to the presence of the internal electric field.

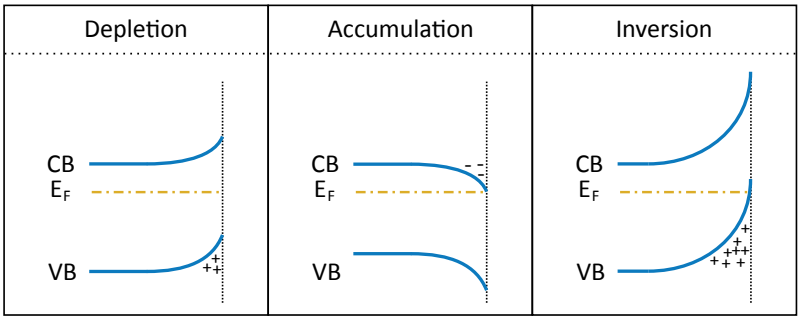

Figure 2.14: Scheme showing charge carrier depletion, accumulation and inversion for an n-type semiconductor. The charges depicted in the scheme are the charges that are left behind near the semiconductor surface after the mobile charge carrier transfer.

Another interface which one may see in optoelectronic devices is the semiconductor/semiconductor interface. The effect of this interface on the device properties depends on the energetic conditions of both semiconductors. The band alignment between the two semiconductors can be described according to three different types (Figure 2.15): 1) type I or straddling gap alignment, 2) type II or staggered gap alignment and 3) type III or broken gap alignment. Especially, type I and type II alignments are often found when designing photo(electro)chemical water splitting devices, whereby type I alignment often results from the preparation of thin passivation contact layers and type II alignment is used to form p-n junctions, create hole/electron selective contacts, or construct stacks of photoabsorbers to increase the photovoltage.

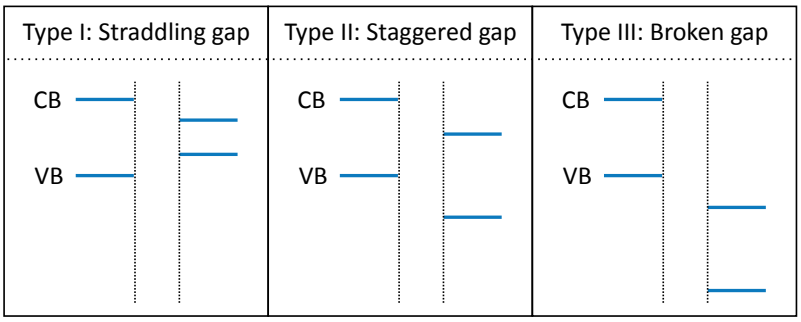

Figure 2.15: Scheme showing Type I, II and III alignment between two semiconductors before contact.[47]

When an n-type and p-type semiconductor are brought into contact, a p-n junction may be established, whereby a depletion region forms at the interface between the two semiconductors. The band diagram of a p-n junction is easily visualised for homojunctions, whereby the p-type and n-type semiconductor are made from the same material. For instance, Figure 2.16 shows how

a homo p-n junction is formed when p-type and n-type Si are brought into contact. Because of the different Fermi levels, charge transfer takes place between p-type and n-type Si, forming a depletion region near the interface at both sides of the interface. The width of the space charge region (w_p-w_n) can again be calculated through the integration of the one dimensional Poisson's equation (Equation 2.9) with the following boundary conditions:

$$(\frac{d\phi}{dx}) = 0, \ \phi = \phi_{SC,n} \qquad \text{at } x = -w_n \tag{2.15}$$

$$(\frac{d\phi}{dx}) = 0, \ \phi = \phi_{SC,p} \qquad \text{at } x = w_p \tag{2.16}$$

$$\phi = \phi_0; \ \frac{d\phi}{dx} \text{ and } \phi \text{ are continuous} \qquad \text{at } x = 0 \tag{2.17}$$

$$w_p * N_A = w_n * N_D \qquad \text{Charge neutrality} \tag{2.18}$$

with w_n,w_p corresponding to the start of the depletion region in the n-type and p-type semiconductor, respectively, N_d,N_a corresponding to the ionized donor and acceptor concentration, respectively, and $x = 0$ corresponding to the position of the semiconductor/semiconductor contact. After integration of Poisson's equation with the above defined boundary conditions:

$$\phi_{SC,p} - \phi_{SC,n} = \frac{e^2 N_d w_n^2 [(N_d/N_a) + 1]}{2\epsilon\epsilon_0} \tag{2.19}$$

Hence, the depletion region width for a semiconductor/semiconductor junction is again dependent on the doping concentration in the semiconductors. Due to the depletion region, the p-n junction acts like a diode. Under forward bias, the depletion region width decreases, thus allowing an electric current to pass, whereas for a reverse bias the depletion region width increases, making the area around the p-n junction interface even more insulating. The creation of p-n junctions is a common strategy in the design of photovoltaics to increase charge carrier separation, because photons absorbed within the depletion region give rise to electron-hole pairs which are more efficiently separated due to the internal electric field.

For a heterojunction between two different semiconductors, the bands do not form a continuity at the interface, due to the difference in conduction and/or valence band positions. In the absence of Fermi level pinning, the Anderson model states that:

$$\Delta E_{CB} = \chi(SC2) - \chi(SC1) \tag{2.20}$$

$$\Delta E_{VB} = I_p(SC2) - I_p(SC1) \tag{2.21}$$

with I_p(SC1), I_p(SC2) the ionization potentials of semiconductor 1 and 2, respectively, and χ(SC1), χ(SC2) the electron affinities of semiconductor 1 and 2, respectively. However, Fermi level pinning may also take place between two semiconductors, with altered band discontinuities as a consequence. Ideally, the lattice and thermal expansion coefficient mismatch between the two contact layers should be as small as possible to avoid the creation of interface defects which may induce inter-gap states.

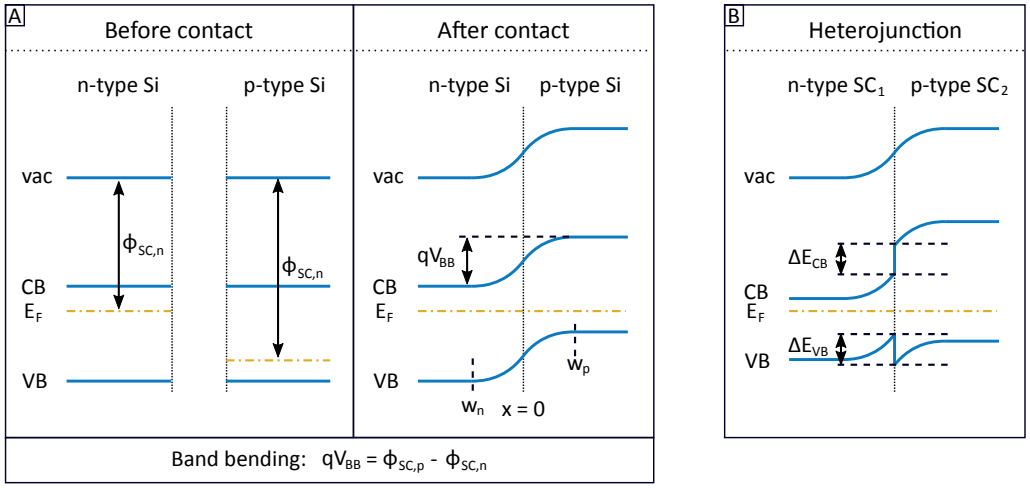

Figure 2.16: Scheme illustrating the band alignment of A) a Si p-n homojunction before and after contact and B) a p-n heterojunction between two semiconductors with different band gaps in the absence of Fermi level pinning. $\phi_{SC,n}$: work function of n-type Si, $\phi_{SC,p}$: work function of p-type Si, qV_{BB}: band bending, ΔE_{CB}: conduction band discontinuity, ΔE_{VB}: valence band discontinuity.

In this work, the heterojunctions between our selected photoabsorbers, $CuFeO_2$ and $BiVO_4$, on one side and several contact layers on the other have been studied for two purposes. First of all, contact layers with differing work functions were selected to investigate whether the photoabsorbers follow the ideal band alignment models. Additionally, the probability of Fermi level pinning is discussed as well as the potential origin of the states responsible for Fermi level pinning. The second purpose was to investigate the junction properties of heterostructures, which have previously been used in devices that have demonstrated relatively high photo(electro)chemical water splitting efficiencies. As such, the interface between $BiVO_4$ and the transparent conducting oxide Sn-doped In_2O_3 (ITO) was investigated, due to ITO having been used before to form transparent conductive Ohmic contacts with $BiVO_4$. Furthermore, the junction between $BiVO_4$ and recognized "cocatalysts" such as NiO and CoO_x was studied to determine whether the interface properties, and then in particular band bending, could be responsible for the previously observed improved efficiencies.

Heterostructures, in this work, have been mostly investigated through interface experiments, which involved photoelectron spectroscopy and thin film sputtering. The experimental proce-

dure of an interface experiment is fully described in Section 3.4.4.1 of Chapter 3. In short, a certain substrate was introduced into an integrated thin film deposition and surface analysis system, which operates entirely under ultra-high vacuum. After removing the extrinsic impurities from the substrate surface through an adequate cleaning procedure, a thin film contact was stepwise sputtered on top of the substrate, whereby photoelectron spectra were measured in between each deposition step. The interpretation of the solid state contact could then be obtained through the analysis of the temporal evolution of the core level spectra, valence band spectra and ultraviolet photoelectron spectra measured after each deposition step. Due to the overlay of the contact layer valence band spectra with the substrate valence band spectra, the substrate valence band maximum, which gives information on the band bending and creation of a space charge region, has to be monitored through the binding energy (BE) changes in the core level spectra of the substrate, a method which was first described by Kraut and Waldrop.[48]

In our group the Kraut method has been used extensively for the interface study of various semiconductor heterojunctions. Morasch et al. found that by contacting Bi_2O_3 with ITO and RuO_2, the E_F-E_{VBM} barrier could be changed to 1.73 eV and 0.75 eV, respectively.[49] Uddin et al. linked the increased photocatalytic dye decomposition efficiency for RuO_2 coated ZnO nanoparticles to the observation of a Schottky-type contact between ZnO and RuO_2.[50] Li et al. found that contacting ferroelectric (Ba,Sr)TiO_3 to the insulating Al_2O_3, led to a limited valence band discontinuity and a strong conduction band discontinuity of > 5 eV, resulting in a high barrier for electron transport.[51] Verena et al. discovered a valence and conduction band offset between anatase and rutile through comparison of the energy band alignment of anatase/RuO_2 and anatase/ITO to the band alignment of rutile/RuO_2 and rutile/ITO. In addition to the study of oxide interfaces, the Kraut method has been used in our group to determine the band alignment of particular II-VI semiconductors.[52–54] All in all, our studies have shown that the Kraut method can be used to study the band alignment for a wide variety of materials and draw conclusions on the junction properties of the interfaces. Properties such as band discontinuities, band bending and Fermi level tunability (variation E_F-E_{VBM}) can be determined, as well as the relative alignment between materials, by assuming transitivity of the alignments of those materials with RuO_2 and ITO.[55,56]

2.2.1.2 Semiconductor-liquid junction

The interface between semiconductor and electrolyte is arguably the most important interface in photo(electro)chemical water splitting, as the transfer of the charge carriers from the photoabsorber to the adsorbed reactants is a crucial step and is what distinguishes photo(electro)chemical water splitting from photovoltaic driven electrolysis. For charge carrier transfer to take place the energetic state of a reactant should lie within the band gap of the semiconductor. As already outlined above, the valence band maximum should be more positive than the O_2/H_2O (1.23 V) standard reduction potential and the conduction band minimum should be more negative than

the H^+/H_2 (0.0 V) standard reduction potential to allow charge transfer in the water oxidation reaction and/or water reduction reaction, respectively. Generally, when a semiconductor is placed in an electrolyte, charge transfer will take place until the Fermi levels of semiconductor and solution are equilibrated (Figure 2.17).

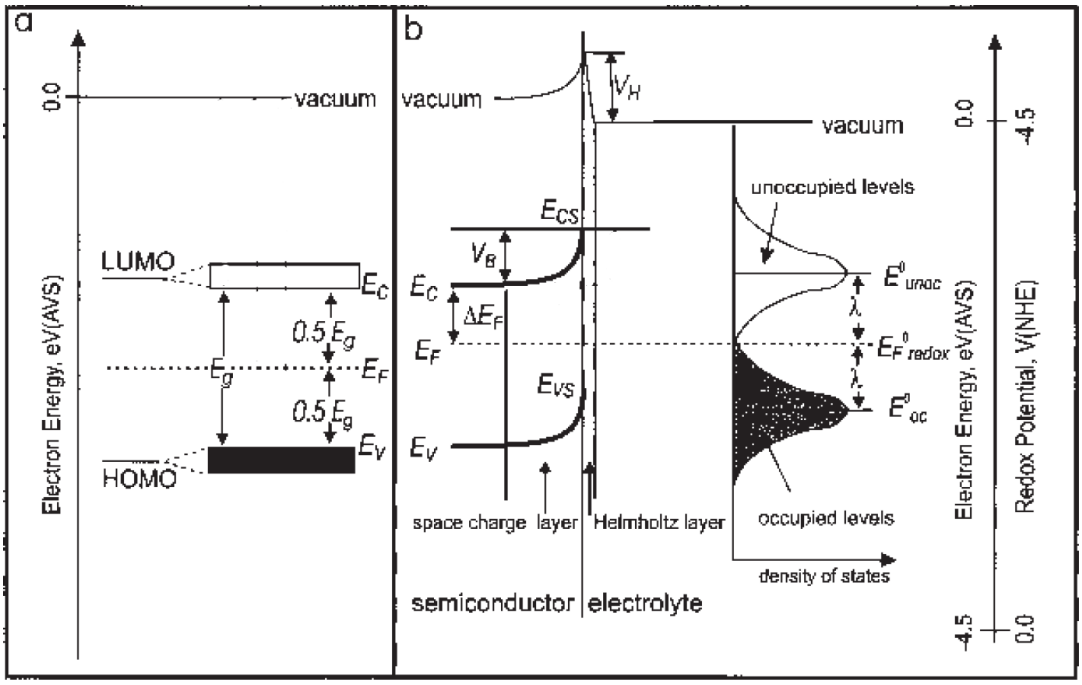

Figure 2.17: Band diagram of semiconductor (a) before and (b) after contact with electrolyte containing a reversible one electron redox couple under open circuit and in the absence of light. V_H is the potential drop of the Helmholtz layer; V_B is the band bending; E_F is the Fermi level of the system at equilibrium; ΔE_F is the difference between the Fermi level and the conduction band edge; $E^0_{F,redox}$ is the standard Fermi level of the redox couple; E_{unoc} and E_{oc}, are the energies of the unoccupied states and the occupied states of the redox couple, respectively; and λ is the reorganization energy.[57]

The Fermi level of a solution can easily be understood for solutes undergoing a one electron redox process, whereby the solutes are defined as electron acceptors (A) or electron donors (D), depending on whether they accept an electron from or donate an electron to the semiconductor. For electron donors and electron acceptors the energy states of importance in charge transfer are the highest occupied energy state E_{occ} and the lowest unoccupied energy state E_{unocc}, respectively. When an electron is transferred from or to the semiconductor, the charge of the solute changes, giving rise to A^- and D^+, respectively. The change in charge makes that the solvation shell around the solute re-orients, which is associated with a change in free energy of the solute, referred to as reorganization energy λ. In addition, thermal vibrations lead to a fluctuation of the solvation shell, so that the energy state of the solute with a particular charge is not associated with one specific energy level E_{occ} or E_{unocc}, but rather with a thermal distribution of states with

E_{occ} or E_{unocc} being the maxima of those distributions. Now, the Fermi level E_F of the redox couple (A/A^- or D/D^+) is defined as the energy level lying midway of E_{occ} and E_{unocc}, and which can be expressed as follows:

$$E_{F,A/A^-} = E_{A/A^-} = E^0_{A/A^-} + RTln\left(\frac{a_{A^-}}{a_A}\right) \tag{2.22}$$

$$E_{F,D/D^+} = E_{D/D^+} = E^0_{D/D^+} + RTln\left(\frac{a_{D^+}}{a_D}\right) \tag{2.23}$$

For a multi-electron process, the situation can be somewhat more complicated, because more than two states could be present in the electrolyte. When more that two states are present, the standard redox potentials of the one-electron steps of the overall reaction govern the charge carrier transfer from semiconductor to electrolyte. Now, the Fermi level of the solution may not be equal to the standard redox potential of the overall reaction due to the overall standard redox potential not necessarily lying midway between the maxima of the E_{occ} and E_{unocc} distributions.

Charge transfer from the semiconductor to the electrolyte leads to a space charge region in the semiconductor, just like for the semiconductor/metal and semiconductor/semiconductor junctions. The band bending due to the semiconductor/liquid is proportional to the difference in semiconductor and solution Fermi level, when no Fermi level pinning takes place. However, in solution due to the charged semiconductor surface, counterions are attracted towards the surface, which results in the formation of a so-called Helmholtz double layer.[58] The Helmholtz layer has a thickness on the order of one angstrom, and leads to an additional potential drop inside the space charge region of the semiconductor. Therefore, to determine the exact band bending value, the potential drop associated with the creation of the Helmholtz layer should be known.

The flat band potential V_{fb} is a measurable physical quantity, which has been introduced to connect the semiconductor energy levels to those of the electrolyte. In essence, the flat band potential is the electrode potential for which the potential drop in the space charge region becomes zero. Nozik et al. expressed V_{fb}, with the Normal Hydrogen Electrode (NHE) as reference electrode, as follows:[59]

$$V_{fb}(NHE) = \chi_{SC} + \Delta E_F + V_H + E_0 \tag{2.24}$$

whereby ΔE_F stands for the energy difference between the Fermi level and the majority carrier band edge, E_0 represents a scale factor between the absolute vacuum level and the standard reference electrode potential (for NHE this amounts to -4.44 eV), V_H being the potential drop across the Helmholtz layer and χ_{SC} being the semiconductor electron affinity. V_H is independent of the charge carrier transfer between semiconductor and electrolyte, and depends solely on the adsorption/desorption equilibrium of electrolyte ions on the semiconductor surface.[60] The potential drop across the Helmholtz layer is mainly governed by the so-called potential determining

ions. For an oxide semiconductor in an aqueous electrolyte, the hydroxide and hydrogen ions are the only potential determining ions,[61] which means that V_H is completely governed by the pH of the solution. In the absence of a Helmholtz layer V_H becomes zero and is referred to as the point of zero charge (pH_{ZPC}). At pH_{ZPC} the flat band potential is equal to the semiconductor Fermi level, and is the only relevant flat band potential. Under the flat band potential at pH_{ZPC} the band positions at the semiconductor/electrolyte interface are the same as the band positions in the bulk of the semiconductor, so that the semiconductor can be positioned on the vacuum scale when combined with the knowledge on E_g and ΔE_F. This has also been illustrated in Figure 2.18.

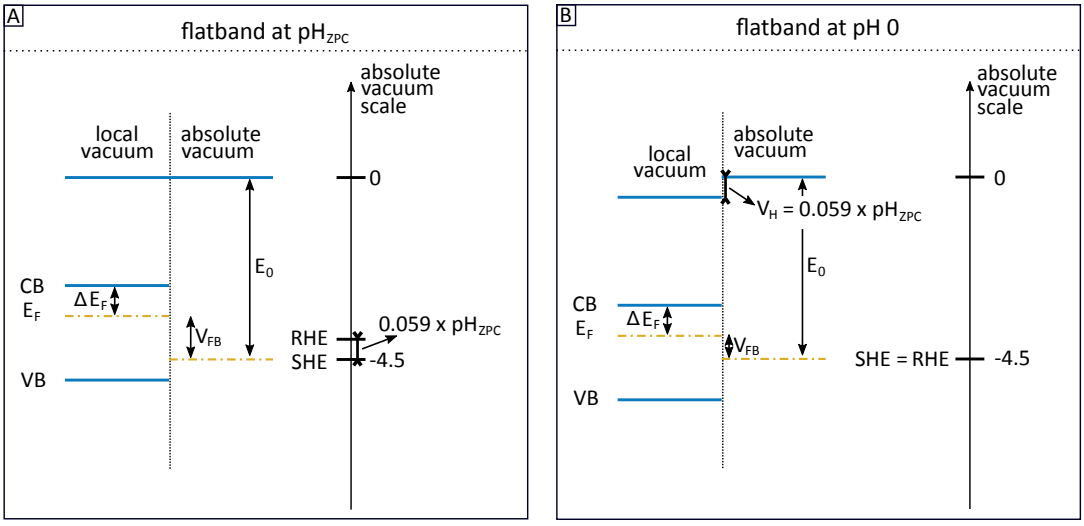

Figure 2.18: Band positions of semiconductor with respect to the absolute vacuum scale, SHE and RHE at flat band potential for pH_{ZPC} and pH 0.

2.2.1.3 Band edge position determination

There are various photo(electro)chemical techniques available to determine the flat band potential, whereby the Mott-Schottky method is used the most. Central in the Mott-Schottky method is the Mott-Schottky equation which relate the capacitance to the applied voltage across the semiconductor/electrolyte interface. The Mott-Schottky equation can be derived from Poisson's equation (Equation 2.9) using Gauss' law to relate the electric field across the semiconductor/electrolyte interface to the charge contained within that region, and the Boltzmann distribution to describe the electron distribution within the space charge region. For a full derivation I refer the reader to the publication of Geldermann et al.[62] For an n-type semiconductor the Mott-Schottky equation becomes:

$$\frac{1}{C^2} = \frac{2}{\epsilon\epsilon_0 A^2 e N_D}\left(V - V_{fb} - \frac{k_B T}{e}\right) \tag{2.25}$$

whereby C is the differential capacity $\frac{\partial Q}{\partial V}$, A is the interfacial area, N_d is the donor density, V is the applied voltage, k_B stands for Boltzmann's constant, T is the absolute temperature, ϵ is the dielectric constant of the semiconductor, ϵ_0 is the vacuum permittivity and e is the elementary charge. Plotting $\frac{1}{C^2}$ relative to the applied voltage V should give a linear correlation, whereby V_{fb} can be found from the intercept on the x axis. Additionally, N_d can be determined from the slope, if ϵ and A are known. Another commonly used photo(electrochemical)method to determine the flat band potential is by determining the anodic photocurrent onset potential from a photocurrent-potential plot.[63]

The Mott-Schottky method was quite popular 30 — 40 years ago, having been used to determine the semiconductor band positions of many semiconductors.[61,63–66] Today, many of those semiconductor band positions are being published relative to each other on the standard hydrogen electrode (SHE), NHE, reversible hydrogen electrode (RHE) or absolute vacuum scale.[13,22,67–69] However, the notion on the stringent experimental conditions to perform exact Mott-Schottky measurements may be lost with the passing of time. I, therefore, refer the reader to the letter of Cardon et al., who listed up the semiconductor and electrolyte conditions which should be met to perform reliable Mott-Schottky measurements.[70] For instance, conditions such as the complete absence of surface states and the allowed presence of only one type of localised electronic defect are already complicated enough to be met by any semiconductor. In the end, only by measuring on thoroughly cleaned specific crystal facets of a precisely doped semiconductor single crystal with a certain surface termination, valid and reproducible Mott-Schottky measurements can be obtained.

Another problem arises from listing up just the band positions on the RHE scale or at pH 0 on the NHE scale, due to the loss of a valuable piece of information, namely the pH_{ZPC}. This means that for oxide semiconductors whose band positions show a Nernstian behaviour with pH, i.e. band position variation according to 0.059 V/pH,[61,65,71] a pH-dependent discrepancy exist between bulk and surface band edge positions. Nonetheless, is the pH_{ZPC} very surface specific so that strong variations between differently prepared semiconductors of the same crystalline structure may occur. Determining pH_{ZPC} is, therefore, anyway recommended for every synthesized system to be able to completely evaluate the interfacial energy diagram.

Besides experimental methods, band edge positions have also been tried to be calculated. However, most Density Functional Theory (DFT) methods are inappropriate for measuring the band edge positions, requiring the introduction of a semi-empirical Coulomb parameter U (DFT+U).[72,73] A more simpler calculation, which was introduced by Butler and Ginley, involves the calculation of the electronegativity of the semiconductor, which is considered to be the geometric mean of the electronegativities of the constituent atoms. For binary oxide semiconductors M_aX_b the equation becomes:[61]

$$E_C = -(\chi_M^a \chi_X^b)^{\frac{1}{a+b}} - \frac{1}{2}E_g + 0.059(pH_{ZPC} - pH) + E_0 \tag{2.26}$$

whereby E_c stands for the conduction band position, E_0 is the scaling factor between electrode potential and absolute vacuum level χ_M, χ_X are the absolute electronegativities of M and X, and 0.059(pH_{ZPC}-pH) reflects the pH dependence of the oxide band positions. Butler and Ginley found that the band positions for many semiconductors calculated through the electronegativity correlate well with those determined through experimentally determined flat band potential measurements (Figure 2.19).[61]

In this work, the theory behind band edge determination given within this Section will be used to evaluate whether the information on the independently determined band edge positions of two semiconductors can be used to evaluate the relative band alignment between those two semiconductors. Specifically, in Section 5.3.3 in Chapter 5 the solid state band alignment schemes which are frequently depicted in literature,[22,68] and which were obtained through the above-explained experimental or theoretical methods of individual band position determination, will be compared to the solid state band alignment estimated from interface experiments with RuO_2 and ITO.

2.2.2 Interfacial charge transfer kinetics

Now that the energetic conditions of photo(electro)chemical water splitting have been described, the interfacial charge transfer kinetics will be introduced briefly in this Subsection.[74,75]

Most of the aspects with regards to the water splitting reaction kinetics described below were derived from electrocatalytic water splitting, but are valid for photo(electro)chemical water splitting as well. The overall water splitting reaction should be split up into the water oxidation reaction and the water reduction reaction, which in electrocatalysis are often denoted as the oxygen evolution reaction (OER) and hydrogen evolution reaction (HER), due to the different mechanisms of both reactions. The HER is a two electron reaction ($2\,H^+ + 2\,e^- \rightarrow H_2$) that involves one reaction intermediate H* (the * here stands for a surface site), and which may follow either the Volmer-Tafel mechanism or the Volmer-Heyrovsky mechanism (Figure 2.20a):[76,77]

$$H^+ + e^- + {}^* \rightarrow H^*(\text{Volmer step}) \tag{2.27}$$

$$2\,H^* \rightarrow H_2 + 2^*(\text{Tafel step}) \tag{2.28}$$

$$H^+ + H^* + e^- \rightarrow H_2 + {}^* \text{ (Heyrovsky step)} \tag{2.29}$$

Herein, the hydrogen adsorption free energy ΔG_H has a strong influence on the rate of the overall hydrogen evolution reaction.[78,79] If hydrogen would bind too strongly or too weakly to the surface, the overall reaction rate would be limited by, respectively, the adsorption step (Volmer step) or the desorption step (Tafel/Heyrovsky). Therefore, ΔG_H should preferably be close to zero.

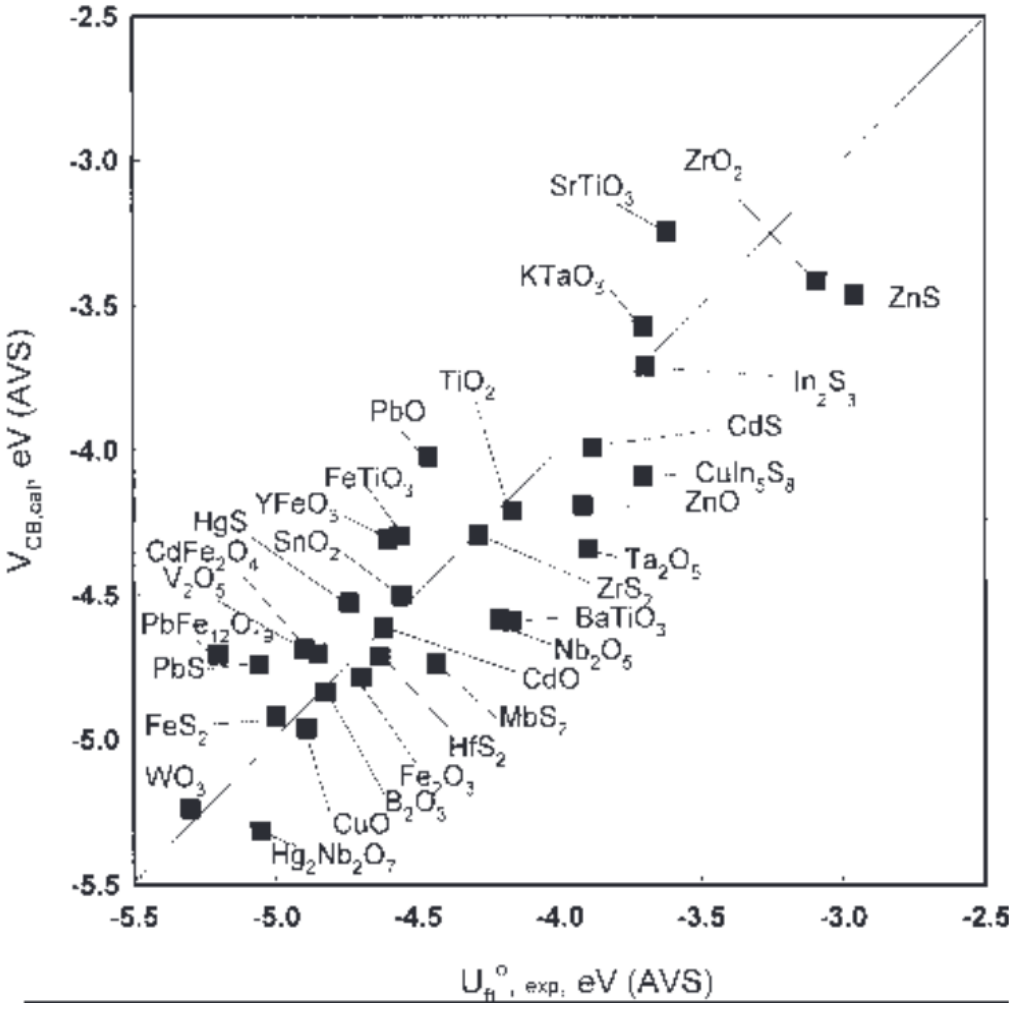

Figure 2.19: Correlation of flatband positions with electron affinity calculation.[57]

Indeed, a plot of the experimentally determined exchange current densities of a series of HER electrocatalysts as a function of ΔG_H, determined through DFT calculations, showed a so called volcano activity relationship with $\Delta G_H \approx 0$ corresponding to the maximum of the volcano (Figure 2.20b).[80–82] However, ΔG_H being close to zero is not the only condition for high HER performance, the kinetic barriers for the elementary steps need to be accounted as well. Although, MoS_2 has a ΔG_H comparable to the noble metals, lower HER activities have been found for MoS_2, which are supposedly caused by higher kinetic barriers.[83] A few authors have tried to model the kinetic barriers for the proton transfer reactions,[82–86] however these are still insufficiently accurate.

There are two different OER mechanisms, one which involves four proton-electron transfers, denoted as four-electron pathway,[88–91] and another which involves two times a two-proton-electron transfer with hydrogen peroxide as intermediate, denoted as the two-electron-two-electron pathway.[92] Depending on the oxygen dissociation barrier on the electrocatalyst surface

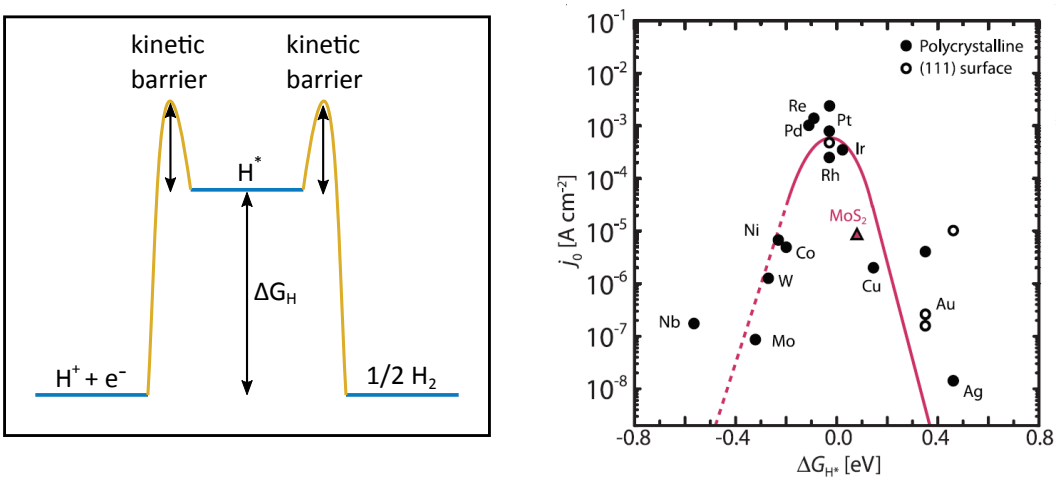

(a) (b)

Figure 2.20: (a) Reaction pathway of HER at 0 V potential and (b) activity volcano plot of HER for metals and MoS_2 at the equilibrium potential of 0 V.[82,87]

a four-electron pathway can either be associative (Figure 2.21a):[90]

$$H_2O{+}^* \rightarrow OH^* + H^+ + e^- \tag{2.30}$$

$$OH^* \rightarrow O^* + H^+ + e^- \tag{2.31}$$

$$O^* + H_2O \rightarrow OOH^* + H^+ + e^- \tag{2.32}$$

$$OOH^* \rightarrow O_2^* + H^+ + e^- \tag{2.33}$$

$$O_2^* \rightarrow O_2{+}^* \tag{2.34}$$

or dissociative:[88,89]

$$2\ H_2O + 2^* \rightarrow 2\ OH^* + 2\ H^+ + 2\ e^- \tag{2.35}$$

$$2\ OH^* \rightarrow 2\ O^* + 2\ H^+ + 2\ e^- \tag{2.36}$$

$$2\ O^* \rightarrow O_2 + 2^* \tag{2.37}$$

whereby the terms associative and dissociative have been derived from the oxygen reduction reaction (ORR), which follow the same elementary steps, but then in opposite direction. The dissociative ORR mechanism relates to the first step in the ORR reaction where oxygen dissociates into two O* on the catalyst surface. The problem in the four-electron pathway is that one electrocatalyst should be optimised for all elementary steps, meaning that the binding energies of all three intermediates OOH*, OH*, O* on the catalyst surface should be optimal to achieve the highest OER rate. However, the adsorption energies of these intermediates have been found to be strongly correlated and cannot be easily decoupled due to scaling relations.[91] The most persistent scaling relation is the one between the adsorption free energies of OOH* and OH*, which amounts to 3.2 ± 0.2 eV for a large set of catalyst surfaces.[75,90,93] The ideal adsorption free energy difference between OOH* and OH* is 2.46 eV so that an overpotential of 0.4 ± 0.1 eV ((3.2 ± 0.2 eV - 2.46 eV)/2 = 0.4 ± 0.1 eV) seems to be inevitable. With $\Delta G_{OOH\text{-}OH}$ fixed, the tunable parameter which has been found to largely determine the activity of electrocatalyst surfaces is the adsorption free energy difference between O* and OH* $\Delta G_{O\text{-}OH}$.[75] The highest OER activity is predicted at a $\Delta G_{O\text{-}OH}$ of 1.6 ± 0.1 eV ((3.2 ± 0.2 eV)/2 = 1.6 ± 0.1 eV). Indeed, this assumption is confirmed by the volcano plot in Figure 2.21b.

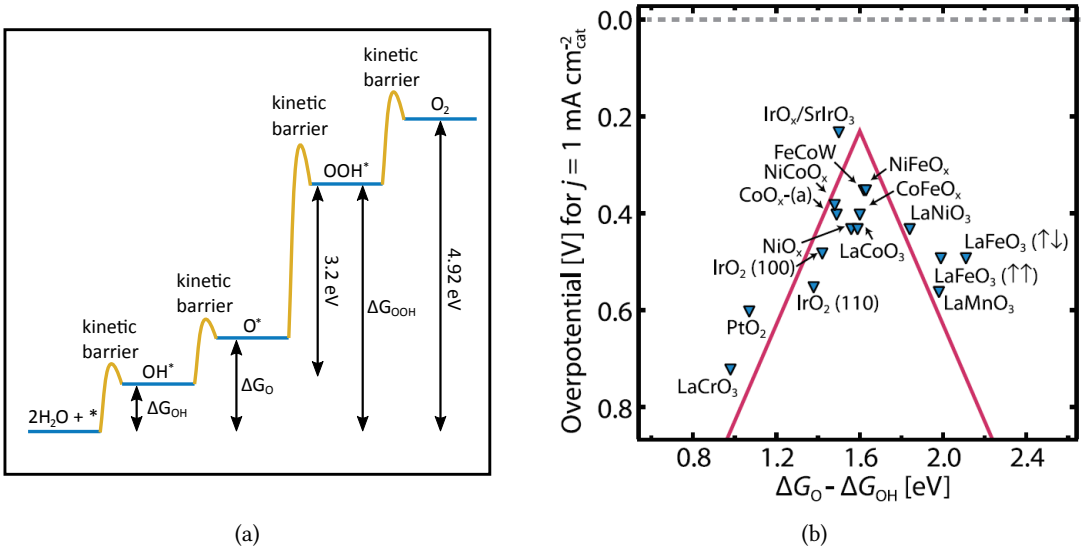

(a) (b)

Figure 2.21: (a) Reaction pathway of associative OER mechanism at 0 V potential and (b) activity volcano plot of OER according to ΔG_O-ΔG_{OH} for a series of oxides.[74]

Another OER mechanism is the two-electron-two-electron pathway with hydrogen peroxide as intermediate:[92]

$$2\ H_2O + 2^* \longrightarrow 2\ OH^* + 2\ H^+ + 2\ e^- \tag{2.38}$$

$$2\ OH^* \rightarrow 2\ H_2O_2 + 2^* \tag{2.39}$$

$$H_2O_2 + ^* \rightarrow OOH^* + H^+ + e^- \tag{2.40}$$

$$OOH^* \rightarrow O_2 + ^* + H^+ + e^- \tag{2.41}$$

The advantage of this pathway is that hydrogen peroxide is a stable intermediate, so that actually a mixture of two catalysts could be used, whereby one has a surface with an optimal ΔG_{OOH} and the other a surface with an optimal ΔG_{OH}. Due to the catalysts only having to be optimized for the adsorption of one intermediate an overpotential of 0 V should be feasible. The problem with the two-electron-two-electron pathway is that the standard reduction potential of the H_2O_2/H_2O reaction equals to 1.78 V, 0.55 V higher than the 1.23 V O_2/H_2O standard reduction potential. Electrocatalytic oxygen evolution through the two-electron-two-electron pathway is, thus, not necessarily more advantageous. However, $BiVO_4$ has a valence band position, which allows the production of oxygen through the two-electron-two-electron pathway.

Originally, noble metals have been studied for the OER and HER reaction, but recent focus has been laid on the use of transition metal compounds for those reactions. McCrory et al. made an extensive comparison of noble metals to transition metal compounds with regards to the overpotentials needed to achieve a current density of 10 mA cm^{-2} for the OER and HER in acidic and basic media (Figure 2.22).[94] Herein, for both OER and HER, non-noble metal compounds generally required higher overpotentials than noble metals in acidic media, whereas in basic media many non-noble metal compounds performed on par or better compared to noble metals. Hence, transition metal compounds could potentially replace noble metals in industrial electrocatalytic water splitting. The hydrogen production cost would then be slightly lower, on the condition that similar stabilities as for noble metal electrocatalysts can be achieved. The lower activation energies of certain transition metal compounds led also to their introduction as cocatalysts in photo(electro)chemical water splitting.[95–97]

For a more thorough description of electrocatalyst kinetics and an overview of the recent state of the art HER and OER systems, I refer the reader to the review written by Seh et al.[54]

2.3 Photo(electro)chemical water splitting materials

The primary material in photo(electro)chemical water splitting is the photoabsorber. As discussed in Section 2.1.3 only few photoabsorbers are suitable for overall water splitting with regards to their band gap and band positions. Therefore, also photoabsorbers with reduced band gaps are considered, which can only be used to perform either water reduction or water oxidation, due

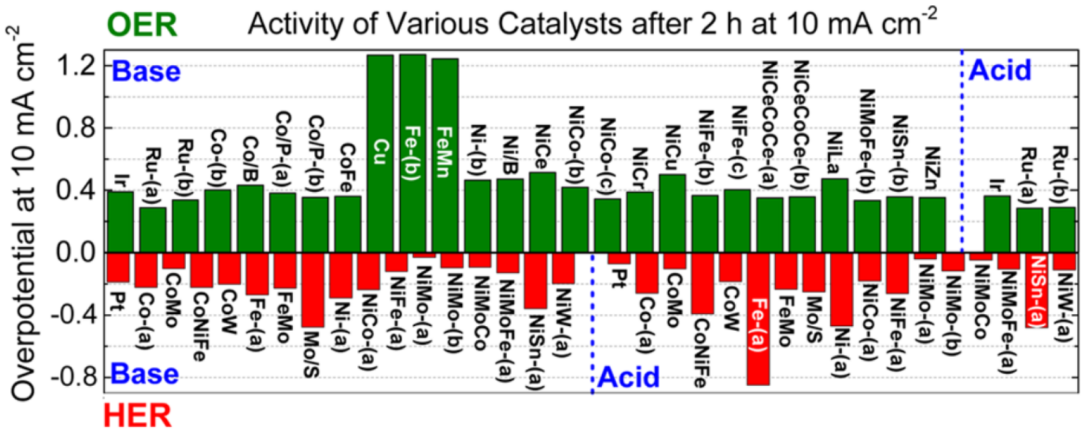

Figure 2.22: Specific activities per electrochemically active surface area, expressed as the overpotential needed to obtain a current density of 10 mA cm^{-2}, for a series of HER and OER electrocatalysts tested in acidic and basic media.[94]

to the photoabosrbers having a suitable conduction band minimum or valence band maximum, respectively. As such, more than 150 compounds have been recognised for (partial) water splitting, which include metal oxides,[68,98] sulphides,[99] oxynitrides,[100,101] III-V semiconductors,[20,102] silicon[103,104] and 2D-materials.[105,106] For a complete overview of the photoabsorbers which have been tested for photo(electro)chemical water splitting, I refer the reader to the reviews written by Jiang et al., Ismail et al. and Sivula et al.[22,107,108]

Bare photoabsorbers are normally not sufficient to realize stable and efficient water splitting, which is why the incorporation of additional contact materials is necessary to improve the water splitting kinetics, corrosion inhibition, surface passivation and/or charge carrier separation. The combination of a photoabsorber with another material is commonly referred to as a heterostructured photocatalyst. Giving a complete description of all published heterostructures for photo(electro)chemical water splitting is out of the scope of this work, due to the sheer amount of possible contact materials and the specific needs for each photoabsorber. Instead, I refer the reader to the thorough reviews of Kudo et al., Osterloh et al. and Qu et al on heterostructured photocatalysts.[68,109,110]

In the next Subsections, a short overview of the properties, design strategies and state of the art photo(electro)chemical water splitting efficiencies are given for the photoabsorbers selected for this work: $BiVO_4$ and $CuFeO_2$.

2.3.1 $BiVO_4$

$BiVO_4$ is an intrinsic n-type semiconductor for which four common polymorphs have been distinguished: orthorhombic pucherite, tetragonal dreyerite, monoclinic clinobisvanite and the closely related tetragonal scheelite-like phase.[25,111,112] However, only the monoclinic clinobisvanite is ac-

tive for photo(electro)chemical water oxidation. The monoclinic $BiVO_4$ crystal structure (Figure 2.23) consists of VO_4 tetrahedra and BiO_8 dodecahedra. The BiO_8 dodecahedra are connected to each other and form arrays along the $[1\bar{1}0]$ direction, whereas the VO_4 tetrahedra are isolated from each other. The BiO_8 dodecahedra connect to the VO_4 tetrahedra by sharing an apex oxygen atom. Moreover, monoclinic clinobisvanite exhibits the characteristics of a layered structure, with the Bi and V atoms being alternated along the crystalline axes, having the -Bi-V- configuration along the c and a axis. This particular layered structure, in addition to the shorter Bi-O bond lengths along the b axis,[113] makes that the (010) plane is the principal cleavage plane.

The electronic states in the $BiVO_4$ VBM have been found to originate from the hybridization of O2p and Bi6s orbitals, whereas the CBM consists of $V3d_{x^2-y^2/z^2}$ states.[113,114] Depending on the determination method, CBMs between 0.0 and 0.3 V vs RHE and VBMs between 2.4 and 2.7 V vs RHE have been assigned to $BiVO_4$.[114–119] The VBM, thus, lies far beneath the O_2/H_2O standard reduction potential, making water oxidation feasible. Doping $BiVO_4$ with a hexavalent ion like Mo^{6+} or W^{6+} generally exhibited a positive effect on its photo(electro)chemical water splitting performance,[26,120] most probably due to an increased charge carrier concentration.[119,121] However, only low charge carrier mobilities have been found for n-type $BiVO_4$. Rettie et al. calculated from Hall effect measurements that the electron drift mobility of W-doped $BiVO_4$ is in the order of 10^{-8} m^{-2} V^{-1} s^{-1}. Likewise, Abdi et al. determined an overall charge carrier mobility of 10^{-8} m^{-2} V^{-1} s^{-1} for W:$BiVO_4$ and related this weak mobility to electron trapping at tungsten induced bulk defects.[122] Other authors, however, state that the low majority charge carrier mobility is intrinsic to the $BiVO_4$ electron conduction mechanism, for which the thermally activated small polaron hopping mechanism[iii] has been postulated.[114,119] For $BiVO_4$ the electrons would then reside at the vanadium lattice sites, implying a reduction of V^{5+} to V^{4+}.[123–125] To move from vanadium to vanadium lattice site, a polaron hopping barrier of 0.46 eV has been calculated by Kweon et al.,[124] corresponding well to the experimentally reported 0.3 eV hopping barrier for 0.3 wt% W:$BiVO_4$.[119] Experimentally, the presence of inter-gap states with $V3d_{z^2}$ character was determined at about 1.8 eV from the VBM through resonant PES, fitting well to the small polaron hopping model between vanadium lattice sites.[121] Recently, Wiktor et al. calculated through hybrid functional molecular dynamics simulations an electron polaron level at 0.9 eV from the CBM and, more remarkably, a hole polaron level at 0.1 eV from the VBM with Bi lattice sites as polaron centres.[126] Due to the low energy difference between the CBM and the hole polaron level, holes should be more weakly localized and, thus, more mobile than electrons. Indeed, the hybrid DFT calculations performed by Kweon et al. predicted that the holes in $BiVO_4$ form weakly bound large polarons, which extend over multiple Bi and O lattice sites.[127]

[iii] Polarons often form in transition metal oxides when the velocity of an electron is low enough, so that the position of the atoms surrounding the electron are altered due to the electron's presence. The atom displacement creates a potential well, which reduces the carrier's energy. As a consequence, the carrier can become self-trapped and may only move when thermal vibrations lead to favourable atom displacement. Self-trapping distinguishes itself from trapping, due to the self-trapped carrier still being able to move. A distinction is made between small and large polarons which extent over one or multiple structural units, respectively. Large polarons, generally, have drift mobilities $> 1 \times 10^{-4}$ m^{-2} V^{-1} s^{-1}, whereas small polarons exhibit drift mobilities of $<< 1 \times 10^{-4}$ m^{-2} V^{-1} s^{-1}.

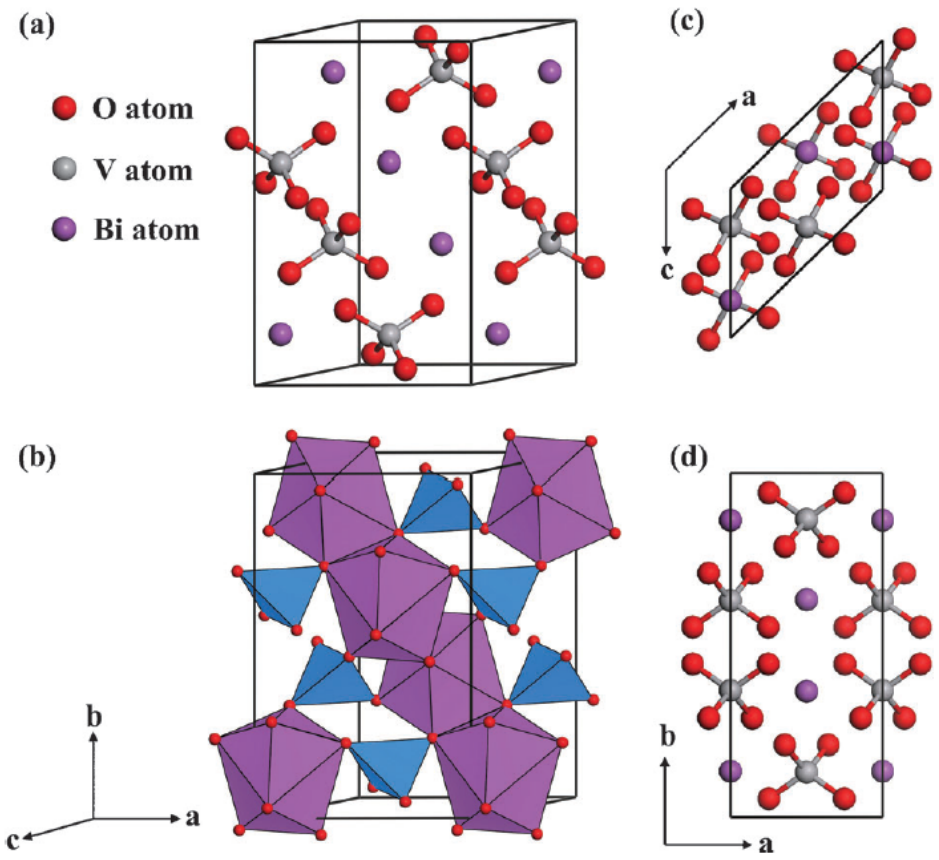

Figure 2.23: (a) Ball-and-stick and (b) polyhedron representation of the monoclinic clinobisvanite $BiVO_4$ crystal structure (with BiO_8 dodecahedron in purple and VO_4 tetrahedron in blue). (c) top and (d) side view of crystal structure.[113]

The band gap of $BiVO_4$ has been a point of discussion, with respect to it being direct or indirect. However, now it has been generally accepted that the band gap of $BiVO_4$ is indirect with only a 70 to 200 meV difference between the first indirect allowed optical transition and the first direct allowed optical transition.[113,128] The direct allowed transition is mostly considered to be at 2.4 — 2.5 eV.[114,121,129,130]

High photocurrents have been demonstrated with $BiVO_4$ based thin film photoanodes under external biases or through coupling to a photovoltaic system. Pihosh et al. demonstrated a water splitting photocurrent of 6.72 mA cm^{-2} under 1 sun illumination at 1.23 V_{RHE} for a $WO_3/BiVO_4$ core-shell nanostructured photoanode with cobalt phosphate (CoPi) as a cocatalyst.[27] When this nanostructured photoanode was coupled to a GaAs/InGaAsP solar cell, an STH efficiency of 8.1% was obtained. Qiu et al. found that a nanocone Mo:$BiVO_4$/Fe(Ni)OOH photoanode exhibited a photocurrent density of 5.82 ± 0.36 mA cm^{-2} under 1 sun illumination at 1.23 V_{RHE}.[131] Abdi et al. reported that a CoPi catalysed 10-step gradient-doped W:$BiVO_4$ photoanode could generate an AM 1.5G photocurrent of 3.6 mA cm^{-2} at 1.23 V_{RHE}.[26] When this gradient

doped $BiVO_4$ photoanode was combined with a double-junction amorphous silicon solar cell an STH efficiency of 4.9% was obtained. Kim et al. showed that a stand-alone $BiVO_4$ photoanode could be efficient as well by obtaining an applied bias photon-to-current efficiency of 1.75% at 0.6 V_{RHE} for a $BiVO_4$/FeOOH/NiOOH system.[132] Furthermore, Higashi et al. reported an unbiased 1.0% STH efficiency for a stand-alone PEC cell with $BiVO_4$ as photoanode and strips of $(ZnSe)_{0.85}(CuIn_{0.7}Ga_{0.3}Se_2)_{0.15}$ as photocathode.[133] Most of these reports indicate that to achieve high water photo-oxidation efficiencies, modifications to bare $BiVO_4$ are required. These modification include doping with a hexavalent ion like Mo^{6+} or W^{6+} to increase the majority charge carrier concentration, nanostructuring to reduce the length over which the charge carriers have to diffuse to reach the surface and heterostructuring which may improve surface passivation, charge carrier separation and/or the water oxidation kinetics. To improve the understanding on how heterostructuring may enhance charge carrier separation, heterostructured $BiVO_4$ thin films were, in this work, studied through interface experiments, whereby thin film contact layers were stepwise deposited onto a $BiVO_4$ substrate, with photoelectron spectroscopy measurements in between each deposition step. The photoelectron spectroscopic data allowed to construct interfacial heterostructure band alignments, which were used to discuss charge carrier separation in heterostructured $BiVO_4$. Specifically, interface experiments were performed to study the solid/solid interfaces of $BiVO_4/RuO_2$, $BiVO_4$/NiO, $BiVO_4/CoO_x$ and $BiVO_4$/ITO.

In particulate water splitting, $BiVO_4$ can be used as the water oxidation compound in a Z-scheme type system (Figure 2.12).[134] Into these $BiVO_4$ Z-scheme systems, CdS,[135,136] $Zn_xCd_{1-x}Se$[137] and rhodium-doped $SrTiO_3$[36,134,138] have been incorporated most frequently as the water reduction compounds. Liquid redox mediators like Fe^{2+}/Fe^{3+}[134] and IO_3^-/I^-[137] have been used as well as solid state redox mediators, such as carbon dots[135] and reduced graphene oxide.[34] The highest STH efficiencies with Z-scheme type systems have been reported when the particles were immobilised on a conductive sheet. By immobilising particulate Mo:$BiVO_4/RuO_x$ and Rh,La-codoped $SrTiO_3$/Ru on a 10 x 10 cm conductive carbon film (Figure 2.24), unassisted pure-water splitting with a state of the art 1.0% STH efficiency could be realised under ambient conditions (331 K and 91 kPa). Also the immobilization on a gold layer yielded a high 1.1% STH efficiency under reduced pressure (331 K and 10 kPa).[36]

For particulate photocatalysts, contact materials were until recently solely deposited in a random manner. Random cocatalyst coverage, however, provide no distinct flow path for photogenerated holes and electrons, so that the problem of bulk and surface recombination could still persist due to insufficient charge carrier separation. Anisotropic photodeposition now allow cocatalysts to be deposited at specific sites on anisotropic crystalline particles. The idea is that after light absorption the photogenerated electrons and holes preferentially accumulate on different crystalline facets, so that reduction and oxidation reactions are spatially separated. Cocatalysts can then be deposited on different sites depending on whether the cocatalyst deposition involves an oxidation or reduction reaction.[139–141] Anisotropic photodeposition on $BiVO_4$ has been extensively studied by Can Li et al. A first finding was that dual exposed {010},{110}

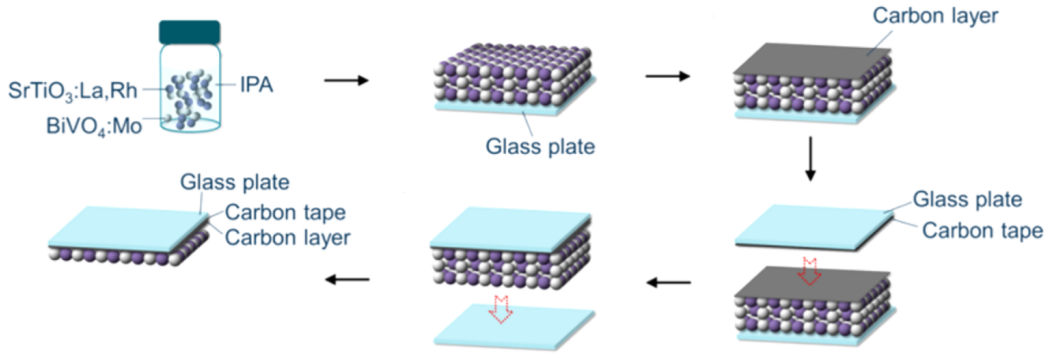

Figure 2.24: Scheme illustrating how Rh,La-codoped $SrTiO_3$ and Mo:$BiVO_4$ were immobilised on a conductive carbon film.[37]

monoclinic $BiVO_4$ crystals exhibited a high photocatalytic oxygen evolution efficiency, dependent on the relative {010},{110} exposure ratio.[142] Initially, it was assumed that highly active $BiVO_4$ centres on the {010} facets were responsible for the high oxygen evolution efficiency, but enhanced charge carrier separation due to the anisotropic morphology seemed more plausible after a series of photodeposition experiments.[143] Field emission secondary electron microscope (FESEM) images showed that metallic deposits were preferentially found on {010} facets after metal ion photoreduction, while metal oxide deposits were found on the {110} facets after metal ion photo-oxidation, providing evidence that electrons and holes accumulate on different sites on anisotropic $BiVO_4$ crystals (Figure 2.25). The origin of the enhanced charge carrier separation on {010},{110} exposed $BiVO_4$ crystallites is not yet fully understood. Liu et al. proposed that anisotropic charge carrier mobilities could be the underlying reason for enhanced charge carrier separation, whereby DFT calculations showed a five orders of magnitude higher electron mobility along the [010] direction compared to the [110] direction and hole mobility along the [110] direction was two orders of magnitude higher compared to the [010] direction.[125] Contrarily, Zhu et al. who performed spatially resolved surface photovoltage spectroscopic measurements on a dual {010},{110} exposed $BiVO_4$ single crystal, concluded that higher upwards band bending near the {110} facets was the primary cause of the anisotropic photoinduced charge transfer between the facets.[145] Besides providing proof of enhanced charge carrier separation, the preferential photodeposition was used to construct $BiVO_4$ photocatalysts with even better photocatalytic oxygen evolution efficiencies by depositing reduction cocatalysts on the more reducing {010} facets and oxidation cocatalysts on the more oxidative {110} facets, with Pt/CoO_x/$BiVO_4$ reaching an oxygen evolution efficiency of 160.3 µmol/h compared to only 1 µmol/h for bare $BiVO_4$.[144] In this work (more specifically in Chapter 4), the photodeposition of Pt, Ag and CoO_x on a dual exposed {010},{110} monoclinic $BiVO_4$ microcrystalline powder was reproduced. The regioselectivity of the deposits and the water oxidation performance of the reproduced heterostructured $BiVO_4$ powders were determined and compared to the properties of a newly synthesized heterostructure, $BiVO_4/NiO_xOH_y$.

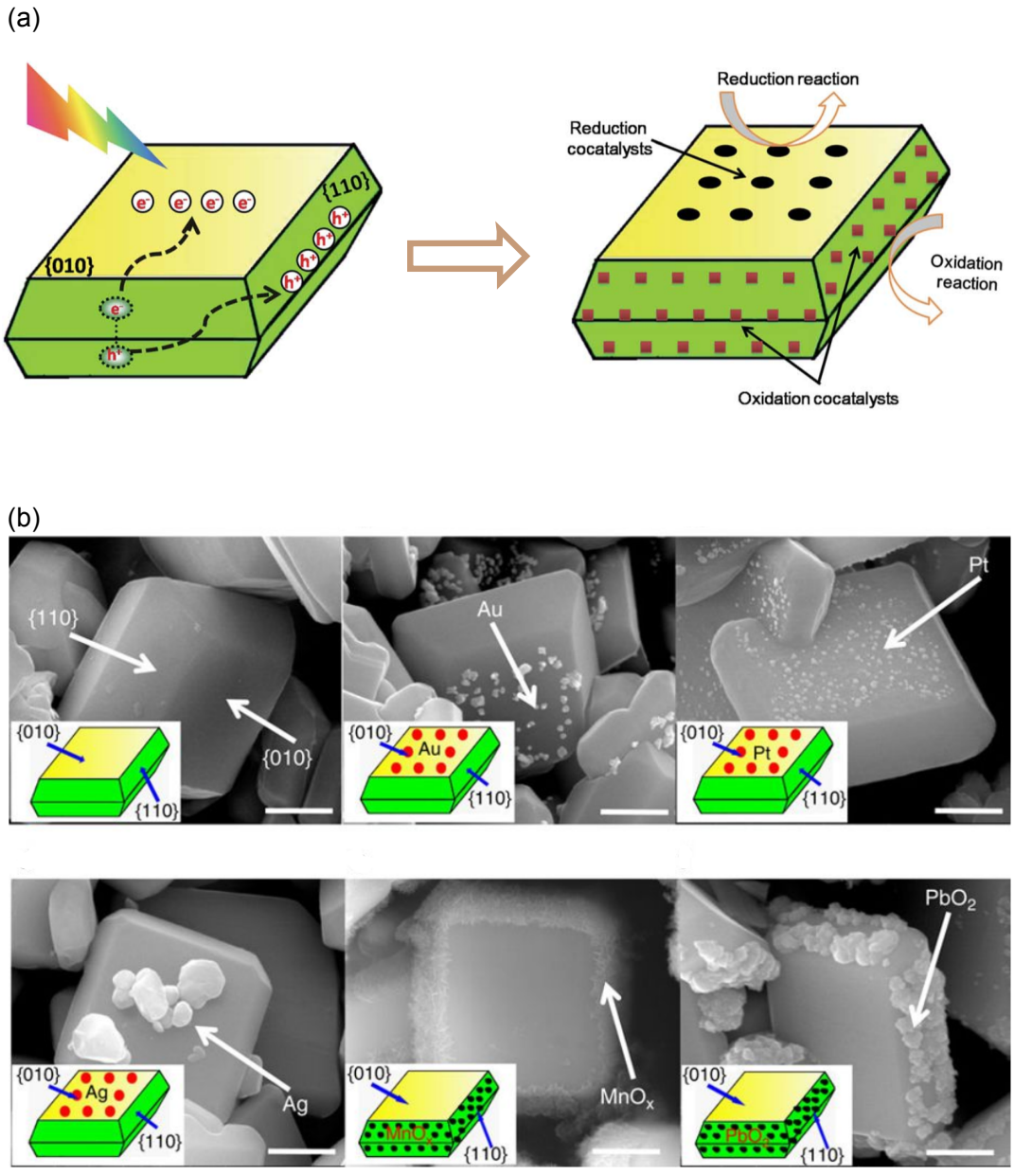

Figure 2.25: (a) Scheme showing the selective deposition of reduction and oxidation cocatalysts on the {010} and {110} $BiVO_4$ facets, respectively, due to anisotropic photoinduced charge carrier migration and (b) FESEM images of a series of anisotropic $BiVO_4$ heterostructures. Scale bar: 500 nm.[143,144]

2.3.2 $CuFeO_2$

$CuFeO_2$ is an intrinsic p-type semiconductor with a delafossite crystal structure, made up by a stacking of alternating [Cu^+] and [FeO^{2-}] layers perpendicular to the c-axis (Figure 2.26). Two polytypes have been associated with the $CuFeO_2$ delafossite crystal structure, which differ from each other with respect to the relative orientation of the [Cu^+] layers. The 3R-polytype with $R\bar{3}m$ symmetry consist of [Cu^+] layers having the same relative orientation, albeit with an offset which extends over a three layer sequence. The 2H-polytype with $P6_3/mmc$ symmetry consists of alternating [Cu^+] layers, which are oriented 180° with respect to each other.

The electrical properties of $CuFeO_2$ have been found to be closely linked to its crystal structure. Resistivity measurements on p-type $CuFeO_2$ single crystals demonstrated a highly anisotropic electrical conductivity, exhibiting specific resistivities of 5 x 10^{-3} Ωm and 3 x 10^{1} Ωm perpendicular and parallel, respectively, to the c-axis.[146] Benko et al. suggested that conductivity in p-type $CuFeO_2$ takes place through a small polaron hopping mechanism, whereby Cu^+ forms the centre of the polarons.[147] This mechanism would agree with the observed anisotropic conductivity, since polaron hopping from Cu to Cu site would be more facile within the [Cu^+] layers perpendicular to the c-axis than between two [Cu^+] layers along the c-axis. Benko et al. further calculated an effective hole mobility in the range of 10^{-4} — 10^{-6} m^2 V^{-1} s^{-1} for polycrystalline p-type $CuFeO_2$ pellets, which agrees well with the overall 2 x 10^{-5} m^2 V^{-1} s^{-1} charge carrier mobility determined through time-resolved microwave conductivity (TRMC) measurements by Prévot et al. for a $CuFeO_2$ thin film.[148] The TRMC measurements further demonstrated a relatively long charge carrier lifetime of 200 ns and a free carrier diffusion length of 225 nm.

There is some ambiguity in literature on the exact band gap of $CuFeO_2$. Experimentally, band gaps of 1.15 eV (indirect) and 2.03 eV (direct);[147] 1.23 eV (indirect) and 1.63 eV (direct);[150] 1.36 eV[151] and 1.55 eV[152] have been determined. Possibly, the magnetic structure of $CuFeO_2$ influences the band gap as Crespo et al. found through first principles calculations that the $CuFeO_2$ band gap differs for ferromagnetic and antiferromagnetic ordering.[153] Indeed, besides its use for photocatalysis, $CuFeO_2$ has been studied for its magnetic properties,[154] whereby antiferromagnetic[155] and ferromagnetic[156] ordering have been recognised. Several experimental[147] and theoretical reports[156,157] have shown that the $CuFeO_2$ valence band maximum is primarily consists of Cu3d and O2p states, whereas the conduction band minimum consists mainly of Fe3d states. The presence of the Cu3d states in the valence band edge is what shifts the $CuFeO_2$ VBM upwards with respect to the VBMs of other oxide semiconductors. Furthermore, the Fe3d states in the CBM are most likely the cause of the lower measured band gaps with respect to Cu_2O, which has a reported band gap of 2.0 — 2.2 eV.[158] CBMs between -0.1 eV and -0.5 eV have been published,[148,150,152,159] making $CuFeO_2$ potentially suitable for water reduction.

Based on the reported band gaps, photocurrents of up to 15 mA cm^{-2} should be feasible with $CuFeO_2$.[148] However, the published water splitting efficiencies have been rather low so far. Read et al. found a steady state photocurrent of only 0.016 mA cm^{-2} at 0.6 V_{RHE} for a bare $CuFeO_2$

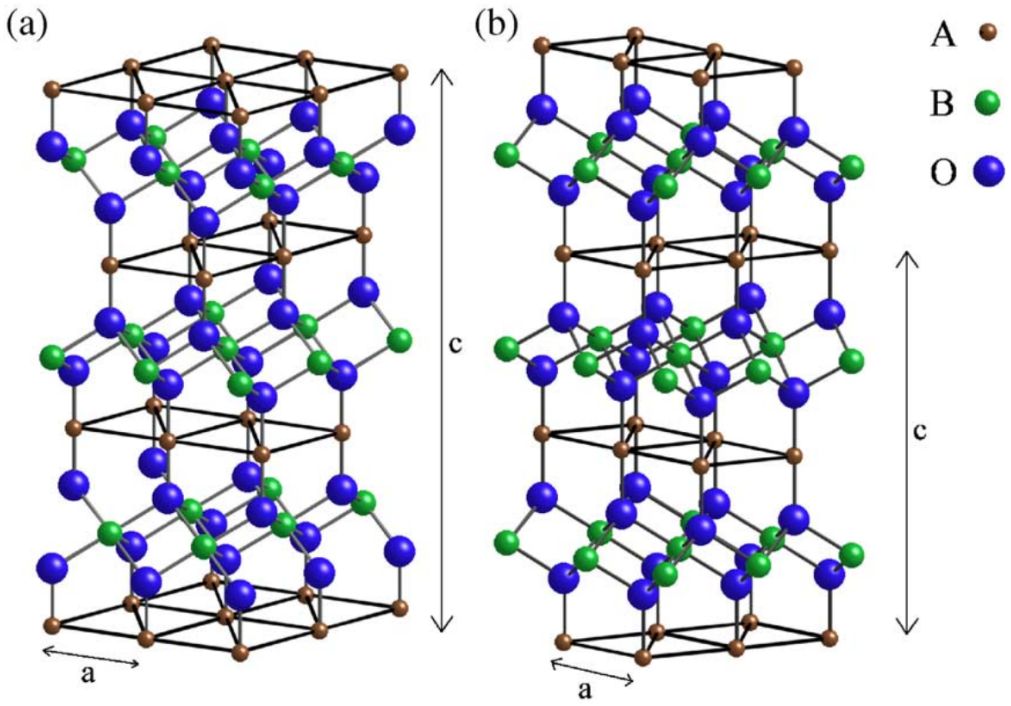

Figure 2.26: Delafossite crystal structure which can crystallize into two polytypes: (a) 3R polytype with $R\bar{3}m$ space group and (b) 2H polytype with $P6_3/mmc$ space group. For $CuFeO_2$ the A cations are Cu^+ and the B cations are Fe^{3+}.[149]

thin film synthesized via an electrodeposition procedure.[152] A slightly better photocurrent of 0.2 mA cm^{-2} at 0.6 V_{RHE} was reported by Oh et al. for an array of 2D photonic crystals coated with $CuFeO_2$.[160] By introducing a hole selective contact, $CuAlO_2$, Prévot et al. found a 2.4 fold increase in photocurrent, up to 2.4 mA cm^{-2} at 0.4 V_{RHE}, for a $CuFeO_2$ thin film using oxygen, instead of water, as electron scavenger.[161] The highest photocurrent published until now with water as electron scavenger, thus real water reduction, is 2.4 mA cm^{-2} at 0.4 V_{RHE} by Jang et al. for a hybrid microwave annealed $CuFeO_2$ photocathode coated with a NiFe-layered double hydroxide/reduced graphene oxide electrocatalyst.[95] These reports show that the addition of a "cocatalyst" benefits the $CuFeO_2$ water reduction efficiency. Furthermore, hydrogen evolution with $CuFeO_2$ only seems to be feasible under an applied bias. The need for a bias suggests that the necessary photovoltage for water reduction cannot be reached. Indeed, Prévot et al. found that, due to Fermi level pinning, only a photovoltage of 0.3 V could be generated, whereby the Fermi level pinning was associated with surface states at the $CuFeO_2$/electrolyte interface. Other suggested reasons for the weak hydrogen evolution efficiencies include Fermi level pinning at inter-gap states in the bulk,[162] photocorrosion[152] and poor catalytic activity.[95]

In this study (Chapter 6), particulate $CuFeO_2$ with a defined morphology was synthesized according to a hydrothermal procedure published by Jin et al.[28] However, the authors found that a thin film, prepared by dropcasting the hexagonal 2H-$CuFeO_2$ nanoplatelet powder, only

led to a limited photocurrent of 8.8 μA at 0 V_{RHE}. In this work, we wanted to study whether heterostructuring of the $CuFeO_2$ nanoplatelets, would allow unbiased particulate photochemical water reduction. Due to the specific morphology and the observed anisotropic charge carrier dynamics, we theorized that the creation of anisotropic $CuFeO_2$ heterostructures should be feasible through photodeposition. Hence, the photodeposition of several metal(oxide)s and the characteristics of the resulting $CuFeO_2$ heterostructures was studied. The performance of the $CuFeO_2$ heterostructured powders was assessed through photochemical sacrificial water splitting in a batch reactor equipped with an automatic burette. Furthermore, interface experiments were performed between pelletized $CuFeO_2$ powder as substrate, and ITO and water as contact layers to investigate bulk Fermi level pinning phenomena, which could limit the $CuFeO_2$ photovoltage.

2.4 Photoelectron spectroscopy

Photoelectron spectroscopy (PES) focuses on the energy analysis of electrons emitted from a substance through the photoelectric effect. The photoelectric effect takes place when an electron is excited by a photon, which has a high enough energy to overcome the binding energy of the electron to the substance, so that the electron is ejected from the substance as a result. Electrons liberated in this way are called photoelectrons. The energy needed to eject the electrons depends on how the electrons are bound in the substance. Photons with an energy of a few eV are sufficient to release delocalized electrons, whereby the lowest photon energy that allows the ejection of the electrons from a solid, is referred to as the solid's work function. Electrons residing in the valence orbitals of an atom, molecule or compound have a higher binding energy and generally require photons from the ultraviolet spectral region to be released. PES with a UV light source is commonly referred to as ultraviolet photoelectron spectroscopy (UPS). Electrons closer to the atomic core, have an even higher binding energy than the outer valence electrons, necessitating the absorption of higher energy photons. Generally, photons from the X-ray spectral region are needed to liberate these core electrons. X-ray photoelectron spectroscopy (XPS) encompasses the technique, whereby photoelectrons, emitted by an X-ray source, are analysed.

In a common photoelectron spectrometer (Figure 2.27), a monochromatized source of photons is focused onto a sample. The photoelectrons released from the sample pass through a set of electrostatic lenses, which decelerate the electrons and focus them into the entrance slit of a hemispherical analyser, which is used to only let electrons with a specific kinetic energy (pass energy) reach the detector channels. The path from sample to detector should be operated under UHV to avoid inelastic scattering of the photoelectrons. Photoelectron spectrograms are generally recorded in sweeping mode, whereby a certain energy region is scanned one or multiple times by fixing the pass energy and sweeping the voltage applied to the electrostatic lenses in such a manner that electrons with a selected kinetic energy are counted for a selected amount of time by the channels of the detector. A certain set of lens functions correspond to a certain electron kinetic energy (E_{kin}) and, thus, to a certain electron binding energy (E_B) according to:

$$E_B = h\nu - E_{kin} - \Phi_{sp} \tag{2.42}$$

with Φ_{sp} being the spectrometer work function and $h\nu$ being the photon energy. For XPS, photons are usually generated through X-ray anodes, whereby monochromatized Al Kα or Mg Kα X-rays with photon energies of 1486.6 eV and 1253.6 eV, and energy widths of 0.85 eV and 0.70 eV, respectively, are the most popular. The photon source in UPS is mostly a helium discharge lamp, which can emit photons with two characteristic energies 21.2 eV and 40.8 eV, denoted as He I and He II photons, respectively. Furthermore, PES systems can be coupled to a synchrotron, whereby the advantages of a synchrotron include the tunability of the photon energy, high brilliance, strong collimation, and high photon flux of synchrotron irradiation.

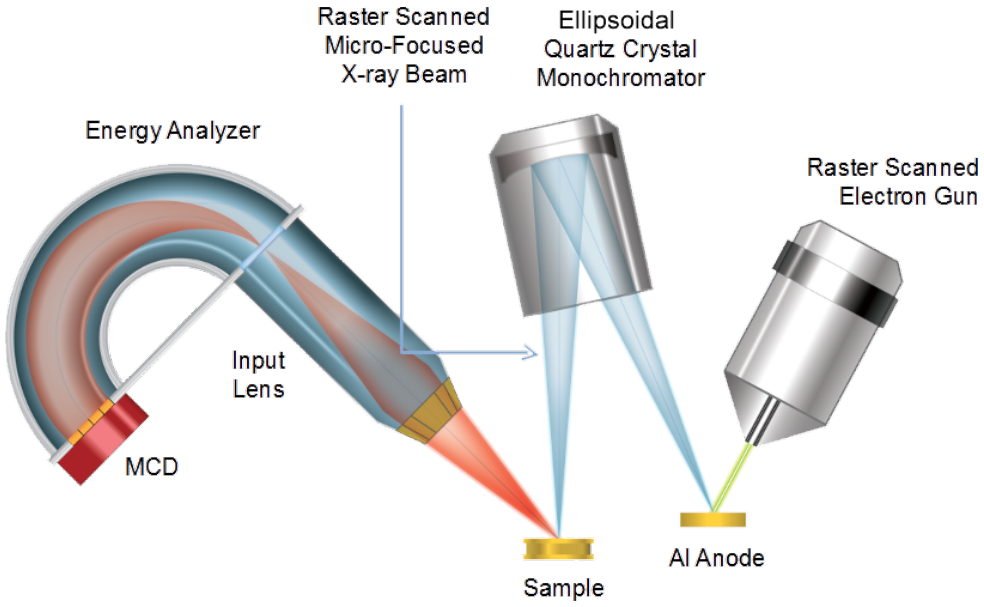

Figure 2.27: Schematic of a PES instrument.©Phi Inc.

Φ_{sp} is a parameter, specific to the photoelectron spectrometer, which can be corrected for by measuring the Fermi level of a cleaned metallic sample and appointing it to a binding energy of zero. This energy calibration is maintained for other conducting samples in electrical contact to the spectrometer, as their Fermi level align with that of the spectrometer. Therefore, the photoelectron binding energies of a conducting sample are measured in reference to the Fermi level of the sample.

An important notice which has to be made is that the binding energy mentioned in Equation 2.42 not only depends on its initial bonding state but also on so called ”final state” effects, which refer to the state of the photohole after the electron is ejected, and extrinsic effects through which the photoelectron loses/gains kinetic energy in between its creation and its escape from

the material. An extensive overview of those effects can be found in the PhD dissertation of Mirko Weidner.[163] Some effects worth mentioning include spin-orbit coupling, electron shake-up, electron shake-off, plasmon excitation and phonon interactions. Spin-orbit coupling is a final state effect, whereby the spin of an unpaired core electron left behind after photo-emission couples with the angular momentum of the orbital. This effect is noticeable for photo-emission of electrons residing in p,d,f,... orbitals and is the reason why, for instance, the Bi4f core level spectrum exhibits two distinct signals, denoted as $Bi4f_{7/2}$ and $Bi4f_{5/2}$, whereby 7/2 and 5/2 are the possible quantum number sums of angular (f-orbital: 3) and spin quantum number (+1/2 or -1/2). Electron shake up and electron shake off phenomena are extrinsic effects, whereby an energy transfer takes place from the photoelectron to another electron that is excited to a higher state or ejected from its atomic core, respectively. These phenomena are in part responsible for the satellite features seen in many transition metal 2p spectra such as Co2p, Fe2p and Ni2p. During plasmon and phonon interactions energy transfer takes place between photoelectrons and the electron gas (delocalized electrons) or phonons, respectively, whereby seemingly higher binding energies are registered for the photoelectrons that were involved in those processes.

PES is, furthermore, a surface sensitive technique. The liberated photoelectrons have kinetic energies which correspond to mean free paths in the range of 0.5 — 5 nm (Figure 2.28) and the PES information depth is generally considered to be ± 3 times the electron mean free path. Hence, the information depth is limited from a few atomic layers to ± 15 nm.

For a more detailed description of photoelectron spectroscopy, I refer the reader to the work of Stefan Hüfner.[7,164]

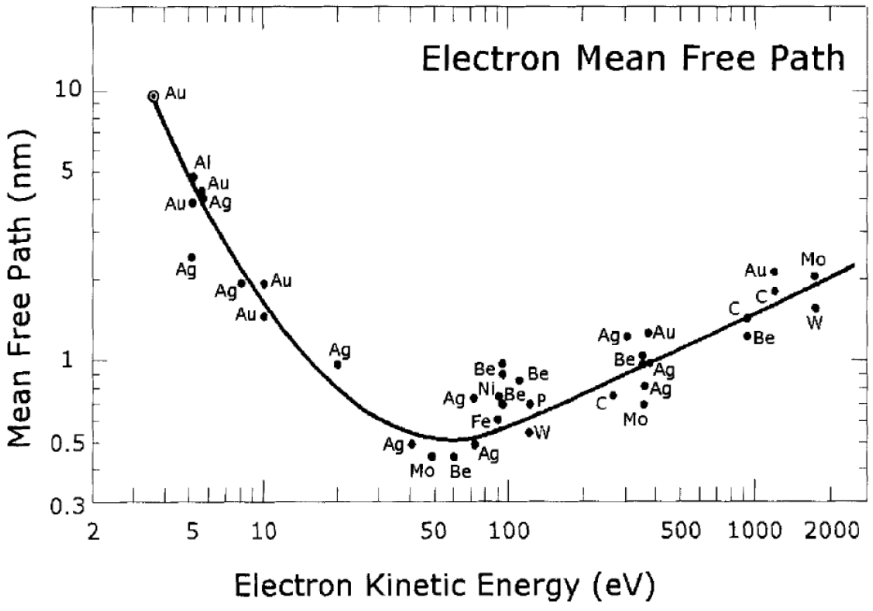

Figure 2.28: Universal curvature of electron mean free path with respect to kinetic energy.[165]

Next, it will be explained how the chemical state of an element can be determined from its most intense core level spectrum, specifically for the core level spectra displayed in this work.

2.4.1 Transition metal core level spectra

Deriving the chemical state of a transition metal from one of its photoelectron core level spectra may be challenging, due to the variety of final state effects that may take place, especially for oxidation states where the metal d-orbitals are partly filled. For some transition metals, it may even be impossible to quantify how much of each species is present in a certain composition, due to the spectra of these species not being well resolved from each other. For these transition metals, only qualitative statements can be made. The discussion below will focus on how certain oxidation states may be determined from the shape of the spectra as well as from the binding energies of certain features of the main core level photoelectron lines of transition metal (hydr)oxides.

2.4.1.1 V2p

The V2p spectrum of vanadium oxides with a single oxidation state generally contain two main signals which are split from each other due to spin-orbit coupling.[166] These signals are generally denoted as $V2p_{3/2}$ and $V2p_{1/2}$. The $V2p_{1/2}$ signal is broadened with respect to $V2p_{3/2}$ due to Coster-Kronig effects,[167] which involve the rapid (in the order of 10^{-15} s) filling of the photohole by an electron of a higher-energy shell with the same principal quantum number as the photohole. Coster-Kronig effects give rise to broad line shapes.[168] As can be seen in Figure 2.29 and Table 2.1, oxides with different vanadium oxidation states have distinct $V2p_{3/2}$ and $V2p_{1/2}$ binding energies for each oxidation state, whereby peak fitting can be applied to give an estimate of the surface composition of a mixed vanadium oxide material. The $V2p_{3/2}$ line of V^{5+} is sharper with respect to the $V2p_{3/2}$ line of the other oxidation states, because V^{5+} does not contain any unpaired electrons which may give rise to additional final state effects. Contrarily, V^{4+} and V^{3+} have unpaired electrons, causing a multiplet splitting and, thus, a broader line shape.

Table 2.1: Spectral fitting parameters for the V2p spectrum of various vanadium oxide species.s.[166,167,169]

Species	$V2p_{3/2}$ (eV)	$V2p_{1/2}$-$V2p_{3/2}$ splitting (eV)
V(0)	512.35	7.50
V(I) and/or V(II)	513.67	7.33
V(III) oxide	515.29	7.33
V(IV) oxide	515.84	7.33
V(V) oxide	517.20	7.33

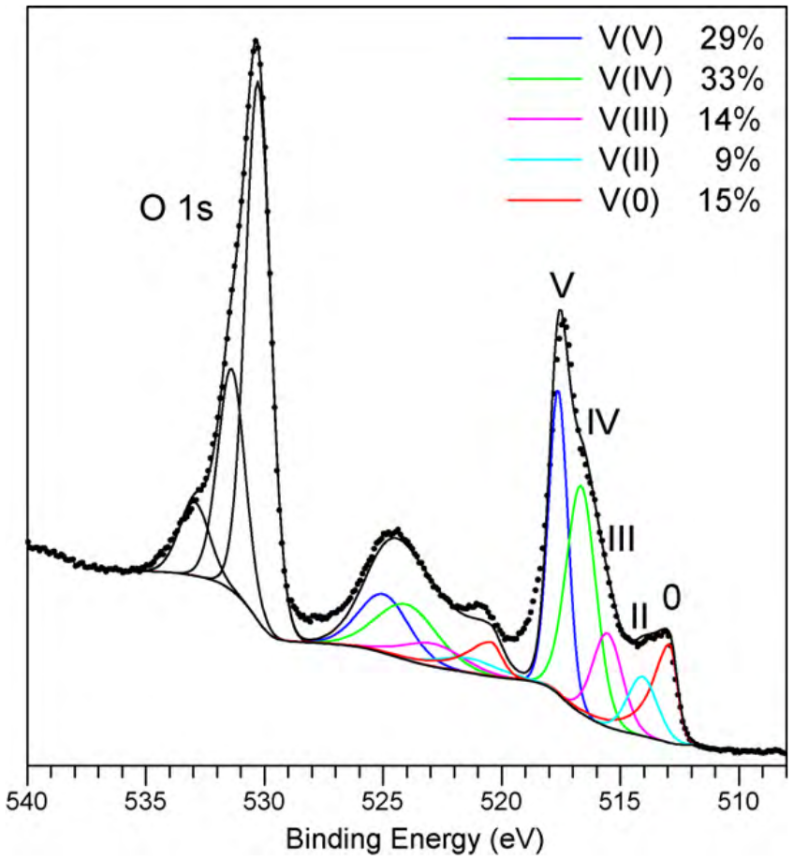

Figure 2.29: V2p (and O1s) core level spectrum of a mixed vanadium oxide sample.[166]

2.4.1.2 Fe2p

The Fe2p spectrum is considerably more complicated than the V2p spectrum. Most Fe2p spectra again consist of two main signals, separated by about 13.4 eV, originating from spin-orbit coupling and are denoted as $Fe2p_{3/2}$ and $Fe2p_{1/2}$. The main iron oxidation states for iron oxide compounds are Fe^{2+} and Fe^{3+}. Due to these oxidation states having unpaired d-electrons which couple to 2p electrons, the main $Fe2p_{3/2}$ and $Fe2p_{1/2}$ lines exhibit a multiplet structure.[170] This multiplet structure gives rise to considerably broadened lines, which makes it difficult to distinguish between Fe(II) oxides from Fe(III) oxides, although distinct $Fe2p_{3/2}$ binding energies at about 708.4 and 710 eV have been found for Fe(II) oxides and Fe(III) oxides, respectively.[171] Additionally, Yamashita found that a satellite at about 716 eV is characteristic for Fe(II) oxides (Figure 2.30), whereas a satellite at 719 eV is found for Fe(III) oxides (Figure 2.31). These satellites are considered to originate from electron shake-up processes.[170,172]

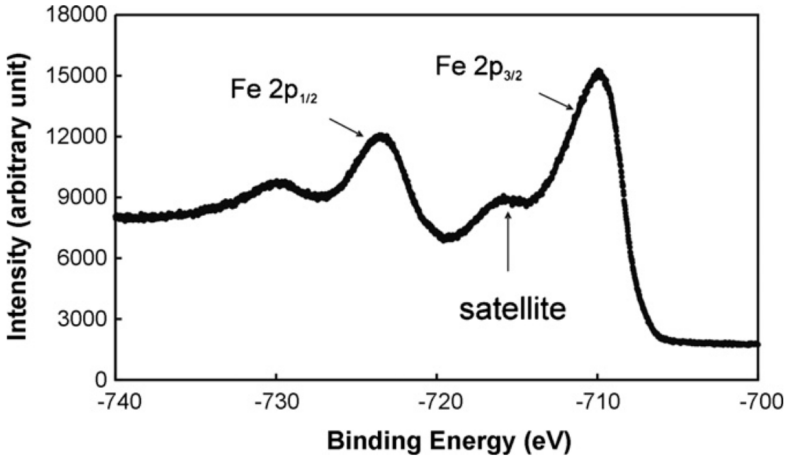

Figure 2.30: Fe2p core level spectrum from the fractured surface of a $Fe_{0.96}O$ standard sample.[173]

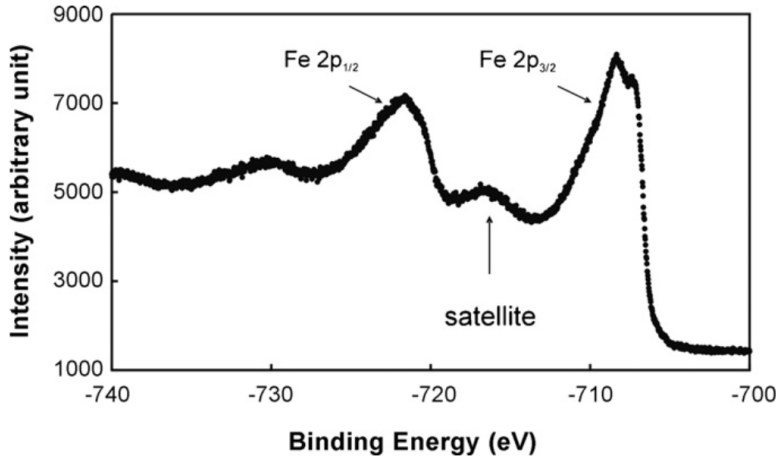

Figure 2.31: Fe2p core level spectrum from the fractured surface of a Fe_2O_3 standard sample.[173]

2.4.1.3 Co2p

The $Co2p_{3/2}$ and $Co2p_{1/2}$ binding energies lie at about 780 eV and 793 eV, respectively, for cobalt hydr(oxide) species (Figure 2.32). Thus, fitting the main $Co2p_{3/2}$ and/or $Co2p_{1/2}$ does not allow a reliable quantification of a mixed cobalt hydr(oxide) phase. However, the distinction between Co^{2+} and Co^{3+} can be made from the satellite structure between $Co2p_{3/2}$ and/or $Co2p_{1/2}$. Co^{2+} namely gives rise to a noticeable satellite at about 786 eV, as can be seen for CoO and $Co(OH)_2$ in Figure 2.32. In contrast, for the mixed Co_3O_4 the satellite at 786 eV is less intense and an additional shake-up satellite at about 789.5 eV appears, which has been associated with Co^{3+}.[171,174,175]

2.4.1.4 Ni2p

One of the most complicated transition metal spectra with respect to species determination is undoubtedly the Ni2p spectrum, as can be seen in Figure 2.33. Generally, determining the composition of nickel hydr(oxide) mixtures through peak fitting generates large absolute errors due to the shape of the main $Ni2p_{3/2}$ and $Ni2p_{1/2}$ lines and their satellite structure being very similar for the different nickel hydr(oxide) species. However, NiO can be distinguished from $Ni(OH)_2$ and γ-NiOOH due to the main $Ni2p_{3/2}$ and $Ni2p_{1/2}$ lines being split up into two distinct signals separated by about 1 eV.

2.4.1.5 Cu2p

The $Cu2p_{3/2}$ and $Cu2p_{1/2}$ lines are separated by about 20 eV. The main $Cu2p_{3/2}$ emission line can be used to distinguish cupric oxide from cuprous oxide and metallic copper, as the binding energy of the $Cu2p_{3/2}$ line of copper(II) oxide generally lies at about 933.6 eV, whereas the $Cu2p_{3/2}$ binding energies of metallic copper and copper(I) oxide generally can be found at about 932.4 — 932.6 eV, as can be seen in Figure 2.34 and Table 2.2.[166,177] Additionally, the Cu2p spectrum of Cu^{2+} distinguishes itself from metallic copper and Cu^{+} by an apparent shake-up satellite feature at about 941 eV.[178] The Cu2p spectra of metallic copper and cuprous oxide are nearly indistinguishable. Instead, the CuLMM Auger spectrum needs to be recorded to make the distinction between metallic copper and cuprous oxide, as both have a different CuLMM binding energy, as can be seen in Figure 2.35 and Table 2.2.

Table 2.2: $Cu2p_{3/2}$ binding energy and modified Auger parameter literature values for copper species.[166,177]

Species	$Cu2p_{3/2}$ (eV)	Modified Auger parameter (Lit. Ave.)
Cu(0)	932.61	1851.23
Cu(I) oxide	932.43	1849.19
Cu(II) oxide	933.57	1851.49

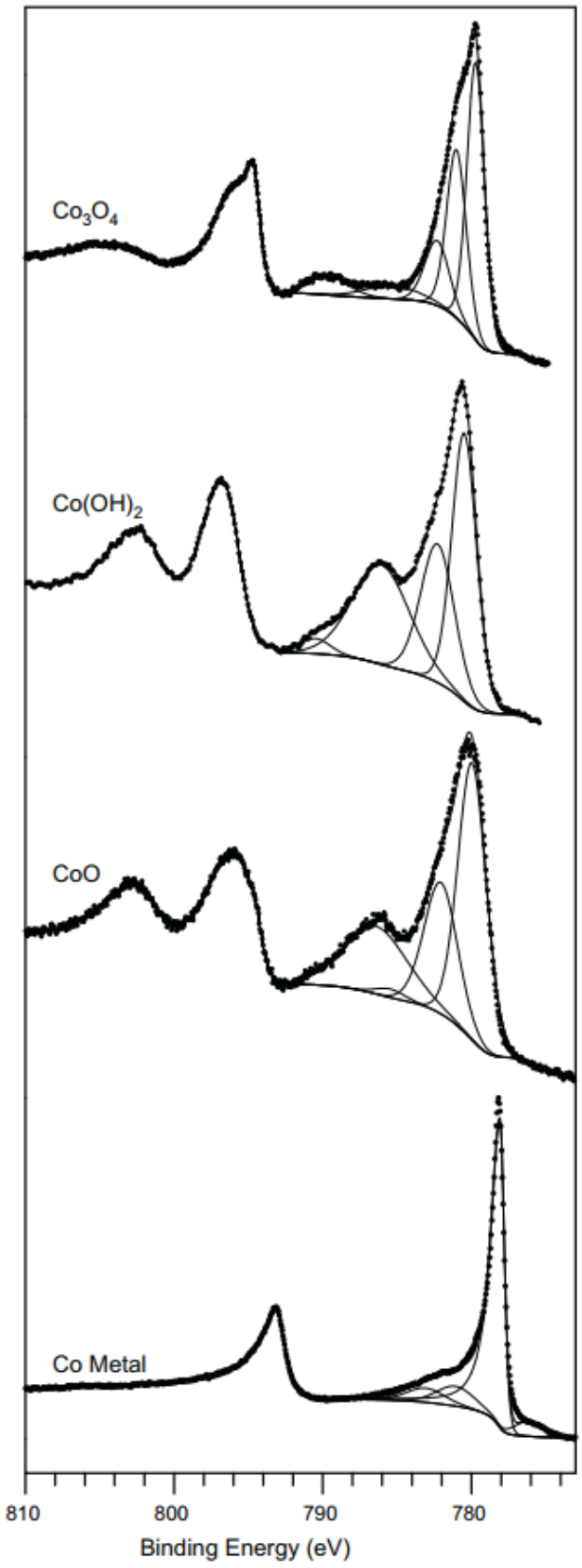

Figure 2.32: Co2p spectra for (bottom to top) Co metal, CoO, $Co(OH)_2$ and Co_3O_4.[171]

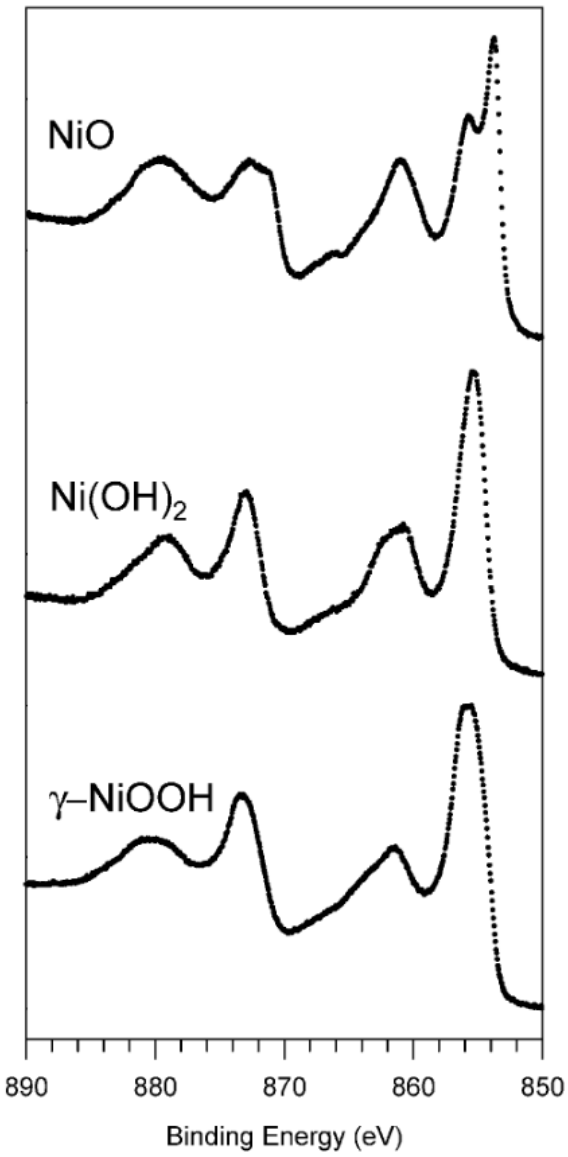

Figure 2.33: Ni2p spectra for NiO, $Ni(OH)_2$ and NiOOH.[176]

2.4.2 Noble metal core level spectra

2.4.2.1 Ag3d

The Ag3d spectrum is used most often to determine the silver species. Generally, the Ag3d spectrum consist of two main signals, $Ag3d_{5/2}$ and $Ag3d_{3/2}$, which originate from spin-orbit coupling. Remarkably, the $Ag3d_{5/2}$ and $Ag3d_{3/2}$ binding energies of silver oxides have been found at lower binding energies (Table 2.3), which is apparently caused by initial state effects related to an ionic charge shift and the lattice potential.[179] Additionally, for metallic silver the line shapes are slightly asymmetric due to bulk and surface plasmon loss features.

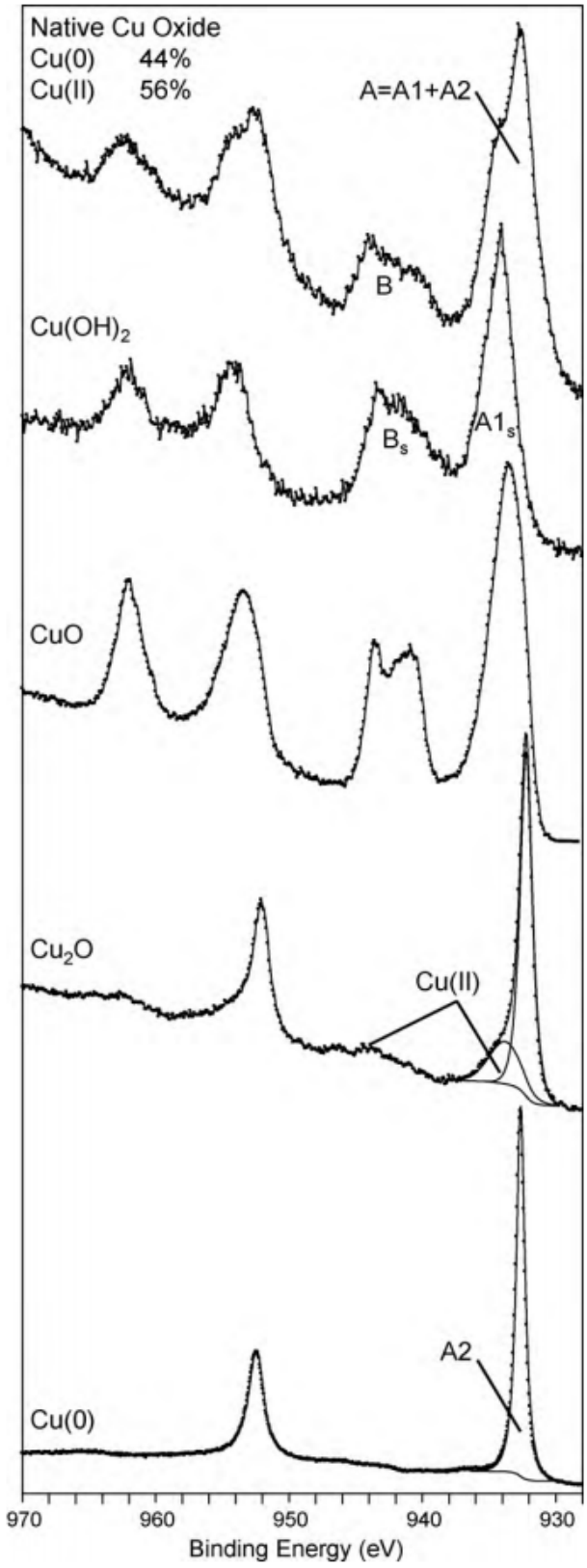

Figure 2.34: Cu2p core level spectra for different copper species.[166]

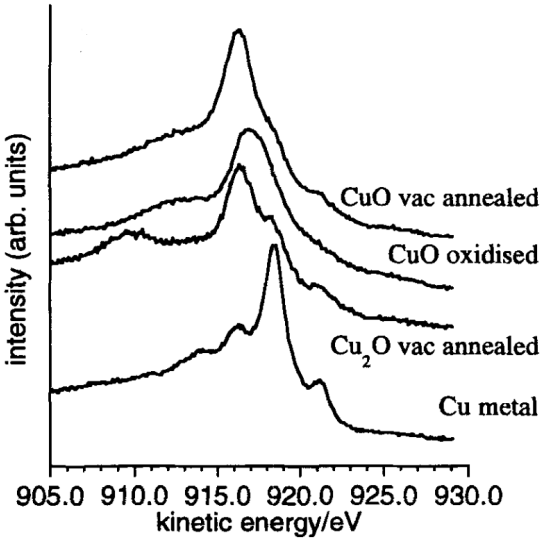

Figure 2.35: CuLMM core level spectra for different copper species.[178]

Table 2.3: Ag3d binding energies for Ag, Ag_2O and AgO.[177,180]

Species	$Ag3d_{5/2}$ (eV)	$Ag3d_{3/2}$-$Ag3d_{5/2}$ splitting (eV)
Ag	368.3	6.0
Ag(I)O	367.9	6.0
Ag(II)O	367.6	6.0

2.4.2.2 Pt4f

Just like the Ag3d spectrum, the Pt4f spectrum consists of two clear signals, which are denoted as $Pt4f_{7/2}$ and $Pt4f_{5/2}$. Due to bulk and surface plasmon loss features slightly asymmetric line shapes are found for metallic platinum. The commonly found binding energies for Pt, PtO and $Pt(OH)_2$ can be found in Table 2.4.

Table 2.4: Pt4f binding energies for Pt, PtO and $Pt(OH)_2$.[177,180]

Species	$Pt4f_{7/2}$ (eV)	$Pt4f_{5/2}$-$Pt4f_{7/2}$ (eV)
Pt	71.1	3.3
$Pt(OH)_2$	72.7	3.3
PtO	74.0	3.3

2.4.3 Bi4f

The Bi4f spectrum is very similar to the Pt4f spectrum in that it only consists of two main signals, split from each other by spin-orbit coupling, $Bi4f_{7/2}$ and $Bi4f_{5/2}$. Bi_2O_3 and Bi(0) can be easily

distinguished from each other, as the $Bi4f_{7/2}$ and $Bi4f_{5/2}$ binding energies of Bi(0) are shifted downwards by about 2.4 eV with respect to the $Bi4f_{7/2}$ and $Bi4f_{5/2}$ binding energies of Bi_2O_3 (Table 2.5).

Table 2.5: $Bi4f_{7/2}$ binding energies for Bi(0) and Bi_2O_3.[177,180]

Species	$Bi4f_{7/2}$ (eV)	$Bi4f_{5/2}$-$Bi4f_{7/2}$ (eV)
Bi(0)	156.9	5.3
Bi_2O_3	159.3	3.3

2.4.4 O1s

The O1s spectrum is often used to determine the oxygen species and consists for a singular oxygen species of 1 main signal with a Pseudo-Voigt shape. Metal oxides can be easily distinguished in O1s spectra as they mostly exhibit O1s binding energies in the range of 529.0 — 530.2 eV.[166,171] Metal hydroxides can be found in the range of 531 — 532 eV.[177,180] However, to determine the metal hydroxide content the sample should not have been exposed to air as the range of 531 — 533 eV is also typical for alcohol and carbonyl groups.[181,182] Water can also easily be distinguished, because it gives rise to a broad signal in the range of 533 — 534 eV.[177,183,184]

2.4.5 Conclusion

In this Chapter an overview was made of the most important fundamental principles and recently published insights regarding semiconductors, solid state and semiconductor-liquid interfaces, photo(electro)chemical water splitting, $BiVO_4$, $CuFeO_2$ and photoelectron spectroscopy. These fundamentals and insights are essential to understand and appreciate the results that will be displayed in the following Chapters of this work, concerning the interface studies with $BiVO_4$ and $CuFeO_2$ substrates, the creation of particulate $BiVO_4$ and $CuFeO_2$ heterostructures, and the assessment of the photochemical water splitting performance of the heterostructured powders. In the next Chapter, the experimental methods, techniques and procedures will be detailed which were used to prepare and analyse the $BiVO_4$ and $CuFeO_2$ based materials and interfaces.

References

(1) Ibach, H.; Lüth, H., *Solid-State Physics*; Springer Berlin Heidelberg: Berlin, Heidelberg, 2009, p 515.

(2) Sze, S. M.; Ng, K. K., *Physics of semiconductor devices*; Wiley-Interscience: 2007, p 815.

(3) Grove, A. S., *Physics and technology of semiconductor devices*; Wiley: 1967, p 366.

(4) Klein, A., *Semiconductor Interfaces. Lecture notes.* Technische Universität Darmstadt: 2008.

(5) Schneider, J.; Bahnemann, D.; Ye, J.; Li Puma, G.; Dionysiou, D. D., *Photocatalysis: Fundamentals and Perspectives*; Energy and Environment Series; Royal Society of Chemistry: Cambridge, 2016, p 436.

(6) Van de. Krol, R.; Grätzel, M., *Photoelectrochemical hydrogen production*; Springer: 2012, p 321.

(7) Hüfner, S., *Photoelectron Spectroscopy : Principles and Applications*, 3rd ed.; Springer Berlin Heidelberg: 2003, p 662.

(8) Grundmann, M., *The physics of semiconductors : an introduction including devices and nanophysics*; Springer: 2006, p 689.

(9) Singleton, J., *Band theory and electronic properties of solids*; Oxford University Press: 2001, p 222.

(10) Braslavsky, S. E. Glossary of terms used in photochemistry, 3rd edition (IUPAC Recommendations 2006). *Pure Appl. Chem.* **2007**, *79*, 293–465.

(11) Hall, R. N. Electron-Hole Recombination in Germanium. *Phys. Rev.* **1952**, *87*, 387–387.

(12) Shockley, W.; Read, W. T. Statistics of the Recombinations of Holes and Electrons. *Phys. Rev.* **1952**, *87*, 835–842.

(13) Li, L.; Salvador, P. A.; Rohrer, G. S. Photocatalysts with internal electric fields. *Nanoscale* **2014**, *6*, 24–42.

(14) Zhou, Y.; Chen, G.; Yu, Y.; Feng, Y.; Zheng, Y.; He, F.; Han, Z. An efficient method to enhance the stability of sulphide semiconductor photocatalysts: a case study of N-doped ZnS. *Phys. Chem. Chem. Phys.* **2015**, *17*, 1870–1876.

(15) Fujii, K.; Karasawa, T.; Ohkawa, K. Hydrogen Gas Generation by Splitting Aqueous Water Using n-Type GaN Photoelectrode with Anodic Oxidation. *Jpn. J. Appl. Phys.* **2005**, *44*, L543–L545.

(16) Kenney, M. J.; Gong, M.; Li, Y.; Wu, J. Z.; Feng, J.; Lanza, M.; Dai, H. High-performance silicon photoanodes passivated with ultrathin nickel films for water oxidation. *Science* **2013**, *342*, 836–40.

(17) Wu, H.; Emadi, A.; de Graaf, G.; Leijtens, J.; Wolffenbuttel, R. Design and Fabrication of an Albedo Insensitive Analog Sun Sensor. *Procedia Eng.* **2011**, *25*, 527–530.

(18) Maeda, K. Z-scheme water splitting using two different semiconductor photocatalysts. *ACS Catal.* **2013**, *3*, 1486–1503.

(19) Pinaud, B. A.; Benck, J. D.; Seitz, L. C.; Forman, A. J.; Chen, Z.; Deutsch, T. G.; James, B. D.; Baum, K. N.; Baum, G. N.; Ardo, S.; Wang, H.; Miller, E.; Jaramillo, T. F. Technical and economic feasibility of centralized facilities for solar hydrogen production via photocatalysis and photoelectrochemistry. *Energy Environ. Sci.* **2013**, *6*, 1983–2002.

(20) Young, J. L.; Steiner, M. A.; Döscher, H.; France, R. M.; Turner, J. A.; Deutsch, T. G. Direct solar-to-hydrogen conversion via inverted metamorphic multi-junction semiconductor architectures. *Nat. Energy* **2017**, *2*, 17028.

(21) Fountaine, K. T.; Lewerenz, H. J.; Atwater, H. A. Efficiency limits for photoelectrochemical water-splitting. *Nat. Commun.* **2016**, *7*, 13706.

(22) Sivula, K.; Van De Krol, R. Semiconducting materials for photoelectrochemical energy conversion. *Nat. Rev. Mater.* **2016**, *1*, 15010.

(23) Guo, L.-J.; Luo, J.-W.; He, T.; Wei, S.-H.; Li, S.-S. Photocorrosion-Limited Maximum Efficiency of Solar Photoelectrochemical Water Splitting. *Phys. Rev. Appl.* **2018**, *10*, 064059.

(24) Takata, T.; Pan, C.; Domen, K. Recent progress in oxynitride photocatalysts for visible-light-driven water splitting. *Sci. Technol. Adv. Mater.* **2015**, *16*, 033506.

(25) Tokunaga, S.; Kato, H.; Kudo, A. Selective preparation of monoclinic and tetragonal $BiVO_4$ with scheelite structure and their photocatalytic properties. *Chem. Mater.* **2001**, *13*, 4624–4628.

(26) Abdi, F. F.; Han, L.; Smets, A. H. M.; Zeman, M.; Dam, B.; van de Krol, R. Efficient solar water splitting by enhanced charge separation in a bismuth vanadate-silicon tandem photoelectrode. *Nat. Commun.* **2013**, *4*, 17594–17598.

(27) Pihosh, Y.; Turkevych, I.; Mawatari, K.; Uemura, J.; Kazoe, Y.; Kosar, S.; Makita, K.; Sugaya, T.; Matsui, T.; Fujita, D.; Tosa, M.; Kondo, M.; Kitamori, T. Photocatalytic generation of hydrogen by core-shell $WO_3/BiVO_4$ nanorods with ultimate water splitting efficiency. *Sci. Rep.* **2015**, *5*, 11141.

(28) Jin, Y.; Chumanov, G. Solution synthesis of pure 2H $CuFeO_2$ at low temperatures. *RSC Adv.* **2016**, *6*, 26392–26397.

(29) Qureshi, M.; Takanabe, K. Insights on Measuring and Reporting Heterogeneous Photocatalysis: Efficiency Definitions and Setup Examples. *Chem. Mater.* **2017**, *29*, 158–167.

(30) Jacobsson, T. J. Photoelectrochemical water splitting: an idea heading towards obsolescence? *Energy Environ. Sci.* **2018**, *11*, 1977–1979.

(31) Sasaki, Y.; Iwase, A.; Kato, H.; Kudo, A. The effect of co-catalyst for Z-scheme photocatalysis systems with an Fe^{3+}/Fe^{2+} electron mediator on overall water splitting under visible light irradiation. *J. Catal.* **2008**, *259*, 133–137.

(32) Maeda, K.; Higashi, M.; Lu, D.; Abe, R.; Domen, K. Efficient Nonsacrificial Water Splitting through Two-Step Photoexcitation by Visible Light using a Modified Oxynitride as a Hydrogen Evolution Photocatalyst. *J. Am. Chem. Soc.* **2010**, *132*, 5858–5868.

(33) Abe, R.; Shinmei, K.; Hara, K.; Ohtani, B. Robust dye-sensitized overall water splitting system with two-step photoexcitation of coumarin dyes and metal oxide semiconductors. *Chem. Commun.* **2009**, *0*, 3577.

(34) Iwase, A.; Ng, Y. H.; Ishiguro, Y.; Kudo, A.; Amal, R. Reduced Graphene Oxide as a Solid-State Electron Mediator in Z-Scheme Photocatalytic Water Splitting under Visible Light. *J. Am. Chem. Soc.* **2011**, *133*, 11054–11057.

(35) Tada, H.; Mitsui, T.; Kiyonaga, T.; Akita, T.; Tanaka, K. All-solid-state Z-scheme in CdS–Au–TiO_2 three-component nanojunction system. *Nat. Mater.* **2006**, *5*, 782–786.

(36) Wang, Q.; Hisatomi, T.; Jia, Q.; Tokudome, H.; Zhong, M.; Wang, C.; Pan, Z.; Takata, T.; Nakabayashi, M.; Shibata, N.; Li, Y.; Sharp, I. D.; Kudo, A.; Yamada, T.; Domen, K. Scalable water splitting on particulate photocatalyst sheets with a solar-to-hydrogen energy conversion efficiency exceeding 1%. *Nat. Mater.* **2016**, *15*, 611–615.

(37) Wang, Q.; Hisatomi, T.; Suzuki, Y.; Pan, Z.; Seo, J.; Katayama, M.; Minegishi, T.; Nishiyama, H.; Takata, T.; Seki, K.; Kudo, A.; Yamada, T.; Domen, K. Particulate photocatalyst sheets based on carbon conductor layer for efficient Z-scheme pure-water splitting at ambient pressure. *J. Am. Chem. Soc.* **2017**, *139*, 1675–1683.

(38) Goto, Y.; Hisatomi, T.; Wang, Q.; Higashi, T.; Ishikiriyama, K.; Maeda, T.; Sakata, Y.; Okunaka, S.; Tokudome, H.; Katayama, M.; Akiyama, S.; Nishiyama, H.; Inoue, Y.; Takewaki, T.; Setoyama, T.; Minegishi, T.; Takata, T.; Yamada, T.; Domen, K. A Particulate Photocatalyst Water-Splitting Panel for Large-Scale Solar Hydrogen Generation. *Joule* **2018**, *2*, 509–520.

(39) Liu, J.; Zhang, Y.; Lu, L.; Wu, G.; Chen, W. Self-regenerated solar-driven photocatalytic water-splitting by urea derived graphitic carbon nitride with platinum nanoparticles. *Chem. Commun.* **2012**, *48*, 8826.

(40) Yoshida, H.; Hirao, K.; Nishimoto, J.-i.; Shimura, K.; Kato, S.; Itoh, H.; Hattori, T. Hydrogen Production from Methane and Water on Platinum Loaded Titanium Oxide Photocatalysts. *J. Phys. Chem. C* **2008**, *112*, 5542–5551.

(41) Mönch, W. Metal-semiconductor contacts: electronic properties. *Surf. Sci.* **1994**, *299-300*, 928–944.

(42) Mönch, W. Role of virtual gap states and defects in metal-semiconductor contacts. *Phys. Rev. Lett.* **1987**, *58*, 1260–1263.

(43) Garrett, C. G. B.; Brattain, W. H. Physical Theory of Semiconductor Surfaces. *Phys. Rev.* **1955**, *99*, 376–387.

(44) Pashley, M. D.; Haberern, K. W.; Feenstra, R. M.; Kirchner, P. D. Different Fermi-level pinning behavior on n- and p-type GaAs(001). *Phys. Rev. B* **1993**, *48*, 4612–4615.

(45) Mead, C. A.; Spitzer, W. G. Fermi Level Position at Metal-Semiconductor Interfaces. *Phys. Rev.* **1964**, *134*, A713–A716.

(46) Mönch, W. Chemical trends of barrier heights in metal-semiconductor contacts: on the theory of the slope parameter. *Appl. Surf. Sci.* **1996**, *92*, 367–371.

(47) Selinsky, R. S.; Ding, Q.; Faber, M. S.; Wright, J. C.; Jin, S. Quantum dot nanoscale heterostructures for solar energy conversion. *Chem. Soc. Rev.* **2013**, *42*, 2963–2985.

(48) Waldrop, J. R.; Kraut, E. A.; Kowalczyk, S. P.; Grant, R. W. Valence-band discontinuities for abrupt (110), (100), and (111) oriented Ge-GaAs heterojunctions. *Surf. Sci.* **1983**, *132*, 513–518.

(49) Morasch, J.; Li, S.; Brötz, J.; Jaegermann, W.; Klein, A. Reactively magnetron sputtered Bi_2O_3 thin films: Analysis of structure, optoelectronic, interface, and photovoltaic properties. *Phys. Status Solidi Appl. Mater. Sci.* **2014**, *211*, 93–100.

(50) Uddin, M. T.; Nicolas, Y.; Olivier, C.; Servant, L.; Toupance, T.; Li, S.; Klein, A.; Jaegermann, W. Improved photocatalytic activity in RuO_2-ZnO nanoparticulate heterostructures due to inhomogeneous space charge effects. *Phys. Chem. Chem. Phys.* **2015**, *17*, 5090–5102.

(51) Li, S.; Wachau, A.; Schafranek, R.; Klein, A.; Zheng, Y.; Jakoby, R. Energy level alignment and electrical properties of (Ba,Sr)TiO_3/Al_2O_3 interfaces for tunable capacitors. *J. Appl. Phys.* **2010**, *108*, 014113.

(52) Klein, A. Energy band alignment in chalcogenide thin film solar cells from photoelectron spectroscopy. *J. Phys. Condens. Matter* **2015**, *27*, 134201.

(53) Türck, J.; Siol, S.; Mayer, T.; Klein, A.; Jaegermann, W. Cu_2S as ohmic back contact for CdTe solar cells. *Thin Solid Films* **2015**, *582*, 336–339.

(54) Adler, T.; Botros, M.; Witte, W.; Hariskos, D.; Menner, R.; Powalla, M.; Klein, A. Valence band offsets at Cu(In,Ga)Se_2/Zn(O,S) interfaces. *Phys. status solidi* **2014**, *211*, 1972–1980.

(55) Li, S. et al. Intrinsic energy band alignment of functional oxides. *Phys. Status Solidi - Rapid Res. Lett.* **2014**, *8*, 571–576.

(56) Hermans, Y.; Klein, A.; Ellmer, K.; van de Krol, R.; Toupance, T.; Jaegermann, W. Energy-Band Alignment of $BiVO_4$ from Photoelectron Spectroscopy of Solid-State Interfaces. *J. Phys. Chem. C* **2018**, *122*, 20861–20870.

(57) Xu, Y.; Schoonen, M. A. A. The Absolute Energy Positions of Conduction and Valence Bands of Selected Semiconducting Minerals. *Am. Mineral.* **2000**, *85*, 543–556.

(58) Helmholtz, H. Ueber einige Gesetze der Vertheilung elektrischer Ströme in körperlichen Leitern mit Anwendung auf die thierisch-elektrischen Versuche. *Ann. der Phys. und Chemie* **1853**, *165*, 211–233.

(59) Nozik, A. J. Photoelectrochemistry: Applications to Solar Energy Conversion. *Annu. Rev. Phys. Chem.* **1978**, *29*, 189–222.

(60) Morrison, S. R., *The Chemical Physics of Surfaces*; Springer US: 1977, p 418.

(61) Butler, M. A. Prediction of Flatband Potentials at Semiconductor-Electrolyte Interfaces from Atomic Electronegativities. *J. Electrochem. Soc.* **1978**, *125*, 228.

(62) Gelderman, K.; Lee, L.; Donne, S. W. Flat-Band Potential of a Semiconductor: Using the Mott–Schottky Equation. *J. Chem. Educ.* **2007**, *84*, 685.

(63) Aricò, A.; Antonucci, V.; Antonucci, P.; Cocke, D.; Russo, U.; Giordano, N. Photoeffects at the polycrystalline pyrrhotite-electrolyte interface. *Sol. Energy Mater.* **1990**, *20*, 323–340.

(64) Kennedy, J. H.; Frese, K. W. Flatband Potentials and Donor Densities of Polycrystalline α-Fe_2O_3 Determined from Mott-Schottky Plots. *J. Electrochem. Soc.* **1978**, *125*, 723.

(65) El Halouani, F.; Deschanvres, A. Interfaces semi-conducteur-electrolyte: Correlations entre le potentiel de bande plate et les echelles d'electronegativite. *Mater. Res. Bull.* **1982**, *17*, 1045–1052.

(66) Koffyberg, F. P.; Benko, F. A. A photoelectrochemical determination of the position of the conduction and valence band edges of p-type CuO. *J. Appl. Phys.* **1982**, *53*, 1173–1177.

(67) Zhao, J.; Wang, X.; Xu, Z.; Loo, J. S. C. Hybrid catalysts for photoelectrochemical reduction of carbon dioxide: a prospective review on semiconductor/metal complex co-catalyst systems. *J. Mater. Chem. A* **2014**, *2*, 15228.

(68) Kudo, A.; Miseki, Y. Heterogeneous photocatalyst materials for water splitting. *Chem. Soc. Rev.* **2009**, *38*, 253–278.

(69) Serpone, N.; Pelizzetti, E., *Photocatalysis : fundamentals and applications*; Wiley: New York, 1989, p 650.

(70) Cardon, F.; Gomes, W. P. On the determination of the flat-band potential of a semiconductor in contact with a metal or an electrolyte from the Mott-Schottky plot. *J. Phys. D. Appl. Phys.* **1978**, *11*, L63–L67.

(71) Matsumoto, Y.; Yoshikawa, T.; Sato, E. Dependence of the Band Bending of the Oxide Semiconductors on pH. *J. Electrochem. Soc.* **1989**, *136*, 1389.

(72) Dudarev, S. L.; Botton, G. A.; Savrasov, S. Y.; Humphreys, C. J.; Sutton, A. P. Electron-energy-loss spectra and the structural stability of nickel oxide: An LSDA+U study. *Phys. Rev. B* **1998**, *57*, 1505–1509.

(73) Liechtenstein, A. I.; Anisimov, V. I.; Zaanen, J. Density-functional theory and strong interactions: Orbital ordering in Mott-Hubbard insulators. *Phys. Rev. B* **1995**, *52*, R5467–R5470.

(74) Seh, Z. W.; Kibsgaard, J.; Dickens, C. F.; Chorkendorff, I.; Nørskov, J. K.; Jaramillo, T. F. Combining theory and experiment in electrocatalysis: Insights into materials design. *Science (80-.).* **2017**, *355*, eaad4998.

(75) Man, I. C.; Su, H. Y.; Calle-Vallejo, F.; Hansen, H. A.; Martínez, J. I.; Inoglu, N. G.; Kitchin, J.; Jaramillo, T. F.; Nørskov, J. K.; Rossmeisl, J. Universality in Oxygen Evolution Electrocatalysis on Oxide Surfaces. *ChemCatChem* **2011**, *3*, 1159–1165.

(76) Jiao, Y.; Zheng, Y.; Jaroniec, M.; Qiao, S. Z. Design of electrocatalysts for oxygen- and hydrogen-involving energy conversion reactions. *Chem. Soc. Rev.* **2015**, *44*, 2060–2086.

(77) Benck, J. D.; Hellstern, T. R.; Kibsgaard, J.; Chakthranont, P.; Jaramillo, T. F. Catalyzing the Hydrogen Evolution Reaction (HER) with Molybdenum Sulfide Nanomaterials. *ACS Catal.* **2014**, *4*, 3957–3971.

(78) Norskov, J. K.; Bligaard, T.; Logadottir, A.; Kitchin, J. R.; Chen, J. G.; Pandelov, S.; Stimming, U. Trends in the Exchange Current for Hydrogen Evolution. *J. Electrochem. Soc.* **2005**, *152*, J23.

(79) Parsons, R. The rate of electrolytic hydrogen evolution and the heat of adsorption of hydrogen. *Trans. Faraday Soc.* **1958**, *54*, 1053.

(80) Greeley, J.; Mavrikakis, M. Alloy catalysts designed from first principles. *Nat. Mater.* **2004**, *3*, 810–815.

(81) Greeley, J.; Jaramillo, T. F.; Bonde, J.; Chorkendorff, I.; Nørskov, J. K. Computational high-throughput screening of electrocatalytic materials for hydrogen evolution. *Nat. Mater.* **2006**, *5*, 909–913.

(82) Skúlason, E.; Tripkovic, V.; Björketun, M. E.; Gudmundsdóttir, S.; Karlberg, G.; Rossmeisl, J.; Bligaard, T.; Jónsson, H.; Nørskov, J. K. Modeling the Electrochemical Hydrogen Oxidation and Evolution Reactions on the Basis of Density Functional Theory Calculations. *J. Phys. Chem. C* **2010**, *114*, 18182–18197.

(83) Huang, Y.; Nielsen, R. J.; Goddard, W. A.; Soriaga, M. P. The Reaction Mechanism with Free Energy Barriers for Electrochemical Dihydrogen Evolution on MoS_2. *J. Am. Chem. Soc.* **2015**, *137*, 6692–6698.

(84) Chan, K.; Nørskov, J. K. Potential Dependence of Electrochemical Barriers from ab Initio Calculations. *J. Phys. Chem. Lett.* **2016**, *7*, 1686–1690.

(85) Chan, K.; Nørskov, J. K. Electrochemical Barriers Made Simple. *J. Phys. Chem. Lett.* **2015**, *6*, 2663–2668.

(86) Fang, Y.-H.; Liu, Z.-P. Surface Phase Diagram and Oxygen Coupling Kinetics on Flat and Stepped Pt Surfaces under Electrochemical Potentials. *J. Phys. Chem. C* **2009**, *113*, 9765–9772.

(87) Jaramillo, T. F.; Jørgensen, K. P.; Bonde, J.; Nielsen, J. H.; Horch, S.; Chorkendorff, I. Identification of active edge sites for electrochemical H_2 evolution from MoS_2 nanocatalysts. *Science (80-.).* **2007**, *317*, 100–2.

(88) Shen, X.; Small, Y. A.; Wang, J.; Allen, P. B.; Fernandez-Serra, M. V.; Hybertsen, M. S.; Muckerman, J. T. Photocatalytic Water Oxidation at the GaN $(10\bar{1}0)$—Water Interface. *J. Phys. Chem. C* **2010**, *114*, 13695–13704.

(89) Akimov, A. V.; Muckerman, J. T.; Prezhdo, O. V. Nonadiabatic Dynamics of Positive Charge during Photocatalytic Water Splitting on GaN$(10\bar{1}0)$ Surface: Charge Localization Governs Splitting Efficiency. *J. Am. Chem. Soc.* **2013**, *135*, 8682–8691.

(90) Rossmeisl, J.; Qu, Z.-W.; Zhu, H.; Kroes, G.-J.; Nørskov, J. Electrolysis of water on oxide surfaces. *J. Electroanal. Chem.* **2007**, *607*, 83–89.

(91) Norskov, J. K.; Rossmeisl, J.; Logadottir, A.; Lindqvist, L.; Kitchin, J. R.; Bligaard, T.; Jónsson, H. Origin of the Overpotential for Oxygen Reduction at a Fuel-Cell Cathode. *J. Phys. Chem. B* **2004**, *108*, 17886–17892.

(92) Siahrostami, S.; Verdaguer-Casadevall, A.; Karamad, M.; Deiana, D.; Malacrida, P.; Wickman, B.; Escudero-Escribano, M.; Paoli, E. A.; Frydendal, R.; Hansen, T. W.; Chorkendorff, I.; Stephens, I. E. L.; Rossmeisl, J. Enabling direct H_2O_2 production through rational electrocatalyst design. *Nat. Mater.* **2013**, *12*, 1137–1143.

(93) Rossmeisl, J.; Logadottir, A.; Nørskov, J. Electrolysis of water on (oxidized) metal surfaces. *Chem. Phys.* **2005**, *319*, 178–184.

(94) McCrory, C. C. L.; Jung, S.; Ferrer, I. M.; Chatman, S. M.; Peters, J. C.; Jaramillo, T. F. Benchmarking Hydrogen Evolving Reaction and Oxygen Evolving Reaction Electrocatalysts for Solar Water Splitting Devices. *J. Am. Chem. Soc.* **2015**, *137*, 4347–4357.

(95) Jang, Y. J.; Park, Y. B.; Kim, H. E.; Choi, Y. H.; Choi, S. H.; Lee, J. S. Oxygen-Intercalated $CuFeO_2$ Photocathode Fabricated by Hybrid Microwave Annealing for Efficient Solar Hydrogen Production. *Chem. Mater.* **2016**, *28*, 6054–6061.

(96) Lv, X.; Xiao, X.; Cao, M.; Bu, Y.; Wang, C.; Wang, M.; Shen, Y. Efficient carbon dots/NiFe-layered double hydroxide/$BiVO_4$ photoanodes for photoelectrochemical water splitting. *Appl. Surf. Sci.* **2018**, *439*, 1065–1071.

(97) Palaniselvam, T.; Shi, L.; Mettela, G.; Anjum, D. H.; Li, R.; Katuri, K. P.; Saikaly, P. E.; Wang, P. Vastly Enhanced $BiVO_4$ Photocatalytic OER Performance by $NiCoO_2$ as Cocatalyst. *Adv. Mater. Interfaces* **2017**, *4*, 1700540.

(98) Aroutiounian, V.; Arakelyan, V.; Shahnazaryan, G. Metal oxide photoelectrodes for hydrogen generation using solar radiation-driven water splitting. *Sol. Energy* **2005**, *78*, 581–592.

(99) Iwashina, K.; Iwase, A.; Ng, Y. H.; Amal, R.; Kudo, A. Z-Schematic Water Splitting into H_2 and O_2 Using Metal Sulfide as a Hydrogen-Evolving Photocatalyst and Reduced Graphene Oxide as a Solid-State Electron Mediator. *J. Am. Chem. Soc.* **2015**, *137*, 604–607.

(100) Abe, R.; Higashi, M.; Domen, K. Facile Fabrication of an Efficient Oxynitride TaON Photoanode for Overall Water Splitting into H_2 and O_2 under Visible Light Irradiation. *J. Am. Chem. Soc.* **2010**, *132*, 11828–11829.

(101) Wu, Y.; Lazic, P.; Hautier, G.; Persson, K.; Ceder, G. First principles high throughput screening of oxynitrides for water-splitting photocatalysts. *Energy Environ. Sci.* **2013**, *6*, 157–168.

(102) Khaselev, O.; Turner, J. A. A Monolithic Photovoltaic-Photoelectrochemical Device for Hydrogen Production via Water Splitting. *Science* **1998**, *280*, 425–427.

(103) Jang, J.-W.; Du, C.; Ye, Y.; Lin, Y.; Yao, X.; Thorne, J.; Liu, E.; McMahon, G.; Zhu, J.; Javey, A.; Guo, J.; Wang, D. Enabling unassisted solar water splitting by iron oxide and silicon. *Nat. Commun.* **2015**, *6*, 7447.

(104) Reece, S. Y.; Hamel, J. A.; Sung, K.; Jarvi, T. D.; Esswein, A. J.; Pijpers, J. J. H.; Nocera, D. G. Wireless solar water splitting using silicon-based semiconductors and earth-abundant catalysts. *Science (80-.).* **2011**, *334*, 645–8.

(105) Li, Y.; Li, Y.-L.; Sa, B.; Ahuja, R. Review of two-dimensional materials for photocatalytic water splitting from a theoretical perspective. *Catal. Sci. Technol.* **2017**, *7*, 545–559.

(106) Su, T.; Shao, Q.; Qin, Z.; Guo, Z.; Wu, Z. Role of Interfaces in Two-Dimensional Photocatalyst for Water Splitting. *ACS Catal.* **2018**, *8*, 2253–2276.

(107) Ismail, A. A.; Bahnemann, D. W. Photochemical splitting of water for hydrogen production by photocatalysis: A review. *Sol. Energy Mater. Sol. Cells* **2014**, *128*, 85–101.

(108) Jiang, C.; Moniz, S. J. A.; Wang, A.; Zhang, T.; Tang, J. Photoelectrochemical devices for solar water splitting – materials and challenges. *Chem. Soc. Rev.* **2017**, *46*, 4645–4660.

(109) Qu, Y.; Duan, X. Progress, challenge and perspective of heterogeneous photocatalysts. *Chem. Soc. Rev.* **2013**, *42*, 2568–2580.

(110) Osterloh, F. E. Inorganic nanostructures for photoelectrochemical and photocatalytic water splitting. *Chem. Soc. Rev.* **2013**, *42*, 2294–2320.

(111) Longo, G.; Fresno, F.; Gross, S.; Štangar, U. L. Synthesis of $BiVO_4/TiO_2$ composites and evaluation of their photocatalytic activity under indoor illumination. *Environ. Sci. Pollut. Res.* **2014**, *21*, 11189–11197.

(112) Frost, R. L.; Henry, D. A.; Weier, M. L.; Martens, W. Raman spectroscopy of three polymorphs of $BiVO_4$: Clinobisvanite, dreyerite and pucherite, with comparisons to $(VO_4)^3$-bearing minerals: namibite, pottsite and schumacherite. *J. Raman Spectrosc.* **2006**, *37*, 722–732.

(113) Zhao, Z.; Li, Z.; Zou, Z. Electronic structure and optical properties of monoclinic clinobisvanite $BiVO_4$. *Phys. Chem. Chem. Phys.* **2011**, *13*, 4746.

(114) Cooper, J. K.; Gul, S.; Toma, F. M.; Chen, L.; Glans, P. A.; Guo, J.; Ager, J. W.; Yano, J.; Sharp, I. D. Electronic structure of monoclinic $BiVO_4$. *Chem. Mater.* **2014**, *26*, 5365–5373.

(115) Jiang, H.; Nagai, M.; Kobayashi, K. Enhanced photocatalytic activity for degradation of methylene blue over $V_2O_5/BiVO_4$ composite. *J. Alloys Compd.* **2009**, *479*, 821–827.

(116) Li, H.; Liu, G.; Duan, X. Monoclinic $BiVO_4$ with regular morphologies: Hydrothermal synthesis, characterization and photocatalytic properties. *Mater. Chem. Phys.* **2009**, *115*, 9–13.

(117) Hong, S. J.; Lee, S.; Jang, J. S.; Lee, J. S. Heterojunction $BiVO_4/WO_3$ electrodes for enhanced photoactivity of water oxidation. *Energy Environ. Sci.* **2011**, *4*, 1781.

(118) Luo, W.; Yang, Z.; Li, Z.; Zhang, J.; Liu, J.; Zhao, Z.; Wang, Z.; Yan, S.; Yu, T.; Zou, Z. Solar hydrogen generation from seawater with a modified $BiVO_4$ photoanode. *Energy Environ. Sci.* **2011**, *4*, 4046.

(119) Rettie, A. J.; Lee, H. C.; Marshall, L. G.; Lin, J. F.; Capan, C.; Lindemuth, J.; McCloy, J. S.; Zhou, J.; Bard, A. J.; Mullins, C. B. Combined charge carrier transport and photoelectrochemical characterization of $BiVO_4$ single crystals: Intrinsic behavior of a complex metal oxide. *J. Am. Chem. Soc.* **2013**, *135*, 11389–11396.

(120) Pilli, S. K.; Furtak, T. E.; Brown, L. D.; Deutsch, T. G.; Turner, J. A.; Herring, A. M. Cobalt-phosphate (Co-Pi) catalyst modified Mo-doped $BiVO_4$ photoelectrodes for solar water oxidation. *Energy Environ. Sci.* **2011**, *4*, 5028.

(121) Jovic, V.; Laverock, J.; Rettie, A. J. E.; Zhou, J.-S.; Mullins, C. B.; Singh, V. R.; Lamoureux, B.; Wilson, D.; Su, T.-Y.; Jovic, B.; Bluhm, H.; Söhnel, T.; Smith, K. E. Soft X-ray spectroscopic studies of the electronic structure of M:$BiVO_4$ (M = Mo, W) single crystals. *J. Mater. Chem. A* **2015**, *3*, 23743–23753.

(122) Abdi, F. F.; Savenije, T. J.; May, M. M.; Dam, B.; van de Krol, R. The Origin of Slow Carrier Transport in $BiVO_4$ Thin Film Photoanodes: A Time-Resolved Microwave Conductivity Study. *J. Phys. Chem. Lett.* **2013**, *4*, 2752–2757.

(123) Rettie, A. J. E.; Chemelewski, W. D.; Emin, D.; Mullins, C. B. Unravelling Small-Polaron Transport in Metal Oxide Photoelectrodes. *J. Phys. Chem. Lett.* **2016**, *7*, 471–479.

(124) Kweon, K. E.; Hwang, G. S.; Kim, J.; Kim, S.; Kim, S. Electron small polarons and their transport in bismuth vanadate: A first principles study. *Phys. Chem. Chem. Phys.* **2015**, *17*, 256–260.

(125) Liu, T.; Zhou, X.; Dupuis, M.; Li, C. The nature of photogenerated charge separation among different crystal facets of $BiVO_4$ studied by density functional theory. *Phys. Chem. Chem. Phys.* **2015**, *17*, 23503–23510.

(126) Wiktor, J.; Ambrosio, F.; Pasquarello, A. Role of Polarons in Water Splitting: The Case of $BiVO_4$. *ACS Energy Lett.* **2018**, *3*, 1693–1697.

(127) Kweon, K. E.; Hwang, G. S. Structural phase-dependent hole localization and transport in bismuth vanadate. *Phys. Rev. B* **2013**, *87*, 205202.

(128) Cooper, J. K.; Gul, S.; Toma, F. M.; Chen, L.; Liu, Y.-S.; Guo, J.; Ager, J. W.; Yano, J.; Sharp, I. D. Indirect Bandgap and Optical Properties of Monoclinic Bismuth Vanadate. *J. Phys. Chem. C* **2015**, *119*, 2969–2974.

(129) Su, J.; Guo, L.; Bao, N.; Grimes, C. A. Nanostructured WO_3/$BiVO_4$ heterojunction films for efficient photoelectrochemical water splitting. *Nano Lett.* **2011**, *11*, 1928–1933.

(130) Merupo, V.; Velumani, S.; Oza, G.; Makowska-Janusik, M.; Kassiba, A. Structural, electronic and optical features of molybdenum-doped bismuth vanadium oxide. *Mater. Sci. Semicond. Process.* **2015**, *31*, 618–623.

(131) Qiu, Y.; Liu, W.; Chen, W.; Zhou, G.; Hsu, P. C.; Zhang, R.; Liang, Z.; Fan, S.; Zhang, Y.; Cui, Y. Efficient solar-driven water splitting by nanocone $BiVO_4$-perovskite tandem cells. *Sci. Adv.* **2016**, *2*, e1501764.

(132) Kim, T. W.; Choi, K.-S. Nanoporous $BiVO_4$ Photoanodes with Dual-Layer Oxygen Evolution Catalysts for Solar Water Splitting. *Science (80-.).* **2014**, *343*, 990–994.

(133) Higashi, T.; Kaneko, H.; Minegishi, T.; Kobayashi, H.; Zhong, M.; Kuang, Y.; Hisatomi, T.; Katayama, M.; Takata, T.; Nishiyama, H.; Yamada, T.; Domen, K. Overall water splitting by photoelectrochemical cells consisting of $(ZnSe)_{0.85}(CuIn_{0.7}Ga_{0.3}Se_2)_{0.15}$ photocathodes and $BiVO_4$ photoanodes. *Chem. Commun.* **2017**, *53*, 11674–11677.

(134) Kato, H.; Hori, M.; Konta, R.; Shimodaira, Y.; Kudo, A. Construction of Z-scheme Type Heterogeneous Photocatalysis Systems for Water Splitting into H_2 and O_2 under Visible Light Irradiation. *Chem. Lett.* **2004**, *33*, 1348–1349.

(135) Wu, X.; Zhao, J.; Wang, L.; Han, M.; Zhang, M.; Wang, H.; Huang, H.; Liu, Y.; Kang, Z. Carbon dots as solid-state electron mediator for $BiVO_4$/CDs/CdS Z-scheme photocatalyst working under visible light. *Appl. Catal. B Environ.* **2017**, *206*, 501–509.

(136) Zhou, F. Q.; Fan, J. C.; Xu, Q. J.; Min, Y. L. $BiVO_4$ nanowires decorated with CdS nanoparticles as Z-scheme photocatalyst with enhanced H_2 generation. *Appl. Catal. B Environ.* **2017**, *201*, 77–83.

(137) Park, H. S.; Lee, H. C.; Leonard, K. C.; Liu, G.; Bard, A. J. Unbiased Photoelectrochemical Water Splitting in Z-Scheme Device Using W/Mo-Doped $BiVO_4$ and $Zn_xCd_{1-x}Se$. *ChemPhysChem* **2013**, *14*, 2277–2287.

(138) Wang, Q.; Li, Y.; Hisatomi, T.; Nakabayashi, M.; Shibata, N.; Kubota, J.; Domen, K. Z-scheme water splitting using particulate semiconductors immobilized onto metal layers for efficient electron relay. *J. Catal.* **2015**, *328*, 308–315.

(139) Wenderich, K.; Mul, G. Methods, Mechanism, and Applications of Photodeposition in Photocatalysis: A Review. *Chem. Rev.* **2016**, *116*, 14587–14619.

(140) Mu, L.; Zhao, Y.; Li, A.; Wang, S.; Wang, Z.; Yang, J.; Wang, Y.; Liu, T.; Chen, R.; Zhu, J.; Fan, F.; Li, R.; Li, C. Enhancing charge separation on high symmetry $SrTiO_3$ exposed with anisotropic facets for photocatalytic water splitting. *Energy Environ. Sci.* **2016**, *9*, 2463–2469.

(141) Wang, H.; Qiao, L.; Xu, H.; Lin, Y.; Shen, Y.; Nan, C. Anisotropy of Photocatalytic Properties in Nanostructured Photocatalysts. *Soft Nanosci. Lett.* **2016**, *6*, 11–30.

(142) Wang, D.; Jiang, H.; Zong, X.; Xu, Q.; Ma, Y.; Li, G.; Li, C. Crystal Facet Dependence of Water Oxidation on $BiVO_4$ Sheets under Visible Light Irradiation. *Chem. - A Eur. J.* **2011**, *17*, 1275–1282.

(143) Li, R.; Zhang, F.; Wang, D.; Yang, J.; Li, M.; Zhu, J.; Zhou, X.; Han, H.; Li, C. Spatial separation of photogenerated electrons and holes among $\{010\}$ and $\{110\}$ crystal facets of $BiVO_4$. *Nat. Commun.* **2013**, *4*, 1432.

(144) Li, R.; Han, H.; Zhang, F.; Wang, D.; Li, C. Highly efficient photocatalysts constructed by rational assembly of dual-cocatalysts separately on different facets of $BiVO_4$. *Energy Environ. Sci.* **2014**, *7*, 1369–1376.

(145) Zhu, J.; Fan, F.; Chen, R.; An, H.; Feng, Z.; Li, C. Direct Imaging of Highly Anisotropic Photogenerated Charge Separations on Different Facets of a Single $BiVO_4$ Photocatalyst. *Angew. Chemie - Int. Ed.* **2015**, *54*, 9111–9114.

(146) Shannon, R. D.; Prewitt, C. T.; Rogers, D. B. Chemistry of noble metal oxides. II. Crystal structures of platinum cobalt dioxide, palladium cobalt dioxide, coppper iron dioxide, and silver iron dioxide. *Inorg. Chem.* **1971**, *10*, 719–723.

(147) Benko, F.; Koffyberg, F. Opto-electronic properties of p- and n-type delafossite, $CuFeO_2$. *J. Phys. Chem. Solids* **1987**, *48*, 431–434.

(148) Prévot, M. S.; Jeanbourquin, X. A.; Bourée, W. S.; Abdi, F.; Friedrich, D.; van de Krol, R.; Guijarro, N.; Le Formal, F.; Sivula, K. Evaluating Charge Carrier Transport and Surface States in $CuFeO_2$ Photocathodes. *Chem. Mater.* **2017**, *29*, 4952–4962.

(149) Marquardt, M. A.; Ashmore, N. A.; Cann, D. P. Crystal chemistry and electrical properties of the delafossite structure. *Thin Solid Films* **2006**, *496*, 146–156.

(150) Omeiri, S.; Bellal, B.; Bouguelia, A.; Bessekhouad, Y.; Trari, M. Electrochemical and photoelectrochemical characterization of $CuFeO_2$ single crystal. *J. Solid State Electrochem.* **2009**, *13*, 1395–1401.

(151) Gu, J.; Wuttig, A.; Krizan, J. W.; Hu, Y.; Detweiler, Z. M.; Cava, R. J.; Bocarsly, A. B. Mg-Doped $CuFeO_2$ Photocathodes for Photoelectrochemical Reduction of Carbon Dioxide. *J. Phys. Chem. C* **2013**, *117*, 12415–12422.

(152) Read, C. G.; Park, Y.; Choi, K.-S. Electrochemical Synthesis of p-Type $CuFeO_2$ Electrodes for Use in a Photoelectrochemical Cell. *J. Phys. Chem. Lett.* **2012**, *3*, 1872–1876.

(153) Tablero Crespo, C. Potentiality of $CuFeO_2$-delafossite as a solar energy converter. *Sol. Energy* **2018**, *163*, 162–166.

(154) Joshi, T.; Senty, T. R.; Trappen, R.; Zhou, J.; Chen, S.; Ferrari, P.; Borisov, P.; Song, X.; Holcomb, M. B.; Bristow, A. D.; Cabrera, A. L.; Lederman, D. Structural and magnetic properties of epitaxial delafossite $CuFeO_2$ thin films grown by pulsed laser deposition. *J. Appl. Phys.* **2015**, *117*, 013908.

(155) Pavunny, S. P.; Kumar, A.; Katiyar, R. S. Raman spectroscopy and field emission characterization of delafossite $CuFeO_2$. *J. Appl. Phys.* **2010**, *107*, 013522.

(156) Guo, S.-D. X-ray emission spectra and gaps of $CuFeO_2$ with the modified Becke–Johnson potential. *J. Magn. Magn. Mater.* **2015**, *377*, 226–228.

(157) Kumar, M.; Zhao, H.; Persson, C. Study of band-structure, optical properties and native defects in $A^IB^{III}O_2$ (A^I = Cu or Ag, B^{III} = Al, Ga or In) delafossites. *Semicond. Sci. Technol.* **2013**, *28*, 065003.

(158) Hara, M.; Kondo, T.; Komoda, M.; Ikeda, S.; Kondo, J. N.; Domen, K.; Hara, M.; Shinohara, K.; Tanaka, A. Cu_2O as a photocatalyst for overall water splitting under visible light irradiation. *Chem. Commun.* **1998**, *0*, 357–358.

(159) van de Krol, R.; Parkinson, B. A. Perspectives on the photoelectrochemical storage of solar energy. *MRS Energy Sustain.* **2017**, *4*, E13.

(160) Oh, Y.; Yang, W.; Tan, J.; Lee, H.; Park, J.; Moon, J. Photoelectrodes based on 2D opals assembled from Cu-delafossite double-shelled microspheres for an enhanced photoelectrochemical response. *Nanoscale* **2018**, *10*, 3720–3729.

(161) Prévot, M. S.; Li, Y.; Guijarro, N.; Sivula, K. Improving charge collection with delafossite photocathodes: a host–guest $CuAlO_2$/$CuFeO_2$ approach. *J. Mater. Chem. A* **2016**, *4*, 3018–3026.

(162) Prévot, M. S.; Guijarro, N.; Sivula, K. Enhancing the Performance of a Robust Sol-Gel-Processed p-Type Delafossite $CuFeO_2$ Photocathode for Solar Water Reduction. *ChemSusChem* **2015**, *8*, 1359–1367.

(163) Weidner, M. Fermi Level Determination in Tin Oxide by Photoelectron Spectroscopy: Relation to Optoelectronic Properties; Band Bending at Surfaces and Interfaces; Modulation Doping., Ph.D. Thesis, TU Darmstadt, 2016, p 427.

(164) Hüfner, S.; Schmidt, S.; Reinert, F. Photoelectron spectroscopy—An overview. *Nucl. Instruments Methods Phys. Res. Sect. A Accel. Spectrometers, Detect. Assoc. Equip.* **2005**, *547*, 8–23.

(165) Briggs, D.; Seah, M. P., *Practical surface analysis. Volume 1 – Auger and X-ray Photoelectron Spectroscopy*; Wiley: Chichester, 1990, p 674.

(166) Biesinger, M. C.; Lau, L. W.; Gerson, A. R.; Smart, R. S. Resolving surface chemical states in XPS analysis of first row transition metals, oxides and hydroxides: Sc, Ti, V, Cu and Zn. *Appl. Surf. Sci.* **2010**, *257*, 887–898.

(167) Silversmit, G.; Depla, D.; Poelman, H.; Marin, G. B.; De Gryse, R. An XPS study on the surface reduction of V_2O_5(001) induced by Ar^+ ion bombardment. *Surf. Sci.* **2006**, *600*, 3512–3517.

(168) Briggs, D.; Grant, J. T., *Surface analysis by Auger and x-ray photoelectron spectroscopy*; IM Publications: 2003, p 899.

(169) Silversmit, G.; Depla, D.; Poelman, H.; Marin, G. B.; De Gryse, R. Determination of the V2p XPS binding energies for different vanadium oxidation states (V^{5+} to V^{0+}). *J. Electron Spectros. Relat. Phenomena* **2004**, *135*, 167–175.

(170) Gupta, R. P.; Sen, S. K. Calculation of multiplet structure of core p-vacancy levels. *Phys. Rev. B* **1974**, *10*, 71–77.

(171) Biesinger, M. C.; Payne, B. P.; Grosvenor, A. P.; Lau, L. W.; Gerson, A. R.; Smart, R. S. C. Resolving surface chemical states in XPS analysis of first row transition metals, oxides and hydroxides: Cr, Mn, Fe, Co and Ni. *Appl. Surf. Sci.* **2011**, *257*, 2717–2730.

(172) Grosvenor, A. P.; Kobe, B. A.; Biesinger, M. C.; McIntyre, N. S. Investigation of multiplet splitting of Fe 2p XPS spectra and bonding in iron compounds. *Surf. Interface Anal.* **2004**, *36*, 1564–1574.

(173) Yamashita, T.; Hayes, P. Analysis of XPS spectra of Fe^{2+} and Fe^{3+} ions in oxide materials. *Appl. Surf. Sci.* **2008**, *254*, 2441–2449.

(174) Chuang, T.; Brundle, C.; Rice, D. Interpretation of the x-ray photoemission spectra of cobalt oxides and cobalt oxide surfaces. *Surf. Sci.* **1976**, *59*, 413–429.

(175) Yang, J.; Liu, H.; Martens, W. N.; Frost, R. L. Synthesis and Characterization of Cobalt Hydroxide, Cobalt Oxyhydroxide, and Cobalt Oxide Nanodiscs. *J. Phys. Chem. C* **2010**, *114*, 111–119.

(176) Biesinger, M. C.; Lau, L. W. M.; Gerson, A. R.; Smart, R. S. C. The role of the Auger parameter in XPS studies of nickel metal, halides and oxides. *Phys. Chem. Chem. Phys.* **2012**, *14*, 2434.

(177) Wagner, C.; Naumkin, A.; Kraut-Vass, A.; Allison, J.; Powell, C.; Rumble Jr, J. NIST Standard Reference Database 20, Version 3.4., 2003.

(178) Poulston, S.; Parlett, P. M.; Stone, P.; Bowker, M. Surface Oxidation and Reduction of CuO and Cu_2O Studied Using XPS and XAES. *Surf. Interface Anal.* **1996**, *24*, 811–820.

(179) Gaarenstroom, S. W.; Winograd, N. Initial and final state effects in the ESCA spectra of cadmium and silver oxides. *J. Chem. Phys.* **1977**, *67*, 3500–3506.

(180) Moulder, J. F.; Stickle, W. F.; Sobol, P. E.; Bomben, K. D., *Handbook of X-ray photoelectron spectroscopy: a reference book of standard spectra for identification and interpretation of XPS data*; Physical Electronics: Eden Prairie MN, 1992, p 261.

(181) Sotoma, S.; Akagi, K.; Hosokawa, S.; Igarashi, R.; Tochio, H.; Harada, Y.; Shirakawa, M. Comprehensive and quantitative analysis for controlling the physical/chemical states and particle properties of nanodiamonds for biological applications. *RSC Adv.* **2015**, *5*, 13818–13827.

(182) Beamson, G.; Briggs, D. High Resolution XPS of Organic Polymers: The Scienta ESCA300 Database. *J. Chem. Educ.* **1993**, *70*, A25.

(183) Weidler, N.; Paulus, S.; Schuch, J.; Klett, J.; Hoch, S.; Stenner, P.; Maljusch, A.; Brötz, J.; Wittich, C.; Kaiser, B.; Jaegermann, W. CoO_x thin film deposited by CVD as efficient water oxidation catalyst: change of oxidation state in XPS and its correlation to electrochemical activity. *Phys. Chem. Chem. Phys.* **2016**, *18*, 10708–10718.

(184) Fingerle, M.; Tengeler, S.; Calvet, W.; Mayer, T.; Jaegermann, W. Water Interaction with Sputter-Deposited Nickel Oxide on n-Si Photoanode: Cryo Photoelectron Spectroscopy on Adsorbed Water in the Frozen Electrolyte Approach. *J. Electrochem. Soc.* **2018**, *165*, H3148–H3153.

Chapter 3

Experimental Methods and Procedures

3.1 Synthesis heterostructured particulate photocatalysts

3.1.1 Chemicals used

Bismuth(III) nitrate pentahydrate (98%, Sigma-Aldrich), ammonium metavanadate (⩾99.0%, Sigma-Aldrich), nitric acid (65%, Sigma-Aldrich), ammonium hydroxide (28 — 30%, Sigma-Aldrich), sodium dodecyl sulphate (⩾ 98.5%, Sigma-Aldrich), iron(III) chloride hexahydrate (⩾ 99%, Sigma-Aldrich), copper(I) iodide (⩾ 99.5%, Sigma-Aldrich), sodium hydroxide (extra pure, Acros Organics), silver nitrate (>99.8%, Sigma-Aldrich), cobalt(III) nitrate hexahydrate (⩾ 98%, Sigma-Aldrich), chloroplatinic acid hexahydrate (⩾ 37.50% Pt basis, Sigma-Aldrich), sodium iodate (> 99%, Alfa Aesar), methanol (⩾ 99.9%, Sigma-Aldrich), rhodamine B (⩾ 95%, Sigma-Aldrich) were used as received. Pure (Type 3) and ultra pure water (Type 1) were provided by a Millipore Milli-Q Direct 8 water purification system.

3.1.2 Preparation of $BiVO_4$ microparticles

The $BiVO_4$ microparticles were synthesized according to a published procedure.[1] First, 1.25 mmol bismuth(III) nitrate pentahydrate and 1.25 mmol ammonium metavanadate were dissolved in 25 mL of a 2.0 mol/L nitric acid solution and 25 mL of a 2.0 mol/L ammonia solution, respectively. To dissolve the ammonium metavanadate, 5 minutes of sonication was occasionally necessary. To the bismuth(III) nitrate solution, 0.85 mmol sodium dodecyl sulphate was added as a templating agent. Under violent stirring (± 1000 RPM) the bismuth(III) nitrate solution was dropwise added to the ammonium metavanadate solution. After a few drops of the bismuth(III) nitrate solution the reaction mixture started to foam and a precipitate formed. After 30 min of stirring at 1000 RPM, the pH was altered from ± 0.5 to a more basic value (exact value depends on the

preferred morphology (See Section 4.2 for exact values) using a 2.0 mol/L ammonia solution. After additionally stirring for 2 h, the reaction mixture was added to a specially designed glass vessel. This glass vessel was put into a 200 mL pressure reactor and heated up to 180 °C using an electric clamp-on band heater for 24 h. Then, the heater was removed and the pressure reactor was allowed to cool down. After 1 h the reaction mixture containing a vivid yellow powder was washed three times with distilled water and three times with ethanol to remove unreacted precursor, waste products and templating agent. Finally, the $BiVO_4$ powder was dried for 8 h at 70 °C in a muffle furnace. Figure 3.1 summarizes the $BiVO_4$ synthesis.

Figure 3.1: $BiVO_4$ synthesis: left: foaming aqueous mixture of bismuth precursor, vanadium precursor and sodium dodecyl sulphate (SDS); middle: treatment in pressure reactor; right: yellow $BiVO_4$ precipitate after removal from pressure reactor.

3.1.3 Preparation of hexagonal $CuFeO_2$ nanoplatelets

The preparation of the hexagonal $CuFeO_2$ nanoplatelets was adapted from a previously published procedure.[2] In a typical synthesis, 14 mL ultra pure (18 mQ) water and a triangular stir bar were added to a 125 mL Teflon beaker. After placing a long needle in the water, nitrogen was bubbled through for at least 30 minutes while stirring at 750 RPM. 3 mmol (571 mg) copper iodide was then added at a stirring speed of 750 — 1000 RPM, which formed a grey suspension. Immediately, 3 mmol iron chloride hexahydrate (811 mg) was added, making the suspension turn brown-green. After 15 min stirring at 1000 RPM, 0.22 mol (8.8 g) NaOH was added, pellet by pellet, over a period of 5 min. The addition of NaOH went together with heat formation and made the suspension turn chocolate-brown. After 30 min of stirring at 1000 RPM the Teflon beaker was inserted in a fitting stainless steel pressure reactor (Figure 3.2) and placed in a preheated oven at 200 °C for 3.5 h. The pressure reactor was then removed from the oven and placed on the bench to cool down for 1 h. Subsequently, the black $CuFeO_2$ powder was separated from the reaction mixture and washed with distilled water by a sequence of centrifugation and redispersion that was repeated for at least 6 times until reaching neutral pH. Finally, the powder was dried at 70 °C during 8 h.

3.1.4 Photodeposition

In this work, anisotropic heterostructured photocatalysts were created through photodeposition. To prepare a certain deposit, photocatalytic particles were first added to a honeypot-shaped glass

Figure 3.2: Teflon beaker and pressure reactor used for the $CuFeO_2$ nanoplatelet synthesis.

beaker, containing an aqueous solution of a metal precursor and sometimes a hole/electron scavenger. Then, the dispersion was sonicated for 10 minutes and stirred for 1 h in the absence of light. Subsequently, a solar simulator was used as a light source to initiate the photodeposition of the metallic precursor on the photocatalytic particles. Figure 3.3 shows the photodeposition set up with and without the solar simulator running. After stirring for 1 — 5 h the solar simulator was switched off and the heterostructured powder was washed at least 5 times with distilled water through cycles of centrifugation and redispersion in water via sonication. The powder was then dried at 70 °C for 8 h. The exact experimental parameters for the photodeposition experiments on $BiVO_4$ and $CuFeO_2$ are listed in Table 4.2 in Section 4.3 and in Table 6.1 in Section 6.3, respectively.

The solar simulator used in this work was a class AAA Newport Oriel Sol3A equipped with a 450 W Xenon lamp as light source and had an output power of 100 mW/cm^2 (1 sun). The spectrum of the solar simulator is shown in Figure 3.4.

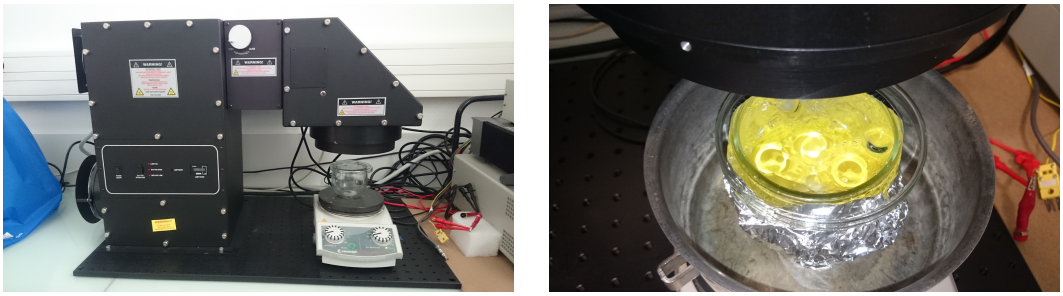

Figure 3.3: Photodeposition set up.

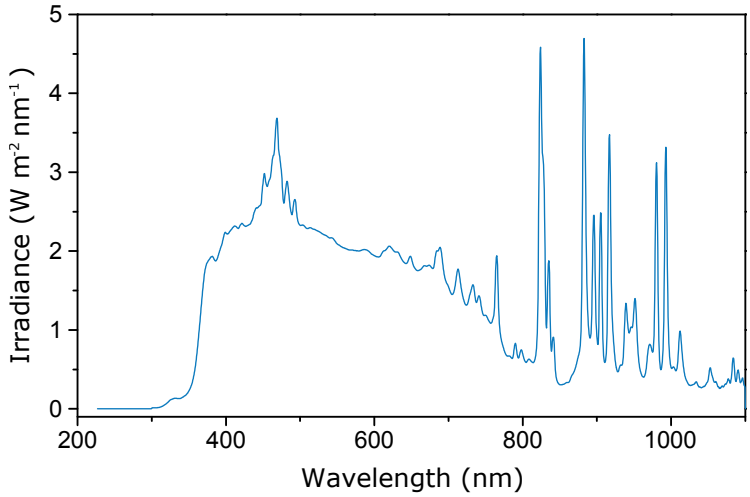

Figure 3.4: Spectrum solar simulator.

3.2 Thin film deposition

3.2.1 Magnetron sputtering

Magnetron sputtering was the main technique used in this work to prepare thin films. Magnetron sputtering is a physical thin film deposition method, wherein a microwave generator is used to transform a gas into a plasma of positively charged ionic species, which are accelerated by an electric field towards a cathode material (target), which will be sputtered as a consequence of the ion bombardment. The sputtered species will then move away from the cathode and may condense on a substrate which was placed underneath the sputter target. Figure 3.5a shows how a typical magnetron sputtering set up looks like.

A series of gases may be used as sputter gas, depending on the target material and the desired thin film composition. Argon is often used as the main magnetron sputtering gas, because of its inertness in non-ionic state and its appropriate mass which allows the sputtering of many compounds. Oxygen is regularly added to the sputter gas when oxide-containing targets are used. Because the sputter process frequently causes the preferential sputtering of lighter elements, oxide containing targets may become slowly deprived of oxygen. The addition of oxygen to the sputter gas may then counter the oxygen deprivation of the target. Thus, preventing the deposition of non stoichiometric oxide thin films. This sputtering process is also called semi-reactive sputtering, because part of the oxide in the deposited thin films comes from the sputter gas. Also reactive sputtering may be performed, whereby all oxygen in an oxide thin film, for instance, originates from the sputter gas.

The magnetron sputtering set up consists of an inner part that functions as the cathode and an outer part that is regarded as the anode. Between those two parts the electric field is applied. As the anode should have a larger area than the cathode, an electrical contact between the former

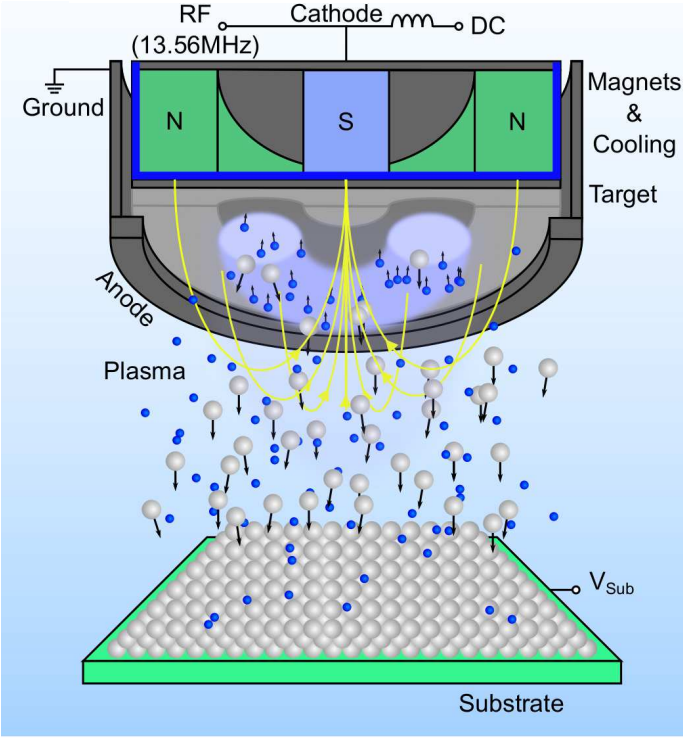

Figure 3.5: Schematic of the magnetron sputtering set up. The grey and blue spheres represent the sputtered target atoms and the sputter gas atoms, representatively.[3]

with the entire sputtering chamber was established to create one large anode. The electric field may be generated through DC, AC or pulsed DC signals, whereby only DC and AC have been used in this work. A DC field can be achieved with a DC generator, whereby a constant voltage is applied between cathode and anode. Although DC sputtering is a straight forward process, only cathodes made from conductive materials can be used. The problem with weak conductors is that the continuous bombardment of the target by cations cannot be sufficiently compensated by electrons, so that the negative potential of the cathode gradually decreases, until the sputter process eventually stops. For weak conducting compounds, an AC signal would be a better choice. Herein, an alternating electric field is generated at a frequency for which no impedance is created at the targets. This requirement is fulfilled for a frequency of 13.56 MHz and has, thus, been chosen as the standard frequency. Because this frequency lies in the radio frequency regime, the technique is also called radio frequency (RF) sputtering. At the beginning of an RF sputtering process, the AC signal is symmetric around zero. However, this changes over time. Due to the alternating electric field, both ions and electrons will be accelerated towards the sputter target. Because the electrons have a lower mass compared to the cations, more electrons than cations will reach the target surface, so that an electron excess forms at the target surface over time. As a consequence, the potential of the target diminishes, allowing the cations to reach the target surface at a steady pace, a mechanism called ”self-biasing”. In a common RF magnetron a circular

magnet array is located above the target. The magnetic field functions as a sort of trap to raise the electron density around the north pole, which as a result causes an increased ionization rate in this area and, thus, a higher sputter rate. Due to the target being consumed at a higher rate in this circular zone, it is also commonly denoted as a ”race track”.

The DC and RF magnetrons used in this work were supplied by Thin Film Consulting and the RF signal was generated by a Hüttinger PFG 300RF RF generator.

3.2.2 Contact films for interface experiments

All interface experiments, for which the exact procedure will be explained further in this Chapter, were performed in the DArmstadt Integrated SYstem for MATerials science (DAISY-MAT) (Figure 3.6). The DAISY-MAT is a system which include chambers for surface cleaning, thin film deposition and surface analysis connected to each other via a distribution chamber operated under ultra-high vacuum (UHV). Because the samples are transferred in vacuum, surface contamination in between thin film deposition and surface analysis is limited. Substrates can be introduced into the DAISY-MAT through a load lock, which can be pumped from atmospheric pressure down to high vacuum.

The interface experiments required the deposition of contact thin films, whereby the thin film deposition was performed through magnetron sputtering. The deposition parameters of the investigated contact materials, RuO_2, NiO, CoO_x and Sn-doped In_2O_3 (ITO), can be found in Table 3.1. RuO_2 and NiO were reactively sputtered from a metallic Ru target (Lesker) and metallic Ni target (Alineason), respectively. CoO_x was semireactively sputtered from a ceramic Co_3O_4 target (Alineason). ITO was sputtered from a ceramic ITO target with 10% Sn (Lesker). All targets had a diameter of 2 inches. For the ITO(400 °C) deposition, heating of the substrates was performed in the process gas atmosphere through a halogen lamp, whereby the temperature was measured through a thermoelement. 10 °C/min was the approximate heating and cooling rate.

Table 3.1: Magnetron sputtering deposition parameters for RuO_2, NiO, CoO_x, ITO(RT) and ITO(400 °C) thin films.

	RuO_2	NiO	CoO_x	ITO(RT)	ITO(400 °C)
T_{sub} (°C)	RT	RT	RT	RT	400
Pr (Pa)	1	0.5	0.5	0.5	0.5
O_2/Ar ratio (%)	7.5	20	10	0	0
P (W)	10 (DC)	40 (DC)	40 (RF)	25 (RF)	25 (RF)
Flux (sccm)	10	20	20	6.6	6.6
d (cm)	9.1	8.0	8.5	9.6	9.6
R ($nm.min^{-1}$)	3	3	1.3	5	5

In the above Table T_{sub} is substrate temperature, RT is room temperature, Pr stands for pressure, P is the power applied to the sputter target, d stands for the target-to-substrate distance and R stands for the deposition rate of the film.

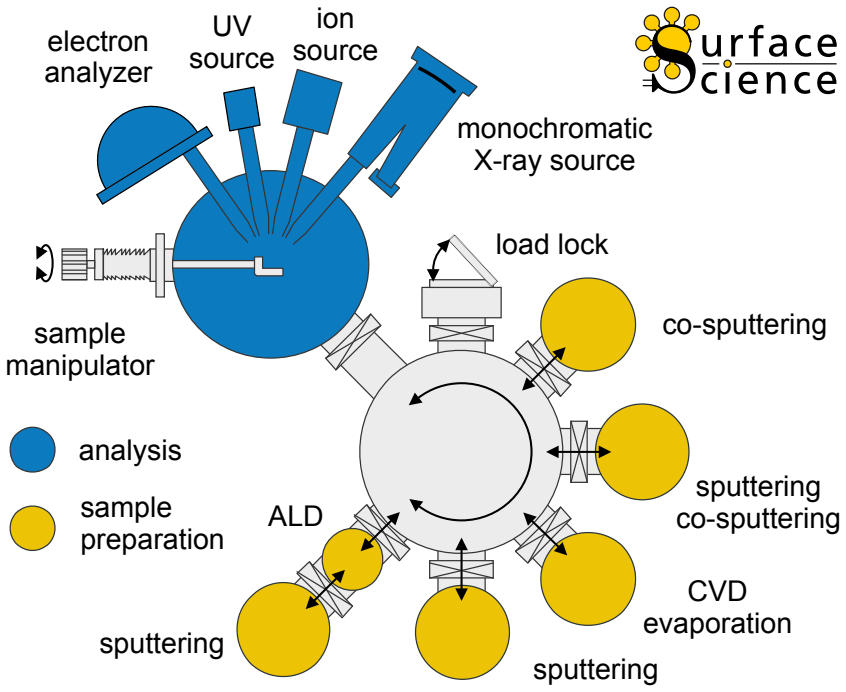

Figure 3.6: Schematic of DArmstadt Integrated SYstem for MATerials science (DAISY-MAT). Adapted from [4].

3.2.3 $BiVO_4$ thin films

The polycrystalline gradient $BiVO_4$ thin films were prepared by Fuxian Wang from the group of our collaboration partner Dr. Klaus Ellmer of the Helmholtz-Zentrum Berlin through reactive magnetron sputtering using a home-built magnetron sputtering system equipped with a load lock.[5] A co-sputtering set up was used with two separate 2 inches diameter metallic Bi (99.9%) and V (99.99%) targets, inclined by 30° to each other and focused onto a soda lime glass substrate with a size of 22 x 22 mm^2 (Figure 3.7a). The glass substrates were coated with a highly conductive and transparent fluoride doped tin oxide F:SnO_2 film, which served as back contact during the XPS measurements. The sputtering atmosphere was an Ar/O_2 gas mixture (20% O_2) at a total sputtering pressure of 1 Pa. The DC power at the Bi target was about 20 — 30 W, while the DC power at the V target was 450 W. While the V-target-to-substrate distance was 6 cm, the Bi-target-to-substrate distance was 12 cm. Since no rotation stage was used during sputtering, every sample contained a Bi/V compositional gradient along the sample width. After sputtering, the films were annealed in a muffle furnace at 500 °C in air for 2 h, using a temperature ramp of 10 K/min. Approximately 150 nm thick films were prepared.

The PLD $BiVO_4$ thin films were prepared by Dr. Sebastián Murcia-López from the Department

of Advanced Materials for Energy, Catalonia Institute for Energy Research (IREC) through pulsed laser deposition (PLD) according to a previously published procedure (Figure 3.7b).[6] In short, a fluorine-doped tin oxide (FTO) glass (Sigma-Aldrich, TEC 7 Ω/square) substrate was first cleaned with a mixture of acetone/isopropanol/water (1:1:1 vol%) through 10 min of sonication. After drying under a N_2 stream, the substrate was entered into the PLD vacuum chamber and heated to 300 °C under an O_2 pressure of 200 mtorr. The $BiVO_4$ layer was then deposited through ablation of a home-made $BiVO_4$ target with laser pulses at a repetition frequency of 10 Hz, with a total energy set at ± 150 mJ and an energy fluency of 0.5 J/cm^2. The target-to-substrate distance was set to 90 mm. Approximately 150 nm thick $BiVO_4$ thin films were obtained by selecting the right number of laser pulses. Then, the $BiVO_4$ thin films were post annealed at 500 °C for 3 h in air. The PLD equipment used in this work was a PLD 5000 equipment (PVD Products) with a 240 nm excimer KrF (λ = 248 nm) laser.

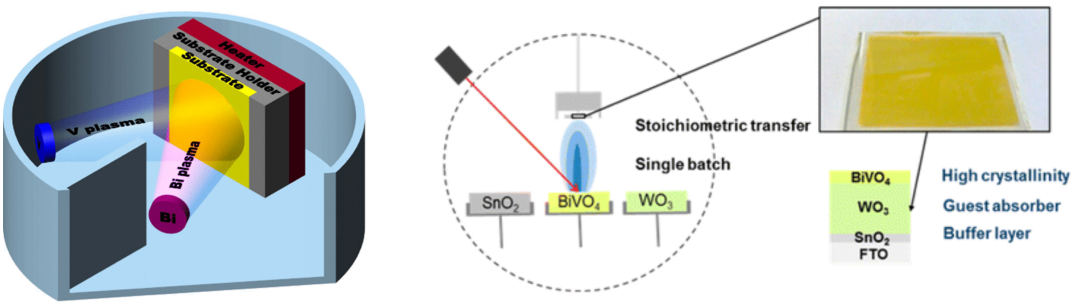

(a) (b)

Figure 3.7: Diagrams of (a) the magnetron cosputtering set up[5] and (b) the PLD set up for the $BiVO_4$ thin film deposition.[6]

3.3 $CuFeO_2$ pellet preparation

$CuFeO_2$ pellets were prepared from the $CuFeO_2$ powder (synthesis procedure in Section 3.1.3), which was not deemed fit for the photodeposition experiments (more thorough explanation in Section 6.5.1). 600 — 700 mg of powder was first homogeneously ground with a pestle and mortar. Then, the powder was uniaxially pressed at room temperature using an hydraulic powder press (CA NC II OSTERWALDER AG) at 300 bar for 15 min. Next, the pellet was further compacted at room temperature with a cold isostatic press (KIP 100E, Paul Otto Weber, Remshalden) at 5000 bar for 30 min. The result was a sturdy pellet with a thickness of 0.5 — 1 cm.

3.4 Characterization

3.4.1 UV-Vis diffuse reflectance spectroscopy

To assess the optical properties of the particulate photoabsorbers and their heterostructures, UV-Vis-NIR diffuse reflectance spectroscopy was carried out. Herein, a light beam is focused onto a powder sample, which is commonly loaded into a cuvette, and the diffuse scattered light is collected, mostly using an integrating sphere. Normal UV-Vis-NIR spectroscopy, which is based on the transmission of light cannot be applied for powdered samples due their opaqueness.

For semiconductors the main electronic excitations induced by light concern the transition of electrons from valence band to conduction band and are governed by the band gap of the semiconductor. Most semiconductors have band gap energies between 1 eV and 4 eV. By applying the following equation:

$$\lambda = \frac{hc}{E} \tag{3.1}$$

with E as the excitation energy, λ as the wavelength, h as the Planck constant and c as the speed of light, one can calculate that band gap optical transitions are induced by photons with wavelengths between 300 — 1240 nm, thus photons in the UV-Vis-NIR region of the light spectrum. For a semiconductor with a certain band gap, photons with energies below the band gap will pass through, whereas photons with an energy higher than the band gap may be absorbed if the electronic selection rules are fulfilled.

In this work, UV-Vis-NIR diffuse reflectance spectroscopy was performed with a Lambda 900 spectrometer (Perkin Elmer), equipped with an Ulbricht integrating sphere. Diffuse reflectance spectra were measured for a wavelength range of 300 — 800 nm and a wavelength range of 300 — 1200 nm for the $BiVO_4$ and $CuFeO_2$ powder samples, respectively. All samples were loaded into a glass cuvette with a pathlength of 1 mm. $BaSO_4$ powder was used as a reference.

The measured reflectance R was transformed into the Kubelka-Munk function F(R) according to:

$$F(R) = \frac{(1-R)^2}{2R} \tag{3.2}$$

whereby the Kubelka-Munk function is equivalent to the absorption coefficient according to the Kubelka-Munk theory:[7,8]

$$F(R) = \frac{\alpha}{s} \tag{3.3}$$

with α as the absorption coefficient and s as the scattering coefficient. respectively. Due to the equivalence of α and F(R) the optical band gap E_g of a semiconductor can be estimated from:

$$F(R)h\nu = A(h\nu - E_g)^n \tag{3.4}$$

with A being a constant and ν being the light frequency. This equation was first introduced by Tauc and is therefore also referred to as Tauc's equation.[9] n relates to the type of optical transition taking place in the semiconductor. Specifically, n = 1/2 and n = 2 refer to the direct and indirect allowed optical transition in the semiconductor. Thus, creating plots of $(F(R)h\nu)^2$ vs $h\nu$ and $(F(R)h\nu)^{\frac{1}{2}}$ vs $h\nu$ allows for an estimation of the direct and indirect optical band gap, respectively, from the intercepts with the x-axis of the extrapolated linear part of these plots.

3.4.2 Raman spectroscopy

Raman spectroscopy is a spectroscopic technique used to obtain chemical and structural information of a sample through the recording of inelastic scattered light of a monochromatic light source. Next to the prevalent elastic scattering (Rayleigh scattering), photons can inelastically scatter (Raman scattering) due to interactions with molecular vibrations or phonons. The energy shifts of the Raman scattered photons (Raman shifts) depend on the energy levels of the functional group vibration they interact with. Thus, Raman spectrograms of scattered light intensity versus Raman shift yield vibrational information that can be used to identify molecules and crystalline phases. Raman spectroscopy is complimentary to IR spectroscopy in the sense that Raman scattering only takes place after interaction with vibrations that change the (molecular) polarizability, while IR absorption bands arise from interactions with vibrations that induce a change in the overall dipole moment.

In this work, a LabRAM HR 800 Raman spectrometer was used to record the Raman spectra of all thin film and powder samples. An argon ion laser was used as an excitation source operating at a wavelength of 488 nm and an approximate laser power of 10 mW on the sample. A 10X objective was used to generate a spot size of approximately 2 μm. Before each set of measurements, the Raman shift wavenumber was calibrated by measuring a silicon substrate and setting the peak position of the main peak to the expected value of 521 cm^{-1}.

3.4.2.1 X-ray diffraction

3.4.2.2 Powder X-ray diffraction (PXRD)

Powder diffraction through X-rays is a popular method for detecting the crystalline phases in a powder sample. When X-ray photons hit a crystalline lattice they are diffracted into specific directions due to the periodical ordering of the atoms in the lattice. This phenomenon is called Bragg diffraction and is a consequence of the interference between waves reflecting from differ-

ent crystal planes. The condition for constructive interference is summarized in Bragg's law:

$$2d\sin\theta = n\lambda \tag{3.5}$$

where λ is the incident X-ray wavelength, d is the crystal plane separation and θ is the incidence angle. Typically, the Bragg-Brentano $\theta/2\theta$ configuration is used to measure powder samples and consists of a fixed X-ray source, a sample stage that is tilted by an angle θ and a detector rotating around the same rotation axis by 2θ. In this configuration the lattice planes parallel to the sample stage surface are probed and for a homogeneously mixed powder sample all the main lattice planes should be registered. The set of recorded diffraction angles and relative intensities allows the determination of the crystalline phases, present in the sample, by comparison with diffractograms from databases.

The $\theta/2\theta$ diffractograms of the powder samples were commonly recorded by a Bruker D2 phaser with a Cu Kα X-ray source (λ = 1.5418 Å), continuously scanning from 10° to 90°. The powder samples were loaded into small disc-like silicon containers. The diffractograms of the $CuFeO_2$ samples, however, exhibited a strong X-ray fluorescence background due to the iron atoms absorbing the Cu Kα X-ray photons. To avoid X-ray fluorescence and to obtain higher resolution $\theta/2\theta$ diffractograms, a PANalitycal X'pert MPD-PRO diffractometer was used, which was equipped with a Cu Kα X-ray anode (operated at 45 kV and 40 mA), a secondary monochromator and an X'celerator detector. The secondary monochromator allowed to filter out the X-ray fluorescence signal generated by the $CuFeO_2$ samples. Herein, the powder samples were placed onto silicon wafer sample holders and flattened with a piece of glass.

3.4.2.3 Rietveld refinement

Rietveld refinement is a more thorough analysis of X-ray powder diffractograms, which is able to determine the amorphous fraction, give an estimate of the crystallite size, allow a more precise determination of the crystalline phases and provide the relative quantity of each crystalline phase. In short, a Rietveld refinement uses a least squares procedure, whereby a theoretical line profile is refined until it matches the measured profile. To begin the refinement, a set of starting parameters need to be given, which include the lattice parameters and crystalline structure of the estimated crystalline phases and the estimated size and morphology of the crystallites. Rietveld analysis was, herein, used to determine whether other crystalline phases were present besides monoclinic clinobisvanite in the $BiVO_4$ powder samples.

The $\theta/2\theta$ diffractograms of the powder samples used for the Rietveld analysis were measured with a STOE STADI P diffractometer, equipped with a Ge 111 monochromator, a Mo Kα 1 X-ray source and a position sensitive detector. Rietveld analysis was carried out with the Fullprof software suite.

3.4.3 Electron microscopy

3.4.3.1 Scanning electron microscopy (SEM)

Scanning electron microscopy (SEM) is a technique that allows obtaining chemical and morphological information of a surface by scanning a focused electron beam over the sample surface. Commonly, the electron beam can be generated through thermionic heating of a solid state crystal (mainly CeB_6 or LaB_6), resistive heating of a tungsten filament or field emission from a tungsten tip. The electrons released in this fashion are then accelerated by a voltage between $1 - 40$ kV and focused through an arrangement of condenser lenses from the source onto the sample surface. Electron beams generated by a field emission gun are narrower and brighter compared to thermionic devices and, thus, allow gaining a higher signal-to-noise ratio and an increased spatial resolution up to 0.5 nm. The electrons in the primary electron beam reach the sample surface with high kinetic energy, allowing them to interact with the sample up to a depth of 1 μm. Essentially, the electrons interact with the atoms in the sample through elastic and inelastic scattering processes, generating various depth-dependent signals including X-rays, back-scattered electrons and secondary electrons (Figure 3.8).

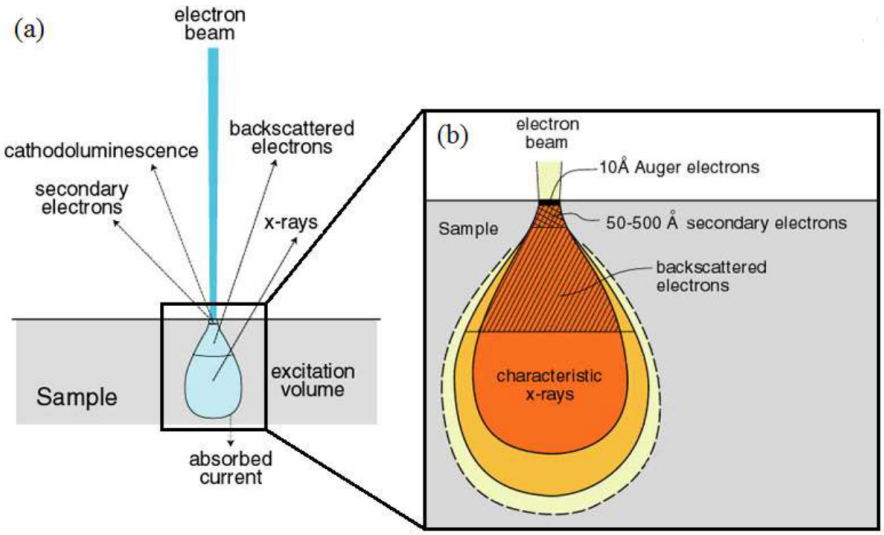

Figure 3.8: Schematic of the interaction of a primary electron beam with a solid state sample, including the escape depth of all measurable secondary signals.[10]

Secondary electrons form the main signal in SEM. Secondary electrons are ”free” electrons that were ejected from their atomic shells, after primary electrons, X-rays or other secondary electrons transferred enough energy to overcome the atomic binding energy of bound electrons. Because of their low kinetic energy, most secondary electrons only escape the sample if they were generated at a sample depth of a $1 - 10$ nm (Figure 2.28). Additionally, the number of secondary electrons that escape the sample depends on the angle of incidence of the primary beam with

the sample surface. Generally, more secondary electrons are released as the curvature and slope of the sample increases. Thus, by scanning the primary beam in a raster-like pattern along the surface and detecting how many secondary electrons are released, a composite topological image of the surface can be created. This technique is called secondary electron imaging (SEI). Image resolutions of less than 0.5 nm are feasible.

As a result of the ejection of core electrons by the primary beam, X-rays can be generated if outer shell electrons migrate to inner shell vacancies. These X-rays have an energy equivalent to the energy difference between the two involved atomic energy levels. Thus, each element correspond to a specific set of "characteristic" X-rays. Consequently, the energy analysis of X-rays emitted from a sample after electron beam bombardment, allows obtaining chemical information of that sample. This X-ray analysis technique is called energy-dispersive X-ray spectroscopy (EDS). The characteristic X-rays are typically detected up to a depth of a few micrometers, due to the strong penetration of the primary electron beam and the high escape depth of X-rays. The lateral resolution varies from 50 to a few 100 nm, depending on the primary electron beam energy and the type of detector. Besides X-rays, Auger electrons can be released when electrons recombine with core holes. These Auger electrons are also element characteristic and have small escape depths of a few angstrom (Figure 3.8) due to their limited inelastic mean free path (Figure 2.28). Therefore, scanning Auger microscopy (SAM) is much more surface sensitive than EDS.

The primary beam electrons can also elastically scatter on the atoms in the sample and when they leave the sample again they are called backscattered electrons. Due to an approximate square root dependence of the scatter probability on the atomic number, elemental contrast can be achieved if the atoms in the sample have sufficiently different atomic numbers. Since the kinetic energy of backscattered electrons barely changes with respect to the primary electrons, the escape depth reaches up to a few 100 nm. Consequently, backscattered electrons yield a lower lateral resolution with respect to secondary electrons.

A Hitachi TM 1000 was used to make low resolution images (up to 10.000 magnification) through SEI of the $BiVO_4$ and $CuFeO_2$ powder samples. A JEOL 6700F, equipped with a field emission gun and detectors for SEI, backscattered electrons (BSE) and EDS, was used to make higher resolution images (up to ± 700.000 magnification) and to perform chemical microanalysis of the (heterostructured) powder samples. SAM was performed with a PHI 710 scanning Auger nanoprobe, having a maximal lateral resolution of 10 nm and a maximal SEI resolution of 3 nm, to elucidate how the contact materials of the heterostructured powder samples were distributed along the particulate photoabsorbers. Different types of measuring modes were used, including point measurements (Auger spectra acquisition on a certain point), zone measurements (Auger spectra acquisition on a certain area) and mapping (Auger intensity acquisition of a certain area by scanning the area in a raster like pattern). Also SAM depth profiling was occasionally tried, whereby an Argon ion gun (sputter rate 10 nm/min) was used to gradually sputter a sample and Auger spectra were measured after each sputter step.

3.4.3.2 Transmission electron spectroscopy (TEM)

In transmission electron microscopy (TEM) an electron beam is focused onto a sample, just as in SEM. However, not the secondary electrons are captured, but the electrons which pass through the sample are. Therefore, samples in TEM are mostly ultrathin specimens, below 100 nm, or nanocrystalline powders suspended onto a conductive grid which allow electron transmission. By capturing the transmitted electrons (bright field) or the diffracted electrons (dark field) by a fluorescent screen or a charge-coupled device (CCD) camera, an image can be made from the sample. Due to the small de Broglie wavelength of electrons, resolutions up to the atom scale can be obtained. Besides imaging, TEM allows the registration of selected area electron diffraction (SAED) patterns for crystalline samples. SAED patterns are measured by placing a selected area aperture into the electron beam path after it passes through the sample. In this way, information on the crystalline structure, crystallinity and texture of a certain area of the sample can be collected. Also, EDS may be performed with TEM, and due to TEM samples being relatively thin, the electron interaction volume will be smaller than for SEM (See Figure 3.8). Additionally, to perform EDS mostly a scanning transmission electron microscope is used, which differs from a conventional TEM, in that it is able to focus the electron beam on a very fine spot (with a size between $0.05 - 0.2$ nm) on the sample. Therefore, EDS with a TEM apparatus allows for a higher lateral resolution compared to SEM-EDS. Additionally to the aforementioned uses of TEM, several other analyses, including electron energy loss spectroscopy (EELS) and high-angle annular dark-field (HAADF) imaging can be performed depending on the chemical and structural nature of the samples. For further reading on the technical principles behind TEM and its applicability in materials science, I refer the reader to the book of Williams and Carter.[11]

TEM measurements, in this work, were performed with a JEOL 2100F, equipped with a field emission gun (FEG) and an Oxford Instruments EDS system. The TEM was operated at an acceleration voltage of 200 kV. The TEM powder samples were prepared by first making a suspension of the powder in ethanol and then putting a small droplet of the suspension onto a holey carbon-coated copper grid. After letting the sample dry, a thin carbon layer was sputtered onto the sample to avoid charging under the electron beam. Due to the relatively weak stability of the $BiVO_4$ powder samples under a focused electron beam, the electron beam was slightly defocused to reduce the intensity of the electron beam hitting the samples.

3.4.4 Photoelectron spectroscopy (PES)

In Chapter 2 in Section 2.4 an overview is given of the fundamentals of photoelectron spectroscopy as well as an explanation on how the core level photoelectron spectra, which will be discussed in this work, may be interpreted. In this Section the way how the photoelectron spectra were measured as well as how data were extracted from the photoelectron spectra is summarised.

All photoelectron spectra in this work were measured with the Physical Electronic PHI 5700

multi-technique surface analysis system, which is part of the DAISY-MAT system (described in Section 3.2.2). The photoelectron spectroscopy chamber is operated at about 10^{-9} mbar. For the XPS measurements a monochromatized Al Kα X-ray source (1486.6 eV) was used, while UPS was measured with He I irradiation (21.2 eV) emitted from a helium discharge lamp. UPS and XPS measurements were recorded at an emission angle (angle between sample and analyser) of 90° and 45°, respectively. Additionally, for UPS a bias of -4 V was applied to the sample in order to accelerate low kinetic energy photoelectrons towards the hemispherical analyser.

To correct for the spectrometer work function Φ_{sp}, PES measurements of a sputter cleaned silver sample were recorded . In short, a piece of silver foil mounted onto a stainless steel sample holder was first sputter cleaned for at least ten minutes using an argon ion gun. An ion kinetic energy of about 1 keV, a sample current of 0.9 μA and a sputtering area of 4 x 4 mm^2 were used as sputtering parameters. Afterwards, a survey (description see below) XP spectrum was measured to confirm the absence of carbonaceous species and water on the silver surface. Then, the silver Fermi edge as well as the $Ag3d_{5/2}$ core level spectrum were measured with the high resolution mode (description see below). The measured $Ag3d_{5/2}$ binding energy can, namely, also be used to calibrate the spectrometer as the $Ag3d_{5/2}$ binding energy of metallic silver should lie at about 368.26 eV. When performing UPS measurements, an additional silver calibration needs to be performed to calibrate the UP spectra, due to UPS being performed under slightly different conditions than XPS (see above). For the binding energy calibration, the silver Fermi edge was measured under the same conditions as the UP spectra.

Photoelectron spectra, in this work, have been measured according to one of two modes, survey and high resolution, whereby the spectra are denoted as survey spectra and high resolution spectra, respectively. In XPS, survey spectra are photoelectron spectra that are recorded rapidly over a broad range of binding energies to assess which chemical species are present at the sample surface, mainly to detect whether the sample surface is contaminated with undesired species. Survey XP spectra, in this work, were measured by performing 1 sweep from -1 eV to 1400 eV with a pass energy of 187.75 eV, an energy step size of 0.800 eV/step and a step duration of 100 ms. Survey XP spectra include signals from valence electrons, core electrons and Auger electrons, and have a background due to inelastically scattered electrons, which increases with increasing binding energy. Figure 3.9 shows how the survey XP spectrum of a cleaned $BiVO_4$ surface looks like.

In the other measuring mode, the high resolution mode, a certain energetic range of interest is sweeped multiple times to acquire a detailed photoelectron spectrum. High resolution XP spectra are mainly carried out to acquire detailed chemical and electronic information by measuring specific core photoelectron, Auger electron and valence band regions. High resolution XP spectra, in this work, were measured by performing a number of sweeps in the energetic range of interest with a pass energy of 5.85 eV, an energy step size of 0.050 eV/step and a step duration of 100 ms.

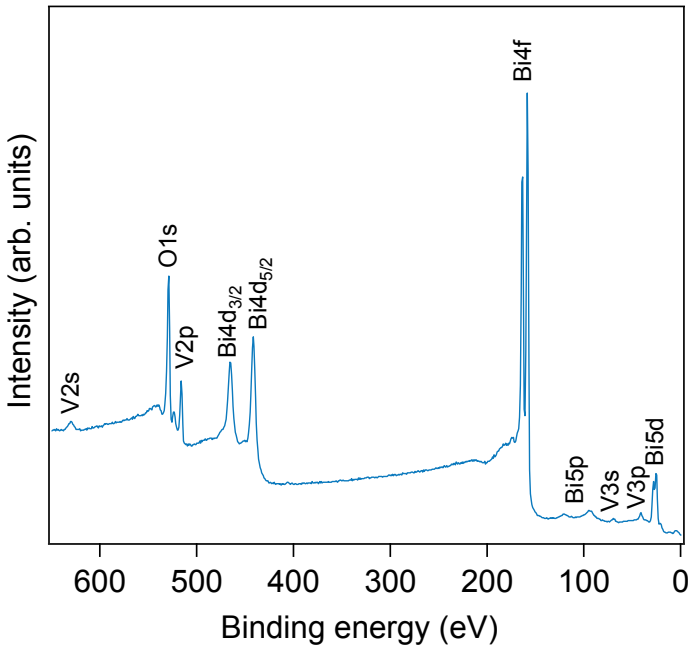

Figure 3.9: Example of a survey spectrum measured on a cleaned $BiVO_4$ thin film surface, whereby the detected $BiVO_4$ related core levels are indicated.

High resolution XP core level spectra contains plenty of information. First of all, the overall shape of the core level spectrum needs to be inspected, as the appearance of secondary features in the form of shoulders or additional peaks can point to an altered chemical composition or the presence of adsorbates. Next, the binding energy of the analysed core level can be determined from the maximum line intensity. Herein, a fitting function was used, which assumed a Gaussian line shape around the maximum of the core electron signal, which is a valid assumption for straightforward core level spectra, such as Bi4f, $V2p_{3/2}$, O1s and $Cu2p_{3/2}$ core level spectra. For more complicated spectra, such as $Fe2p_{3/2}$, $Co2p_{3/2}$ and $Ni2p_{3/2}$, the maximum of the core level spectra had to be determined manually by drawing a straight line towards the maximum of intensity.

Additionally, the chemical surface composition can be determined from the XP core level spectra. The surface ratio $x_{A/B}$ of two elements A and B can be calculated according to the following formula:

$$x_{A/B} = \frac{I_A^{CL}/S_A^{CL}}{I_B^{CL}/S_B^{CL}} \tag{3.6}$$

whereby I_A^{CL} and I_B^{CL} are the intensities of a particular core level corresponding to element A and B, respectively, and S_A^{CL} and S_B^{CL} are the atomic sensitivity factors of a particular core level corresponding to element A and B, respectively. The atomic sensitivity factors depend on the different photoelectron generation cross sections of different core level electrons as well as on

the instrumental parameters, which normally do not vary for different core levels.

The intensities in Equation 3.6 can be determined by integrating the corresponding high resolution core level spectra, after removing the inelastic scattered electron background from the core level spectra. Polynomials could be used to remove the background, but that would not be correct from a physical point of view. Better is to use the more physically correct photoelectron background removal procedure introduced by Shirley in 1972[12] or the one described by Tougaard and Jansson in 1992.[13] Also, for difference spectra, whereby the difference is taken of spectra from the same core level region to inspect minor chemical differences, background subtraction had to be performed. In this work, the Bi/V surface ratio was determined frequently by taking the ratio of the integrated Bi4f intensity and $V2p_{3/2}$ ratio. However, as will be shown in Chapter 5, a correction factor has to be applied to obtain the real Bi/V surface ratio, due to the tabulated sensitivity factors not correcting adequately for the different photoelectron generation cross sections of Bi4f and $V2p_{3/2}$. In addition, difference spectra for the Bi4f, $V2p_{3/2}$, $Cu2p_{3/2}$ and Fe2p region were occasionally created. Before making the difference spectra, the background of the $V2p_{3/2}$, O1s and $Cu2p_{3/2}$ spectra were removed with a Shirley function, whereas the background of the Bi4f and Fe2p spectra were removed with a Tougaard function. Figure 3.10 shows the effect of the Shirley and the Tougaard background removal functions on a high resolution Bi4f spectrum. The differences between both functions are minor, however, the Tougaard function follows the curvature of the Bi4f spectrum in between the $Bi4f_{7/2}$ and $Bi4f_{5/2}$ core level signals slightly better. The $Bi4f_{7/2}$ and $Bi4f_{5/2}$ line maxima are not influenced by the background removal functions.

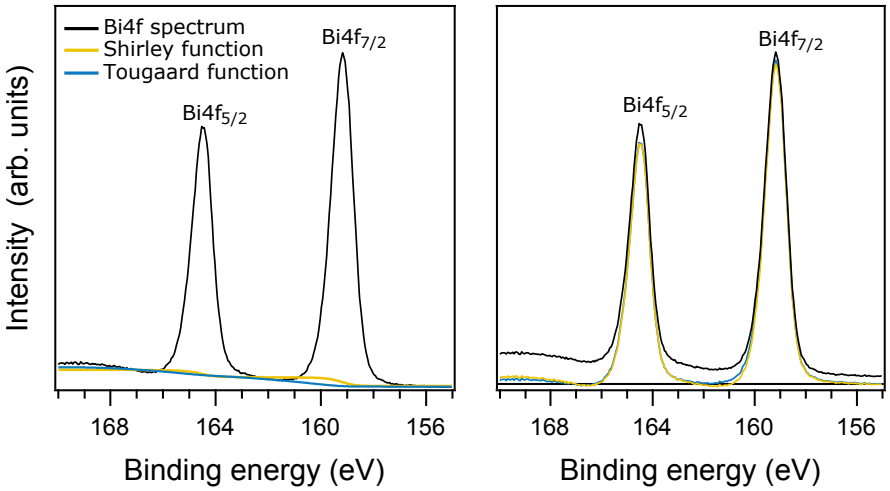

Figure 3.10: Example of a high resolution Bi4f core level spectrum for which a Shirley and Tougaard function have been used to remove the background.

UPS measurements could be carried out in the survey mode as well as on the high resolution mode by sweeping once or a few times in the range of -1 eV to 21 eV (no bias), having a pass energy of 2.95 eV, an energy step size of 0.025 eV/step, a step duration of 100 ms and a bias of -4 V. UPS was mainly performed to determine the work function and occasionally to determine the

valence band maximum. Figure 3.11a shows an example of a UP spectrum of $BiVO_4$. The middle of the left most edge of the spectrum correspond to the secondary electron cut-off E_{SEC}, which can be used to determine the work function ϕ according to the formula:

$$\phi = h\nu - E_{SEC} - \phi_{bias} \tag{3.7}$$

with $h\nu$ corresponding to the photon energy, which for UPS is mostly 21.2 eV (He I) and ϕ_{bias} being the applied bias (here -4 V). The onset of the valence band region in UPS (right most region) correspond to the valence band maximum E_{VBM}^{UPS} and can be determined (Figure 3.11b) by extrapolating the linear part of the valence band region to the lower part of the low binding energy side. In a similar way, the valence band maximum (E_{VBM}^{XPS}) can be determined from the valence band region in XPS (Figure 3.11c). Unless stated otherwise, VBMs were collected in this work from the XPS valence band region. The main reason is that the UPS valence band regions of $CuFeO_2$ and $BiVO_4$ at the low binding energy side appeared to be too rounded, so that a linear extrapolation would not be reliable.

3.4.4.1 Interface experiments

Interface experiments in this work were performed to determine the junction properties between photoabsorbers ($BiVO_4$ and $CuFeO_2$) and selected contact materials (ITO, RuO_2, NiO and CoO_x). The preparation of the $BiVO_4$ thin film substrates and $CuFeO_2$ pellets is described in Section 3.2.3 and Section 3.3, respectively. The contact materials were sputtered onto the substrates through magnetron sputtering (See Section 3.2.1) using the parameters listed in Table 3.1.

In a particular interface experiment, the surface of a substrate was first cleaned with distilled water and, subsequently, dried using compressed air to remove any dust attached to the substrate surface. Then, the substrate was mounted onto a stainless steel substrate holder and kept in place using screws and washers. Next, the sample was introduced into the DAISY-MAT system (described in Section 3.2.2) through a load lock to move from ambient pressure to vacuum (10^{-7} — 10^{-9} mbar). After that the substrate surface was subjected to a further cleaning step to remove water and carbonaceous species adsorbed onto the sample surface. For the $CuFeO_2$ pellets, this cleaning step represented a heating step whereby the samples were heated for at least 3 h in an oxygen atmosphere (flow: 5 sccm; 4 x 10^{-4} mbar) at a temperature of 200 °C. The $BiVO_4$ were cleaned with a more rapid oxygen plasma treatment. The working principle of an oxygen plasma source can be found in the paper of Anton et al.[14] In this work, the oxygen plasma treatment was carried out with a GenII Atom/Ion Hybrid Plasma source by Tectra. This plasma source generated an atom flux of 2 x 10^{16} atoms cm^{-2} s^{-1} at the working distance of 10 cm. For the oxygen plasma treatments, an oxygen flow of 2 sccm was used, which resulted in a working pressure of approximately 1 x 10^{-4} mbar. A 40 mA plasma current was maintained for 15 minutes. The plasma was operated at a power of about 180 W.

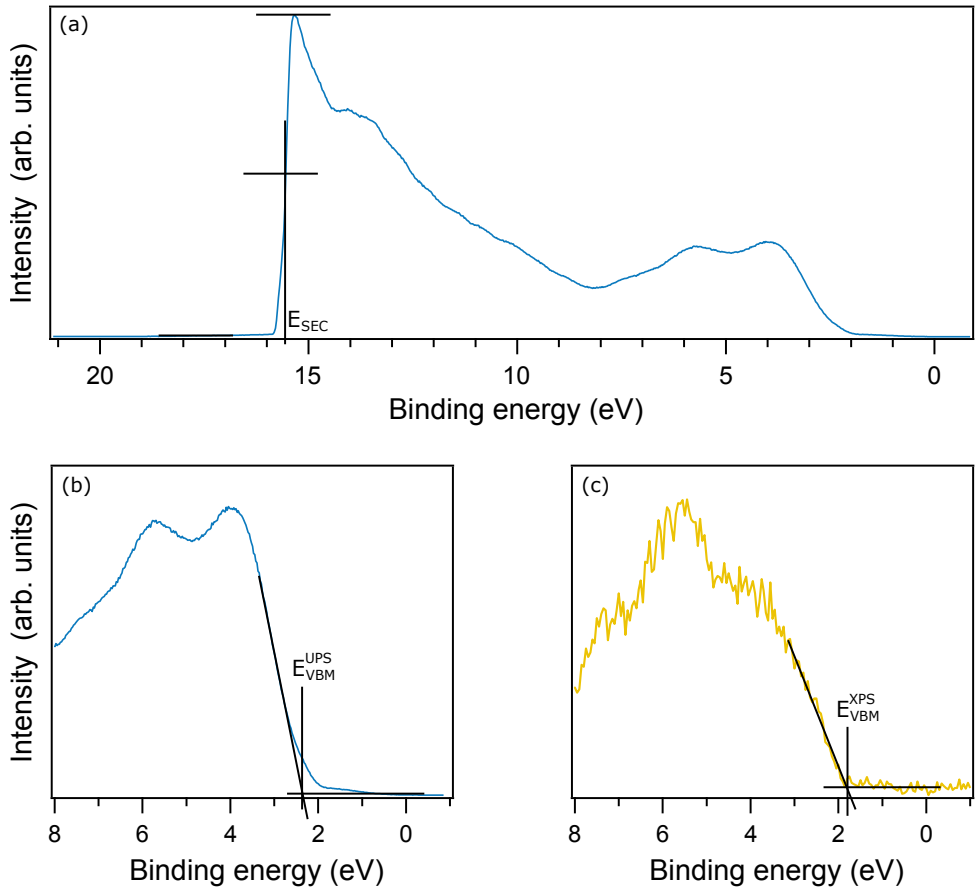

Figure 3.11: (a) Example of UP spectrum of $BiVO_4$, (b) valence band region UPS and (c) valence band region XPS. E_{SEC}: secondary electron cut-off; E_{VBM}^{UPS}: valence band maximum from UPS valence band region; E_{VBM}^{XPS}: valence band maximum from XPS valence band region.

After cleaning the sample surface, a first set of PES measurements (description in Section 3.4.4) was performed to assess the chemical and electronic properties of the bare substrate. After that a contact thin film was deposited onto the substrate in a stepwise fashion, whereby PES measurements were performed after each deposition step to determine how the substrate core level spectra change as a response to the growing film. In the last deposition step, a relatively thick layer of the contact material was deposited to measure the electronic and chemical properties of the contact film by PES. The whole procedure of an interface experiment is also schematically represented in Figure 3.12a. To represent the interface experiments in this work, all relevant core level spectra and valence band spectra of substrate and film will be stacked above each other in the same figure, whereby the stacking order from bottom to top represents the subsequent deposition steps.

All the PES data measured during an interface experiment could then be used to interpret the interfacial band alignment between the two materials that form the contact. For the bare

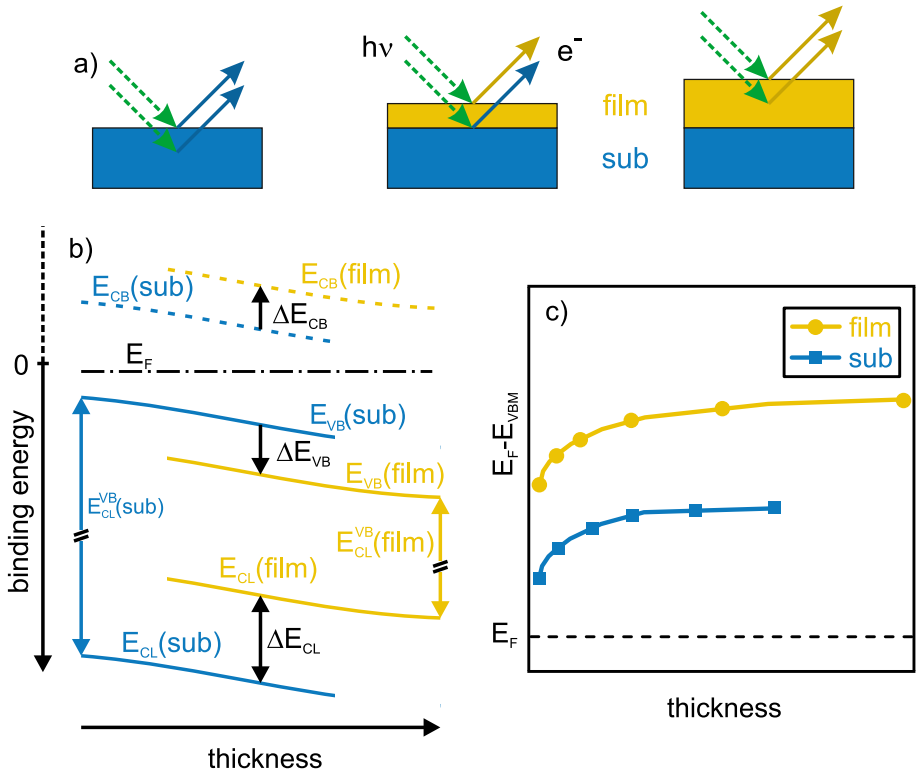

Figure 3.12: (a) Representation of an interface experiment, (b) Evolution of the binding energy with film thickness for the core levels, VBM and CBM of the substrate and the deposited contact film, (c) Evolution of the VBM of the substrate and the film with respect to the Fermi level position as a function of the film thickness. Adapted from [15].

substrate, first, the VBM ($E_{VB,0}$(sub)) and the energetic distance between core levels and VBM ($E^{VB}_{CL,0}$(sub)) would be extracted. Then, the UPS measurement performed on the bare substrate was used to determine the work function of the bare substrate. Next, all substrate and film core level binding energies after each deposition step were determined. Due to the relatively low film thickness after the first few deposition steps, the substrate core photoelectrons could still be detected, thus, allowing the determination of the substrate related core level binding energies. After a relatively thick film had been deposited, the substrate core level photoelectrons could not penetrate through the film any more. After this observation, a final deposition was made to obtain a sufficiently thick film so that the VBM ($E_{VB,final}$(film)) and the energetic distance between core levels and VBM ($E^{VB}_{CL,final}$(film) of the thick film could be extracted from the PES measurements on this thick contact layer. Additionally, the work function of the contact layer would be determined from a UPS measurement taken of the contact film. When the chemical state of the elements in substrate and film did not change during the interface experiment, the distance between VBM and core levels was considered to be constant for both the substrate and the film. It should be noted that in most cases the VBM of the substrate cannot be determined any more after the first

contact film deposition step, because of the overlap of the contact film valence band spectrum with that of the substrate. In Figure 3.12b it is shown that the core levels and VBMs of substrate and film change in parallel with increasing contact film thickness. These data can then be used to determine how the VBM and core level binding energies shift with respect to the Fermi level (Figure 3.12c), which allows to construct a band alignment diagram between substrate and film to visualize phenomena like band bending and Schottky type barriers. Additionally, the shape of the core level spectra should be checked to analyse whether any chemical changes take place during the interface experiment.

Additionally, for the $BiVO_4$ substrates, the thickness of the deposited contact films could be estimated from the difference in attenuation of the Bi4f and $V2p_{3/2}$ core level intensity. Since the kinetic energy of the photoelectrons from the Bi4f emission is higher than for the $V2p_{3/2}$ emission, the Bi4f photoelectrons are attenuated less because of the higher inelastic mean free path of these photoelectrons. The thickness of a thin film growing on top of the $BiVO_4$ substrate can then be evaluated, under the assumption that the surface V/Bi ratio does not change during film growth, according to following formula:

$$t = \frac{\ln\left(\frac{I_V \text{ x } I_{Bi,0}}{I_Bi \text{ x } I_{V,0}}\right) \text{ x } \lambda_V \text{ x } \lambda_{Bi}}{\lambda_V - \lambda_{Bi}} \tag{3.8}$$

where t: film thickness; I_V: integrated $V2p_{3/2}$ core level intensity at film thickness t; I_{Bi}: integrated Bi4f core level intensity at film thickness t; $I_{V,0}$: integrated $V2p_{3/2}$ core level intensity at zero film thickness; $I_{Bi,0}$: integrated Bi4f core level intensity at zero film thickness; λ_V: electron effective attenuation length of $V2p_{3/2}$ photoelectrons; λ_{Bi}: electron effective attenuation length of Bi4f photoelectrons. The electron effective attenuation lengths were calculated using the "NIST Electron Effective-Attenuation-Length Database", based on the density, number of valence electrons and band gap of the deposited film.

3.4.4.2 Water exposure experiments

In addition to normal interface experiments, where a contact thin film was gradually sputtered onto a substrate, a special type of interface experiments were performed, whereby a water layer was adsorbed onto the substrate. These water exposure experiments were just like the other interface experiments carried out to determine how the substrate binding energy would shift after a water layer was adsorbed onto the substrates. In addition, also the chemical changes related to the water exposure could be interpreted through PES measurements.

In a typical water exposure experiment, a cleaned substrate was first placed into the atomic layer deposition (ALD) chamber in the DAISY-MAT. The ALD chamber is one of the chambers in the DAISY-MAT, which is mainly used to deposit Al_2O_3 thin films via ALD, but was used in this work solely for the water exposure experiments. Onto the ALD chamber, a closed glass vessel

containing distilled water was attached via an ALD valve. The ALD valve forms the connection between the glass vessel, at ambient pressure, and the chamber, under high vacuum. By opening the ALD valve for a short period of time, water vapour flows into the chamber and may condense onto the substrate surface. The complete water exposure experiment followed several cycles, whereby the ALD valve of the water reservoir was opened for a certain duration, followed by a period of pumping down the chamber. In our experiments, we performed 15 cycles with an exposure duration of 100 ms and a pumping down duration of 300000 ms. Due to the pumping down to vacuum no physisorbed water remains on the substrate surface. Before and after the water exposure, PES measurements of the substrate were taken.

The closed gas vessel contains two arms which are needed when the water in the reservoir is replenished and needs to be degassed. For the degassing, the water placed in one arm of the reservoir is frozen with liquid nitrogen, after which the ALD valve is opened for a few seconds to create a vacuum in the glass reservoir. Then, the other arm is cooled with liquid nitrogen while the arm with the frozen water is heated. In this way, the water evaporates in the one arm and condenses in the other. Thereafter, the ALD valve is opened again for a few seconds. This procedure was repeated 4 times in total.

The ALD valve used, was a Swagelok 6LVV-ALD3FR4-P-C valve, which was pneumatically controlled with a MAC 34C-ABA-GDFC-1KT controller. For a complete overview of the ALD chamber I refer the reader to the work of Mirko Weidner.[16]

3.4.4.3 Water desorption experiments

Water desorption experiments were carried out in the Darmstadt Integrated System for Fundamental research (DAISY-FUN),[17] which consists of several chambers operated under UHV and dedicated to sample preparation and/or surface analysis (Figure 3.13). The characteristics of DAISY-FUN are described in detail elsewhere.[18]

For a water desorption experiment, the $BiVO_4$ thin film substrate was first of all thoroughly rinsed with distilled water and dried with compressed air. Then, the substrate was mounted onto an Omicron sample holder and inserted via a load lock into the DAISY-FUN. Subsequently, a calcination step was performed to remove the atmospheric surface contaminations. The calcination was performed for 5 h at 400 °C under an O_2 atmosphere (10^{-3} mbar).

Afterwards, the $BiVO_4$ sample was placed into the XPS-chamber, operated at a base pressure of 1 x 10^{-9} mbar. The XPS-chamber is equipped with a SPECS Phoibos 150 analyser and a SPECS Focus 500 X-ray source to perform XPS measurements using the monochromatized AlKα line at 1486.7 eV. The HeI (21.2 eV) and HeII (40.8 eV) line of a helium-discharge lamp were used to perform UPS. A bias-voltage of -3 V was applied during UPS measurements. A sputtered Au foil served as reference sample in order to calibrate the spectrometer by making use of the $Au4f_{7/2}$ transition at 84.0 eV and the Fermi edge.

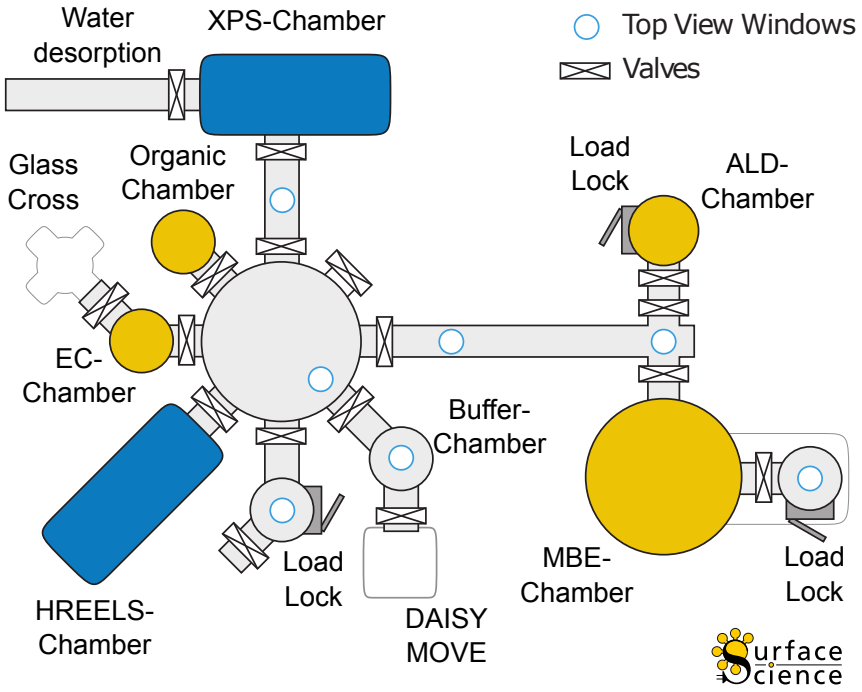

Figure 3.13: Schematic of DArmstadt Integrated SYstem for FUNdamental research (DAISY-FUN). Adapted from [18].

Additionally, a glass water vessel is mounted onto a small pipe connected to the XPS-chamber. This water vessel contains ultra-pure water, which was degassed through the freeze-pump cycling procedure explained above. The dosage of water was precisely controlled by a leak valve and the exposure time was varied stepwise to match the desired dosage using uncorrected pressure readings.

For the water desorption experiment, the $BiVO_4$ sample was first cooled to 77 K using liquid nitrogen (LN). Then, frozen water was stepwise deposited onto the $BiVO_4$ sample by opening the leak valve connected to the water vessel for specific amounts of time. After the deposition of 10 — 15 langmuir of water, the sample was slowly heated up to room temperature. XPS and UPS measurements were performed before cooling down, after cooling down, in between each deposition and after heating up the sample.

3.4.4.4 Peak fitting

For the $V2p_{3/2}$ and O1s core level spectra measured during the water exposure and water desorption experiments, peak fitting was performed to determine the relative amount of components in the $V2p_{3/2}$ and O1s spectra. All components were fitted using pseudo-Voigt profiles. The fitting parameters of V^{5+} and O^{2-} (in $BiVO_4$) were determined by fitting the $V2p_{3/2}$ and O1s spectra, relatively, that were measured after the calcination of the $BiVO_4$ sample. The 0.12 Lorentzian-to-Gaussian ratio (L/G) determined for O^{2-} was also used for all other O1s components. For the

$BiVO_4$ sample calcined in DAISY-FUN there was a second O1s component due to leftover carbonaceous species, which was fitted as well. The fitting parameters of the other components V^{4+}, OH (DAISY-MAT) and H_2O (DAISY-FUN), found after water exposure/water adsorption/water desorption were fitted while keeping the previously determined fitting parameters for V^{5+}, O^{2-}, OH/CO (DAISY-FUN) fixed. All fitting parameters can be seen in Table 3.2.

Table 3.2: Fitting parameters O1s and $V2p_{3/2}$ components.

		DAISY-MAT			DAISY-FUN		
Line	Signal	L/G	FWHM	ΔBE (eV)	L/G	FWHM	ΔBE (eV)
$V2p_{3/2}$	S1(V^{5+})	0.45	1.1	-	0.64	0.9	-
$V2p_{3/2}$	S2(V^{4+})	0.32	1.7	-0.76	0.32	1.7	-0.76
O1s	S1(O^{2-})	0.12	1.1	-	0.12	1.0	-
O1s	S2(OH/CO)	0.12	1.9	1.05	0.12	2.8	1.25
O1s	S3(H_2O)	-	-	-	0.12	1.6	3.3

Sx: signal x, L/G: Lorentzian-to-Gaussian ratio, ΔBE: Binding energy between Sx and S1, FWHM: full width at half maximum.

The fitting parameters for V^{5+} and V^{4+} correspond quite well with what was found earlier for vanadium oxides.[19,20] Namely, that for V^{4+} the L/G decreases and the full width at half maximum (FWHM) increases with respect to V^{5+}. The 0.76 eV binding energy difference between V^{5+} and V^{4+} is, however, lower than the 1.2 eV difference found for vanadium oxides. The higher FWHM of the second signal in the O1s spectra measured during the water desoprtion experiment in DAISY-FUN is due to the presence of carbonaceous species which have a similar binding energy as hydroxyl groups.[21]

3.4.5 Photocatalytic efficiency assessment

3.4.5.1 Rhodamine B degradation

As a first test of the photocatalytic efficiency, the particulate $BiVO_4$ samples were tested for their dye degradation performance, where rhodamine B (Rhd B) was used as the dye. Rhd B was not chosen for any particular reason besides that the wavelength of maximum absorbance λ_{max} (554 nm), is higher than the band gap of $BiVO_4$ (516 nm). The dye degradation experiments were performed with the same set up as the one used for the photodeposition experiments (Figure 3.3). All experiments were performed under ambient pressure and temperature. In a typical dye degradation experiment, 50 mg of the photocatalyst powder was loaded into the honeypot shaped glass beaker together with 100 mL of a Rhd B solution (10 mg/L in distilled water). The beaker was covered with parafilm and placed for 10 min in an ultrasonic bath to disperse the powdered photocatalyst. After that, the top of the glass vessel was covered with a loose transparent Petri dish and the sides of the glass vessel were covered with aluminium foil. Then, a 1.2 mL aliquot of the dispersion was taken. Subsequently, the dispersion was stirred at 750 RPM in the dark for 30 min, after which another 1.2 mL aliquot was taken to determine whether the

dye already degraded in the dark. At that point the shutter of the solar simulator, which was allowed to warm up for 30 min, was opened and the dispersion was illuminated. Then at time intervals of 30 min, 1.2 mL aliquots were take from the dispersion during a period of 2 h. Next, all recuperated aliquots (normally 6 in total) were centrifuged to separate the photocatalyst powder from the Rhd B solution. For each aliquot, 1 mL was taken, diluted to 3 mL with distilled water, and loaded into a quartz cuvette with a 1 cm path length. Thereafter, the cuvette was placed into a UV-Vis spectrophotometer (Shimadzu, UV-1650PC) and a UV-Vis spectrum in the range from 200 nm to 800 nm was recorded, as well as the absorbance at λ_{max} . Then, absorbance plots as a function of degradation time were made to visualize how the absorbance and, thus, the concentration of the undegraded dye decreases. Also, blank experiments in the absence of photocatalyst were performed. All experiments were at least repeated once to assess the reproducibility of the experiments.

3.4.5.2 Sacrificial photochemical water splitting

To test the photochemical water splitting performance of $BiVO_4$ and $CuFeO_2$ a sacrificial agent has to added, due to $BiVO_4$ and $CuFeO_2$ only being able to perform one part of the overall water splitting reaction, i.e. water oxidation and water reduction, respectively. Herein, the sacrificial agent is supposed to consume the charge carrier which is not involved in the photochemical water splitting process. The photochemical water splitting tests with $BiVO_4$ and $CuFeO_2$ are thus referred to as sacrificial photochemical water splitting tests. To test how the (heterostructured) powder samples perform in sacrificial photochemical water splitting, a specific set up (Figure 3.14) at the LIKAT centre (Rostock, Germany) was used.

All used solvents in the experiments were thoroughly degassed by bubbling argon through the solvents for at least 1 h and then stored under argon. A 300 W Xe lamp (LOT-QuantumDesign GmbH) with an output power of 1.5 W and equipped with a 420 nm cut-off filter was used as light source for testing the water oxidation performance of the $BiVO_4$ powders. A Hg vapour UV lamp (LUMATEC SUPERLITE 400) with a wavelength in the range of 320 to 400 nm and an output power of 1.6 W was used as a light source for the water reduction assessment of the $CuFeO_2$ powders.

The sacrificial (photochemical) water splitting experiments were carried out in a double walled and thermostatically controlled reaction vessel (at a constant temperature of 25.0 °C), which was connected through a condenser to an automatic gas burette, operated at a constant pressure (1 ± 0.05 atm). In a typical catalytic test, the reactor and condenser were first several times evacuated and filled with argon to remove any other gases. Then, the photocatalyst powder (50 mg) and for the $BiVO_4$ experiments also the $NaIO_4$ (1 mmol) sacrificial agent was added to the reaction vessel under argon counter flow. The reactor and burette were then again evacuated and flushed with argon for another three times. Subsequently, the reaction medium was loaded into the reaction vessel under argon counter flow. For the tests with $CuFeO_2$ powder, the

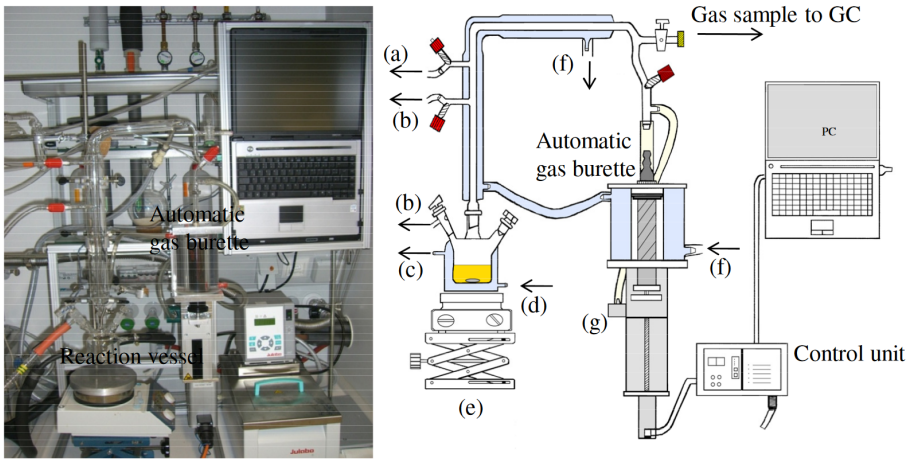

Figure 3.14: Experimental set up to determine the sacrificial water splitting performance of the $CuFeO_2$ and $BiVO_4$ (heterostructured) powders. (a) Effluent (b) vacuum/Ar (c) thermostat outlet (d) thermostat inlet (e) thermostatically controlled reaction vessel (f) thermostat inlet and out let (g) pressure sensor.

reaction medium consisted of a mixture of water and methanol (1:1, 10 mL), whereby methanol was inserted as the sacrificial agent. For the $BiVO_4$ powders, a 10 mL phosphate (10 mmol/L, pH 7.0) buffered solution was used as the reaction medium. Next, the reaction mixture was stirred for approximately 10 min to reach thermal equilibrium. In the mean time, the light source was covered and switched on to let it heat up and the automatic burette was flushed at least three times with argon. Next, for the experiments with $BiVO_4$, a gas sample was taken with a gas-tight syringe and inserted into a gas chromatograph (GC) to determine the amount of air still present in the reaction vessel. After stirring for 10 min, the light source was uncovered and the sacrificial water oxidation/reduction was initiated. The amount of evolved gases were continuously determined by the automatic gas burette, connected to a pressure sensor. After stopping the reaction, a 1 mL gas sample was taken and analysed with a GC (Agilent GC HP 6890N) equipped with a carboxen 1000 column and a thermal conductivity detector (TCD), having argon as carrier gas. Most catalytic tests were run for 20 h.

References

(1) Li, C.; Zhang, P.; Lv, R.; Lu, J.; Wang, T.; Wang, S.; Wang, H.; Gong, J. Selective Deposition of Ag_3PO_4 on Monoclinic $BiVO_4$ (040) for Highly Efficient Photocatalysis. *Small* **2013**, *9*, 3951–3956.

(2) Jin, Y.; Chumanov, G. Solution synthesis of pure 2H $CuFeO_2$ at low temperatures. *RSC Adv.* **2016**, *6*, 26392–26397.

(3) Lohaus, C. The Fermi Level in Hematite., Ph.D. Thesis, TU Darmstadt, 2018, p 257.

(4) Klein, A. Interface Properties of Dielectric Oxides. *J. Am. Ceram. Soc.* **2016**, *99*, 369–387.

(5) Gong, H.; Freudenberg, N.; Nie, M.; van de Krol, R.; Ellmer, K. $BiVO_4$ photoanodes for water splitting with high injection efficiency, deposited by reactive magnetron co-sputtering. *AIP Adv.* **2016**, *6*, 045108.

(6) Murcia-López, S.; Fàbrega, C.; Monllor-Satoca, D.; Hernández-Alonso, M. D.; Penelas-Pérez, G.; Morata, A.; Morante, J. R.; Andreu, T. Tailoring Multilayered $BiVO_4$ Photoanodes by Pulsed Laser Deposition for Water Splitting. *ACS Appl. Mater. Interfaces* **2016**, *8*, 4076–4085.

(7) Kubelka, P.; Munk, F. Ein Beitrag zur Optik der Farbanstriche. *Zeitschrift für Tech. Phys.* **1931**, *12*, 593–601.

(8) Nobbs, J. H. Kubelka-Munk Theory and the Prediction of Reflectance. *Rev. Prog. Color. Relat. Top.* **1985**, *15*, 66–75.

(9) Tauc, J. Optical properties and electronic structure of amorphous Ge and Si. *Mater. Res. Bull.* **1968**, *3*, 37–46.

(10) Bacon, S. Interactions between latent fingermarks, deposition surfaces and development agents., Ph.D. Thesis, University of Surrey, 2012, p 96.

(11) Williams, D. B.; Carter, C. B., *Transmission Electron Microscopy*; Springer US: Boston, MA, 2009, p 775.

(12) Shirley, D. A. High-Resolution X-Ray Photoemission Spectrum of the Valence Bands of Gold. *Phys. Rev. B* **1972**, *5*, 4709–4714.

(13) Tougaard, S.; Jansson, C. Background correction in XPS: Comparison of validity of different methods. *Surf. Interface Anal.* **1992**, *19*, 171–174.

(14) Anton, R.; Wiegner, T.; Naumann, W.; Liebmann, M.; Klein, C.; Bradley, C. Design and performance of a versatile, cost-effective microwave electron cyclotron resonance plasma source for surface and thin film processing. *Rev. Sci. Instrum.* **2000**, *71*, 1177.

(15) Bein, N. The Fermi Level in Bismuth Ferrite., Ph.D. Thesis, TU Darmstadt, 2018, p 117.

(16) Weidner, M. Fermi Level Determination in Tin Oxide by Photoelectron Spectroscopy: Relation to Optoelectronic Properties; Band Bending at Surfaces and Interfaces; Modulation Doping., Ph.D. Thesis, TU Darmstadt, 2016, p 427.

(17) Jaegermann, W.; Kaiser, B.; Ziegler, J.; Klett, J. In *Photoelectrochem. Sol. Fuel Prod.* Springer International Publishing: Cham, 2016, pp 199–280.

(18) Tengeler, S. Cubic silicon carbide for direct photoelectrochemical water splitting., Ph.D. Thesis, TU Darmstadt, 2017, p 183.

(19) Silversmit, G.; Depla, D.; Poelman, H.; Marin, G. B.; De Gryse, R. Determination of the V2p XPS binding energies for different vanadium oxidation states (V^{5+} to V^{0+}). *J. Electron Spectros. Relat. Phenomena* **2004**, *135*, 167–175.

(20) Demeter, M.; Neumann, M.; Reichelt, W. Mixed-valence vanadium oxides studied by XPS. *Surf. Sci.* **2000**, *454-456*, 41–44.

(21) Moulder, J. F.; Stickle, W. F.; Sobol, P. E.; Bomben, K. D., *Handbook of X-ray photoelectron spectroscopy: a reference book of standard spectra for identification and interpretation of XPS data*; Physical Electronics: Eden Prairie MN, 1992, p 261.

Chapter 4

Anisotropic $BiVO_4$ Heterostructures

4.1 Introduction

As mentioned in the main Introduction in Section 2.3.1, photodeposition is an effective way to create dissymmetric heterostructured powders. The scientific articles published by Li et al. are essentially groundbreaking, as they showed that through photodeposition, oxide and reduction cocatalysts could be loaded onto different facets of a $\{010\}/\{110\}$ dual facet exposed $BiVO_4$ microcrystalline powder.[1,2] Furthermore, they found that the creation of heterostructures with a single cocatalyst on a particular facet, like $BiVO_4$/Pt, $BiVO_4/MnO_x$, $BiVO_4/Co_3O_4$ could boost the water oxidation performance of bare $BiVO_4$ and that the creation of heterostructures with both a reduction and oxidation cocatalyst on different facets, like $BiVO_4$/Pt/Co_3O_4, yielded an even higher water oxidation performance. We wanted to first reproduce the $BiVO_4$/Pt, $BiVO_4$/Ag and $BiVO_4/Co_3O_4$ heterostructures to gain knowledge on how to create these kind of structures, so that we could create similar heterostructures with the other photoabsorber studied in this work, $CuFeO_2$. Additionally, a new heterostructured $BiVO_4$ powder was prepared through photodeposition of NiO_xOH_y. NiO_xOH_y was chosen, because nickel based contact materials have already shown their merit for water photo-oxidation. Mccrory et al. showed that Ni based compounds in a basic medium have electrocatalytic oxygen evolution overpotentials which are among the lowest and on par with state of the art noble metal catalysts.[3] Furthermore, nickel based compounds have already shown to increase the water oxidation performance of $BiVO_4$ thin films, whereby the nickel contact layer was deposited through photodeposition or electrodeposition.[4–6]

In this Chapter, first, the experimental parameter optimization for the $BiVO_4$ synthesis and its twofold upscaling will be detailed, whereby the effect of each parameter on the morphology and crystalline phase composition will be shown. Next, the structural and chemical properties of the $BiVO_4$/Pt, $BiVO_4$/Ag, $BiVO_4/CoO_xOH_y$ and the novel $BiVO_4/NiO_xOH_y$ heterostructured powders will be described, which were manufactured through photodeposition. Herein, the emphasis is laid on analysis techniques, which helped to demonstrate whether the metal(oxide)

deposits that adhered onto the $BiVO_4$ microcrystalline particles exhibit a certain regioselectivity. Finally, the newly synthesized $BiVO_4/NiO_xOH_y$ heterostructure will be compared to the other heterostructured $BiVO_4$ powders with regards to its ability for dye degradation and sacrificial water oxidation.

4.2 Synthesis of monoclinic $BiVO_4$ microcrystals

To be able to explore new anisotropic $BiVO_4$ heterostructures, truncated bipyramidal $BiVO_4$ with exposed {010} and {110} crystal facets had to be synthesised in large quantities first. According to literature several synthesis procedures are available to obtain the truncated bipyramidal morphology (see Table 4.1). However, none of the published synthesis procedures, we tried, resulted straightforwardly in monodisperse monoclinic $BiVO_4$ powders with the truncated bipyramidal morphology. This specific morphology could only be obtained after tuning several reaction parameters. In Section 3.1.2 the optimised synthesis procedure is explained in detail and in what follows the way towards the optimised synthesis conditions is described.

Most published synthesis procedures make use of $Bi(NO_3)_3$ and NH_4VO_3 as the bismuth and vanadium precursor, respectively, whereby stoichiometric amounts of both precursors are first dissolved and then thoroughly mixed to form an aqueous reaction mixture that is subsequently subjected to a hydrothermal treatment, after which monoclinic $BiVO_4$ microcrystals with a truncated bipyramidal shape are obtained. As can be seen in Table 4.1, there seems to be some flexibility in the reaction parameters since the presence of a surfactant is not necessarily required, the reaction mixture which is put in the autoclave can be acidic or neutral, the autoclave temperature can be varied from 160 °C — 200 °C and even an autoclave treatment does not appear to be compulsory.

For a start, the synthesis procedure mentioned in the first reference in Table 4.1 was tried, thus, with sodium dodecyl sulphate (SDS) as surfactant, with a reaction mixture brought to pH 7, at an autoclave temperature of 180 °C and with an autoclave time of 24 h.[7] These parameters will be referred to as the baseline parameters throughout this Section. Through this synthesis procedure, monoclinic $BiVO_4$ was obtained, as evidenced by the X-ray powder diffractogram in Figure 4.1a. Indeed, the diffraction pattern corresponds exclusively to monoclinic $BiVO_4$.[16] However, the morphology of the obtained powder seems quite irregular with no indication of truncated bipyramidal shaped crystals (Figure 4.1b). Therefore, a series of syntheses were performed, whereby the parameters of the baseline experiment were varied one by one to figure out which ones affected the $BiVO_4$ morphology. Specifically, the pH, autoclave temperature, autoclave time, autoclave stirring and presence of surfactant was changed, since previous research pointed out that these parameters had an influence on the appearance of the $BiVO_4$ particles.[17,18]

In Figure 4.2 the recorded secondary electron images show the effect of the pH on the morphology. For a pH between 3 and 7, the resulting $BiVO_4$ particles have mostly irregular shapes

Table 4.1: Reaction parameters for the synthesis of monoclinic $BiVO_4$ powders with a truncated bipyramidal morphology, including the literature references to the synthesis procedures.

Reaction mixture				Autoclave		Reference
Bi precursor	V precursor	Surfactant	pH	T (°C)	t (h)	
$Bi(NO_3)_3.5H_2O$	NH_4VO_3	SDS	7	180	24	[7]
$Bi(NO_3)_3.5H_2O$	NH_4VO_3	EDTA	7	180	24	[8]
$Bi(NO_3)_3.5H_2O$	NH_4VO_3	-	2	200	24	[2]
$Bi(NO_3)_3.5H_2O$	NH_4VO_3	-	2	200	24	[9]
$Bi(NO_3)_3.5H_2O$	NH_4VO_3	-	2	200	24	[1]
$Bi(NO_3)_3.5H_2O$	NH_4VO_3	-	2	180	24	[10]
$Bi(NO_3)_3.5H_2O$	NH_4VO_3	-	0.6	180	24	[11]
$Bi(NO_3)_3.5H_2O$	NH_4VO_3	$TiCl_3$	2	180	24	[12]
$BiCl_3$	NH_4VO_3	ethanolamine	6.15	160	12	[13]
Bi_2O_3	V_2O_5	-	0	-	-	[14]
Bi_2O_3	V_2O_5	-	0	-	-	[15]

EDTA: ethylenediaminetetraacetic acid

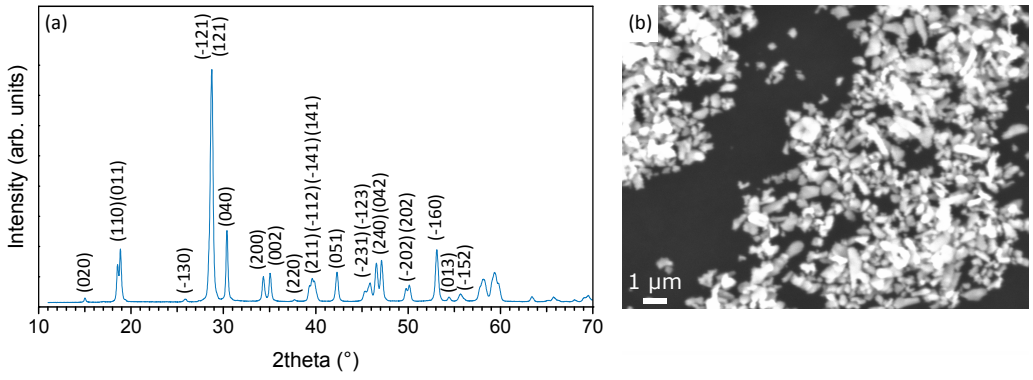

Figure 4.1: (a) Powder X-ray diffractogram and (b) secondary electron image of monoclinic $BiVO_4$ with irregular morphology synthesized according to the baseline parameters (pH 7, SDS, $T_{autoclave}$: 180 °C and $t_{autoclave}$: 24 h).

with no clear indication of exposed crystalline facets, whereas a pH of 9 resulted in the formation of dendritic $BiVO_4$ crystals. Remarkably, only when the synthesis was carried out at a pH of 1.5, particles with a defined polyhedron shape were obtained. The low resolution of the used SEM apparatus, however, hinders the determination of the exact shape of the polyhedrons. Hence, high resolution FESEM had to be performed. The high resolution secondary electron image in Figure 4.3 reveals that the exact shape of the polyhedrons is in fact the desired truncated bipyramidal shape. Also, the dendritic shape of the powder prepared at pH 9 can be more clearly observed in the FESEM image. For all tested pH, no other crystalline phases besides monoclinic $BiVO_4$ can be observed in the powder diffractograms (Figure 4.2).

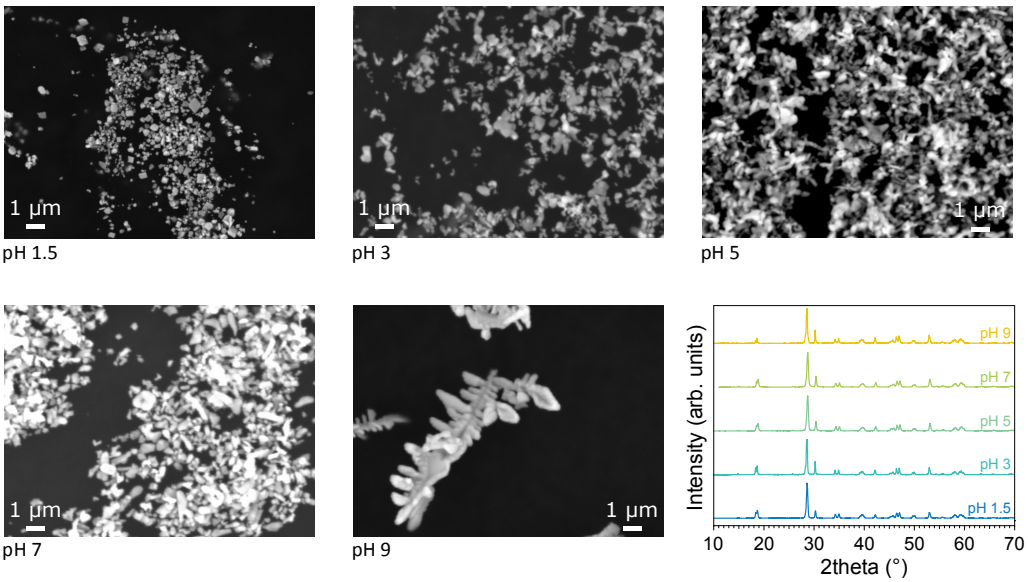

Figure 4.2: Secondary electron images and powder X-ray diffractograms for $BiVO_4$ synthesized at different pH.

Secondly, the autoclave temperature was varied, while a reaction mixture pH of 7 was maintained (Figure 4.4). No big differences in morphology can be seen in the secondary electron images for autoclave reaction temperatures between 180 °C and 220 °C. However, the {010} reflections in the X-ray diffractogram of the powder prepared at an autoclave temperature of 220 °C seem to be relatively more intense, thus, indicating that the particles are overall more oriented along the [010] direction.

The SEM images in Figure 4.5 show that the autoclave reaction time had a pronounced effect on the $BiVO_4$ morphology, since a higher reaction time led to particles with a more defined shape. The TEM image in Figure 4.6 confirms the truncated bipyramidal shape of the $BiVO_4$ microcrystalline powder obtained after an autoclave reaction time of 64 h. No remarkable differences can be seen in the diffractograms of the powders synthesized at different autoclave reaction times.

The secondary electron images in Figure 4.7 show that for $BiVO_4$ syntheses carried out in the absence of SDS, drastically different powder morphologies were obtained, with holey particles

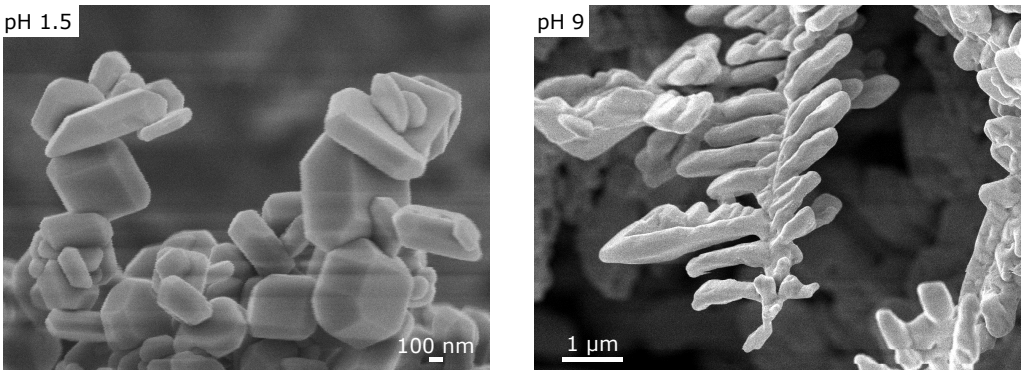

Figure 4.3: FESEM images of $BiVO_4$ prepared at pH 1.5 and pH 9.

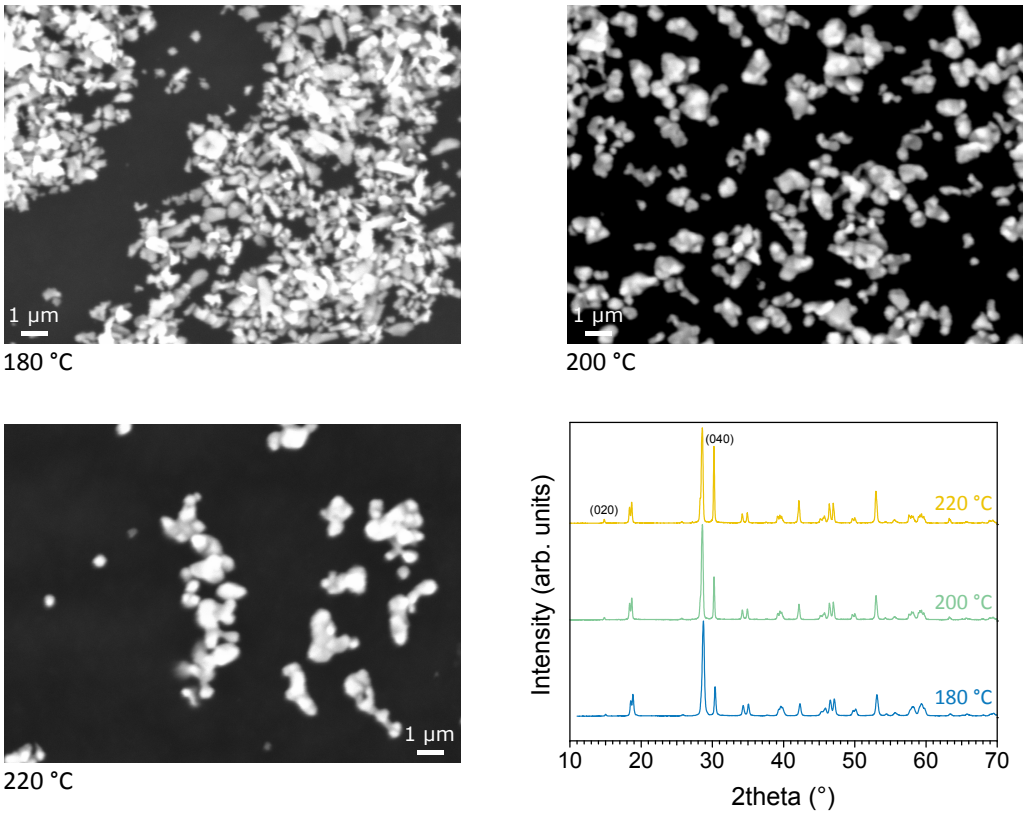

Figure 4.4: Secondary electron images and powder X-ray diffractograms for $BiVO_4$ synthesized at different autoclave temperatures.

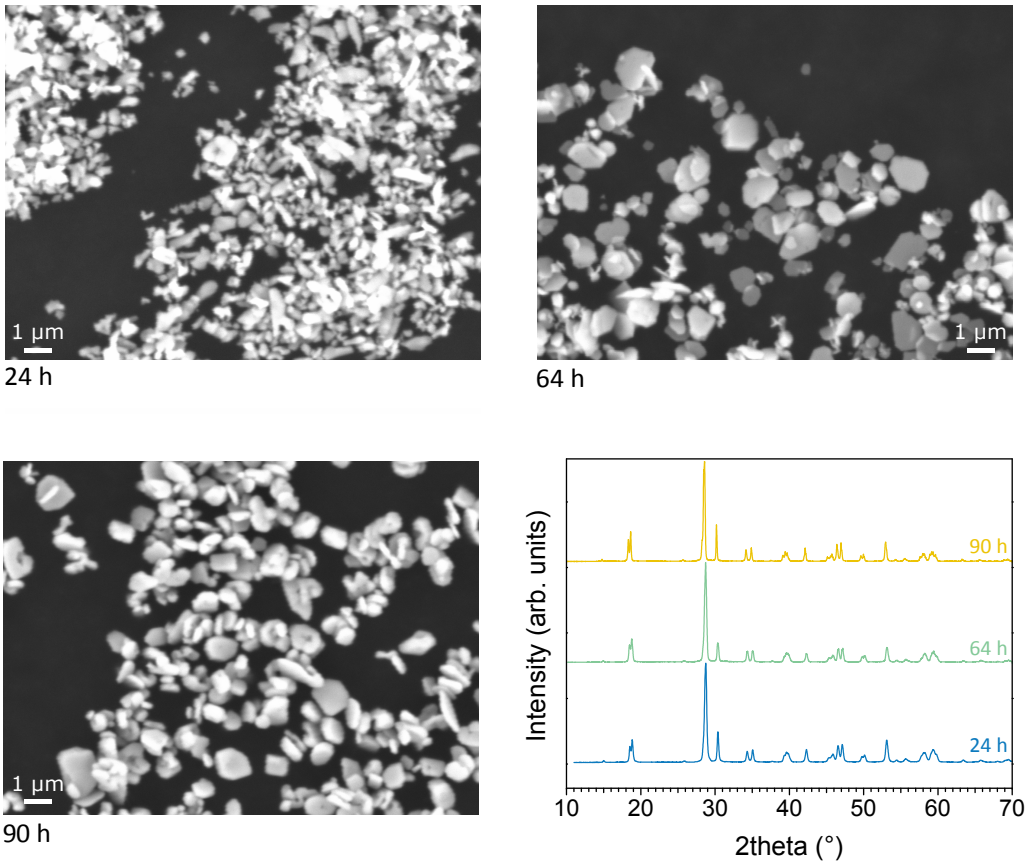

Figure 4.5: Secondary electron images and powder X-ray diffractograms for $BiVO_4$ synthesized with different autoclave reaction times.

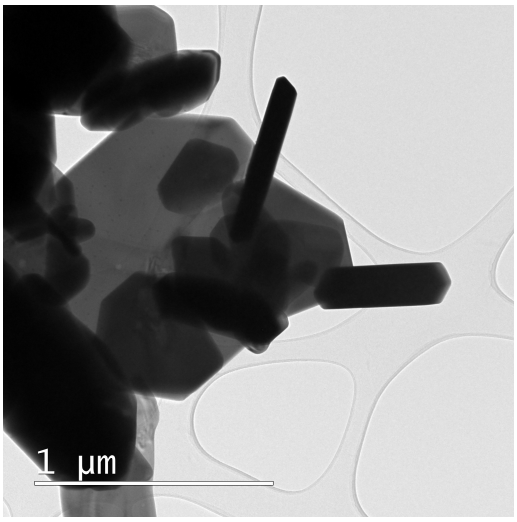

Figure 4.6: TEM image of $BiVO_4$ prepared with an autoclave reaction time of 64 h.

for a synthesis performed at pH 7 and aggregations of needle like crystals for a synthesis accomplished at pH 2. Additionally, the powder diffractogram reflections, for the powder prepared at pH 2, are much broader compared to those of the diffractograms shown previously. According to the Scherrer equation, this could be an indication that the crystallites in the powder have a smaller size.[19] The Scherrer equation can, however, not be reliably applied here to estimate the crystallite size because the crystallites are needle like with a diameter in the order of several hundreds of nm, whereas the validity of the Scherrer equation is limited to crystallites in the order of 1 — 100 nm.[19]

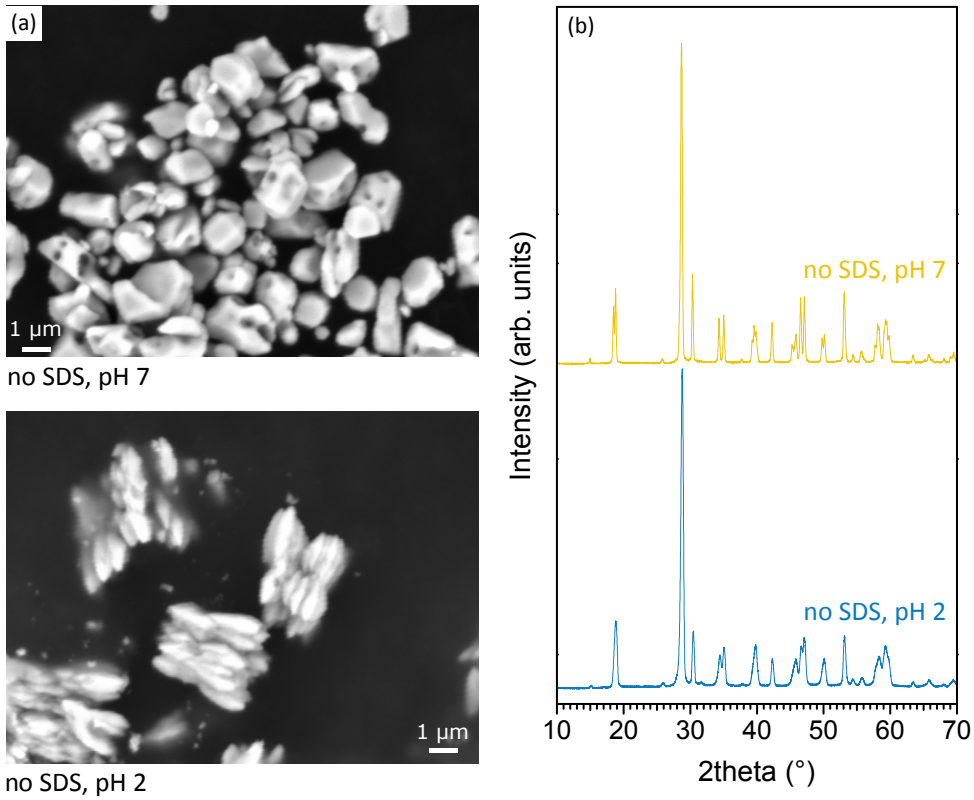

Figure 4.7: (a) Secondary electron images and (b) powder X-ray diffractograms for $BiVO_4$ synthesized without SDS at different pH.

All in all, bringing the reaction mixture pH to pH 1.5 and increasing the autoclave reaction time to 64 h seem to be adequate measures to obtain $BiVO_4$ with a truncated bipyramidal morphology. However, to ensure that those measures lead systematically to truncated bipyramidal $BiVO_4$ particles, several reproductions of those synthesis conditions had to be performed. Therefore, the procedures with a pH of 1.5 and an 64 h autoclave time reaction conditions were repeated several times. However, only the adjustment of the pH to pH 1.5 led to reproducible results over multiple syntheses. As can be seen in Figure 4.8, all powders synthesized at pH 1.5, are purely monoclinic $BiVO_4$ and consist of particles with clearly exposed crystalline facets.

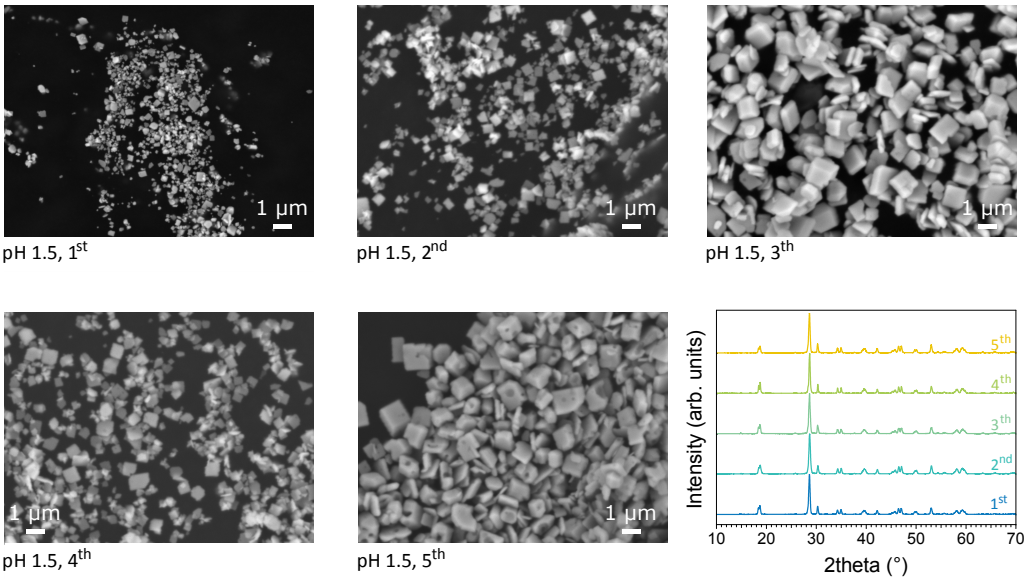

Figure 4.8: Secondary electron images and powder X-ray diffractograms for 5 $BiVO_4$ syntheses at pH 1.5.

Next, the synthesis procedure had to be upscaled, because only ± 300 mg of $BiVO_4$ powder was obtained after each synthesis, while we estimated that a batch of 10 g was needed to perform all the planned photodeposition experiments. Multiplying the amount of every reactant by two, however, did not result in the preferred particle characteristics any more. Indeed, Figure 4.9 shows that the powder looks to be more aggregated and irregularly shaped. Non-aggregated homogeneously shaped $BiVO_4$ particles could be obtained through two modifications to the synthesis procedure; namely by multiplying the amount of SDS by three instead of two and by stirring the reaction mixture during the hydrothermal treatment in the autoclave.

The fully optimised $BiVO_4$ synthesis procedure yields ± 600 mg and was repeated 17 times to establish a 10 g batch of truncated bipyramidal $BiVO_4$ for the photodeposition experiments.

4.2.1 Photocatalysis

The observation that different unexpected morphologies were obtained during the truncated bipyramidal $BiVO_4$ experimental parameter optimization was welcomed to explore the characteristics and oxidation performance of several morphologies further. In particular, the irregular, dendritic and truncated bipyramidal shaped $BiVO_4$ powders were studied further, and compared with each other and to a commercial $BiVO_4$ powder purchased from Alfa Aesar.

First, Rietveld refinement was carried out to determine whether other crystalline phases besides monoclinic $BiVO_4$ are present in any of the samples. However, due to the similarity of the diffractograms of tetragonal and monoclinic clinobisvanite $BiVO_4$ phases[20] new diffractograms were recorded with a Mo K-alpha 1 X-ray source, which has only one X-ray line compared to

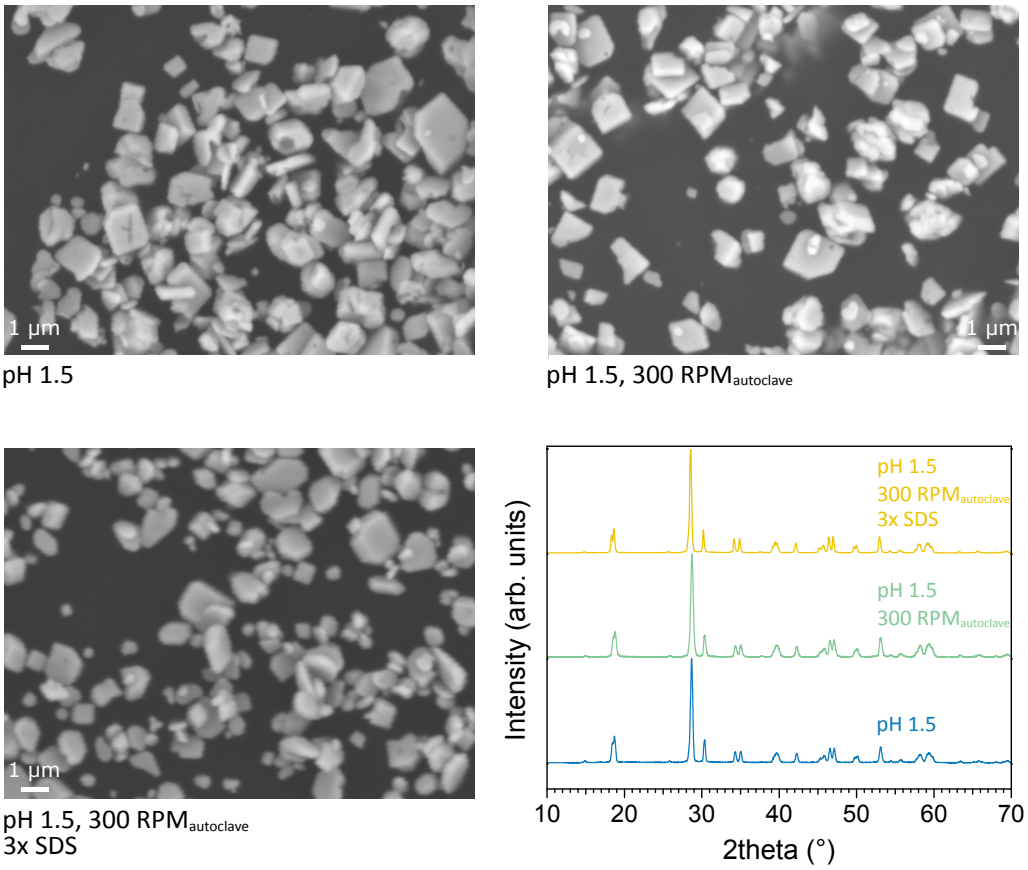

Figure 4.9: Secondary electron images and powder X-ray diffractograms for 2x upscaled $BiVO_4$ syntheses with different modifications to the baseline parameters.

the two X-ray lines in a standard Cu K-alpha X-ray source. As a result, diffractograms with an overall lower peak broadening and, thus, a higher resolution could be obtained. On these newly acquired diffractograms, Rietveld refinement was performed. As is shown in Figure 4.10, the presence of tetragonal $BiVO_4$ for the truncated bipyramidal shaped and irregular shaped powders seems unlikely, due to the absence of any reflections characteristic for tetragonal $BiVO_4$ and the Rietveld refinement suggesting a presence below 5% for tetragonal $BiVO_4$. In contrast, for the commercial $BiVO_4$ sample, reflections of tetragonal and orthorhombic bismuth vanadate phases can be easily seen in Figure 4.10. The Rietveld refinement suggested that the commercial $BiVO_4$ powder seemingly contains 5% of the orthorhombic bismuth vanadate phase and 15% of the tetragonal bismuth vanadate phase, however the real share of the tetragonal phase will very likely be lower due to the mismatch of the Rietveld fit with the measured diffractogram.

In Figure 4.11 the morphology of the commercial $BiVO_4$ powder is shown. A very high size dispersity can be noticed with particles having a size between < 1 µm and 50 µm. Additionally, the powder morphology seems to be completely irregular, as no distinct shapes can be recognized.

Diffuse reflectance spectroscopy was performed to determine the direct optical band gap of

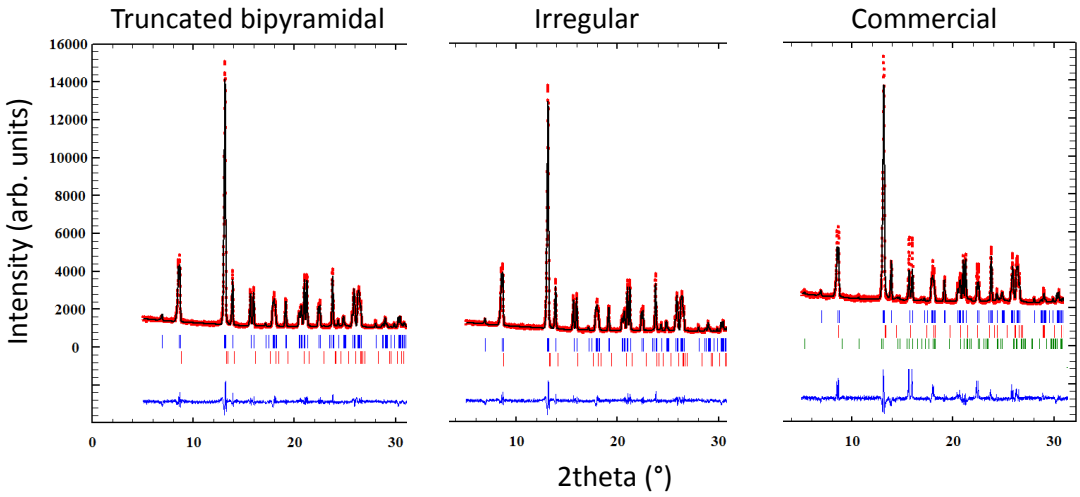

Figure 4.10: Rietveld refinement on truncated bipyramidal $BiVO_4$, irregular $BiVO_4$ and commercial $BiVO_4$ with the measured diffractogram in black, the fit in red and the difference in blue. In the refinement monoclinic clinobisvanite (blue, JCPDS: 75-7867), tetragonal clinobisvanite (red, JCPDS: 78-1534) and orthorhombic $Bi_2VO_{5.5}$ (green, JCPDS: 88-870) were considered.

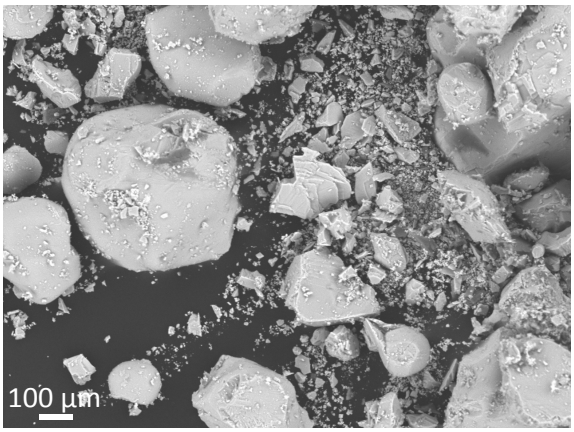

Figure 4.11: Secondary electron image of commercial $BiVO_4$.

the different powders (Figure 4.12). As can be seen in the Tauc plot $[F(R)h\nu]^2$ vs $h\nu$, the absorption onset lies around 2.5 eV for the truncated bipyramidal and irregular shaped $BiVO_4$, which agrees well to the 2.4 — 2.5 eV direct band gap that others have found for undoped monoclinic $BiVO_4$.[16,21,22] For the commercial $BiVO_4$ powder, the absorption onset lies lower, at 2.35 eV, which can be due to the presence of the $Bi_2VO_{5.5}$ phase, as detected during the Rietveld refinement analysis. Indeed, an optical band gap of about 1.9 eV was previously determined for $Bi_2VO_{5.5}$.[23]

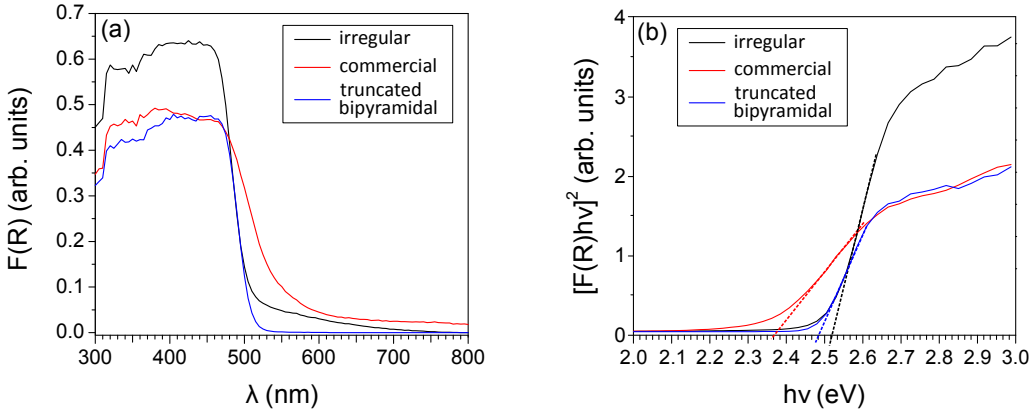

Figure 4.12: (a) UV-vis diffuse reflectance spectra and (b) Tauc plots for $BiVO_4$ with different morphologies.

X-ray photoelectron (XP) spectra were recorded to determine any differences in the chemical characteristics of the $BiVO_4$ powders. The survey spectra in Figure 4.13 do not show any differences between the different morphologies. All signals correspond to bismuth, vanadium, oxygen, indium or carbon core level photoelectrons. The indium photoelectrons originate from the indium foil onto which the powders were pressed, while the carbon related signals are typical for samples that have been in contact to air. Additionally, high resolution Bi4f, $V2p_{3/2}$ and O1s core level spectra were recorded (Figure 4.14). Due to the relatively low electronic conductivity of $BiVO_4$, the core level spectra of the $BiVO_4$ powder samples show small signs of inhomogeneous surface charging, like the small bump at a binding energy of 162 eV in the Bi4f spectrum.[24] The inhomogeneous sample charging during the XPS measurements, however, does not prevent the determination of the binding energies in this case. The $Bi4f_{7/2}$ core level binding energy is situated between 159.0 eV and 159.3 eV, which matches to Bi^{3+} in $BiVO_4$ and the $V2p_{3/2}$ core level position between 516.7 and 517.0 eV is typical for V^{5+} in $BiVO_4$.[25] The 0.3 eV difference is possibly related to electronic shifts due to different doping levels. Additional oxidation states cannot be observed in the $V2p_{3/2}$ and the $Bi4f_{7/2}$ spectra, because inhomogeneous surface charging induces line broadening and extra features at higher binding energies, which interfere with potential minority signals belonging to other elemental oxidation states or different local chemical environments. In the O1s spectrum two signals can be seen at about 530 eV and at about 532 eV, which correspond to metal oxides and alcohol+carbonyl groups, respectively.[26] The hydroxyl+carbonyl signal is due to the sample being prepared under ambient conditions.

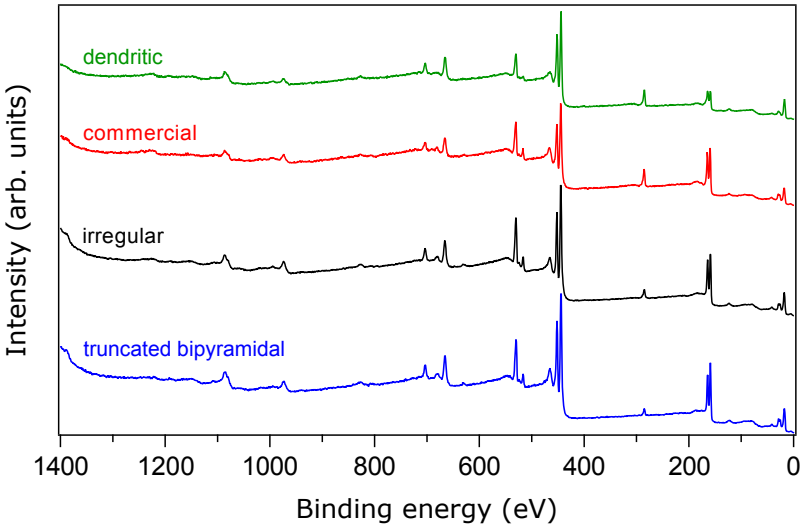

Figure 4.13: Survey X-ray photoelectron (XP) spectra for $BiVO_4$ with truncated bipyramidal, irregular, commercial and dendritic morphology.

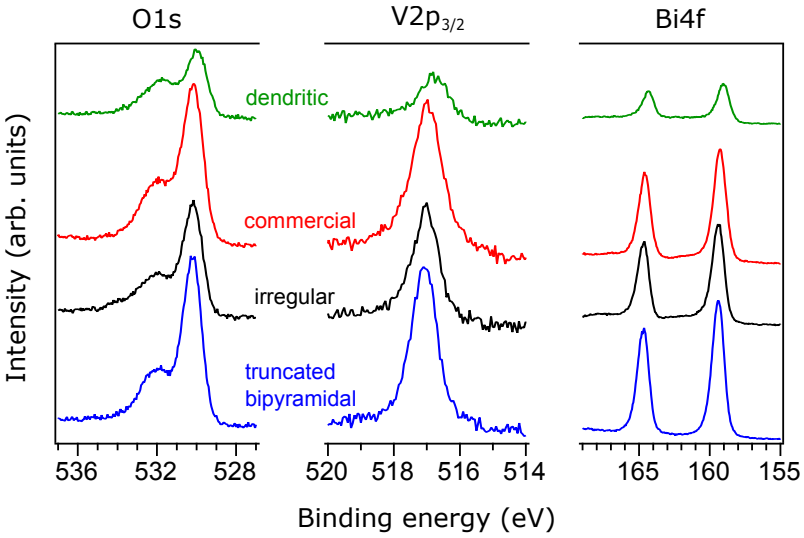

Figure 4.14: High resolution Bi4f, $V2p_{3/2}$ and O1s core level XP spectra for $BiVO_4$ with truncated bipyramidal, irregular, commercial and dendritic morphology.

Finally, the photocatalytic oxidation performance of the differently shaped $BiVO_4$ powders was tested by evaluating at which rate the in water dispersed powders could degrade a dissolved organic dye in the presence of light. The whole dye degradation procedure is explained in detail in Section 3.4.5.1. Figure 4.15 shows how the absorbance of rhodamine B, the dye used in this work, decreases over time during a dye degradation experiment. Due to the dye absorbance being proportional to the concentration of the unreacted dye, the dye degradation efficiency can be determined by registering how the absorbance of the peak maximum, here at 554 nm, changes over time (Figure 4.16). Without light or in the absence of $BiVO_4$, no decrease in absorbance of the dye was noticed, seemingly confirming the photocatalytic nature of the dye degradation process. Remarkably, the irregular shaped $BiVO_4$ powder had the best rhodamine B degradation efficiency, because only 10% of the original absorbance was left after a degradation time of 120 min. Worse efficiencies were obtained with the other powders. Over the photodegradation time span of 120 min the drop in dye absorbance (at 554 nm) for dendritic, commercial and truncated bipyramidal $BiVO_4$ amounted on average to 57%, 49% and 46%, respectively.

The photodegradation of Rhd B through $BiVO_4$ is considered to be a first order chemical reaction,[27] which should follow the first order rate equation:

$$\ln\left(\frac{A_t}{A_0}\right) = kt \tag{4.1}$$

with t being the degradation time and k corresponding to the first order rate constant. The first order rate constant can then be determined from the slope of a $\ln\left(\frac{A_t}{A_0}\right)$ vs t plot. These plots and all first order rate constants are shown in Figure 4.16. The first order rate model seems to fit more or less, as the linear regression yield R^2 values in the range of $0.96 - 0.99$. Especially, the irregular shaped $BiVO_4$ powder seems to have a high first order rate constant.

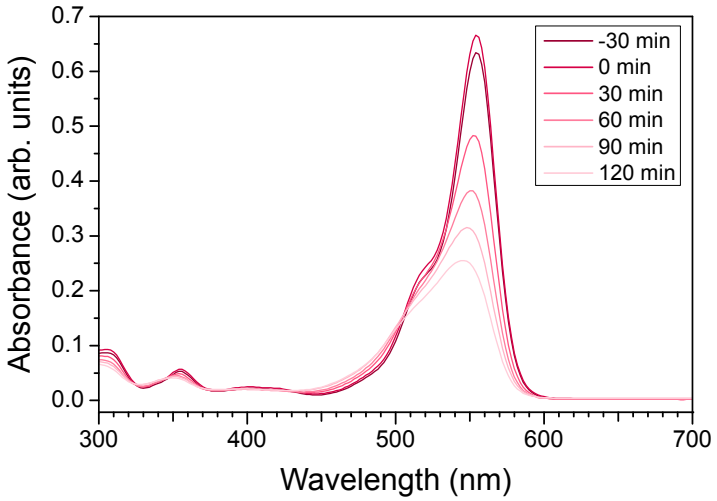

Figure 4.15: Rhd B degradation profile for dendritic $BiVO_4$. The reaction mixture was stirred for 30 min in dark, so that 0 min is the point in time at which the light was switched on.

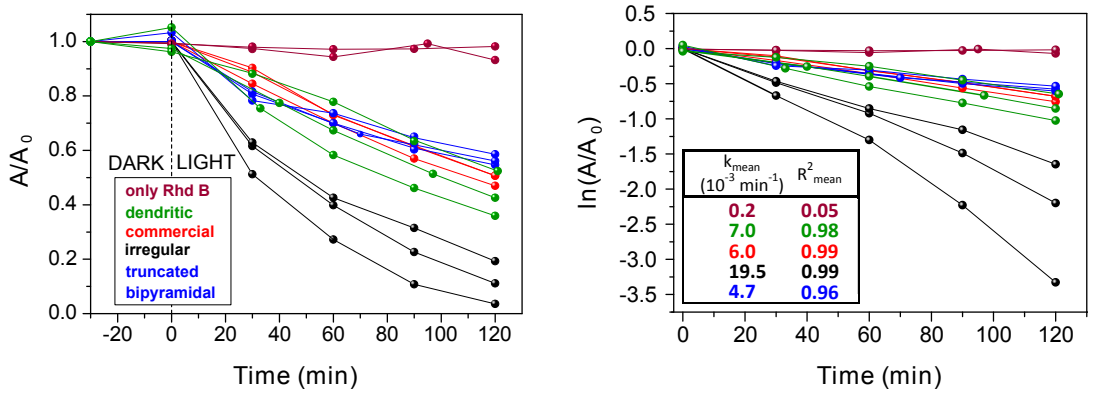

Figure 4.16: Photocatalytic degradation of Rhd B for $BiVO_4$ with different morphologies. Left: Absorbance (at 554 nm) and right: natural logarithm of absorbance versus the degradation time with light switched on at 0 min. The mean first order rate constants k_{mean} and mean R^2 linear fitting parameter are denoted in the graph.

Thus, one could argue whether the truncated bipyramidal morphology is the best $BiVO_4$ morphology to use for oxygen evolution. However, the dye degradation efficiency does not always correspond to the water splitting performance,[2,28] most likely due to a difference in reaction mechanisms.

4.3 Anisotropic photodeposition on $BiVO_4$

After synthesizing a batch of 10 g of coexposed $\{010\}/\{110\}$ truncated bipyramidal $BiVO_4$ powder, photodeposition experiments were carried out to test whether new $BiVO_4$ based anisotropic heterostructures could be synthesised. The general photodeposition procedure is disclosed in Section 3.1.4 and the experimental details for the photodeposition experiments can be found in Table 4.2.

4.3.1 $BiVO_4$/Ag

The photoreduction of silver nitrate to metallic silver is a standard test to assess whether a certain light absorber is qualified for the photodeposition process, because the light induced silver reduction is a straightforward reaction that only involves the transfer of one electron:

$$AgNO_3(aq) + e^- \longrightarrow Ag(s) + NO_3^-(aq)$$

Also, due to the relatively large size and cubic morphology, silver deposits are easy to distinguish in FESEM.[29,30] The facet-selectivity of the silver photodeposition on truncated bipyramidal $BiVO_4$ has been tested before and was found to result in the selective deposition of silver onto the $\{010\}$ facets,[1] which are the facets on which, after light absorption, electrons reportedly accumulate.[31]

Table 4.2: Experimental details for the $BiVO_4$ based heterostructured powders fabricated through photodeposition.

Heterostructure	m_{BiVO_4} (mg)	Precursor	Hole/electron scavenger	pH	V (mL)	$t_{illum.}$ (h)
$BiVO_4$/Ag	100	$AgNO_3$	MeOH (25 vol%)	7	20	5
$BiVO_4$/Pt	100	H_2PtCl_6	-	Various	20	4.5
$BiVO_4/CoO_xOH_y$	100	$Co(NO_3)_2$	$NaIO_3$ (0.01 mol/L)	7	20	3
$BiVO_4/NiO_xOH_y$	100	$NiCl_2$	-	9.2 (KBi buffer)	20	2
$BiVO_4/RuO_x$	100	$Ru(acac)_3$	$FeCl_3$	-	20 (THF/ CH_3COOH)	3

$t_{illum.}$: solar simulator illumination time. MeOH: methanol, KBi: potassium borate; THF: tetrahydrofuran, acac: acetylacetonate.

Herein, the photodeposition of silver was tried out to verify whether our synthesized truncated bipyramidal $BiVO_4$ particles were susceptible for photodeposition and whether silver would again be selectively deposited on the {010} facets. As can be seen in the FESEM images in Figure 4.17 silver deposits indeed seem to be preferentially situated on the {010} facets of the $BiVO_4$ particles, whereby the size of the deposits ranges from a hundred to a few hundred nanometre

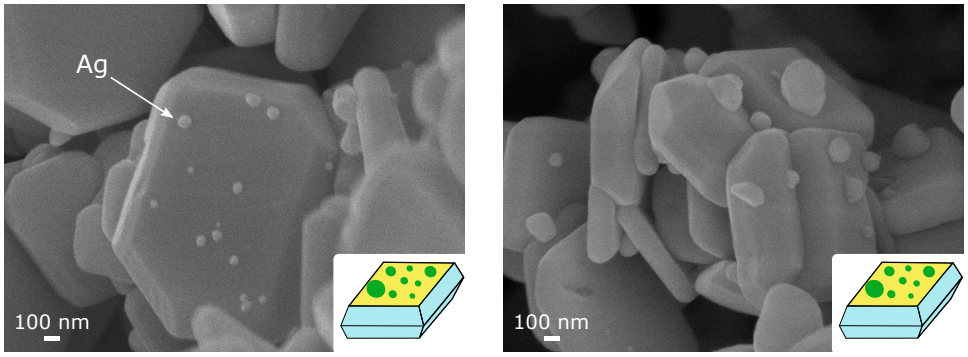

Figure 4.17: FESEM images of $BiVO_4$/Ag (10 wt%).

EDS mapping was performed to examine the chemical nature and the spatial distribution of the deposits. EDS was feasible, because the relatively large size of the apparent silver deposits allowed the accumulation of enough silver characteristic X-rays. Moreover, as explained in Section 3.4.3.1, EDS has a limited lateral resolution through which only deposits with a size of 50 nm or more can be visualized in EDS elemental maps. The EDS elemental maps in Figure 4.18 confirm the realization of a heterostructured Ag/$BiVO_4$ powder. However, the facet-selectivity of the Ag deposition can not be distinguished easily in the EDS maps, because the morphology of the $BiVO_4$ particles cannot be recognized as clearly as in Figure 4.17, because the electron beam parameters needed for EDS analysis are suboptimal for secondary electron image registration.

Some deposits that can be seen in Figure 4.18a do not show up in the silver EDS map, which is due to the shadowing of the characteristic silver X-rays by the $BiVO_4$ particles.

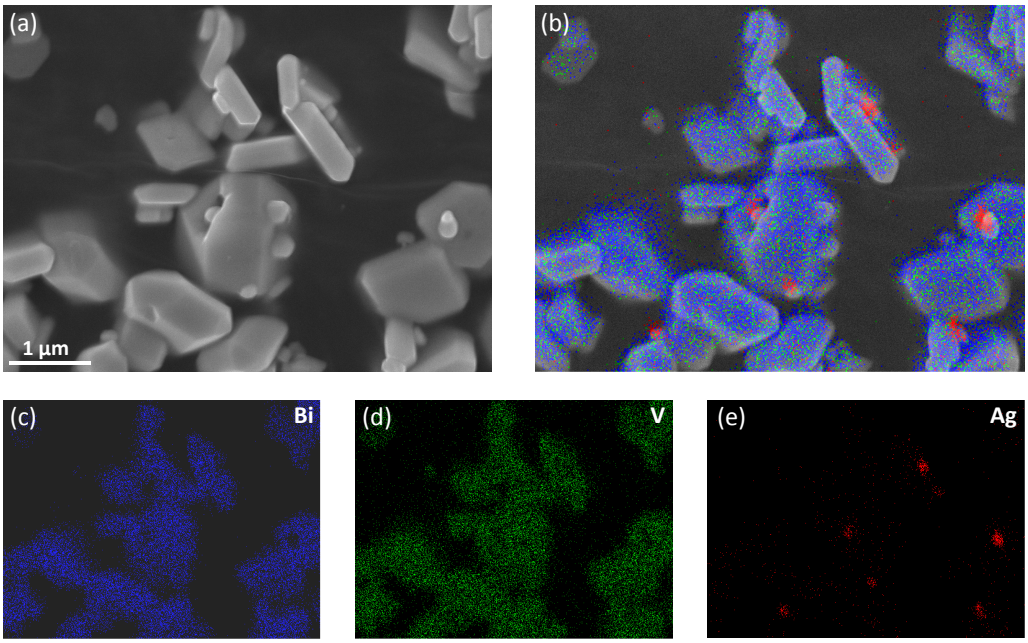

Figure 4.18: (a) FESEM image of $BiVO_4$/Ag (10 wt%) and EDS elemental maps: (b) composite, (c) Bi, (d) V and (e) Ag.

XPS was used to determine the oxidation state of the silver deposit (Figure 4.19). Here, the sample does not seem to have suffered noticeably from inhomogeneous surface charging, since the line shapes of the Bi4f and V2$p_{3/2}$ core level spectra appear to be quite symmetric and because no extra signals besides those belonging to Bi^{3+} and V^{5+} can be observed. In the Ag3d spectrum two signals can be seen with binding energy maxima situated at 368.3 eV and 374.3 eV, indicative of Ag3$d_{5/2}$ and Ag3$d_{3/2}$, respectively. Those binding energies are characteristic for metallic silver,[26] confirming that the photodeposition of silver follows a reduction process. Please also take a look at Section 2.4 where all the main core level spectra, which can be found in this work, are described.

4.3.2 $BiVO_4$/Pt

The next material which was used to coat the $BiVO_4$ particles through photodeposition was platinum. Overall, platinum is considered to be one of the best water reduction electrocatalysts[3] and just like silver, platinum has been found to be selectively deposited onto the {010} facets of $BiVO_4$ through the photodeposition method.[1] The Pt deposits were, however, considerably smaller than the Ag deposits, more in the range of 5 — 10 nm, which make them slightly more complicated to spot in FESEM images. An additional complication is the use of the acidic H_2PtCl_6 precursor for Pt photodeposition,[1,32,33] because the molar concentration of this precursor and, thus, the Pt

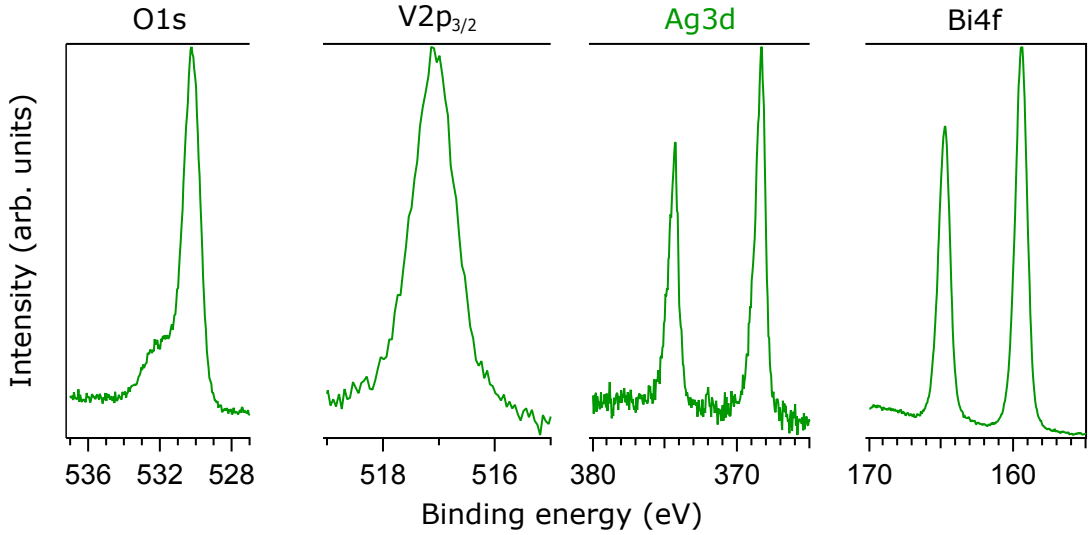

Figure 4.19: Ag3d, Bi4f, $V2p_{3/2}$, O1s core level XP spectra of $BiVO_4$/Ag (10 wt%).

weight percentage that is aimed for, influences the pH of the reaction mixture. These pH differences can have an impact on the morphology and oxidation state of the platinum deposit, as was shown previously for the pH controlled photodeposition of Pt onto TiO_2 single crystals.[34] In our experiments, a reaction mixture pH of approximately 2.5 and 3.6 were measured for the photodeposition experiments where a 10 wt% Pt and 1 wt% Pt, respectively, were intendedly deposited. In Figure 4.20 the effect of different pHs and Pt wt% can be seen. At a pH of 2.5 the deposited Pt particles seem to be scarce and have sizes of about 100 nm. Additionally, the $BiVO_4$ particles have lost part of their shape, which is most likely due to the chemical instability of $BiVO_4$ in an acidic environment.[35] Therefore, an additional experiment was performed at a higher pH, namely at pH 5.8 through the adjustment of the pH with NaOH. The deposit seems to be considerably smaller and more spread out over the $BiVO_4$ particles. Facet-selectivity could not be clearly observed, but the deposited particles on the $\{010\}$ facets seem to be somewhat larger. For the 1 wt% Pt deposit, the platinum particles cannot be easily distinguished in the FESEM images due to the relatively small size, just a few nm, and the low contrast of the images. However, the Pt particles seem to have selectively accumulated onto the $\{010\}$ exposed surfaces.

EDS could not be used any more to study the spatial distribution of the deposited Pt particles, because of the platinum particles being smaller than the 50 nm lateral resolution of EDS. Instead, scanning Auger microscopy (SAM) was tried, because of the higher surface sensitivity and the slightly better lateral resolution, as explained in Section 3.4.3.1. There were, however, a few difficulties to collect elemental maps with SAM. The possibility of obtaining elemental maps with a higher lateral resolution compared to EDS is an advantage, which in consequence require more points to be scanned in order to acquire a complete elemental map of a certain area. Combined with the long acquisition times per measurement point, the scan time to obtain a complete elemental map of a certain area with SAM is substantially longer than with EDS.

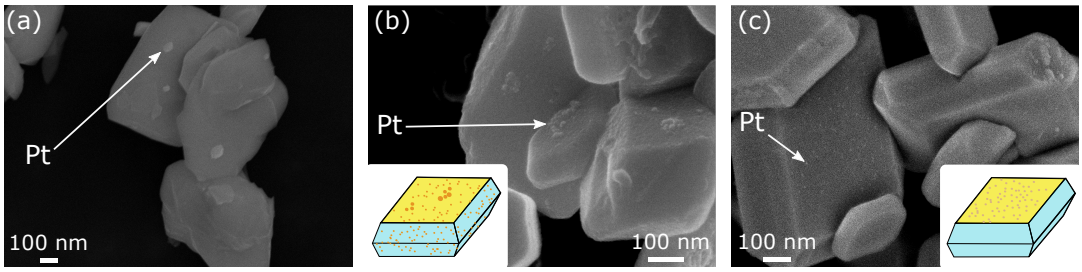

Figure 4.20: FESEM images of (a) $BiVO_4$/Pt (10 wt%)-pH 2.5, (b) $BiVO_4$/Pt (10 wt%)-pH 5.8 and (c) $BiVO_4$/Pt (1 wt%)-pH 3.6.

Long scan times are, however, problematic for the poor electron conducting micron-sized $BiVO_4$ particles, because they tend to charge during the exposure to the primary electron beam. This charging phenomenon caused image drift during map acquisition, and for scan times exceeding 30 minutes, often led to the (partial) degradation of the $BiVO_4$ particles. Therefore, the total acquisition time had to be drastically reduced, which was done here by selecting just a few measurement zones, which were not scanned but measured as a whole. Specifically, zones across the exposed {010} and {110} facets were chosen. On these zones a SAM sputter depth profile was acquired. However, due to the argon ions approaching from a certain direction not all regions were sputtered in the same proportion. The results of the SAM acquisition of the $BiVO_4$/Pt(10 wt%) sample prepared at a pH of 5.8 can be seen in Figure 4.21. Approximately, the same Pt N_7VV Auger signal intensity is obtained for measurement zones on both the {010} and {110} facets, meaning that the Pt photodeposition in this case was not selective to a certain crystalline facet. This observation agrees well with the FESEM images shown above. The Pt N_7VV Auger signal intensity decreases in different proportion for different zones which confirms the orientation dependence of the sputtering process. The $BiVO_4$/Pt(1 wt%) sample prepared at a pH of 3.6 was not selected for the SAM analysis, because we perceived the deposited platinum particles as too small with respect to the lateral resolution of the SAM technique. Therefore, we reasoned that a platinum elemental map would not have been able to show the exact spatial distribution of platinum. However, zone measurements would have been able to obtain information on the facet-selectivity of the Pt deposits. Unfortunately, the sample selection process was made before the problems with $BiVO_4$ SAM mapping were observed and a switch to zone measurements was made.

High resolution XP core level spectra for several heterostructured $BiVO_4$/Pt samples are shown in Figure 4.22. Considering all Pt4f spectra, three different Pt4f doublets can be noticed. Peak fitting was not performed because the pseudo-Voigt profile of the platinum doublets was somewhat lost due to inhomogeneous sample charging, which was especially noticeable for the $BiVO_4$/Pt(10 wt%)-pH 2.5 sample due to prominent Bi4f line broadening. For $BiVO_4$/Pt(10 wt%)-pH 2.5 only one doublet can be observed, in which the two signals at 71.2 eV and 74.6 eV likely correspond to $Pt4f_{7/2}$ and $Pt4f_{5/2}$, respectively, of metallic platinum.[26] For the $BiVO_4$/Pt(10 wt%)-

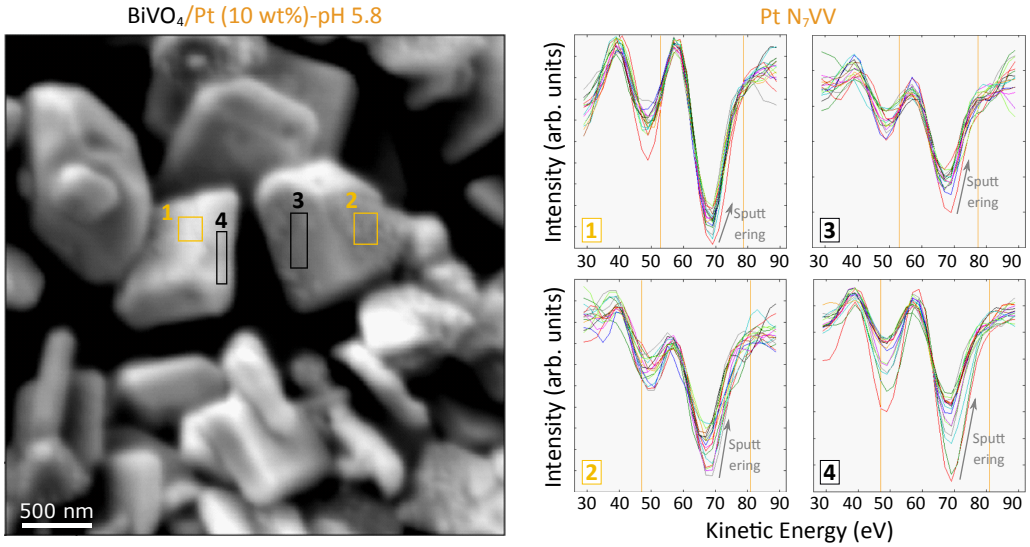

Figure 4.21: Left: FESEM image of $BiVO_4$/Pt(10 wt%)-pH 5.8 sample with the SAM measurement zones indicated in yellow (on {010} facets) and black (on {110} facets). Right: SAM sputter depth profile showing the 1st derivative of Pt N_7VV Auger signal for the different measurement zones.

pH 5.8 three doublets can be noticed, in which the signals at 71.2 eV, 72.5 eV and 75.0 eV likely correspond to the $Pt4f_{7/2}$ binding energies of metallic platinum, platinum hydroxides and platinum oxides, respectively.[26] Additionally, the O1s signal at a binding energy of 531.4 eV, which is characteristic for hydroxides, is stronger than for the other $BiVO_4$/Pt samples, which is also proof of the presence of platinum hydroxides. Then, in the $BiVO_4$/Pt(1 wt%)-pH 3.6 core level spectra only two Pt4f doublets can be seen, which likely corresponded to platinum oxide and hydroxides. These results indicate that the pH of the solution plays a strong role in the chemical nature of the platinum deposits, with more platinum hydroxide and platinum oxide being present at a higher pH. Confirmingly, Li et al. also observed the presence of platinum oxides in the Pt4f core level XP spectrum for heterostructured $BiVO_4$/Pt prepared through photodeposition at pH 3.60.[1] Based on the XPS observations, following chemical reactions could take place during the platinum photodeposition on $BiVO_4$:

$$H_2PtCl_6(aq) \longrightarrow 2\,H^+(aq) + [PtCl_6]^{2-}(aq)$$

$$[PtCl_6]^{2-}(aq) + 4\,e^- \longrightarrow Pt(s) + 6\,Cl^-(aq)$$

$$[PtCl_6]^{2-}(aq) + H_2O(l) + 2\,e^- \longrightarrow PtO(s) + 2\,H^+(aq) + 6\,Cl^-(aq)$$

Here, the formation of metallic platinum and PtO are effective reduction reactions. Additionally, Xi et al discussed that $[PtCl_6]^{2-}$ can undergo hydrolysis during the photodeposition process:[36]

$$[Pt(OH)nCl_{6-n}]^{2-}(aq) + OH^-(aq) \longleftrightarrow [Pt(OH)_{n+1}Cl_{5-n}]^{2-}(aq) + Cl^-(aq)$$

Wenderich et al. hypothesized that the hydrolysed platinum precursor may form $Pt(OH)_2$

through the reaction:[37]

$$[Pt(OH)_2Cl_4]^{2-}(aq) + 2\,e^- \longrightarrow Pt(OH)_2(s) + 4\,Cl^-(aq)$$

Additionally, Spieker at al. found that hydrolysis of H_2PtCl_6 is accelerated in the presence of light and favoured for increased pH and/or lower H_2PtCl_6 concentration.[38] All in all, this explains why the platinum photodeposition carried out with a lower platinum precursor concentration or after the addition of NaOH resulted in the presence of platinum oxide and hydroxide signals in XPS. Hence, to favour the photodeposition of metallic platinum the pH should preferably be maintained between 2.5 and 3.0.

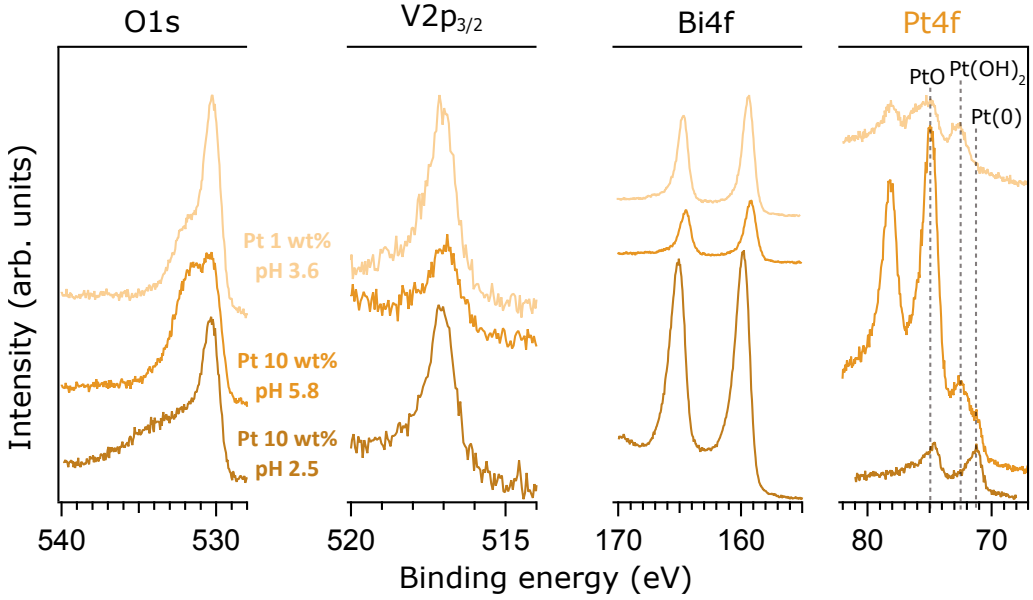

Figure 4.22: Pt4f, Bi4f, $V2p_{3/2}$, O1s core level XP spectra of $BiVO_4$/Pt samples. In the Pt4f spectra the $Pt4f_{7/2}$ features of Pt(0), $Pt(OH)_2$ and PtO are denoted.

4.3.3 $BiVO_4/CoO_xOH_y$

For {010}/{110} dual exposed $BiVO_4$ particles, electrons have been found to accumulate on the {010} facets, while holes tend to accumulate on the {110} facets, which has allowed the selective deposition of transition metal oxides such as MnO_x and CoO_x onto the {110} facets through a photo-oxidation process.[1,2] We again tested the facet-selectivity of the photo-oxidation of $Co(NO_3)_2$ on our truncated bipyramidal $BiVO_4$ particles. Indeed, the increased roughness on the {110} facets on the $BiVO_4$ particles, which is seen in Figure 4.23, corresponds most likely to cobalt based particles, as Li et al. found a similar morphology for heterostructured truncated bipyramidal $BiVO_4/CoO_xOH_y$.[2] The {010} facets remain largely uncovered.

Again, SAM was tried to figure out how cobalt is exactly distributed over the $BiVO_4$ particles. Luckily, the $BiVO_4/CoO_xOH_y$ sample did not degrade during the acquisition of the elemental

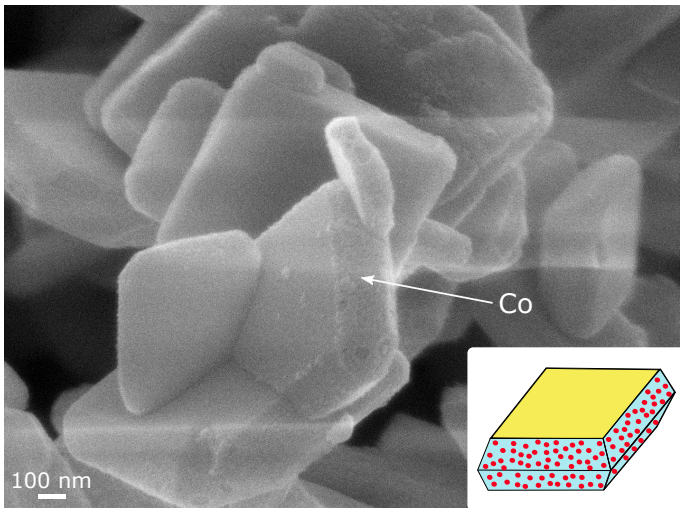

Figure 4.23: FESEM image of $BiVO_4/CoO_xOH_y$ (2 wt%).

maps. The elemental maps in Figure 4.24 confirm more clearly that cobalt is more or less restricted to the $\{110\}$ facets. Another remarkable finding in these maps is that the bismuth and vanadium signal intensity vary for the different facets. The surface of the $\{010\}$ facets seems to be more vanadium rich while the $\{110\}$ facets seem to be more bismuth rich. Previously, anisotropic charge carrier mobilities[39] or higher upwards band bending for the $\{011\}$ facets[31,40] have been cited as potential reasons for the stronger hole accumulation on these facets. However, the observation that the V/Bi surface stoichiometry is facet specific could also influence charge carrier separation.

XPS was performed to determine the oxidation state of the cobalt species of the heterostructured $BiVO_4/CoO_xOH_y$ (Figure 4.25). Inhomogeneous surface charging seems to be largely suppressed, as no substantial line broadening or additional unexpected signals appear in the $V2p_{3/2}$ and Bi4f core level spectra. Thus, the $Co2p_{3/2}$ spectrum could be carefully analysed to find indications of the chemical speciation of cobalt. The $Co2p_{3/2}$ spectrum is quite complicated, consisting of an asymmetric main line and several satellites due to plasmon loss features, electron correlations and final-state processes.[41,42] Through peak fitting the exact cobalt species can be obtained.[41] However, it has been stressed that high resolution spectra should be used and that preferably the $Co2p_{1/2}$ is included in the fitting procedure.[43] Fitting of the Co2p spectrum was in our case not feasible due to the relatively high amount of noise and the possibility of inhomogeneous surface charging. However, the $Co2p_{3/2}$ spectrum in Figure 4.25 can be compared to the spectra of well prepared, well defined cobalt species. The $Co2p_{3/2}$ spectrum of our sample is similar to CoO, and $Co(OH)_2$ with a broad main line at a binding energy around 780 eV and a shoulder at 786 eV.[41,44] The $Co2p_{3/2}$ satellite structure of CoOOH and Co_3O_4 is considerably different, as these species show a much smaller shoulder at 786 eV and an additional bump at a binding energy of 790 eV,[41,45] which some authors explain by the (partial) cobalt oxidation state

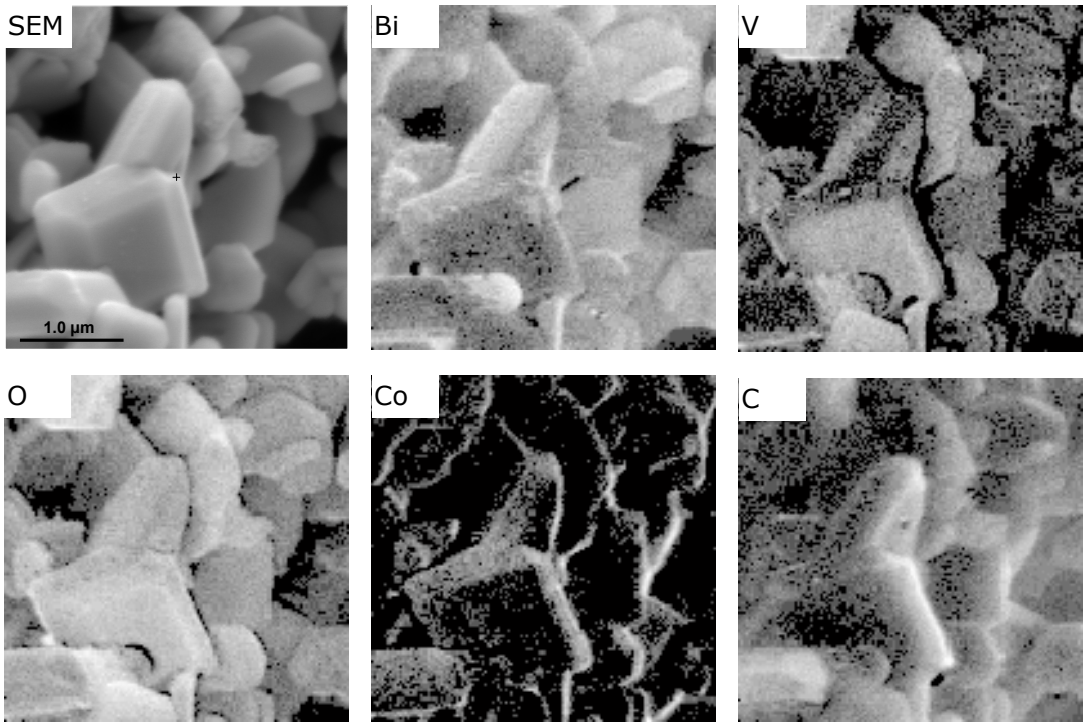

Figure 4.24: FESEM image and SAM elemental maps of $BiVO_4/CoO_xOH_y$ (2 wt%).

change from Co^{2+} to Co^{3+} for CoOOH and Co_3O_4.[44,46] Thus, our sample contains seemingly more Co^{2+}, indicating that cobalt is most likely only partly oxidized during the photodeposition process. Furthermore, Li et al. found a similar $Co2p_{3/2}$ spectrum for their photodeposited cobalt species.[2] Additionally, the cobalt species has been found to change during the photo-oxidation of water.[44,47] Therefore, we opted to denote the deposited cobalt species as CoO_xOH_y.

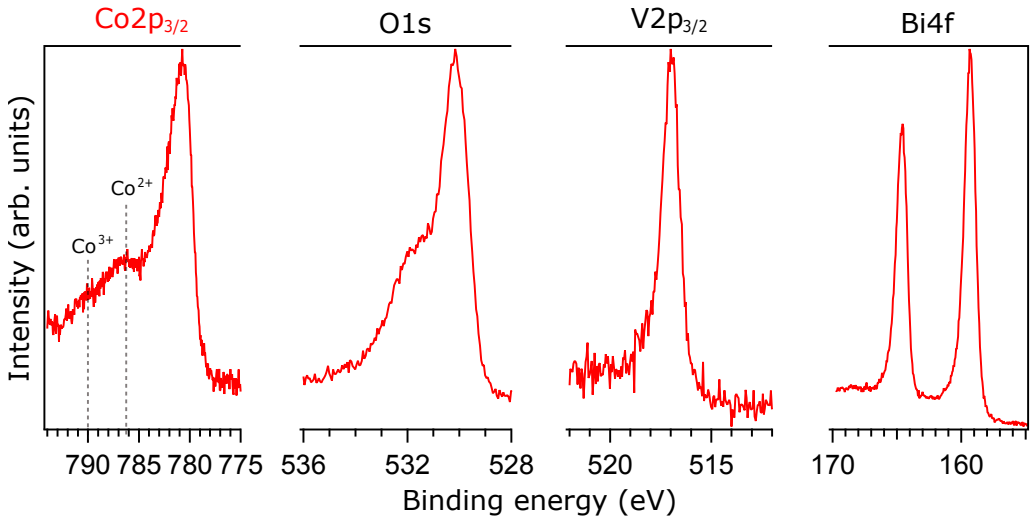

Figure 4.25: $Co2p_{3/2}$ Bi4f, $V2p_{3/2}$, O1s core level XP spectra of $BiVO_4/CoO_xOH_y$ (2 wt%).

4.3.4 $BiVO_4/NiO_xOH_y$

So far we know, the regioselectivity of the photodeposition of nickel based oxides onto particulate truncated bipyramidal $BiVO_4$ and its effect on the photocatalytic efficiency has not yet been extensively studied, although nickel based compounds are considered to be performant oxidation electrocatalysts.[48,49] Nevertheless, the photodeposition of nickel based compounds has already been realised before; having been successfully deposited onto several semiconductors, such as SiO_2,[50] CdS[51] and even on $BiVO_4$ thin films.[52] Moreover, Ni based compounds have proven to enhance the photochemical water oxidation efficiency of $BiVO_4$ thin film photoanodes.[4,52,53]

We have used the experimental nickel photodeposition procedure published by Choi et al,[52] which involves $Ni(NO_3)_2$ as nickel precursor and a potassium borate (KBi) buffer solution to fix the reaction mixture pH to 9.2. However, the nickel concentration in the reaction mixture should not be too high, since nickel then reacts to form $Ni(OH)_2$, which directly precipitates. For instance, a blue $Ni(OH)_2$ precipitate was detected when we wanted to prepare a 10 wt% nickel solution. In this case, the precipitate was discarded and the solution which then yielded less nickel was used, so that the deposit that resulted from this reaction mixture is referred to as the ± 10 wt% nickel deposit. For the 1 wt% and 0.1 wt% nickel solution no $Ni(OH)_2$ was perceived.

The FESEM images in Figure 4.26 seemingly show that the regioselectivity of the nickel-based deposit depends on the weight percentage of nickel we wanted to obtain. For the samples containing ± 10 wt% and 1 wt% Ni, nickel seems to be unselectively deposited over the entirety of the $BiVO_4$ particles, which is in contrast to the observed facet-selective photo-oxidation of cobalt. Possibly, the pH plays a role in the regioselectivity of the nickel species, as was also previously noticed for the platinum photoreduction. So far, only the silver and cobalt photodeposition processes followed the expected facet-selectivity and these were deposited at pH 7. Elemental EDS mapping of nickel (Figure 4.26c) also shows that the surface of the $BiVO_4$ particles seems to be completely covered by nickel deposits for the $BiVO_4/NiO_xOH_y$ (± 10 wt%). Contrarily, for the low 0.1 wt% nickel deposit, a certain regioselectivity can be observed in the FESEM images, as the nickel deposit seems to be preferably deposited on the edge between two {110} facets.

The regioselectivity of the nickel deposit was further studied with SAM. Unfortunately, no elemental maps could be made due to gradual sample degradation under the electron beam. Hence, zone measurements, which require a much shorter acquisition time, were again performed to probe the different facets. The edges between the {110} facets could not be selectively measured due to the limited lateral resolution. For the $BiVO_4/NiO_xOH_y$ (1 wt%) sample (Figure 4.27), an intense Ni L_3VV Auger signal was detected for every zone. Hence, the SAM zone measurements confirm the observations made earlier based off the FESEM images. Namely, that nickel seems to be omnipresent. On the other hand, for the $BiVO_4/NiO_xOH_y$ (0.1 wt%) sample (Figure 4.28), the Ni L_3VV Auger signal is only visible when zones on the {010} surfaces were measured. Therefore, the 0.1 wt% NiO_xOH_y deposit appears to be limited to the {010} facets and to the edges between the {110} facets.

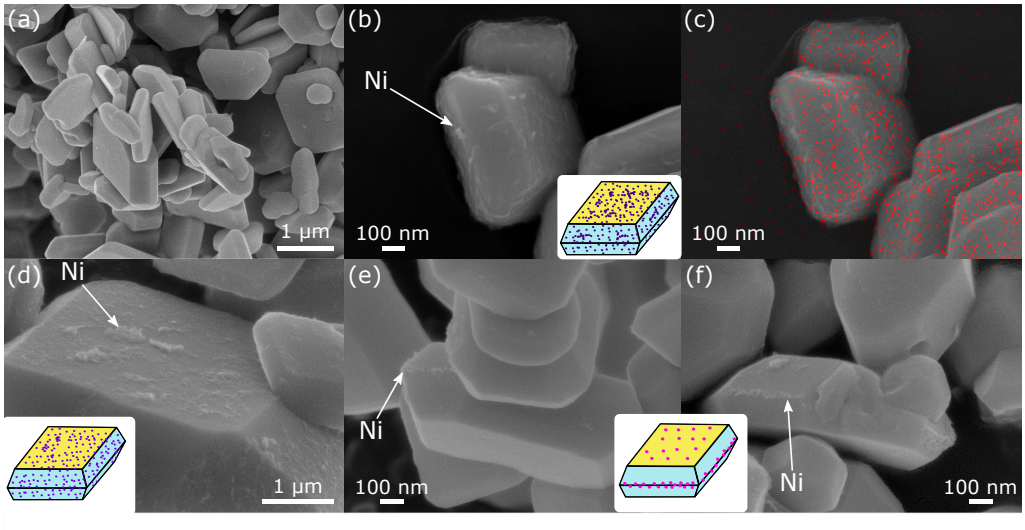

Figure 4.26: FESEM images: (a) bare $BiVO_4$, (b) $BiVO_4/NiO_xOH_y$ (± 10 wt%) (c) + Ni EDS, (d) $BiVO_4/NiO_xOH_y$ (1 wt%) and (f,g) $BiVO_4/NiO_xOH_y$ (0.1 wt%).

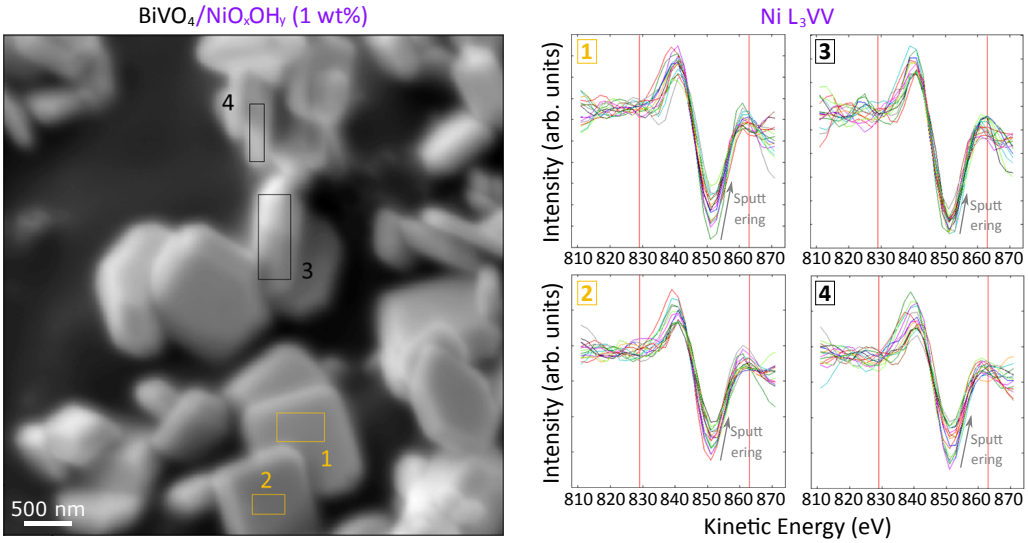

Figure 4.27: Left: FESEM image of $BiVO_4/NiO_xOH_y$ (1 wt%) sample with the SAM measurement zones indicated in yellow (on {010} facets) and black (on {110} facets). Right: SAM sputter depth profile showing the 1st derivative of Pt N_7VV Auger signal for the different measurement zones.

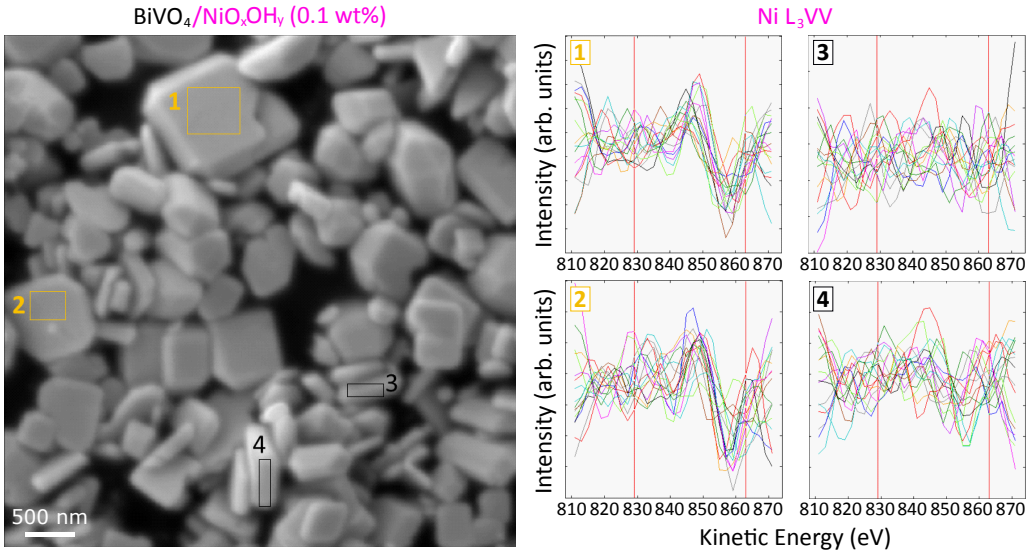

Figure 4.28: Left: FESEM image of $BiVO_4/NiO_xOH_y$ (0.1 wt%) sample with the SAM measurement zones indicated in yellow (on {010} facets) and black (on {110} facets). Right: SAM sputter depth profile showing the 1st derivative of Pt N_7VV Auger signal for the different measurement zones.

(S)TEM-EDS analysis was attempted to further examine the regioselectivity of the Ni deposit, whereby (S)TEM-EDS has the advantage of having a superior lateral resolution up to the nm scale. There were, however, two problems. First, the $BiVO_4/NiO_xOH_y$ (0.1 wt%) sample degraded under the focused electron beam of the TEM apparatus, which was solved by defocusing the electron beam. Secondly, the micron-sized $BiVO_4$ particles were actually too large for proper (S)TEM-EDS analysis, so that only measurements on the edges of the $BiVO_4$ particles could be performed. In Figure 4.29 the results of the (S)TEM-EDS analysis on $BiVO_4/NiO_xOH_y$ (0.1 wt%) are shown. A deposit can be seen in the bright-field and dark-field (S)TEM images on the edge of the {110} facets of a $BiVO_4$ particle and EDS analysis demonstrated that this particle contained nickel and oxygen. However, more information on the regioselectivity of nickel could not be obtained, due to the low Ni coverage of the sample and due to the inability to distinguish the different exposed facets.

The dependence of the regioselectivity of the nickel photodeposition on the wt% of nickel in the reaction mixture can possibly be explained by considering the nickel redox reactions that take place and solving the Nernst equations for each of these chemical reactions. First, it has to be considered that the valence band maximum and conduction band minimum of metal oxides depend on the pH according to the Nernstian relation:[54]

$$E_{VBM/CBM} = E_{VBM/CBM,pH\,0} - 0.059\ V\ x\ pH \tag{4.2}$$

Because the reduction potentials of H^+/H_2 and O_2/OH^- have the same pH dependence, the

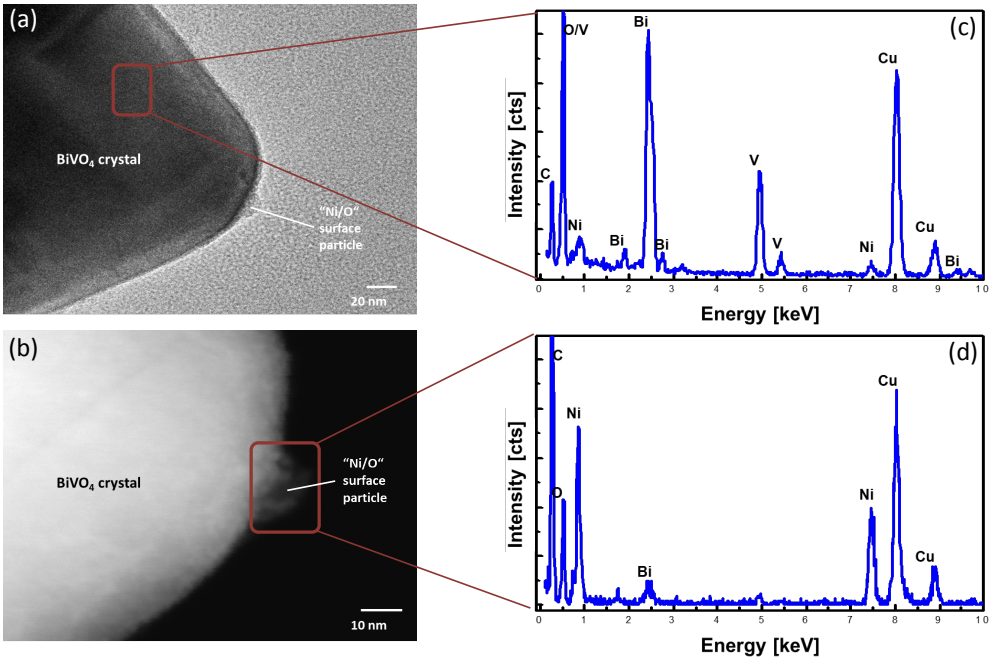

Figure 4.29: (a) TEM bright-field and (b) STEM dark-field image of $BiVO_4/NiO_xOH_y$ (1 wt%). (c) EDS of $BiVO_4$ microparticle and of (d) NiO_xOH_y nanodeposit.

band positions of metal oxides relative to the H^+/H_2 and O_2/H_2O stay the same. The pH dependence of the reduction potential changes for redox reactions with a different hydroxide anion and/or hydrogen cation stoichiometry. For Ni^{2+}, following redox reactions are plausible:

$$Ni^{2+} + 2\,e^- \rightleftharpoons Ni(s)$$
$$NiOOH(s) + 3\,H^+ + e^- \rightleftharpoons Ni^{2+} + 2\,H_2O$$

with the standard reduction potentials E^0 of Ni^{2+}/Ni and $NiOOH/Ni^{2+}$ being -0.236 V and 2.05 V, respectively.[55] The actual reduction potential of those reactions can be calculated according to the Nernst equation, here modified to accommodate the pH dependence of the reversible hydrogen electrode (reactions were carried out at room temperature):

$$bX + cY + ne^- \rightleftharpoons dZ$$

$$E(RHE) = E_0 + \frac{0.059\ V}{n} \times \log\left(\frac{a_X^b a_Y^c}{a_Z^d}\right) + 0.059\ V \times pH \tag{4.3}$$

with a_X,a_Y,a_Z the activities of X,Y and Z, relatively, and n the number of electrons involved in the reaction. For the Ni^{2+}/Ni reaction the Nernst equation transforms into:

$$E_{Ni^{2+}/Ni}(RHE) = E_0 + \frac{0.059\ V}{2}\ x\ \log([Ni^{2+}]^2) + 0.059\ V\ x\ pH \tag{4.4}$$

For a 1 wt% nickel solution, which contains 0.85 mmol/L nickel, and a pH of 9.2:

$$E_{Ni^{2+}/Ni,1wt\%Ni}(RHE) = -0.236\ V + 0.059\ V\ x\ \log(0.00085) + 0.059\ V\ x\ 9.2 \tag{4.5}$$

$$E_{Ni^{2+}/Ni,1wt\%Ni}(RHE) = 0.13\ V \tag{4.6}$$

For a 0.1 wt% nickel solution, which contains 0.085 mmol/L nickel, and a pH of 9.2:

$$E_{Ni^{2+}/Ni,0.1wt\%Ni}(RHE) = -0.236\ V + 0.059\ V\ x\ \log(0.000085) + 0.059\ V\ x\ 9.2 \tag{4.7}$$

$$E_{Ni^{2+}/Ni,0.1wt\%Ni}(RHE) = 0.07\ V \tag{4.8}$$

For the $NiOOH/Ni^{2+}$ reaction the Nernst equation transforms into:

$$E_{NiOOH/Ni^{2+}}(RHE) = E_0 + \frac{0.059\ V}{1}\ x\ \log(\frac{[H^+]^3}{[Ni^{2+}]^2}) + 0.059\ V\ x\ pH \tag{4.9}$$

$$E_{NiOOH/Ni^{2+}}(RHE) = E_0 - 0.059\ V\ x\ \log([Ni^{2+}]^2) - 0.118\ V\ x\ pH \tag{4.10}$$

Again, for a 1 wt% nickel solution, which contains 0.85 mmol/L nickel, and a pH of 9.2:

$$E_{NiOOH/Ni^{2+},1wt\%Ni}(RHE) = 2.05\ V - 0.118\ V\ x\ \log(0.00085) - 0.118\ V\ x\ 9.2 \tag{4.11}$$

$$E_{NiOOH/Ni^{2+},1wt\%Ni}(RHE) = 1.33\ V \tag{4.12}$$

For a 0.1 wt% nickel solution, which contains 0.085 mmol/L nickel, and a pH of 9.2:

$$E_{NiOOH/Ni^{2+},0.1wt\%Ni}(RHE) = 2.05\ V - 0.118\ V\ x\ \log(0.000085) - 0.118\ V\ x\ 9.2 \tag{4.13}$$

$$E_{NiOOH/Ni^{2+},0.1wt\%Ni}(RHE) = 1.44\ V \tag{4.14}$$

When considering the calculated reduction potentials, and the VBM and CBM of $BiVO_4$ at 0.1 eV and at 2.5 eV, respectively,[56] it can be evaluated whether the reduction and/or oxidation of Ni^{2+} by $BiVO_4$ is thermodynamically allowed. The $NiOOH/Ni^{2+}$ oxidation reaction can take place for both 1 wt% and 0.1 wt% nickel solutions since the $BiVO_4$ VBM is much more positive than the calculated reduction potentials of both solutions. Contrarily, the $BiVO_4$ CBM is situated closely to the reduction potentials calculated for the Ni^{2+}/Ni reduction reaction. Thus, the reduction of Ni^{2+} when utilizing a 1 wt% nickel solution could still take place, whereas the Ni^{2+} reduction for the 0.1 wt% nickel solution, which has a lower reduction potential, could be thermodynamically

restricted. Remarkably, because nickel was preferably found on the {010} facets for the 0.1 wt% nickel solution, this would mean that the oxidation of Ni^{2+} at a pH of 9.2 happens preferably on the {010} facets, which are normally considered to be the more reducing facets of truncated bipyramidal $BiVO_4$ particles.[1] It could possibly be that the regioselectivity of the photodeposition on $BiVO_4$ is pH sensitive.

Figure 4.30 shows the high resolution XP core level spectra for the $BiVO_4/NiO_xOH_y$ powders. The sample with ± 10 wt% NiO_xOH_y is not included, as it was charging to a degree that the Ni2p spectrum could not give any accurate information any more Inhomogeneous surface charging can still be noticed in the Bi4f spectrum for the 1 wt% NiO_xOH_y sample with extra bumps being present at higher binding energies. The XP core level spectra show that more nickel is present in the $BiVO_4/NiO_xOH_y$ (1 wt%) sample since the Ni2p-to-Bi4f intensity ratio is higher for the $BiVO_4/NiO_xOH_y$ (1 wt%) sample compared to the $BiVO_4/NiO_xOH_y$ (0.1 wt%) sample. Similar to the Co2p core level spectrum, the Ni2p spectrum consists of many satellites which require proper peak fitting to be certain of the analysed nickel species. However, inhomogeneous surface charging and a low intensity-to-noise ratio did not allow proper peak fitting, so that the nickel species can only be roughly estimated from the Ni2p line shape. Pure NiO can be excluded, since that would give rise to a noticeable peak splitting of the main $Ni2p_{3/2}$ line at a binding energy around 856.5 eV,[57] which is not seen in our Ni2p spectra. Instead, the Ni2p line shape resembles more that of a mixed nickel oxyhydroxide.[57,58] Furthermore, in the O1s core level XP spectrum of the $BiVO_4/NiO_xOH_y$ (1 wt%) sample, a strong signal at a binding energy of 532.1 eV can be seen, which is an indication of the presence of nickel hydroxides.[26,58] The hydroxide signal is commonly present for samples prepared under ambient conditions, as these conditions promote the adsorption of carbohydrates and water onto the exposed samples. However, the signal here is considerably stronger than usual and even higher than the O^{2-} signal at a binding energy of 530.3 eV. Therefore, the deposited nickel species is denoted as NiO_xOH_y. Above, the photoreduction of Ni^{2+} to metallic nickel was perceived as a possible reaction for solutions with a high enough Ni^{2+} concentration. However, in the Ni2p spectrum no indication of metallic nickel, which has a characteristic Ni $2p_{3/2}$ binding energy of 852.6 eV,[59] could be found. This could be due to the high reactivity of metallic nickel, having been found to oxidise at a relatively high rate at room temperature. In a photochemical process the deposited metallic nickel is most likely involved in a follow-up redox reaction, wherein metallic nickel reacts with hydroxides according to:

$$Ni(OH)_2(s) + 2\,e^- \rightleftharpoons Ni(s) + 2\,OH^-$$

Due to the very low standard reduction potential of $Ni(OH)_2/Ni$, -0.714 V,[55] the photo-oxidation of Ni is thermodynamically allowed and likely to happen.

4.3.5 $BiVO_4/RuO_x$

RuO_x is another good water oxidation electrocatalyst[48] for which, to our knowledge, the regioselectivity on truncated bipyramidal $BiVO_4$ has not been studied before. Photodeposition of RuO_x

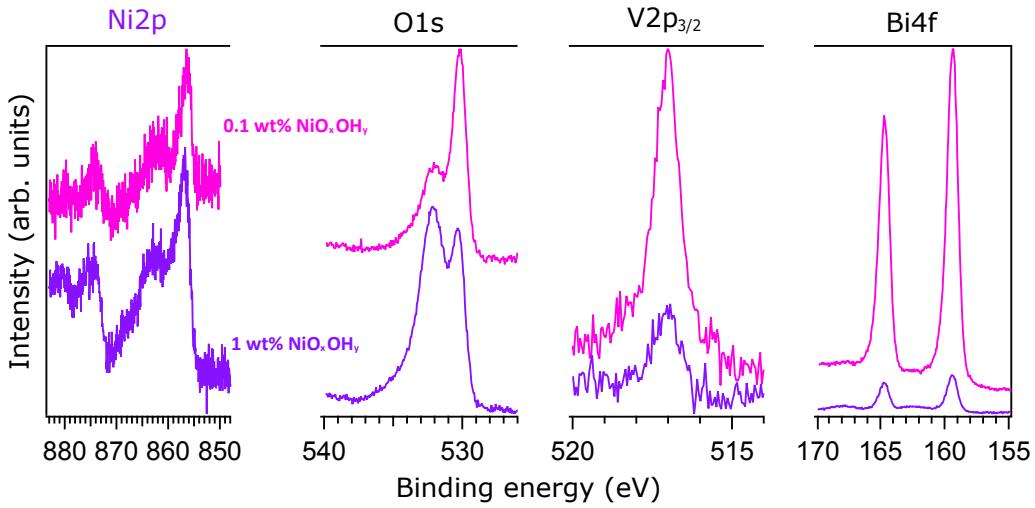

Figure 4.30: Ni2p, Bi4f, $V2p_{3/2}$ and O1s core level XP spectra of $BiVO_4/NiO_xOH_y$ samples.

has already been demonstrated through a photo-oxidation process, using $RuCl_3.3H_2O$ as ruthenium precursor,[60] and a photoreduction process, using $KRuO_4$ as ruthenium precursor.[61] We tried both ruthenium precursors but their limited water solubility was a serious problem. Only ruthenium solutions for the deposition of 0.1 wt% Ru or lower could be prepared with $RuCl_3.xH_2O$ and $KRuO_4$. At the time, we thought that 0.1 wt% Ru would be too low to study the ruthenium regioselectivity with FESEM and SAM, so that the $BiVO_4/RuO_x$ (0.1 wt%) samples were not further investigated. However, as is shown above for the $BiVO_4/NiO_xOH_y$ samples, which were prepared later, the regioselectivity of deposits with a coverage as low as 0.1 wt% may be studied through FESEM and SAM. Thus, in principle one could look again at the regioselectivity of the photodeposition of RuO_x on truncated bipyramidal $BiVO_4$ with only 0.1 wt% Ru water based solutions.

Another way to deposit more ruthenium is to use another solvent system in which the solubility of ruthenium is higher. Ruthenium acetylacetonate, $Ru(acac)_3$, has a high solubility in acetic acid and THF, making it possible to establish a 10 wt% Ru solution. Because sodium iodate did not dissolve in either THF and acetic acid, $FeCl_3$ was added instead as an electron scavenger. Figure 4.31a shows, however, that the immersion in acetic acid had an adverse effect on the $BiVO_4$ morphology, as the particles appear to be more aggregated and seem to have lost their truncated bipyramidal shape in part. These adverse effects are most probably due to the instability of $BiVO_4$ in acidic media. For the photodeposition in THF, the $BiVO_4$ particles maintained their shape and a deposit can be seen, which is seemingly spread out over the entirety of the $BiVO_4$ particles (Figure 4.31b).

However, when measuring the Ru3d core level spectrum, only a signal at a binding energy of 285 eV could be detected, which is characteristic for C1s photoelectrons of adventitious carbon.[62] Thus, RuO_2 seems not to be present, as it should have generated a signal at a binding energy of

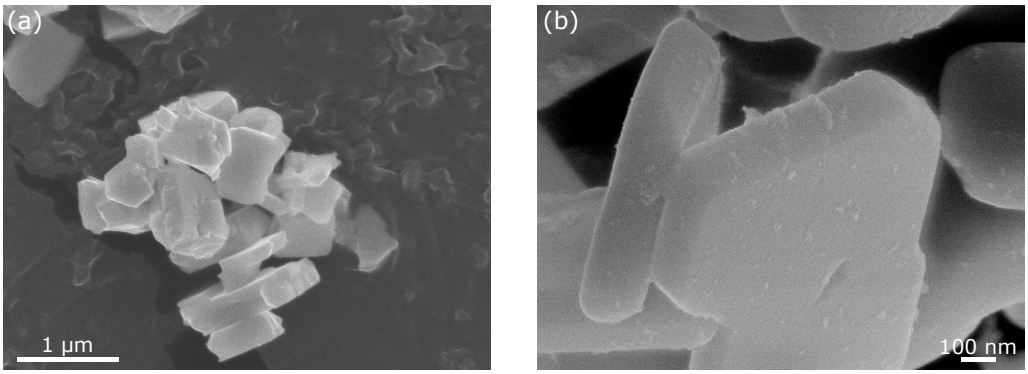

Figure 4.31: FESEM images: photodeposition of $Ru(acac)_3$ on $BiVO_4$ with $FeCl_3$ as electron scavenger in (a) acetic acid and (b) THF.

about 281 eV, the characteristic $Ru3d_{5/2}$ photoelectron binding energy for RuO_2.[26] Instead, iron characteristic photoelectrons were detected, suggesting that the deposit seen in Figure 4.31b was the result of iron photoreduction. We were, however, not interested in the deposition of iron based particles, so that we did not further investigate the supposed photoreduction of iron.

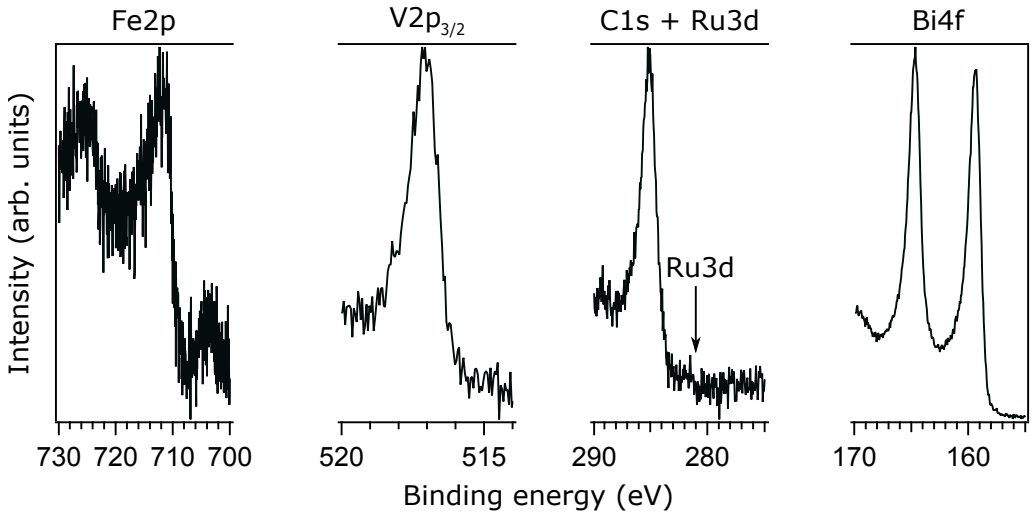

Figure 4.32: Fe2p, $V2p_{3/2}$, C1s, Ru3d and Bi4f core level XP spectra of $BiVO_4$ sample after photodeposition of $Ru(acac)_3$ with $FeCl_3$ as electron scavenger in THF.

4.3.6 Photocatalysis

4.3.6.1 UV-Vis diffuse reflectance

Before analysing the photocatalytic performance of the different heterostructured $BiVO_4$ samples, the differences in light absorption were studied through UV-Vis diffuse reflectance spectroscopy. Remarkably, the Tauc plot in Figure 4.33 shows that the deposited contact materials

do not have a strong influence on the optical band gap of $BiVO_4$, because all heterostructures appear to have an optical band gap in the range of 2.48 — 2.52 eV.

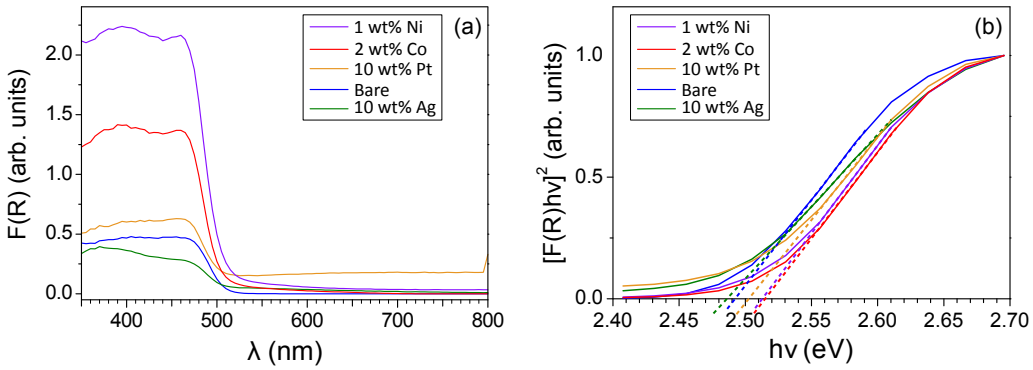

Figure 4.33: (a) UV-Vis diffuse reflectance spectra and (b) Tauc plots for heterostructured $BiVO_4$ powders.

4.3.6.2 Rhd B photodegradation

With all the heterostructures fully characterized, the Rhd B photodegradation efficiency was tested. The procedure of Rhd B photodegradation is explained in Section 3.4.5.1. In Figure 4.15 the evolution of a Rhd B photodegradation experiment is depicted by means of UV-Vis spectra, which were measured for aliquots taken from the Rhd B solution at specific points in time.

Figure 4.34 shows the photocatalytic degradation of Rhd B for the various heterostructured $BiVO_4$ photocatalysts. Here, $BiVO_4/NiO_xOH_y$ and $BiVO_4$/Ag seem to be the most efficient, as the original absorbance drops by about 50% after 2 h of photodegradation. In contrast, $BiVO_4/CoO_xOH_y$ appears to have a similar Rhd B photodegradation efficiency as bare $BiVO_4$. $\ln\left(\frac{A_t}{A_0}\right)$ vs t plots as well as the first order rate constants, determined from these plots, are shown in Figure 4.34b. The first order rate model seems to fit more or less, as the linear regression yield R^2 values in the range of 0.95 — 0.99. Overall, all heterostructures have rate constants which are only slightly higher than the one of bare truncated bipyramidal $BiVO_4$. This is in part due to the already high first order rate constant of bare $BiVO_4$, which is here 3.3 x 10^{-3} min^{-1}, whereas Li et al. found a first order rate constant of 1.7 x 10^{-3} min^{-1}.[2] The authors also found rate constants of an equivalent order of magnitude, as the ones we found, for heterostructured truncated bipyramidal $BiVO_4$ covered by a single cocatalyst. Additionally, they report that only for $BiVO_4$ coated by both a reduction and oxidation cocatalyst, a strong increase in the Rhd B degradation efficiency was obtained.

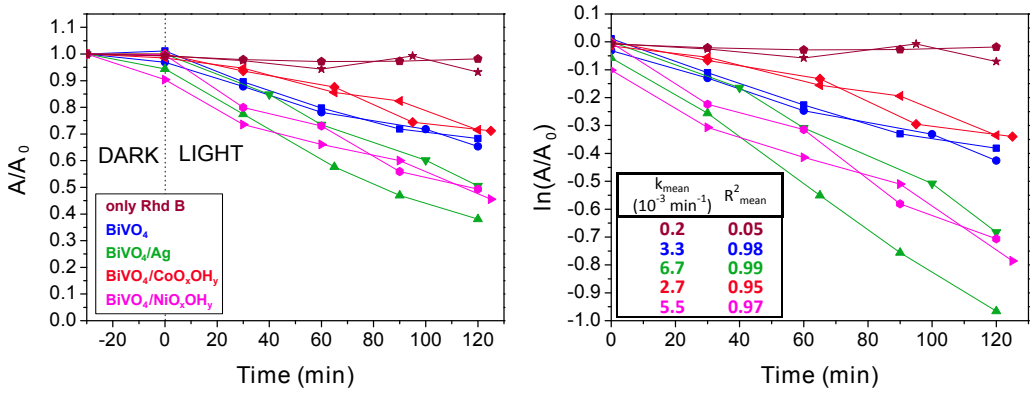

Figure 4.34: Photocatalytic degradation of Rhd B for several heterostructured $BiVO_4$ photocatalysts. Left: absorbance (at 554 nm) and right: natural logarithm of absorbance versus the degradation time with light switched on at 0 min. The mean first order rate constants k_{mean} and mean R^2 linear fitting parameter are denoted in the graph. For each heterostructure there was a 0.1 wt% loading of contact material.

4.3.6.3 Sacrificial water oxidation

Photochemical sacrificial water oxidation experiments were performed to assess how the performance of the newly synthesized $BiVO_4/NiO_xOH_y$ relates to previously studied heterostructures. The sacrificial water oxidation experiments were performed within a closed reactor, coupled to an automatic burette to register the gas volume increase during the reaction. The exact experimental procedure is described in Section 3.4.5.2. In Figure 4.35 the gas evolution of all the $BiVO_4$ heterostructures is depicted. The gas evolution curves show that the sacrificial water oxidation with $BiVO_4$ follows a photocatalytic mechanism, as in the absence of light or $BiVO_4$ (Figure 4.36) no steady gas evolution occurs. Nevertheless, a volume increase of about 1 mL can be seen for the blank experiments without $BiVO_4$ (Figure 4.36). This increase is largely due to the set up searching for a new equilibrium after the light source is focused onto the reactor. In addition, a small amount of air present in the reaction medium likely contributes to the small amount of detected gas as well, since GC measurements, ran after the blank experiment, revealed an increased nitrogen signal with respect to the GC measurements ran before the blank experiment.

A first remarkable observation is that for all $BiVO_4$ powders, gas evolution takes place until a gas volume of approximately 12 mL (or 11 mL after subtracting the blank volume) is reached. This volume corresponds to the concentration of sacrificial agent (1 mmol), as 11.2 ml amounts to half of the millimolar gas volume according to the ideal gas law at ambient conditions and because $NaIO_4$ scavenges two electrons per molecule according to:

$$IO_4^- + 2\,H^+ + 2\,e^- \rightleftharpoons IO_3^- + H_2O$$

In other words, to produce 0.5 mmol (11.2 mL) of O_2, which consumes 4 holes (See Section 2.1.3), 1 mmol of $NaIO_4$, which consumes 2 electrons, is needed. The IO_4^-/IO_3^- reaction has a

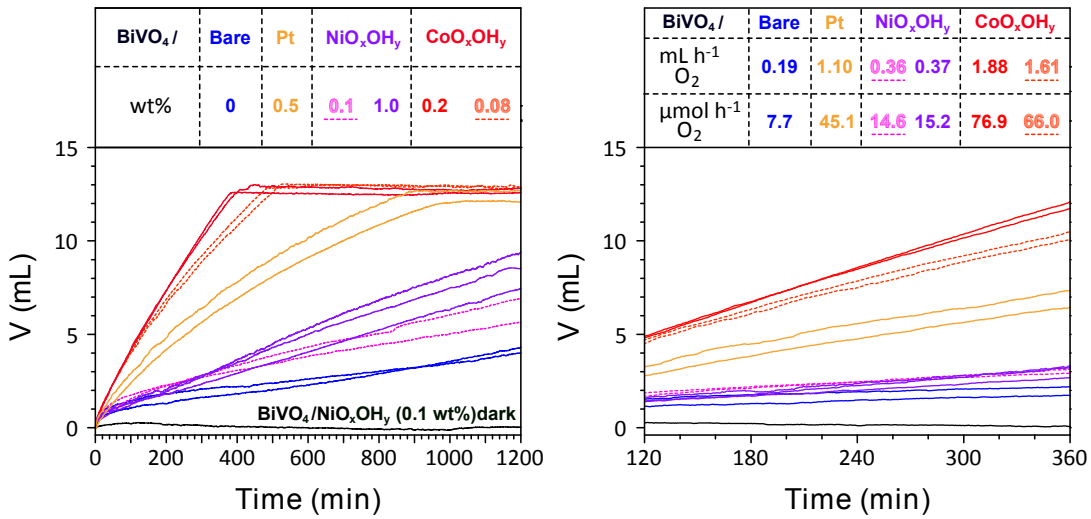

Figure 4.35: Sacrificial water oxidation for several heterostructured $BiVO_4$ photocatalysts: gas evolution versus time. Gas evolution rates (mL h^{-1} O_2) are depicted as well. 1 mmol $NaIO_4$ was used as sacrificial agent and the amount of photocatalyst powder was 50 mg.

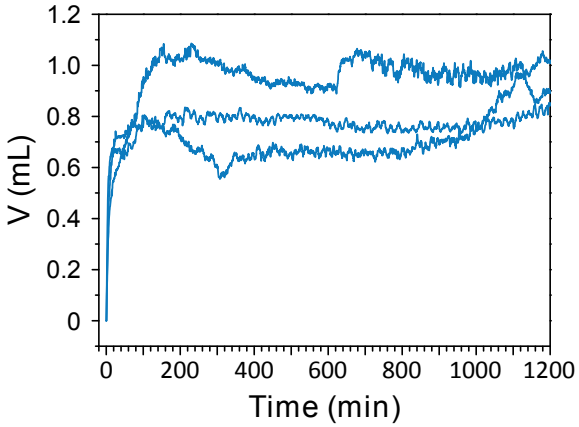

Figure 4.36: Gas evolution (mL) versus time (min) for blanks containing no photocatalytic material.

standard reduction potential of 1.589 V,[55] which means that $NaIO_4$ is a strong oxidative agent and should be easily reduced by $BiVO_4$.

Thus, the oxygen evolution stops when no IO_4^- is present any more and, as can be seen in Figure 4.35, the gas evolution then stops quite suddenly, reaching a volume of about 12 mL. This is a remarkable observation, first, because it demonstrates that the reduction of IO_4^- is not the rate-limiting step and, secondly, because it means that IO_3^-, here, does not act as a sacrificial agent, despite the reactions:

$$IO_3^- + 6\,H^+ + 5\,e^- \longrightarrow \tfrac{1}{2}\,I_2(s) + 3\,H_2O$$

$$IO_3^- + 5\,H^+ + 4\,e^- \longrightarrow HOI + 2\,H_2O$$

$$IO_3^- + 3\,H_2O + 6\,e^- \longrightarrow I^- + 6\,OH^-$$

having high standard reduction potentials of 1.210 V, 1.154 V and 0.269 V, respectively.[55] Due to the high standard reduction potentials, these reactions should not be thermodynamically limited for $BiVO_4$. Indeed, $NaIO_3$ has been used sometimes in sacrificial water oxidation[1,2] or as a redox shuttle (IO_3^-/I^-) in Z-scheme water splitting systems.[63,64] However, the tests we ran with $NaIO_3$ as sacrificial agent did not show any gas evolution.

To determine the oxygen evolution rate of all heterostructures, a linear regression was performed on the linear part of the gas evolution curves, i.e. at a reaction time between 120 min and 360 min (Figure 4.35). The raw data of the linear regression can be found in Appendix A. Seemingly, the implementation of CoO_xOH_y and Pt as contact materials boost the water oxidation performance of $BiVO_4$ by about 10 times and 5.9 times, respectively, with respect to bare $BiVO_4$. In comparison, Li et al. found that bare $BiVO_4$, $BiVO_4/Co_3O_4$ and $BiVO_4$/Pt yielded oxygen evolution rates of 1.0, 2.5 and 16.8 μmol h^{-1}, respectively.[2] Thus, qualitatively, their results compare well to ours, in the sense that we both found boosted water oxidation performance for cobalt and platinum based contact materials. However, we found much higher absolute gas evolution rates for all $BiVO_4$ systems, while the relative boost to the water oxidation performance by Pt and Co is lower than what Li et al. found. Under the assumption that we can compare the absolute results, our bare $BiVO_4$ powder seems to be of a better quality than the one synthesized by Li et al, especially because the authors used a threefold higher amount of photocatalyst and sacrificial agent in their procedure. Additionally, it is remarkable that in the publication of Li et al. Pt, perceived as a reduction cocatalyst, yielded a higher boost than Co_3O_4, a perceived oxidation cocatalyst. This could be an indication that in their testing procedure, the reduction of the sacrificial agent was the rate limiting step, which is not a good way to assess the water oxidation performance of $BiVO_4$ heterostructures. The problem could be that the $NaIO_3$ sacrificial agent, as observed in this work, has a much lower reactivity than $NaIO_4$. The use of $NaIO_3$ instead of $NaIO_4$ could also explain why Li et al. obtained lower absolute oxygen evolution rates.

Unfortunately, our newly synthesized $BiVO_4/NiO_xOH_y$ heterostructure exhibits a rather poor water oxidation performance compared to the other heterostructures, as the oxygen evolution rate is only two times higher with respect to bare $BiVO_4$.

4.4 Conclusion

The $\{010\}/\{110\}$ dual facet exposed $BiVO_4$ microcrystalline powder could not be straightforwardly synthesized according to any of the previously published synthesis procedures we attempted. However, by optimizing the parameters of one of the most promising synthesis procedures we could obtain $BiVO_4$ powder with the appropriate morphology and phase purity. The optimised parameters included a pH of 1.5, having an autoclave temperature of 200 °C, an autoclave time of 20—24 h, and having SDS as surfactant. The synthesis could then easily be upscaled by a factor of two by multiplying the amount of all chemicals used by a factor of two, except for the amount of SDS, which had to be multiplied by three. Additionally, the reaction mixture was stirred at 300 RPM while performing the hydrothermal treatment. A remarkable finding was that syntheses performed at different pH yielded $BiVO_4$ powders with different morphologies, giving rise to dendritic and irregular shapes besides the desired truncated bipyramidal shape. It was shown that the irregular morphology exhibited a slightly better dye decomposition performance than the other morphologies.

$BiVO_4$/Pt, $BiVO_4$/Ag, $BiVO_4/CoO_x$ and the new $BiVO_4/NiO_xOH_y$ heterostructures could be successfully synthesized through a photodeposition procedure. Thorough electron microscopy analysis clearly showed that silver was selectively deposited onto the $\{010\}$ facets and CoO_xOH_y could be selectively deposited onto the $\{110\}$ facets. This facet-selectivity was also observed previously in literature. Platinum seems to be deposited selectively onto the $\{010\}$ facets for weight percentages below 10%. However, this facet-selectivity is somewhat more uncertain, because the platinum particles could not be easily visualised through FESEM. The regioselectivity of NiO_xOH_y was remarkable, because there seems to be an increased amount on the edges of the $\{110\}$ facets as well as on top of the $\{010\}$ facets, as was shown by FESEM and SAM.

For dye decomposition, $BiVO_4$/Ag and $BiVO_4/NiO_xOH_y$ were almost twice as efficient compared to bare $BiVO_4$, whereas $BiVO_4/CoO_xOH_y$ did not improve upon bare $BiVO_4$. In contrast, for sacrificial water oxidation, $BiVO_4/CoO_xOH_y$ yielded a tenfold increase in oxygen evolution rate with respect to bare $BiVO_4$. This proves again that heterostructured photocatalyts which are efficient at dye degradation are not necessarily good at water oxidation and vice versa. Further, coating $BiVO_4$ with platinum effectively increased the water oxidation performance by a factor of 5.9. The water oxidation performance boost with cobalt and platinum contact materials was observed before by Li et al.,[2] however we surprisingly obtained a seven times higher absolute oxygen evolution rate for bare $BiVO_4$ with three times as less $BiVO_4$ powder. An unfortunate finding was that our newly synthesized $BiVO_4/NiO_xOH_y$ heterostructure only boosted the oxy-

gen evolution rate by a factor of two, thus much lower than what we obtained with CoO_xOH_y as contact material.

Without question, our results show that heterostructuring a photoabsorber with noble and transition metal compounds have a noticeable boost on its photocatalytic performance. But why those contact materials exactly benefit the photoabsorber is still an open question. In the next Chapter we try to solve part of this puzzling question.

References

(1) Li, R.; Zhang, F.; Wang, D.; Yang, J.; Li, M.; Zhu, J.; Zhou, X.; Han, H.; Li, C. Spatial separation of photogenerated electrons and holes among {010} and {110} crystal facets of $BiVO_4$. *Nat. Commun.* **2013**, *4*, 1432.

(2) Li, R.; Han, H.; Zhang, F.; Wang, D.; Li, C. Highly efficient photocatalysts constructed by rational assembly of dual-cocatalysts separately on different facets of $BiVO_4$. *Energy Environ. Sci.* **2014**, *7*, 1369–1376.

(3) McCrory, C. C. L.; Jung, S.; Ferrer, I. M.; Chatman, S. M.; Peters, J. C.; Jaramillo, T. F. Benchmarking Hydrogen Evolving Reaction and Oxygen Evolving Reaction Electrocatalysts for Solar Water Splitting Devices. *J. Am. Chem. Soc.* **2015**, *137*, 4347–4357.

(4) Kim, T. W.; Choi, K.-S. Nanoporous $BiVO_4$ Photoanodes with Dual-Layer Oxygen Evolution Catalysts for Solar Water Splitting. *Science (80-.).* **2014**, *343*, 990–994.

(5) Shi, X.; Choi, I. Y.; Zhang, K.; Kwon, J.; Kim, D. Y.; Lee, J. K.; Oh, S. H.; Kim, J. K.; Park, J. H. Efficient photoelectrochemical hydrogen production from bismuth vanadate-decorated tungsten trioxide helix nanostructures. *Nat. Commun.* **2014**, *5*, 4775.

(6) Seabold, J. A.; Choi, K.-S. Efficient and Stable Photo-Oxidation of Water by a Bismuth Vanadate Photoanode Coupled with an Iron Oxyhydroxide Oxygen Evolution Catalyst. *J. Am. Chem. Soc.* **2012**, *134*, 2186–2192.

(7) Li, C.; Zhang, P.; Lv, R.; Lu, J.; Wang, T.; Wang, S.; Wang, H.; Gong, J. Selective Deposition of Ag_3PO_4 on Monoclinic $BiVO_4$ (040) for Highly Efficient Photocatalysis. *Small* **2013**, *9*, 3951–3956.

(8) Wang, W.; Huang, X.; Wu, S.; Zhou, Y.; Wang, L.; Shi, H.; Liang, Y.; Zou, B. Preparation of p–n junction $Cu_2O/BiVO_4$ heterogeneous nanostructures with enhanced visible-light photocatalytic activity. *Appl. Catal. B Environ.* **2013**, *134-135*, 293–301.

(9) Xu, T.; Zhu, R.; Zhu, G.; Zhu, J.; Liang, X.; Zhu, Y.; He, H. Mechanisms for the enhanced photo-Fenton activity of ferrihydrite modified with $BiVO_4$ at neutral pH. *Appl. Catal. B Environ.* **2017**, *212*, 50–58.

(10) Ye, F.; Li, H.; Yu, H.; Chen, S.; Quan, X. Constructing $BiVO_4$-Au@CdS photocatalyst with energic charge-carrier-separation capacity derived from facet induction and Z-scheme bridge for degradation of organic pollutants. *Appl. Catal. B Environ.* **2018**, *227*, 258–265.

(11) Liu, Q.; Liu, Y.; Gao, B.; Chen, Y.; Lin, B. Hydrothermal synthesis of In_2O_3-loaded $BiVO_4$ with exposed {010}{110} facets for enhanced visible-light photocatalytic activity. *Mater. Res. Bull.* **2017**, *87*, 114–118.

(12) Wang, D.; Jiang, H.; Zong, X.; Xu, Q.; Ma, Y.; Li, G.; Li, C. Crystal Facet Dependence of Water Oxidation on $BiVO_4$ Sheets under Visible Light Irradiation. *Chem. - A Eur. J.* **2011**, *17*, 1275–1282.

(13) Xi, G.; Ye, J. Synthesis of bismuth vanadate nanoplates with exposed {001} facets and enhanced visible-light photocatalytic properties. *Chem. Commun.* **2010**, *46*, 1893.

(14) Tan, H. L.; Tahini, H. A.; Wen, X.; Wong, R. J.; Tan, X.; Iwase, A.; Kudo, A.; Amal, R.; Smith, S. C.; Ng, Y. H. Interfacing $BiVO_4$ with Reduced Graphene Oxide for Enhanced Photoactivity: A Tale of Facet Dependence of Electron Shuttling. *Small* **2016**, *12*, 5295–5302.

(15) Tan, H. L.; Wen, X.; Amal, R.; Ng, Y. H. $BiVO_4$ {010} and {110} Relative Exposure Extent: Governing Factor of Surface Charge Population and Photocatalytic Activity. *J. Phys. Chem. Lett.* **2016**, *7*, 1400–1405.

(16) Merupo, V.; Velumani, S.; Oza, G.; Makowska-Janusik, M.; Kassiba, A. Structural, electronic and optical features of molybdenum-doped bismuth vanadium oxide. *Mater. Sci. Semicond. Process.* **2015**, *31*, 618–623.

(17) Jiang, H.; Dai, H.; Meng, X.; Zhang, L.; Deng, J.; Liu, Y.; Au, C. T. Hydrothermal fabrication and visible-light-driven photocatalytic properties of bismuth vanadate with multiple morphologies and/or porous structures for methyl orange degradation. *J. Environ. Sci. (China)* **2012**, *24*, 449–57.

(18) Meng, X.; Zhang, L.; Dai, H.; Zhao, Z.; Zhang, R.; Liu, Y. Surfactant-assisted hydrothermal fabrication and visible-light-driven photocatalytic degradation of methylene blue over multiple morphological $BiVO_4$ single-crystallites. *Mater. Chem. Phys.* **2011**, *125*, 59–65.

(19) Scherrer, P. Determination of the Size and Internal Structure of Colloidal Particles using X-rays. *Nachr. Ges. Wiss. Göttingen* **1918**, *2*, 98.

(20) Tokunaga, S.; Kato, H.; Kudo, A. Selective preparation of monoclinic and tetragonal $BiVO_4$ with scheelite structure and their photocatalytic properties. *Chem. Mater.* **2001**, *13*, 4624–4628.

(21) Cooper, J. K.; Gul, S.; Toma, F. M.; Chen, L.; Glans, P. A.; Guo, J.; Ager, J. W.; Yano, J.; Sharp, I. D. Electronic structure of monoclinic $BiVO_4$. *Chem. Mater.* **2014**, *26*, 5365–5373.

(22) Jovic, V.; Laverock, J.; Rettie, A. J. E.; Zhou, J.-S.; Mullins, C. B.; Singh, V. R.; Lamoureux, B.; Wilson, D.; Su, T.-Y.; Jovic, B.; Bluhm, H.; Söhnel, T.; Smith, K. E. Soft X-ray spectroscopic studies of the electronic structure of M:$BiVO_4$ (M = Mo, W) single crystals. *J. Mater. Chem. A* **2015**, *3*, 23743–23753.

(23) Al-Areqi, N. A.; Al-Alas, A.; Al-Kamali, A. S.; Ghaleb, K.; Al-Mureish, K. Photodegradation of 4-SPPN dye catalyzed by Ni(II)-substituted $Bi_2VO_{5.5}$ system under visible light irradiation: Influence of phase stability and perovskite vanadate–oxygen vacancies of photocatalyst. *J. Mol. Catal. A Chem.* **2014**, *381*, 1–8.

(24) Abdi, F. F.; Savenije, T. J.; May, M. M.; Dam, B.; van de Krol, R. The Origin of Slow Carrier Transport in $BiVO_4$ Thin Film Photoanodes: A Time-Resolved Microwave Conductivity Study. *J. Phys. Chem. Lett.* **2013**, *4*, 2752–2757.

(25) Chen, L.; Alarcón-Lladó, E.; Hettick, M.; Sharp, I. D.; Lin, Y.; Javey, A.; Ager, J. W. Reactive sputtering of bismuth vanadate photoanodes for solar Water splitting. *J. Phys. Chem. C* **2013**, *117*, 21635–21642.

(26) Moulder, J. F.; Stickle, W. F.; Sobol, P. E.; Bomben, K. D., *Handbook of X-ray photoelectron spectroscopy: a reference book of standard spectra for identification and interpretation of XPS data*; Physical Electronics: Eden Prairie MN, 1992, p 261.

(27) Sundararajan, M.; Sailaja, V.; John Kennedy, L.; Judith Vijaya, J. Photocatalytic degradation of rhodamine B under visible light using nanostructured zinc doped cobalt ferrite: Kinetics and mechanism. *Ceram. Int.* **2017**, *43*, 540–548.

(28) Uddin, M. T.; Babot, O.; Thomas, L.; Olivier, C.; Redaelli, M.; D'Arienzo, M.; Morazzoni, F.; Jaegermann, W.; Rockstroh, N.; Junge, H.; Toupance, T. New Insights into the Photocatalytic Properties of RuO_2/TiO_2 Mesoporous Heterostructures for Hydrogen Production and Organic Pollutant Photodecomposition. *J. Phys. Chem. C* **2015**, *119*, 7006–7015.

(29) Pacholski, C.; Kornowski, A.; Weller, H. Site-Specific Photodeposition of Silver on ZnO Nanorods. *Angew. Chemie Int. Ed.* **2004**, *43*, 4774–4777.

(30) Debroye, E.; Van Loon, J.; Yuan, H.; Janssen, K. P. F.; Lou, Z.; Kim, S.; Majima, T.; Roeffaers, M. B. J. Facet-Dependent Photoreduction on Single ZnO Crystals. *J. Phys. Chem. Lett.* **2017**, *8*, 340–346.

(31) Zhu, J.; Fan, F.; Chen, R.; An, H.; Feng, Z.; Li, C. Direct Imaging of Highly Anisotropic Photogenerated Charge Separations on Different Facets of a Single $BiVO_4$ Photocatalyst. *Angew. Chemie - Int. Ed.* **2015**, *54*, 9111–9114.

(32) Yoneyama, H.; Nishimura, N.; Tamura, H. Photodeposition of palladium and platinum onto titanium dioxide single crystals. *J. Phys. Chem.* **1981**, *85*, 268–272.

(33) Murcia, J.; Hidalgo, M.; Navío, J.; Araña, J.; Doña-Rodríguez, J. Study of the phenol photocatalytic degradation over TiO_2 modified by sulfation, fluorination, and platinum nanoparticles photodeposition. *Appl. Catal. B Environ.* **2015**, *179*, 305–312.

(34) Zhang, F.; Chen, J.; Zhang, X.; Gao, W.; Jin, R.; Naijia, G.; Li, Y. Synthesis of Titania-Supported Platinum Catalyst: The Effect of pH on Morphology Control and Valence State during Photodeposition. *Langmuir* **2004**, *20*, 9329–9334.

(35) Zhao, Y.; Xie, Y.; Zhu, X.; Yan, S.; Wang, S. Surfactant-Free Synthesis of Hyperbranched Monoclinic Bismuth Vanadate and its Applications in Photocatalysis, Gas Sensing, and Lithium-Ion Batteries. *Chem. - A Eur. J.* **2008**, *14*, 1601–1606.

(36) Chanjuan Xi; Zhengshi Chen; Qinglin Li; Zhensheng Jin Effects of H^+, Cl^- and CH_3COOH on the photocatalytic conversion of $PtCl_6^{2-}$ in aqueous TiO_2 dispersion. *J. Photochem. Photobiol. A Chem.* **1995**, *87*, 249–255.

(37) Wenderich, K.; Mul, G. Methods, Mechanism, and Applications of Photodeposition in Photocatalysis: A Review. *Chem. Rev.* **2016**, *116*, 14587–14619.

(38) Spieker, W.; Liu, J.; Miller, J.; Kropf, A.; Regalbuto, J. An EXAFS study of the co-ordination chemistry of hydrogen hexachloroplatinate(IV): 1. Speciation in aqueous solution. *Appl. Catal. A Gen.* **2002**, *232*, 219–235.

(39) Liu, T.; Zhou, X.; Dupuis, M.; Li, C. The nature of photogenerated charge separation among different crystal facets of $BiVO_4$ studied by density functional theory. *Phys. Chem. Chem. Phys.* **2015**, *17*, 23503–23510.

(40) Zhu, J.; Pang, S.; Dittrich, T.; Gao, Y.; Nie, W.; Cui, J.; Chen, R.; An, H.; Fan, F.; Li, C. Visualizing the Nano Cocatalyst Aligned Electric Fields on Single Photocatalyst Particles. *Nano Lett.* **2017**, *17*, 6735–6741.

(41) Biesinger, M. C.; Payne, B. P.; Grosvenor, A. P.; Lau, L. W.; Gerson, A. R.; Smart, R. S. C. Resolving surface chemical states in XPS analysis of first row transition metals, oxides and hydroxides: Cr, Mn, Fe, Co and Ni. *Appl. Surf. Sci.* **2011**, *257*, 2717–2730.

(42) Mayer, B.; Uhlenbrock, S.; Neumann, M. XPS satellites in transition metal oxides. *J. Electron Spectros. Relat. Phenomena* **1996**, *81*, 63–67.

(43) Cabrera-German, D.; Gomez-Sosa, G.; Herrera-Gomez, A. Accurate peak fitting and subsequent quantitative composition analysis of the spectrum of Co 2p obtained with Al Kα radiation: I: cobalt spinel. *Surf. Interface Anal.* **2016**, *48*, 252–256.

(44) Weidler, N.; Paulus, S.; Schuch, J.; Klett, J.; Hoch, S.; Stenner, P.; Maljusch, A.; Brötz, J.; Wittich, C.; Kaiser, B.; Jaegermann, W. CoO_x thin film deposited by CVD as efficient water oxidation catalyst: change of oxidation state in XPS and its correlation to electrochemical activity. *Phys. Chem. Chem. Phys.* **2016**, *18*, 10708–10718.

(45) Yang, J.; Liu, H.; Martens, W. N.; Frost, R. L. Synthesis and Characterization of Cobalt Hydroxide, Cobalt Oxyhydroxide, and Cobalt Oxide Nanodiscs. *J. Phys. Chem. C* **2010**, *114*, 111–119.

(46) McIntyre, N. S.; Cook, M. G. X-ray photoelectron studies on some oxides and hydroxides of cobalt, nickel, and copper. *Anal. Chem.* **1975**, *47*, 2208–2213.

(47) Lin, F.; Boettcher, S. W. Adaptive semiconductor/electrocatalyst junctions in water-splitting photoanodes. *Nat. Mater.* **2014**, *13*, 81–86.

(48) McCrory, C. C. L.; Jung, S.; Peters, J. C.; Jaramillo, T. F. Benchmarking Heterogeneous Electrocatalysts for the Oxygen Evolution Reaction. *J. Am. Chem. Soc.* **2013**, *135*, 16977–16987.

(49) Liu, X.; Wang, X.; Yuan, X.; Dong, W.; Huang, F. Rational composition and structural design of in situ grown nickel-based electrocatalysts for efficient water electrolysis. *J. Mater. Chem. A* **2016**, *4*, 167–172.

(50) Rodríguez, J. L.; Valenzuela, M. A.; Tiznado, H.; Poznyak, T.; Flores, E. Synthesis of nickel oxide nanoparticles supported on SiO_2 by sensitized liquid phase photodeposition for applications in catalytic ozonation. *J. Mol. Catal. A Chem.* **2014**, *392*, 39–49.

(51) Chen, X.; Chen, W.; Lin, P.; Yang, Y.; Gao, H.; Yuan, J.; Shangguan, W. In situ photodeposition of nickel oxides on CdS for highly efficient hydrogen production via visible-light-driven photocatalysis. *Catal. Commun.* **2013**, *36*, 104–108.

(52) Choi, S. K.; Choi, W.; Park, H. Solar water oxidation using nickel-borate coupled $BiVO_4$ photoelectrodes. *Phys. Chem. Chem. Phys.* **2013**, *15*, 6499.

(53) Dang, K.; Chang, X.; Wang, T.; Gong, J. Enhancement of photoelectrochemical oxidation by an amorphous nickel boride catalyst on porous $BiVO_4$. *Nanoscale* **2017**, *9*, 16133–16137.

(54) Xu, Y.; Schoonen, M. A. A. The Absolute Energy Positions of Conduction and Valence Bands of Selected Semiconducting Minerals. *Am. Mineral.* **2000**, *85*, 543–556.

(55) Harris, D. C., *Quantitative Chemical Analysis*; W.H. Freeman: New York, 2015, p 928.

(56) Sivula, K.; Van De Krol, R. Semiconducting materials for photoelectrochemical energy conversion. *Nat. Rev. Mater.* **2016**, *1*, 15010.

(57) Grosvenor, A. P.; Biesinger, M. C.; Smart, R. S. C.; McIntyre, N. S. New interpretations of XPS spectra of nickel metal and oxides. *Surf. Sci.* **2006**, *600*, 1771–1779.

(58) Weidler, N.; Schuch, J.; Knaus, F.; Stenner, P.; Hoch, S.; Maljusch, A.; Schäfer, R.; Kaiser, B.; Jaegermann, W. X-ray Photoelectron Spectroscopic Investigation of Plasma-Enhanced Chemical Vapor Deposited NiO_x, $NiO_x(OH)_y$, and $CoNiO_x(OH)_y$: Influence of the Chemical Composition on the… *J. Phys. Chem. C* **2017**, *121*, 6455–6463.

(59) Biesinger, M. C.; Lau, L. W. M.; Gerson, A. R.; Smart, R. S. C. The role of the Auger parameter in XPS studies of nickel metal, halides and oxides. *Phys. Chem. Chem. Phys.* **2012**, *14*, 2434.

(60) Wang, Q.; Hisatomi, T.; Jia, Q.; Tokudome, H.; Zhong, M.; Wang, C.; Pan, Z.; Takata, T.; Nakabayashi, M.; Shibata, N.; Li, Y.; Sharp, I. D.; Kudo, A.; Yamada, T.; Domen, K. Scalable water splitting on particulate photocatalyst sheets with a solar-to-hydrogen energy conversion efficiency exceeding 1%. *Nat. Mater.* **2016**, *15*, 611–615.

(61) Mills, A.; Duckmanton, P. A.; Reglinski, J. A simple, novel method for preparing an effective water oxidation catalyst. *Chem. Commun.* **2010**, *46*, 2397.

(62) Barr, T. L.; Seal, S. Nature of the use of adventitious carbon as a binding energy standard. *J. Vac. Sci. Technol. A Vacuum, Surfaces, Film.* **1995**, *13*, 1239–1246.

(63) Abe, R.; Sayama, K.; Domen, K.; Arakawa, H. A new type of water splitting system composed of two different TiO_2 photocatalysts (anatase, rutile) and a IO_3^-/I^- shuttle redox mediator. *Chem. Phys. Lett.* **2001**, *344*, 339–344.

(64) Abe, R.; Higashi, M.; Domen, K. Overall Water Splitting under Visible Light through a Two-Step Photoexcitation between TaON and WO_3 in the Presence of an Iodate-Iodide Shuttle Redox Mediator. *ChemSusChem* **2011**, *4*, 228–237.

Chapter 5

Band Alignment of Heterostructured $BiVO_4$

5.1 Introduction

As described in the previous Chapter, $BiVO_4$ based devices should be carefully structured to overcome the inherent slow reaction kinetics and inefficient charge carrier separation of $BiVO_4$. Successful structuring strategies that have previously been identified are nanostructuring, co-catalyst deposition and creation of p-n junctions.[1–5] Combining these strategies with the incorporation of hexavalent ions, like Mo^{6+} or W^{6+}, have allowed $BiVO_4$ based photoanodes to achieve photocurrents which are among the highest that have been measured for photoanodes, admittedly using an external bias of 1.23 V_{RHE} or through coupling to a photovoltaic system.[3,6–8] To reach high efficiencies heterostructuring seems essential, however, the exact influence of a specific contact material on the water oxidation efficiency is not yet fully understood. Therefore, current research efforts focus on determining and quantifying the effects of heterostructuring to figure out whether surface passivation, improved reaction kinetics or enhanced charge carrier collection has the strongest influence on the efficiency of $BiVO_4$.

Especially cobalt and nickel containing compounds have been found to enhance the $BiVO_4$ water oxidation efficiency, whereas traditionally high performing noble metal based electrocatalysts have only been sparsely reported as $BiVO_4$ cocatalysts.[1–3,6,8–11] Diverse reasons have been stated for the good effects of the transition metal oxides ranging from improved kinetics,[9,10,12,13] suppression of surface recombination[10,14,15] and more efficient charge carrier separation.[14,16,17] However, many of those conclusions were drawn based on theoretical models or through techniques that cannot fully differentiate between surface passivation, oxidation kinetics and charge carrier recombination. Techniques which are able to elucidate specific effects of heterostructures include intensity modulated photocurrent spectroscopy (IMPS),[15] which can be used to distinguish between surface recombination and charge carrier injection, transient absorption spec-

troscopy (TAS),[17] which gives information on charge carrier dynamics, surface photovoltage spectroscopy (SPS),[18] which can determine the photovoltage and detect charge carrier trapping, and dual-working-electrode (DWE) photoelectrochemistry,[19] which is useful to study junction behaviour in situ.

Although, IMPS, TAS, SPS and DWE photoelectrochemistry may help to understand heterostructures, they are still "indirect" techniques in the sense that they give no direct information on the interfacial electronic band structure and how that affects the contact properties in the photoanode. Due to the apparent lack of straightforward experimental techniques, the interfacial contact properties are often estimated from the band positions before contact.[20–23] One way of determining the band positions before contact is through (electrochemical) flat band potential measurements at the point of zero zeta potential, whereby the Mott-Schottky analysis is used most often.[24–28] These band positions should, however, be carefully interpreted since the Mott-Schottky approach is based on several assumptions which are not always met experimentally.[29] Another way of estimating the band positions was popularised by Butler and Ginley, who derived empiric equations that allowed to estimate the valence band edge from the electronegativity of the semiconductor, which was calculated from the electronegativity of the constituent atoms of the semiconductor.[30] Xu et al. demonstrated that for many semiconductors the band edge positions obtained through flat band potential measurements or electronegativity calculations were the same or within a few 100 meV from each other.[31] However, Koffyberg et al. found that the Butler-Ginley equation only gave reliable valence band edge positions for transition metal oxides whose valence bands were mainly built up by O2p orbitals. When the valence band contained primarily contributions from the transition metal d-orbitals, valence band positions were calculated which did not correspond to experimentally determined valence band positions. The semiconductor band positions are often referenced with respect to the hydrogen reduction potential. Now, to obtain the interfacial alignment of two materials from the individual band positions one can subtract the energy level alignment with respect to the hydrogen evolution potential. However, this is not a direct measurement but assumes that band alignments are transitive. Up to now, this hypothesis has not been demonstrated yet for electrochemical alignments and has been proven to not be valid for classical semiconductors.[32] Moreover, this kind of interfacial band alignment neglects the actual surface and interface structures and the possibility of Fermi level pinning.

In this Chapter an alternative approach, based on the combination of thin film sputtering and photoelectron spectroscopy, for studying the interfacial alignment will be described with respect to $BiVO_4$ based heterostructures. This technique, which was first used by Waldrop and Kraut, gives direct information on the interfacial electronic structure.[33] A more detailed description of this technique can be found in Section 3.4.4.1. These so-called interface experiments were carried out with thin film $BiVO_4$ substrates, which were fabricated through magnetron sputtering and pulsed laser deposition. In the first Section of this Chapter the surface properties of these thin films will be described. Then, the results of the Waldrop and Kraut method will be revealed for

the $BiVO_4$/ITO, $BiVO_4$/RuO_2, $BiVO_4$/CoO_x and $BiVO_4$/NiO heterostructures. The contact materials were chosen because of two criteria. On the one hand, contact materials with different work functions were chosen, with ITO having a low work function and NiO, RuO_2 and CoO_x having high work functions.[34–36] On the other hand, the aforementioned contact materials were considered because of their role in $BiVO_4$ based devices, with NiO, CoO_x and RuO_2 being identified as performant oxidation electrocatalysts,[37] and ITO as a transparent conductive electrode that can serve as a back contact.[6,38]

5.2 $BiVO_4$ thin film substrates

5.2.1 Gradient $BiVO_4$

Two different $BiVO_4$ thin film substrates were used, which are denoted throughout the manuscript as gradient $BiVO_4$ thin films and as PLD $BiVO_4$ thin films. The gradient $BiVO_4$ thin film substrates were fabricated through reactive magnetron cosputtering. The complete experimental details can be found in Section 3.2. In this Subsection the characteristics of the gradient $BiVO_4$ thin films will be exhaustively described.

Due to the absence of sample rotation during the $BiVO_4$ thin film co-sputtering process, a lateral variation in the V/Bi composition is observed. Raman spectroscopy was used to identify the phases along the Bi/V gradient. Raman spectra at specific positions along the lateral Bi/V gradient are shown in Figure 5.1. Along the entire gradient, monoclinic $BiVO_4$ is observed as the main phase with characteristic bands at 127, 213, 328, 370, 712, 828 cm^{-1}.[39] Features at 828 and 712 cm^{-1} can be attributed to antisymmetric and symmetric stretching vibration modes of the VO_4 tetrahedra.[40] The bending modes of the VO_4 tetrahedra are the cause of the bands at 370 and 328 cm^{-1} whereas those at 213 and 147 cm^{-1} correspond to external modes[41] and crystal lattice vibration of $BiVO_4$.[40] In the V rich part of the film additional signals appear at 147, 287, 531, 997 cm^{-1}. These signals most likely correspond to the frequencies of the Raman active modes of orthorhombic V_2O_5.[39,42] Towards the middle of the film, at 10 mm distance from the Bi edge, no extra bands can be observed any more, which indicates that no other phases besides monoclinic $BiVO_4$ are present. The amount of noise increases while moving further to the Bi rich edge, making it difficult to distinguish any other phases besides monoclinic $BiVO_4$.

Photoelectron spectroscopy was used to study the surface composition and electronic properties of the gradient $BiVO_4$ thin films. First, the samples were cleaned by an oxygen plasma treatment to remove the upper contamination layer containing carbonaceous species and hydroxides. As can be seen in the XP survey spectra (Figure 5.2a) no core level emissions corresponding to carbon could be detected after the oxygen plasma treatment. Besides the removal of carbon from the surface, the oxygen plasma caused slight binding energy shifts but did not change the chemical composition of the film as can be noticed from the more detailed core level spectra of Bi4f, $V2p_{3/2}$ and O1s in Figure 5.2b.

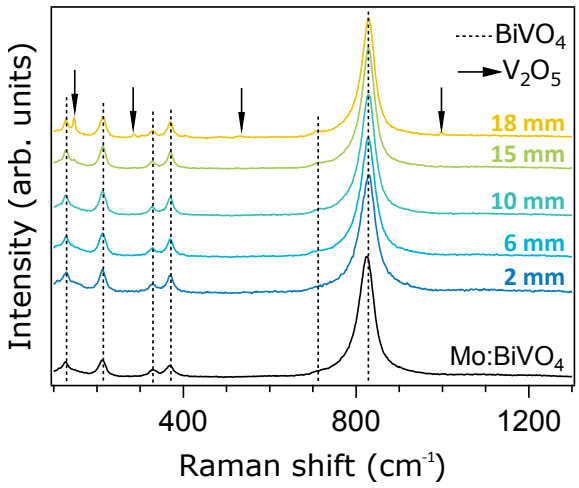

Figure 5.1: Raman spectra of a $BiVO_4$ gradient thin film and of a Mo:$BiVO_4$ single crystal. The Raman spectra of the gradient thin film were measured at specific distances from the Bi rich edge.

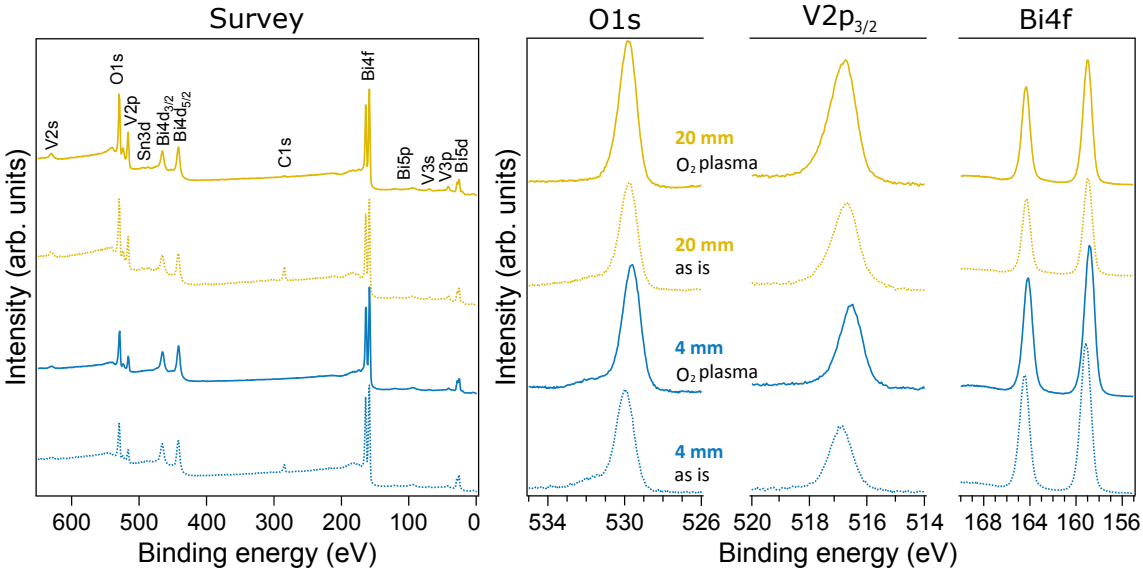

Figure 5.2: Survey and high resolution core level XP spectra of a gradient $BiVO_4$ thin film at specific distances from the Bi rich edge before and after oxygen plasma.

In Figure 5.3 X-ray photoelectron survey spectra were recorded with a spot size of 1 mm^2 along the Bi/V gradient. The main elements present at the film surface are Bi, V and O since the Bi4d, Bi4f, Bi5p, Bi5d, V2p, V3s, V3p and O1s core level emissions are detected at every measurement position. Additionally, at some positions a weak signal of the Sn3d core level was registered. The detection of tin is due to small holes between the grains of the $BiVO_4$ film that form during coalescence of the grains at elevated temperatures, exposing some of the underlying FTO layer.

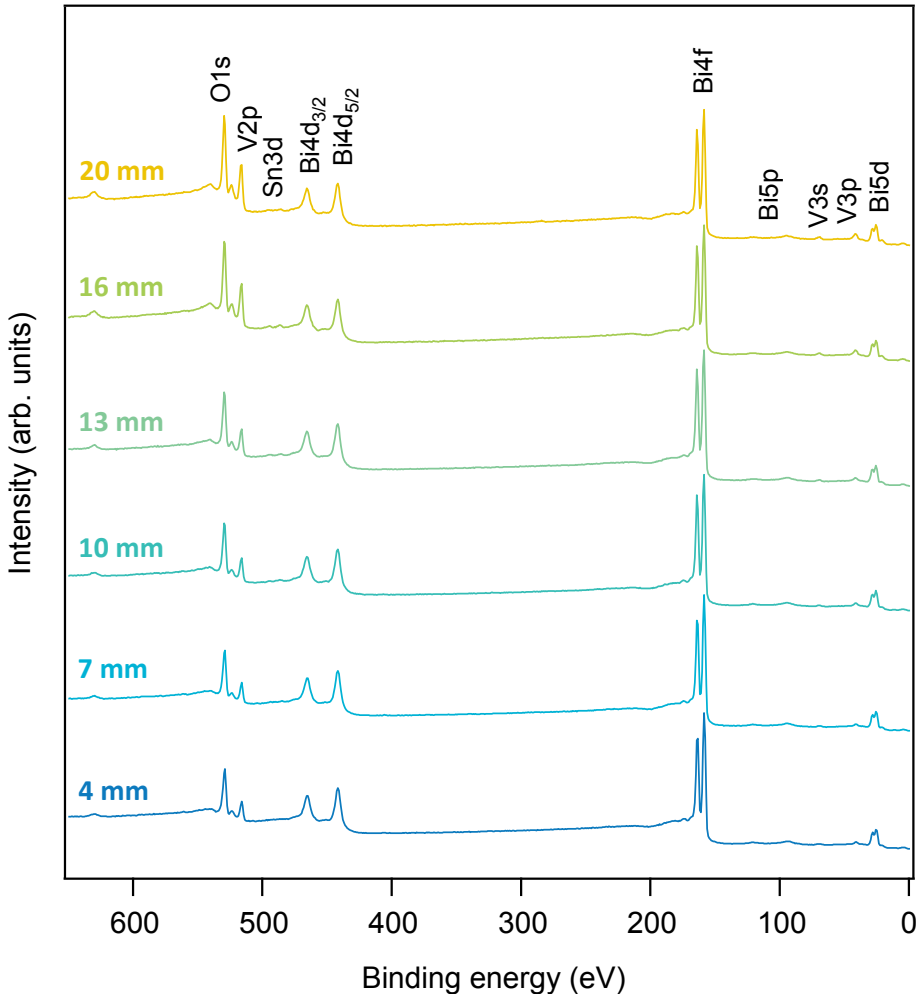

Figure 5.3: Survey XP spectra of a gradient $BiVO_4$ thin film at specific distances from the Bi rich edge along the entire sample width (22 mm).

More detailed core level spectra were recorded for Bi4f, $V2p_{3/2}$ and O1s (Figure 5.4). The $Bi4f_{7/2}$ core level binding energy is found around 159.0 eV, which matches to Bi^{3+} in $BiVO_4$ and the $V2p_{3/2}$ core level position around 516.7 eV is typical for V^{5+} in $BiVO_4$.[39] All core level binding energies shift towards higher energies with increasing V content in the film. Likely, part of the

energy shift is due to a change in Fermi level position, as the Bi4f and O1s spectra both shift similarly by 0.18 eV from Bi rich edge to V rich edge. However, the $V2p_{3/2}$ spectra shift 0.30 eV up in energy, which is slightly different from the other core level shifts, and is probably due to a change in surface chemistry. The change in surface chemistry can be due to the presence of V_2O_5, which was detected with Raman spectroscopy. The change in surface chemistry can be noticed in the valence band spectra as well, as the shoulder at a binding energy of 3 eV, which corresponds to the hybridised Bi6s/O2p state, decreases in intensity moving from Bi rich edge to V rich edge of the gradient $BiVO_4$ thin film, whereas the signal at 5.5 eV, which belongs to the V3d state, is more pronounced around the V rich edge.[43]

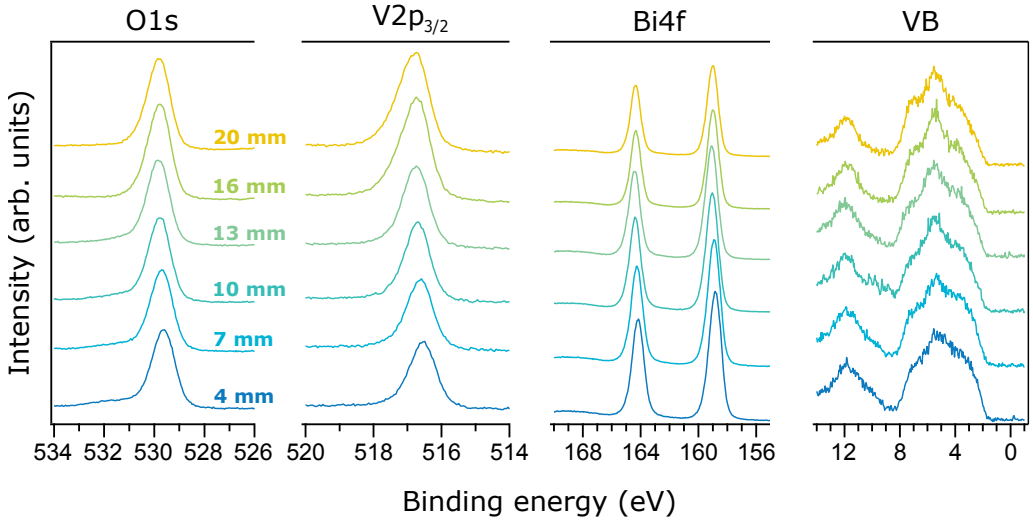

Figure 5.4: Bi4f, $V2p_{3/2}$, O1s core level and valence band XP spectra of a gradient $BiVO_4$ thin film at specific distances from the Bi rich edge along the entire sample width (22 mm).

The core level spectra were also used to determine the surface V/Bi ratio by integrating the areas of the Bi4f and $V2p_{3/2}$ core levels, and multiplying the integrated areas by the tabulated sensitivity factors, 7.632 and 1.275, respectively.[44] In Figure 5.5 the V/Bi ratios are shown as a function of the distance to the Bi rich edge of the film. Preferably, interface experiments are performed on stoichiometric $BiVO_4$ for which a V/Bi ratio of 1:1 would be expected. However, no position on the gradient $BiVO_4$ thin film exhibit a 1:1 V/Bi ratio: from 4 mm to 13 mm the V/Bi ratio increases almost linearly from 0.5 to 0.76, indicating a Bi rich surface, and at 15 mm from the Bi rich edge, a sudden V/Bi ratio increase to 1.4 can be noticed, indicating a V rich surface. The higher V/Bi ratio near the V rich edge is probably due to the presence of a vanadium oxide phase, as was detected by Raman spectroscopy.

However, during Raman spectroscopy no additional vibrations besides those of $BiVO_4$ were detected, so that the presence of a crystalline Bi rich phase seems unlikely. Possibly, the calculated V/Bi surface ratios differ from the actual V/Bi surface ratios, which can happen when the sensitivity factors used to calculate the V/Bi ratios, do not properly correct for the difference in

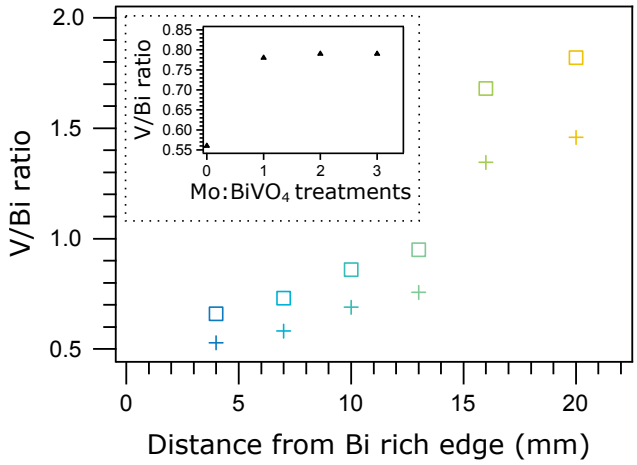

Figure 5.5: V/Bi surface ratio of a gradient $BiVO_4$ thin film using the tabulated sensitivity factors (crosses) and after applying the correction factor determined from the (010) exposed Mo:$BiVO_4$ single crystal (squares). In the inset the V/Bi ratio of the (010) Mo:$BiVO_4$ single crystal is shown after various treatments: 0: no treatment; 1: polished; 2: polished + 15 min O_2 plasma; 3: 2nd time polished + 15 min O_2 plasma.

detection probability of Bi4f and V2$p_{3/2}$ core electrons. Tabulated instrument-specific sensitivity factors were used, but it could be that they are not applicable to $BiVO_4$. As a matter of fact, whenever compounds with large cations were being studied with our surface analysis system improper surface stoichiometry was observed, as was the case for example for CdS.[45]

In order to determine whether the calculated V/Bi ratios are incorrect, a monoclinic 1% Mo doped $BiVO_4$ single crystal with a (010) exposed crystal facet was tested as a reference in our surface analysis system. The Raman spectrum of the Mo:$BiVO_4$ single crystal in Figure 5.1 confirms the monoclinic $BiVO_4$ phase, because the observed bands (at 127, 213, 328, 370, 712, 828 cm^{-1}) correspond to the Raman active modes expected for monoclinic $BiVO_4$.[39]

The single crystal was polished along the (010) surface to expose the internal structure, then introduced in the DAISY-MAT via a load lock and, subsequently, sputter cleaned with an oxygen plasma for 15 minutes. In Figure 5.6a the Bi4f, V2$p_{3/2}$ and valence band X-ray photoelectron spectra of the polished and sputter cleaned Mo:$BiVO_4$ single crystal are shown as well as those of a sputter cleaned gradient $BiVO_4$ thin film at 13 mm from the Bi rich edge. The Bi4f and V2$p_{3/2}$ spectra of the single crystal are shifted by about 0.2 eV towards higher binding energies and its E_F-E_{VBM} difference is measured at 2.2 eV, compared to the measured E_F-E_{VBM} of 1.8 eV of the gradient thin film. The shift towards higher binding energies could be due to a shift in the Fermi level position, originating from the Mo doping in the single crystal, or due to surface charging, because of a too low electrical conductivity of $BiVO_4$. The effect of surface charging can be clearly seen in the UP spectra of the corresponding samples (Figure 5.6b), where the E_F-E_{VBM} and secondary electron cut-off of the single crystal are shifted by about 2.5 eV towards higher binding energies, a shift too large to be caused exclusively by impurity doping. The observed

surface charging has, however, no effect on the XP core level areas, so that V/Bi surface ratios could still be reliably determined from the integrated $Bi4f_{7/2}$ and $V2p_{3/2}$ areas (inset Figure 5.5). After polishing and O_2 plasma exposure, a V/Bi ratio of 0.79 was obtained using the standard instrument sensitivity factors. This V/Bi ratio differs largely from the expected ratio of 0.99, considering that 1% of the vanadium lattice sites are substituted by molybdenum. Thus, the V/Bi surface ratios calculated from the tabulated sensitivity factors are most likely incorrect and should be adjusted by a correction factor. A correction factor of 1.25 can be calculated by dividing the expected surface V/Bi ratio of 0.99 through the calculated ratio of 0.79. Using this correction factor the surface V/Bi ratios for the gradient $BiVO_4$ thin films were calculated again (Figure 5.5). A V/Bi surface ratio of 0.95 is obtained at 13 mm from the Bi edge, which is close to stoichiometric $BiVO_4$. To obtain the bulk V/Bi ratio EDS was used. At 11 mm from the Bi rich edge a bulk V/Bi ratio of 1.02 was determined, thus, very similar to the surface V/Bi ratio (Figure 5.7). Closer to the V rich edge no increase in the bulk V/Bi ratio is observed with EDS, indicating that the V_2O_5 phase is probably limited to the $BiVO_4$ surface.

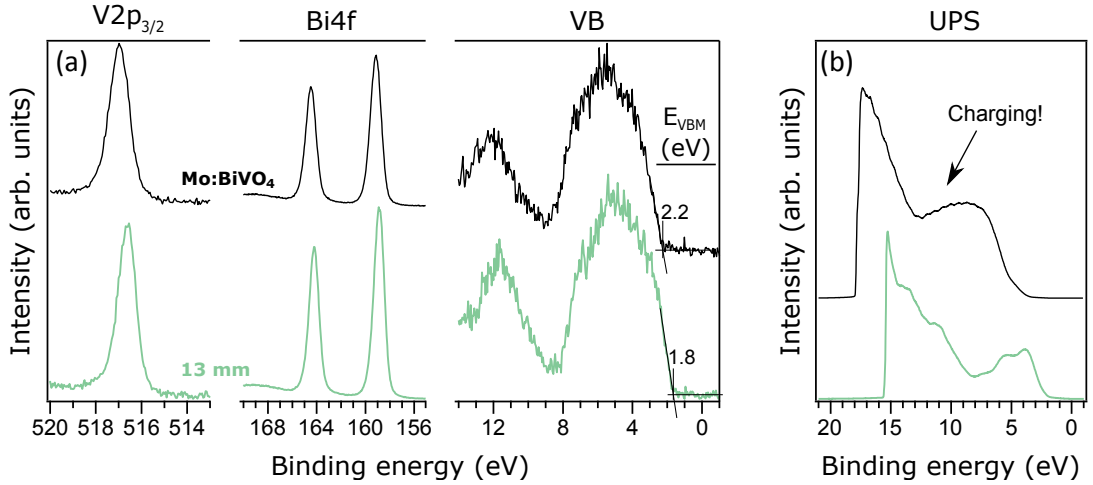

Figure 5.6: (a) $V2p_{3/2}$, Bi4f core level and valence band XP spectra and (b) UP spectra of the gradient $BiVO_4$ thin film at 13 mm from the Bi rich edge (green) and the polished (010) surface of the Mo:$BiVO_4$ single crystal (black). Both samples were cleaned by sputtering with an oxygen plasma.

From Raman, EDS and XPS measurements it can be concluded that at 13 mm distance from the Bi rich edge the gradient film consists of single phase monoclinic polycrystalline near-stoichiometric $BiVO_4$. Therefore, at 13 mm distance from the Bi rich edge all photoelectron spectra were measured that were used to evaluate the interface properties of the interface experiments carried out with the gradient $BiVO_4$ thin films.

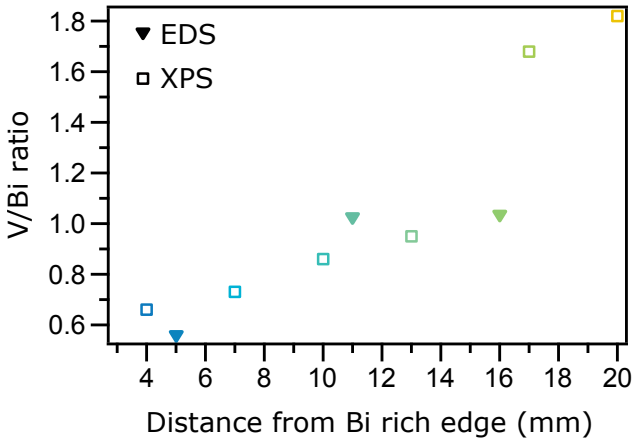

Figure 5.7: V/Bi ratio of gradient $BiVO_4$ thin film: determined from the Bi4f and $V2p_{3/2}$ XP core level areas after using the tabulated sensitivity factors and applying the correction factor determined from the (010) exposed Mo:$BiVO_4$ single crystal (squares) and determined through EDS after applying the correction factor (1.08) determined from the EDS measurements of (010) exposed Mo:$BiVO_4$ single crystal (triangles).

5.2.2 PLD $BiVO_4$

Part of the interface experiments were carried out using $BiVO_4$ thin films prepared through PLD. PLD $BiVO_4$ thin films were chosen after the complicated surface stoichiometry of the gradient $BiVO_4$ thin films was discovered. However, some time was needed to prepare those thin films, so that a first set of interface experiments was performed with the gradient $BiVO_4$ thin films. The exact synthesis conditions of the PLD $BiVO_4$ thin films can be found in Section 3.2. The PLD $BiVO_4$ thin films were prepared by our collaboration partners from the Institut de Recerca en Energia de Catalunya (IREC) who have published the structural and compositional characteristics of those thin films.[46] The reader is, thus, referred to this publication for additional details on the PLD $BiVO_4$ thin films.

In this Subsection, the surface analysis of the PLD $BiVO_4$ thin films is described as well as the differences with regards to the gradient $BiVO_4$ thin films. Murcia et al. characterised the PLD $BiVO_4$ thin films before, whereby PXRD revealed that the thin films were composed of phase pure $BiVO_4$ and EDS showed that the thin films had a bulk V/Bi ratio which was approximately 1:1.[46] Hence, the PLD $BiVO_4$ thin films seem to be more stoichiometric and homogeneous than the gradient $BiVO_4$ thin films.[46] To determine the surface V/Bi ratio, the $BiVO_4$ thin film substrates were mounted on a stainless steel substrate holder, introduced into the DAISY-MAT, cleaned with an oxygen plasma and analysed with our surface analysis set up. As can be seen in Figure 5.8a the C1s signal disappears after the oxygen plasma treatment, indicating that the oxygen plasma treatment effectively removed the upper contamination layer. Moreover, the $BiVO_4$ core level spectra (Figure 5.8b) show that the oxygen plasma did not induce a chemical change, only a small binding energy shift of about 0.15 eV for all core level spectra. The binding energies of 159.3

eV for $Bi4f_{7/2}$ and 517.0 eV for $V2p_{3/2}$ differ by 0.3 eV with respect to the $Bi4f_{7/2}$ and $V2p_{3/2}$ binding energies of the gradient $BiVO_4$ thin films, which is, however, still well within range of what can be expected for $BiVO_4$.[39] A series of PLD $BiVO_4$ thin film samples was analysed by photoelectron spectroscopy and the V/Bi surface ratios of these samples were calculated (Table 5.1). Again, the tabulated surface sensitivity factors were not appropriate for calculating the surface V/Bi ratio. Thus, the correction factor determined with the Mo:doped $BiVO_4$ single crystal (Section 5.2.1) was used to obtain more accurate surface V/Bi ratios. Some variation in the V/Bi ratio was observed with some films being apparently vanadium deficient. However, difference spectra of Bi4f and $V2p_{3/2}$ between films with different V/Bi ratios did not show any dissimilarities between the spectra. In addition, only a variation of about 0.15 eV is observed for the $\Delta BE_{V2p_{3/2},Bi4f_{7/2}}$ binding energy difference. Therefore, the measured off-stoichiometry is not likely due to the presence of additional crystalline phases.

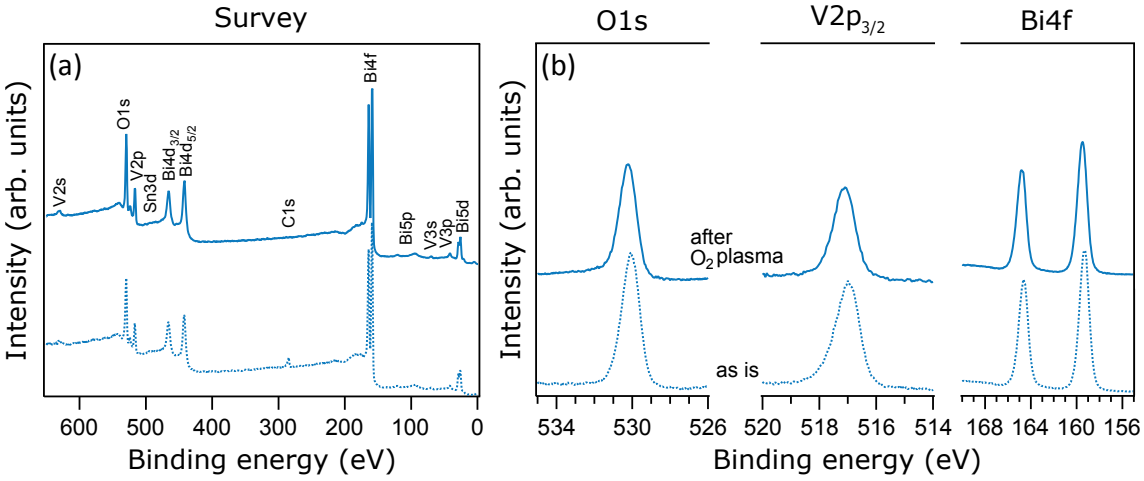

Figure 5.8: (a) Survey and (b) high resolution core level XP spectra of a PLD $BiVO_4$ thin film before and after oxygen plasma.

5.2.3 PES on bare $BiVO_4$ thin films

Figure 5.9 summarizes all photoelectron spectra which were measured on bare (no contact layers) $BiVO_4$ thin film substrates for which reasonable V/Bi surface ratios were determined. Reasonable V/Bi ratios here means ratios between 0.64 and 0.96 or between 0.8 and 1.2 after the 1.25 correction factor was applied. The $Bi4f_{7/2}$, $V2p_{3/2}$ and O1s binding energies all linearly correlate with one another with slopes close to 1, as is expected for samples whose chemical structure does not change. Thus, interface experiments using $BiVO_4$ thin film substrates with a corrected V/Bi surface ratio between 0.8 — 1.2 are all considered to be representative for $BiVO_4$. The linear correlation of E_F-E_{VBM} with the core level binding energies is less clear, since R^2 is quite low for the linear fitting of the data points in the E_F-E_{VBM} vs $BE_{Bi4f_{7/2}}$ plot. The low R^2 is partly due to the lower precision of the E_F-E_{VBM} determination, through linear extrapolation, compared to the

Table 5.1: Areas of Bi4f and $V2p_{3/2}$ core levels, calculated surface V/Bi ratios, and $V2p_{3/2}$ to $Bi4f_{7/2}$ binding energy difference for a series of PLD $BiVO_4$ thin films.

n^0	Bi4f	$Bi4f_{tab.}$	$V2p_{3/2}$	$V2p_{3/2,tab.}$	xBi	xV	V/Bi	$V/Bi_{corr.}$	$\Delta BE_{V2p_{3/2},Bi4f_{7/2}}$ (eV)
1	48488	6353	6068	4759	0.57	0.43	0.75	0.94	357.68
2	43087	5646	5422	4253	0.57	0.43	0.75	0.94	357.69
3	63905	8373	7361	5773	0.59	0.41	0.69	0.86	357.80
4	67541	8850	7754	6082	0.59	0.41	0.69	0.86	357.64
5	43777	5736	5694	4466	0.56	0.44	0.78	0.97	357.72
6	40231	5271	5244	4113	0.56	0.44	0.78	0.98	357.67
7	47049	6165	5369	4211	0.59	0.41	0.68	0.85	357.69
-	-	-	-	Mean	0.58	0.42	0.73	0.91	357.70

$Bi4f_{tab.}$ and $V2p_{3/2,tab.}$ are the respective Bi4f and $V2p_{3/2}$ areas divided by the tabulated sensitivity factors 7.632 and 1.275, respectively, whereby the surface V/Bi ratios were calculated from these areas. $V/Bi_{corr.}$ ratio was calculated by multiplying the V/Bi ratio with the correction factor 1.25 determined from the XPS measurements on the (010) exposed Mo:$BiVO_4$ single crystal.

core level binding energy determination, through peak maximum fitting. Another reason could be that there is also a small chemical shift of the binding energies, which is not unreasonable since the data were collected on samples before and after cleaning the surface. Anyhow, the overall difference in the shift between core level binding energies and E_F-E_{VBM} is smaller than the shift itself. The shift of the O1s, $Bi4f_{7/2}$ and $V2p_{3/2}$ binding energies, seen for all samples, amounts to 0.35 eV, whereas the E_F-E_{VBM} amounts to 0.29 eV. Hence, the shift in the core level binding energies is mostly due to band bending or due to a shift in the Fermi level position. Both possibilities are reasonable considering that the different surface treatments can alter the number of surface states and the number of oxygen vacancies. Oxygen vacancies can alter the $BiVO_4$ Fermi level position as DFT calculations have shown that they act as shallow donors in $BiVO_4$.[47,48] The small discrepancy between the E_F-E_{VBM} shift and the core level binding energy shift can be due to the aforementioned relative imprecision of the E_F-E_{VBM} determination or due to small changes in the valence band structure around the VBM.

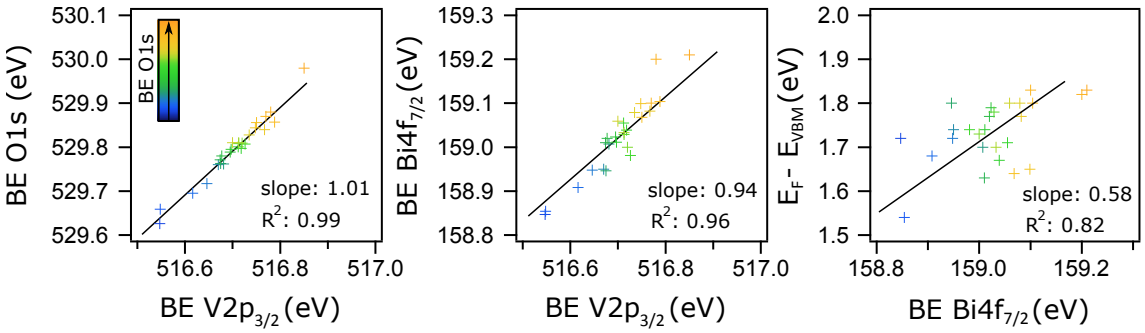

Figure 5.9: Summary of photoelectron spectroscopy analysis on $BiVO_4$ thin film substrates by plotting the determined binding energies of O1s, $V2p_{3/2}$, $Bi4f_{7/2}$ and E_F-E_{VBM} relative to one another.

To verify whether the valence band structure stays the same, the O1s, $V2p_{3/2}$, $Bi4f_{7/2}$ and valence band difference spectra of two samples, one with high core level binding energies and one with low core level binding energies, were determined (Figure 5.10). No significant change in the valence band, $Bi4f_{7/2}$ or $V2p_{3/2}$ XP spectra can be seen. Only in the O1s region a signal at 531.2 eV can be observed for the sample with high core level binding energies. Some authors suggest that the signal at 531.2 eV is representative for oxygen vacancies.[49,50] Another possibility is that peroxo-species, also found around 531.2 eV,[51] were formed due to the sample being treated by an oxygen plasma. For other non-cleaned samples, an O1s signal around 531 eV, is often related to the presence of hydroxyl and carbonyl groups.

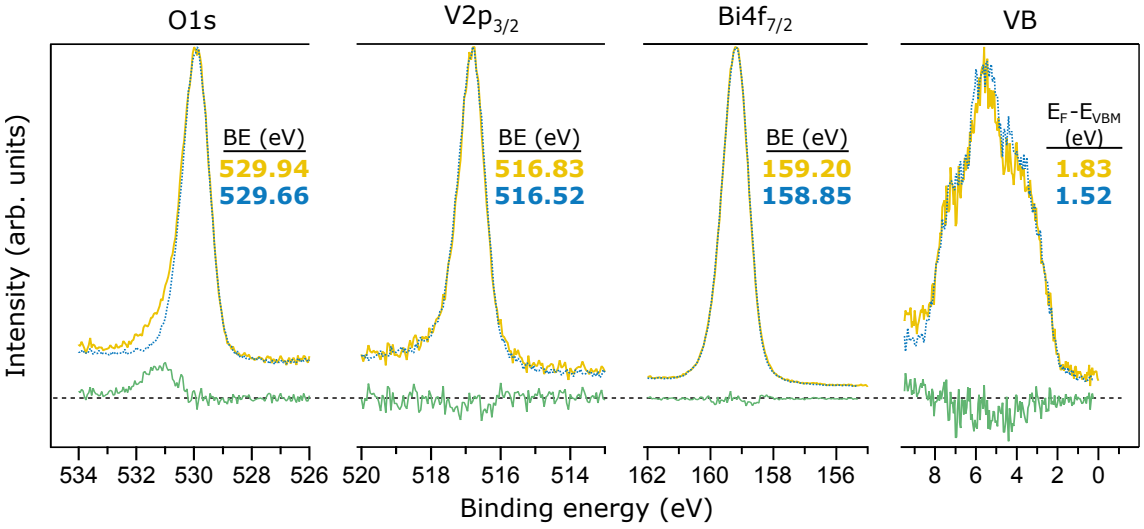

Figure 5.10: Difference spectra of O1s, $V2p_{3/2}$, $Bi4f_{7/2}$ and valence band of a sample with a high O1s binding energy (gradient $BiVO_4$ after 15 min oxygen plasma (yellow) and a sample with a low O1s binding energy (PLD $BiVO_4$ after 2 h of heating at 400 °C in oxygen atmosphere (blue). The spectra were normalized and shifted to the same binding energy.

5.3 Interface alignment

5.3.1 Interface experiments

With the surface stoichiometry of the different polycrystalline $BiVO_4$ thin film substrates fully characterised, interface experiments were carried out to elucidate the interface structure between the $BiVO_4$ thin films and a few selected contact materials. All the procedural steps of an interface experiment are described in Section 3.4.4.1. In short, in a typical interface experiment a $BiVO_4$ thin film substrate was first introduced into the DAISY-MAT system, after which the surface was cleaned through an oxygen plasma treatment, followed by a stepwise coverage of another thin film oxide through magnetron sputtering. Photoelectron spectra were recorded in between each

deposition step. By analysing the change in the high resolution photoelectron spectra of the $BiVO_4$ core levels, information could be gathered about the in situ formed junction. Due to the samples being transferred in UHV between deposition and analysis no surface contamination could take place. The deposition parameters of the selected contact films can be found in Section 3.2.2. In this Subsection the results of the $BiVO_4/RuO_2$ and $BiVO_4$/ITO interface experiments, carried out with the gradient $BiVO_4$ thin film substrates, and the $BiVO_4/CoO_x$ and $BiVO_4$/NiO interface experiments, performed with PLD $BiVO_4$ thin films, are described.

First, the interface between $BiVO_4$ and RuO_2 was studied. In Figure 5.11 the X-ray photoelectron Bi4f, $V2p_{3/2}$, O1s, Ru3d core level and valence band spectra after each RuO_2 deposition step are shown. The growing RuO_2 film thickness is noticeable from the increasing Ru3d core level line intensity, the decreasing intensity of the Bi4f and $V2p_{3/2}$ core level lines and the O1s intensity not changing much with each RuO_2 deposition step. The spectral features as measured for the growing RuO_2 films are in good agreement to spectra measured before for RuO_2 samples.[35,52] Normally, to investigate how the energy bands between semiconducting $BiVO_4$ and metallic RuO_2 align, the change in valence band maximum (VBM) of $BiVO_4$ should be followed, which is, however, not feasible here, due to the superposition of the $BiVO_4$ and RuO_2 valence band spectra. Therefore, the changing VBM has to be evaluated from the binding energy shift of the $BiVO_4$ core levels, a method commonly referred to as the Kraut method.[33] Both Bi4f and $V2p_{3/2}$ core levels exhibit a similar downwards binding energy shift of 0.71 eV, which was confidently attributed to a $BiVO_4$ Fermi level change, caused by RuO_2 induced band bending.

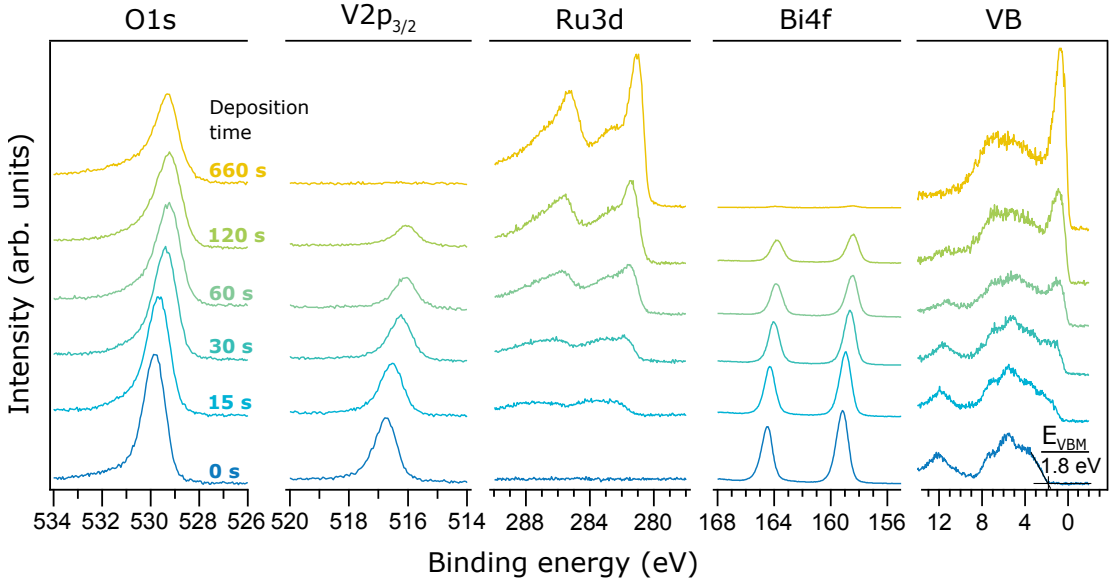

Figure 5.11: O1s, $V2p_{3/2}$, Ru3d, Bi4f core level and valence band XP spectra for the $BiVO_4/RuO_2$ interface. RuO_2 deposition times are denoted in the O1s spectra.

Next, the interface between ITO and $BiVO_4$ was investigated with ITO deposited at room

temperature. The XP Bi4f, $V2p_{3/2}$, O1s, $In3d_{3/2}$ core level and valence band spectra for the stepwise sputter deposition of ITO on $BiVO_4$ are displayed in Figure 5.12. As the In3d core level intensity increases, the Bi4f, $V2p_{3/2}$ core level intensity drops, while the O1s core level intensity remains approximately constant. In contrast to the RuO_2 deposition, the $Bi4f_{7/2}$ and $V2p_{3/2}$ core levels shift to higher binding energies after ITO deposition, which is expected regarding the substantially lower work function of ITO compared to that of RuO_2. After the first deposition step the $V2p_{3/2}$ and $Bi4f_{7/2}$ spectra both shift by approximately 0.16 eV. Thereafter, both spectra stay around the same value with increasing film thickness. Due to both $V2p_{3/2}$ and Bi4f spectra shifting in the same way, this shift is likely to be caused by downward band bending. Also, in the $V2p_{3/2}$ spectrum a signal at a lower binding energy seemingly appears after the first ITO deposition step, which may indicate a reduction of V^{5+} to V^{4+}. Further in this Chapter a closer look is taken at this feature. The final 452.3 eV $In3d_{3/2}$ binding energy is typical for ITO,[53] as well as the valence band spectral features observed here for the growing ITO film.[35,54]

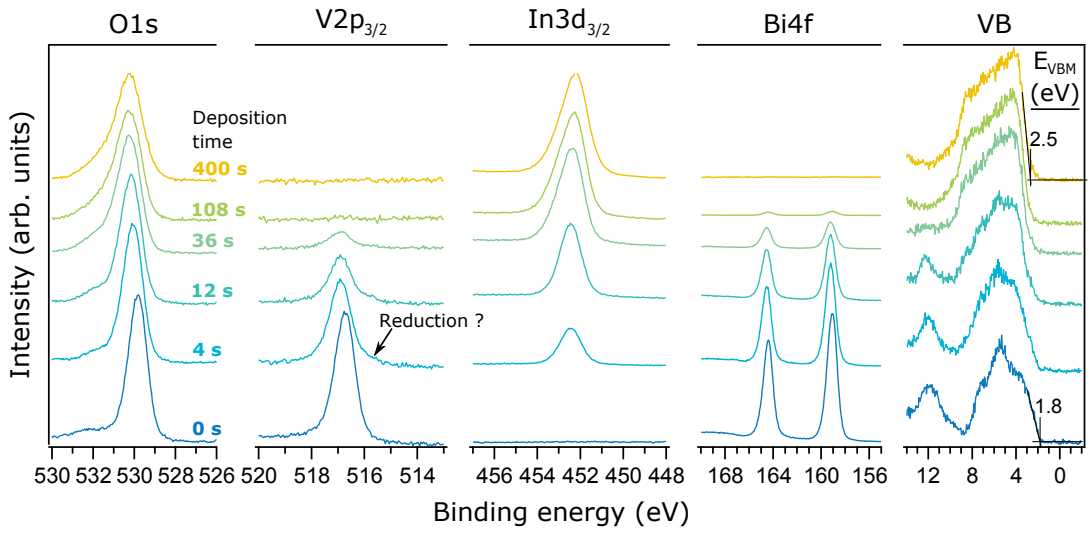

Figure 5.12: O1s, $V2p_{3/2}$, $In3d_{3/2}$, Bi4f core level and valence band XP spectra for $BiVO_4$/ITO(RT) interface. ITO deposition times are denoted in the O1s spectra.

Since the ITO deposited at room temperature was not yet degenerately doped, a second $BiVO_4$/ITO interface experiment was performed, but this time the $BiVO_4$ substrate was heated to 400 °C before each ITO deposition step, while maintaining a pure argon atmosphere during heating and cooling down. In this way, the amount of oxygen vacancies in ITO and, thus, the Fermi level position could be increased. Indeed, for ITO now the E_F-E_{VBM} amounts to a value of 2.8 eV (see Figure 5.13), indicating that the Fermi level coincides with the CBM, considering a 2.8 eV band gap.[55] This ITO interface experiment again demonstrates that the $Bi4f_{7/2}$ and $V2p_{3/2}$ spectra shift towards higher binding energies. More precisely, a shift of 0.30 eV can be observed after the first deposition step after which the Bi4f and $V2p_{3/2}$ core level spectra do not shift any more with further ITO deposition steps. As was observed for the interface experiment with ITO

deposited at room temperature, an additional signal seems to appear at a lower binding energy in the $V2p_{3/2}$ spectrum after the first ITO deposition step. Moreover, in the Bi4f spectrum two additional signals appear as well, whereby the signal at 157.1 eV is characteristic for metallic bismuth.[44] Further in this Chapter the apparent reduction of the bismuth vanadate substrate due to the contact with ITO will be discussed.

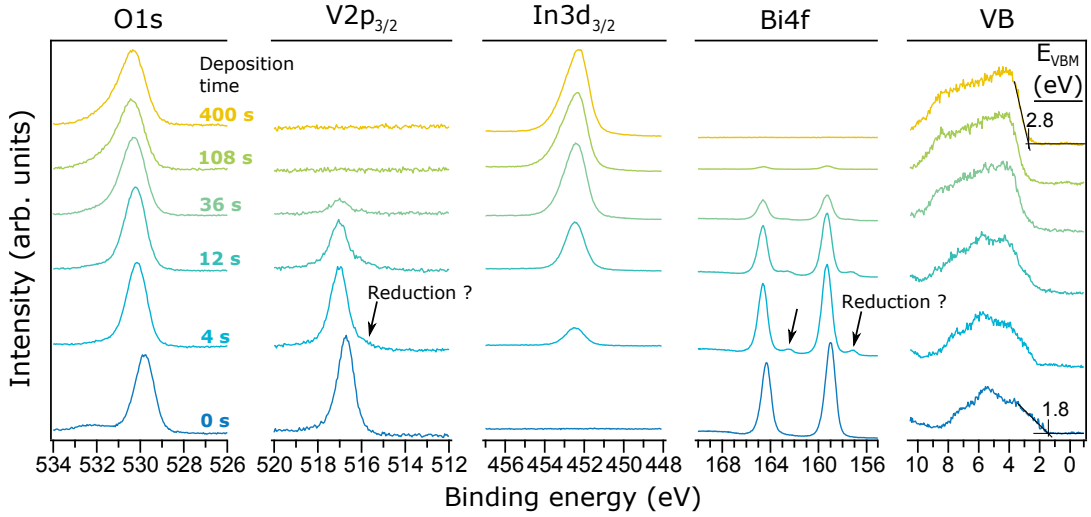

Figure 5.13: O1s, $V2p_{3/2}$, $In3d_{3/2}$, Bi4f core level and valence band XP spectra for $BiVO_4$/ITO(400 °C) interface. ITO deposition times are denoted in the O1s spectra.

Next, NiO was gradually sputtered on top of a PLD $BiVO_4$ thin film (Figure 5.14). The NiO deposition is noticeable from the increasing Ni2p core level line intensity, the decreasing intensity of the Bi4f and $V2p_{3/2}$ core level lines and the O1s intensity not changing much with each NiO deposition step. The first deposition step of 5 s, already induces a strong upward binding energy shift of 0.6 eV and a strong attenuation of the Bi4f and $V2p_{3/2}$ core level emissions. The strong decrease in Bi4f and $V2p_{3/2}$ core level intensity is likely caused by a relatively thick NiO film being deposited during the first deposition step. From the differently attenuated $V2p_{3/2}$ and Bi4f photoelectrons, the contact layer thickness can be calculated[i] and, indeed, a relatively thick 1.3 nm NiO film seems to be deposited after the first 5 s deposition step (Figure 5.15). After the second deposition step, the Bi4f and $V2p_{3/2}$ core level spectra shift an additional 0.1 eV. Afterwards, no more shifts are observed for further deposition steps. After a total deposition time of 8 min a

[i] Due to the Bi4f photoelectrons having a higher kinetic energy than the $V2p_{3/2}$ photoelectrons, the inelastic mean free path of the Bi4f photoelectrons is larger, so that the attenuation of Bi4f photoelectrons is lower. The thickness of a thin film deposited on top of a $BiVO_4$ substrate can then be evaluated, under the assumption that the surface V/Bi ratio does not change during film growth, according to following formula: $t = \frac{ln(\frac{I_V * I_{Bi,0}}{I_{Bi} * I_{V,0}}) * \lambda_V * \lambda_{Bi}}{\lambda_V - \lambda_{Bi}}$ with t: film thickness; I_V: integrated $V2p_{3/2}$ core level intensity at film thickness t; I_{Bi}: integrated Bi4f core level intensity at film thickness t; $I_{V,0}$: integrated $V2p_{3/2}$ core level intensity at zero film thickness; $I_{Bi,0}$: integrated Bi4f core level intensity at zero film thickness; λ_V: electron effective attenuation length of $V2p_{3/2}$ photoelectrons; λ_{Bi}: electron effective attenuation length of Bi4f photoelectrons. The electron effective attenuation lengths were calculated using the "NIST Electron Effective-Attenuation-Length Database", based on the density, number of valence electrons and band gap of the deposited film.

rather thick NiO layer has been deposited. As a consequence no Bi4f and $V2p_{3/2}$ photoelectrons could be detected any more. The Ni2p spectrum measured after the last deposition step shows a main line and satellite structure typical for NiO.[56] Therefore, the nickel based contact layer can be assumed to be NiO. In the O1s spectrum after the last deposition step a main emission line at 529.5 eV and a smaller one at 531.5 eV can be observed. Dupin et al. have observed similar shoulders in the O1s spectrum of other transition metal oxides, which they ascribed to O^- species. The O^- species were believed to originate from oxygen sites where oxygen has a decreased coordination.[51]

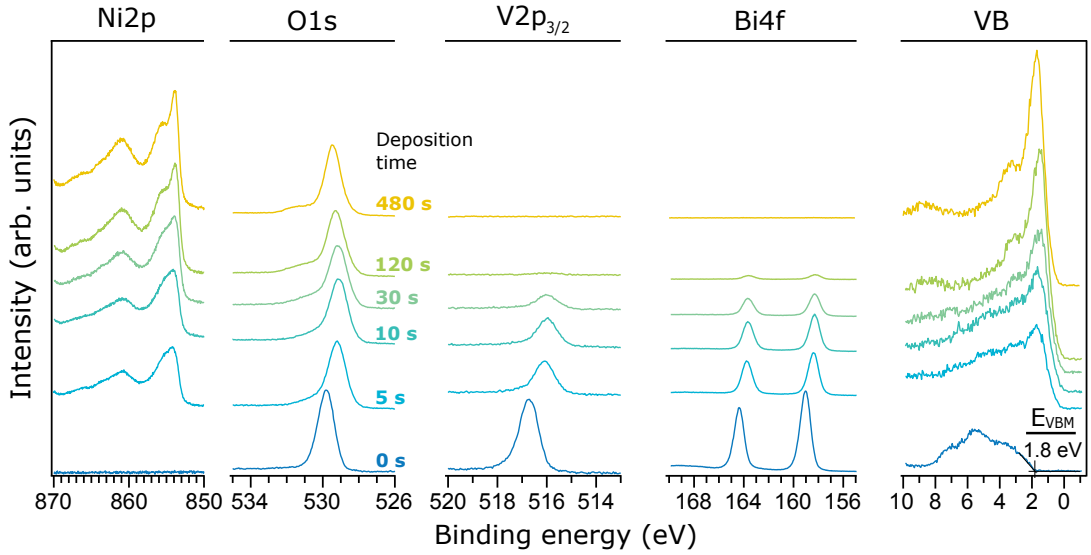

Figure 5.14: Ni2p, O1s, $V2p_{3/2}$, Bi4f core level and valence band XP spectra for the $BiVO_4$/NiO interface. NiO deposition times are denoted in the O1s spectra.

In the final interface experiment, a CoO_x contact layer was stepwise sputtered on top of $BiVO_4$ (Figure 5.16). The $Bi4f_{7/2}$ and $V2p_{3/2}$ binding energies, 158.7 eV and 516.4 eV, respectively, are 0.3 eV lower compared to the ones measured for the other $BiVO_4$ substrates. These slightly lower binding energies are most likely due to a shift of the Fermi level, as the $BiVO_4$ valence band maximum (E_F-E_{VBM}) of this substrate is situated at an 0.3 eV lower position as well, at 1.5 eV. Similar to the $BiVO_4$ interfaces with nickel oxide and ruthenium oxide, the Bi4f and $V2p_{3/2}$ spectra shift towards lower binding energies as a reaction to the contact with the cobalt oxide contact layer. The binding energy shift is less drastic compared to the $BiVO_4$/NiO experiment due to CoO_x being deposited at a lower rate, which is also noticeable from the $Bi4f_{7/2}$ and $V2p_{3/2}$ line intensities not dropping strongly after the first deposition step. The $Bi4f_{7/2}$ and $V2p_{3/2}$ binding energies both shift in a similar fashion by 0.45 eV, seen over all deposition steps. After 1 h of sputtering a sufficiently thick CoO_x layer was obtained, so that the $Bi4f_{7/2}$ and $V2p_{3/2}$ core level photoelectrons could not be detected any more. Co^{2+} and Co^{3+} can be distinguished from each other in the satellite structure of the Co2p spectrum with a Co^{2+} feature being apparent at a binding energy of 786 eV and Co^{3+} at 789 eV.[57] Here, both features are clearly visible, which

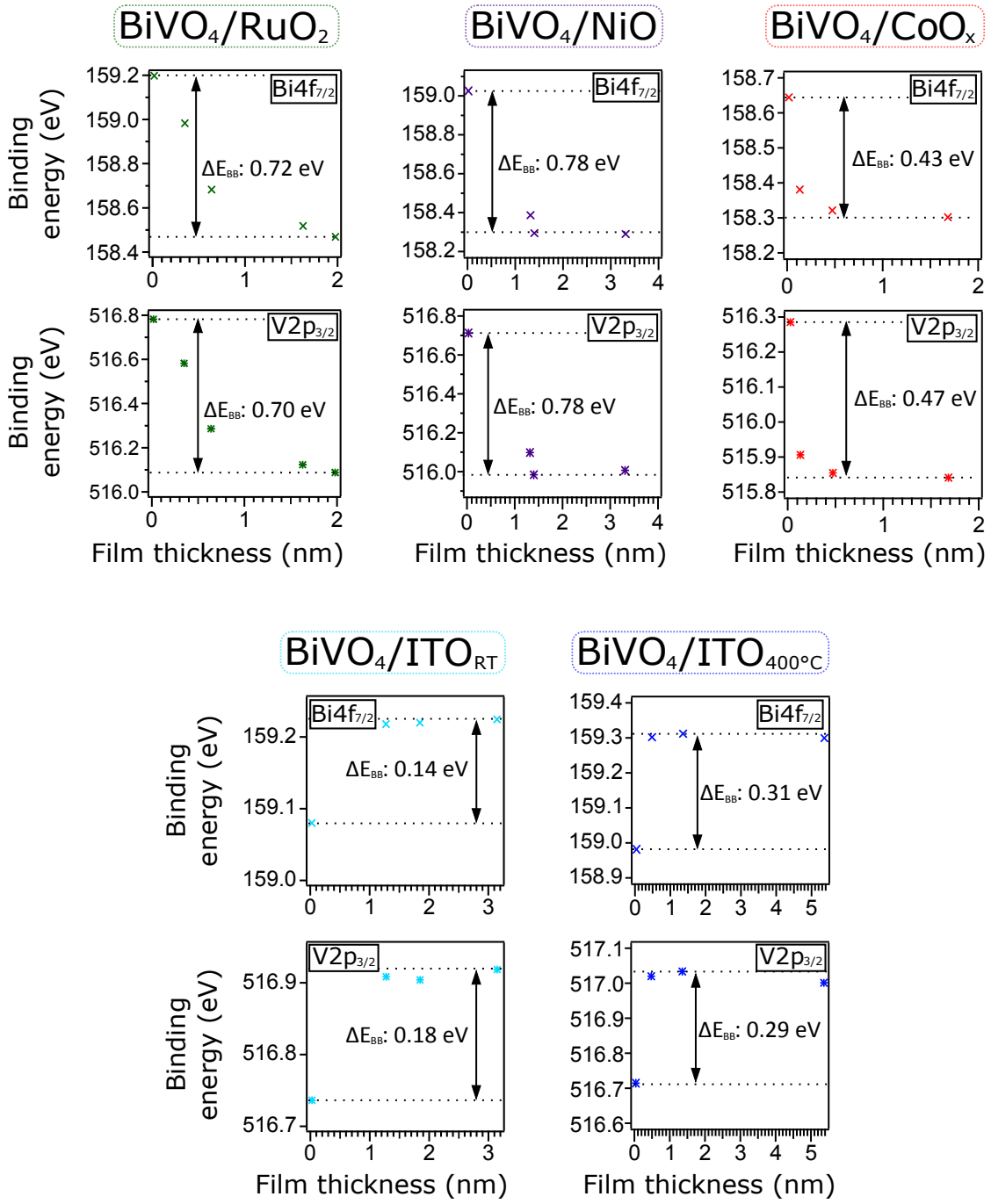

Figure 5.15: Evolution of the $Bi4f_{7/2}$ and $V2p_{3/2}$ core level binding energies with respect to the contact layer thickness for the $BiVO_4$/ITO, $BiVO_4/RuO_2$, $BiVO_4$/NiO and $BiVO_4/CoO_x$ interface experiments. The thickness was estimated according to Equation 3.8 as explained in Section 3.4.4.1.

indicates that the deposited cobalt oxide is a mixed oxide. Also, the valence band spectrum resembles the valence band spectrum of a mixed cobalt oxide.[58] Therefore, the deposited cobalt oxide film is denoted as CoO_x. Off course, Co_3O_4 also yields both Co^{2+} and Co^{3+}. However, due to the CoO_x thin film deposition being performed at room temperature, the thin film was assumed to be amorphous. Thus, it cannot be associated to Co_3O_4, which is a crystalline structure with a particular stoichiometry.

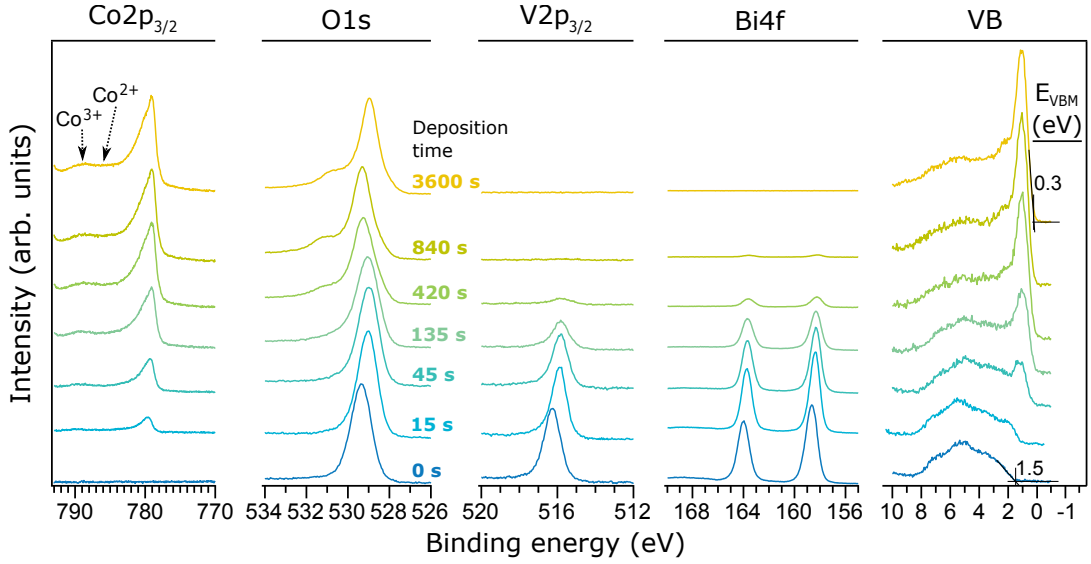

Figure 5.16: $Co2p_{3/2}$, O1s, $V2p_{3/2}$, Bi4f core level and valence band XP spectra for the $BiVO_4/CoO_x$ interface. CoO_x deposition times are denoted in the O1s spectra.

Additionally, ultraviolet photoelectron spectra were recorded for all $BiVO_4$ thin films and contact materials (Figure 5.17). The secondary electron cut-offs in the UP spectra were used to determine the work functions. The work function of the $BiVO_4$ substrates, used for the RuO_2, ITO and NiO interface experiments, can be found at 5.6 — 5.9 eV, whereas a 6.6 eV work function is determined for the substrate used in the $BiVO_4/CoO_x$ interface experiment. This higher work function finds again its origin in the lower Fermi level position of this substrate, which is here also noticeable in the valence band region of the $BiVO_4$ UP spectrum. The work function of RuO_2 was found to be 6.5 eV, similar to earlier published values.[59,60] Work functions of 5.4 eV and 5.7 eV were determined for NiO and CoO_x, respectively. These work functions agree with earlier determined values within our group.[61,62] However, Greiner et al. measured work functions between 6 eV and 7 eV for NiO and Co_3O_4 after an extensive photoelectron spectroscopic analysis of the first row transition metal oxides.[34] Prior, Greiner et al. found that NiO thin films prepared through in situ oxidation yielded work functions up to 6.7 eV, which, however, dropped below 6.0 eV over time in vacuum, which the authors explained by the adsorption of residual gases in the vacuum.[63] A similar effect could take place on sputtered CoO_x thin films. Additionally, as was explained above, an extra line besides the main O^{2-} line was observed in the O1s spectrum of the CoO_x and

NiO thin films, which could be due to O^- species in the subsurface.[51] Reasonably, these species could create a positive dipole at the surface and, thus, be the cause of a lower than expected work function. Since the NiO VBM could not be unambiguously determined from the XP valence band spectrum, the UP spectrum was used instead. A NiO VBM of 0.4 eV was obtained, confirming the p-type character of the NiO film. A 4.4 eV and 4.5 eV work function were found for ITO(RT) and ITO(400 °C), respectively, which should actually be higher, considering the relatively low Fermi level positions of 2.5 eV and 2.8 eV and the correlation between Fermi level position and work function suggested by Klein et al.[64] Possibly, this dissimilarity in measured and expected work function indicates a surface dipole at the ITO surface.

5.3.2 Band diagrams

The $Bi4f_{7/2}$ and $V2p_{3/2}$ core level binding energy shifts for all interface experiments can be found in Figure 5.15 and are represented more visually appealing in Figure 5.18. The $Bi4f_{7/2}$ and $V2p_{3/2}$ binding energies for the $BiVO_4$/NiO, $BiVO_4$/RuO_2, $BiVO_4$/ITO(RT) and $BiVO_4$/ITO(400 °C) interface experiment shift in a similar way, which indicates an electronic shift, i.e. Fermi level position shift, rather than a chemical shift. The shift is less coherent for the $BiVO_4$/CoO_x interface experiment. First of all, the initial binding energy positions differ from the other substrates which, as explained above, is most likely due to a different doping level in this $BiVO_4$ substrate. Additionally, the $Bi4f_{7/2}$ binding energy shift is 40 meV lower than the $V2p_{3/2}$ shift, so that chemical changes during the CoO_x deposition are not unlikely. Since CoO_x was reactively sputtered in an oxygen atmosphere part of the cobalt ions reaching the $BiVO_4$ could extract oxygen atoms from the surface instead from the sputtering atmosphere. Nevertheless, the 40 meV difference is relatively small compared to the overall 0.45 eV shift, meaning that the observed binding energy shift originates mainly from an electronic shift. Also remarkable is that the binding energy shift for all contact materials, besides RuO_2, is quite abrupt, indicating that a very thin contact layer (see Figure 5.15 for thickness estimations) already fixes the electronic properties of the junction.

The most important energetic values of the interface experiments are summarised in Table 5.2 and based on this accumulated photoelectron spectroscopy data complete energy band diagrams can be constructed for all the studied interfaces. To construct these band diagrams, the band gaps 2.4 eV for $BiVO_4$, 2.8 eV for ITO and 3.6 eV for NiO were taken from literature.[55,65,66] The band gap of CoO_x is somewhat chosen arbitrarily since the exact stoichiometry is not known and because widely varying band gaps have been published for mixed cobalt oxides, for instance the optical band gap of Co_3O_4 has been found to range between 0.8 — 2.5 eV.[58,62,67,68] The energy band diagrams displayed in Figure 5.19 and Figure 5.20 include the vacuum energy levels of the materials, which are derived from work function measurements using UPS. According to the measured work functions, the vacuum energies of $BiVO_4$ and RuO_2 are aligned, while there is a dipole potential step of about 1 eV between $BiVO_4$ and ITO (RT and 400 °C), and a dipole potential step of 1.3 eV for the $BiVO_4$/CoO_x and $BiVO_4$/NiO. The dipole potential step for the

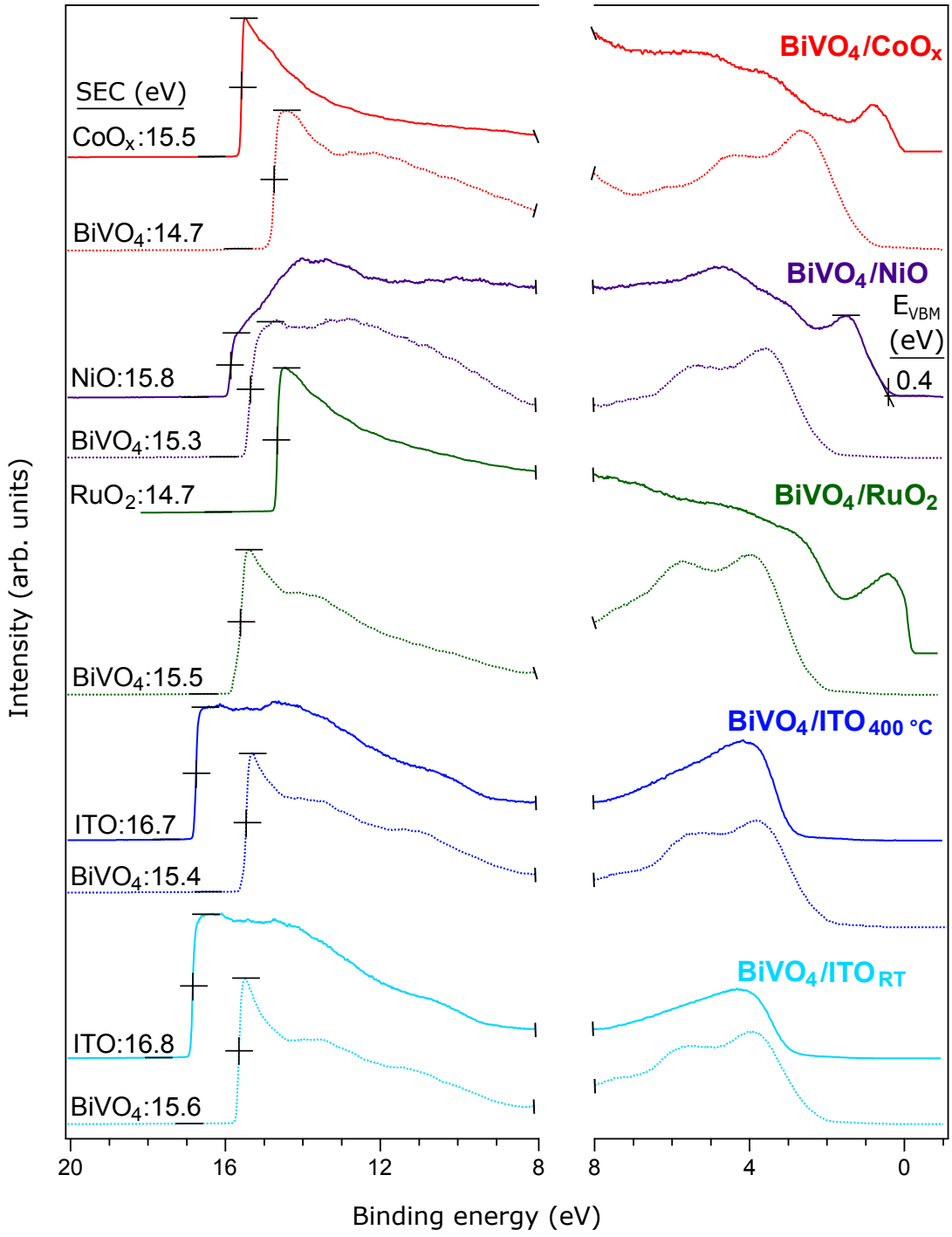

Figure 5.17: UP spectra (He I excitation) of the $BiVO_4$ substrate and the contact layer for the $BiVO_4$/ITO(RT) (light blue), $BiVO_4$/ITO(400 °C) (dark blue), $BiVO_4/RuO_2$ (green), $BiVO_4$/NiO (purple) and $BiVO_4/CoO_x$ (red) interface experiments with the respective secondary electron cut-offs (SEC) depicted in the Figure.

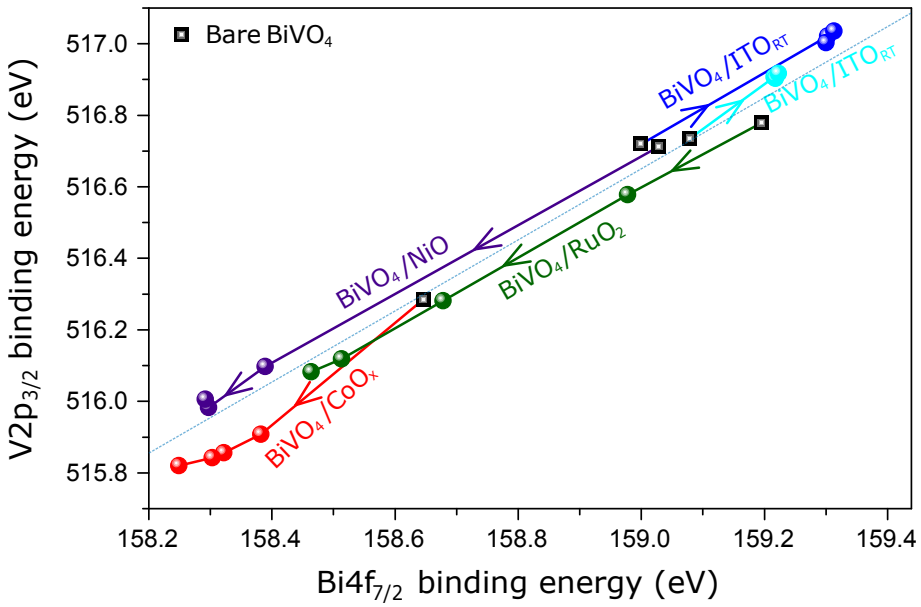

Figure 5.18: Shift of the $V2p_{3/2}$ and $Bi4f_{7/2}$ binding energies with increasing contact layer thickness (arrows) for all the interface experiments. The dashed blue line represents a slope of 1.

Table 5.2: Summary of important energetic values of all $BiVO_4$ based interface experiments.

	$BiVO_4/RuO_2$	$BiVO_4$/ITO (RT)	$BiVO_4$/ITO (400 °C)	$BiVO_4$/NiO	$BiVO_4/CoO_x$
$BE_{Bi4f_{7/2},0\ s}$	159.18	159.08	159.00	159.03	158.65
$BE_{Bi4f_{7/2},final}$	158.46	159.22	159.31	158.25	158.22
$BE_{V2p_{3/2},0\ s}$	516.78	516.74	516.71	516.71	516.29
$BE_{V2p_{3/2},final}$	516.08	516.92	517.00	515.93	515.82
VBM_{BiVO_4}	1.8	1.8	1.8	1.8	1.5
WF_{BiVO_4}	5.7	5.6	5.8	5.9	6.6
VBM_{CL}	0	2.5	2.8	0.4*	0.3
WF_{CL}	6.5	4.4	4.5	5.4	5.7

Binding energies (BE) of the $Bi4f_{7/2}$ and $V2p_{3/2}$ core levels at 0 s coverage and for the final spectrum that could still be observed, valence band maxima (VBM) and work functions (WF) for the interface experiments. CL: contact layer. All values are denoted in eV. *Determined from UPS measurements.

$BiVO_4$/ITO interfaces might be caused, as explained above, by a surface dipole at the ITO surface. It is also known, however, that semiconducting oxides often exhibit a huge dipole potential step upon forming a Schottky barrier with RuO_2.[69] These Schottky barrier heights would imply a work function of RuO_2 of about 5.6 eV; if this work function would be considered instead of the measured 6.5 eV work function, a similar dipole potential step would be present at both the $BiVO_4$/RuO_2 and $BiVO_4$/ITO interfaces. The dipole potential step is possibly partly due to the oxygen plasma treatment of the $BiVO_4$ surface, as the oxygen plasma may create an O_2^- surface layer, which increases the surface dipole.[70,71] During the interface experiments this surface dipole would then disappear due to the formation of the oxide contact layer which would incorporate the excess oxygen in its lattice. Additionally, the experimentally determined work function of $BiVO_4$ is higher than expected since the $BiVO_4$ electron affinity obtained in this work is situated between 5.3 — 5.9 eV, which is in contrast to an electron affinity of 4.5 — 4.8 eV commonly published in literature.[3,42,43] As explained above the experimental NiO and CoO_x work functions are lower than expected, which partly explain the dipole potentials step of the $BiVO_4$/CoO_x and $BiVO_4$/NiO interfaces. All in all, the dependence of the work function on surface dipoles here demonstrate that the band alignment of a junction cannot be reliably determined from UPS work function measurements alone.

The band diagrams in Figure 5.19 and Figure 5.20 also show how far the Fermi level can move according to the difference in work functions of the contact materials. Due to the low work function of ITO, high barrier heights ($\Phi_{B,p}$) of 1.96 eV and 2.10 eV are obtained for, respectively, the $BiVO_4$/ITO(RT) and $BiVO_4$/ITO(400 °C) interface experiments. The slightly higher $\Phi_{B,p}$ caused

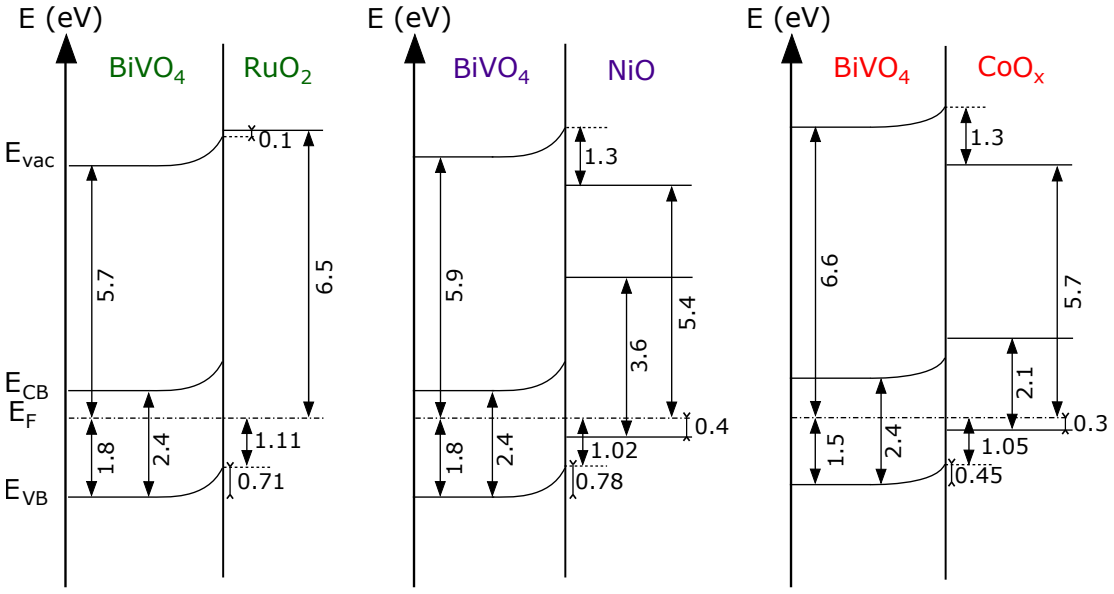

Figure 5.19: Energy band diagrams for the $BiVO_4$/RuO_2, $BiVO_4$/NiO, $BiVO_4$/CoO_x interfaces. All energy values are denoted in eV. The band gaps of $BiVO_4$, NiO, CoO_x were taken from literature.[65,66,68]

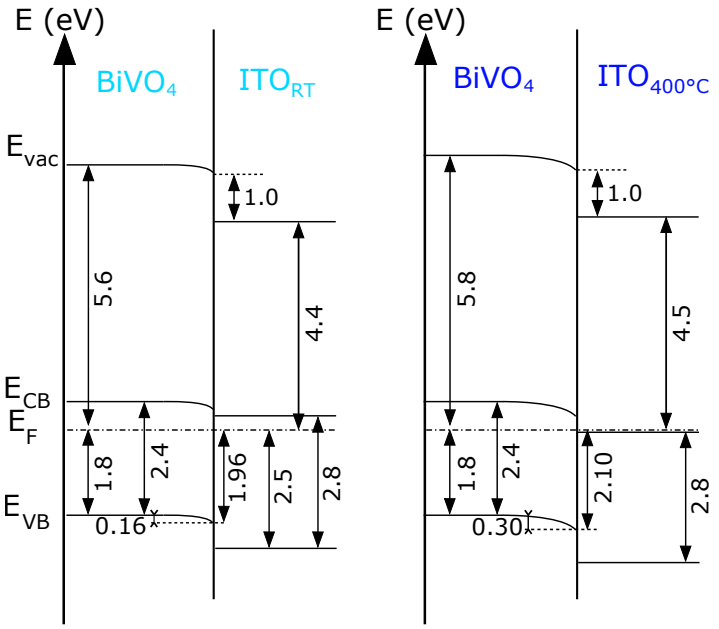

Figure 5.20: Energy band diagrams for the $BiVO_4$/ITO(RT) and $BiVO_4$/ITO(400 °C) interfaces. All energy values are denoted in eV. The band gap of $BiVO_4$ and ITO were taken from literature.[55,65]

by the ITO deposited at 400 °C is most likely due to the higher doping level in this ITO layer. In contrast, low $\Phi_{B,p}$ between 1.0 — 1.1 eV are observed for the $BiVO_4$ interfaces with the high work function compounds RuO_2, NiO and CoO_x. Hence, the total barrier height difference amounts to 1.08 eV, which demonstrate that the Fermi level position in $BiVO_4$ can be changed over a wide range. In other words, Fermi level pinning because of intrinsic surface states or defect compensation seems to be limited in $BiVO_4$. However, to exclude the possibility of Fermi level pinning one has to observe if and how the $BiVO_4$ electronic structure changes upon contact formation. To verify the changes in electronic structure a closer look was taken to the evolution of the $Bi4f_{7/2}$, $V2p_{3/2}$ core level and valence band XP spectra with respect to the contact layer deposition time, as presented in Figure 5.21. For the $BiVO_4$/ITO(RT) interface a second signal appears at a lower binding energy in the $V2p_{3/2}$ core level spectra, whereas for the $BiVO_4$/ITO(400 °C) interface in both the $V2p_{3/2}$ and $Bi4f_{7/2}$ core level spectra a second signal at a lower binding energy is found, which originate most likely from the partial reduction of the $BiVO_4$ surface (Figure 5.21). The second signal in the $Bi4f_{7/2}$ spectra has a binding energy of around 157.0 eV, which corresponds to the binding energy of metallic bismuth.[44] The exact binding energy of the second signal in $V2p_{3/2}$ is difficult to obtain since V^{5+} can be reduced to V^{4+} or V^{3+} which have similar binding energies. The reduction of V^{5+} and Bi^{3+} could be due to Fermi level pinning, whereby electrons are not situated in the conduction band states, but form small polaron states with bismuth and vanadium atoms as the centres of these polaron states. The creation of a small polaron state on a vanadium lattice site after the injection of an electron into the $BiVO_4$ lattice

has been theoretically predicted through DFT calculations with the polaron state having V $3dz^2$ character and shifted from the conduction band edge into the band gap.[72,73] Furthermore, the localized polaron state has been experimentally verified for molybdenum and tungsten doped $BiVO_4$ single crystals through resonant XPS.[74] Indeed, upon closer inspection of the valence band spectrum after 4 s of ITO deposition (Figure 5.21) an additional signal appears in the band gap about 0.9 eV from the CBM, the position where the localized polaron state due to V^{4+} would be expected.[72–74] With further ITO deposition the mixing of the ITO and $BiVO_4$ valence band states does not allow further observation of the supposed polaron state.

For NiO, RuO_2 and CoO_x similar Schottky-type barrier heights between 1.0 — 1.1 eV are obtained, despite the different work functions of the contact materials. The similarity of these Schottky-type barrier heights strongly indicate that a maximum shift of E_F is reached. The reason for this could be Fermi level pinning. Another possibility is that the work function of CoO_x, NiO and RuO_2 is not high enough to obtain further band bending. During the deposition of RuO_2, NiO and CoO_x no significant change in the $Bi4f_{7/2}$ core level spectrum can be observed (Figure 5.22). There is a small bump appearing at a higher binding energy around 160.5 — 161.0 eV. This could be due to the oxidation of Bi^{3+} to Bi^{5+}, however since this level only shows up in a low intensity we could not reliably deduce its existence. In addition, the distinction between Bi^{3+} and Bi^{5+} in Bi4f spectra can be vague, as was observed for mixed bismuth oxides such as $BaBiO_3$.[75–77]

Figure 5.23 summarizes the interface experiments by showing the range over which the $BiVO_4$ Fermi level position can be changed relative to the band positions. The $BiVO_4$ band positions are here given with respect to the SHE scale based on previously performed Mott-Schottky measurements and work function measurements, which were carried out to determine the energetic distance of the $BiVO_4$ band positions with respect to the H^+/H_2 reduction level.[20,43,78] However, to my knowledge none of the reliable Mott-Schottky measurements were performed at the pH_{ZPC}. Therefore, the presence of a Helmholtz layer cannot be excluded, so that the band positions at the absolute vacuum scale are actually unknown. Please take a look at Figure 2.18 for the relation between SHE, RHE and vacuum level. Therefore, in the discussion below the relative energetic positions are relevant, but the absolute positions should be taken with a grain of salt. The SHE and not the RHE scale is taken here, because the equivalence of the SHE scale with the absolute vacuum scale (E_{Vac}-E_{SHE} = 4.44 eV) allows to position the polaron levels as well as the standard reduction potentials in a straightforward manner.

Based on the interface experiments, the range over which the Fermi level position can be shifted seems to be limited to 1.1 eV with the lower limit at -1.5 eV vs SHE and the upper limit at -0.4 eV vs SHE. Thus, defects intrinsic to $BiVO_4$ do not prevent water oxidation since the H_2O/O_2 reduction potential is situated well within the range over which the Fermi level can be changed. Nevertheless, in many occasions Fermi level pinning has been identified as a main reason for poor $BiVO_4$ photoanode efficiency.[15,79–81] However, as has been recently pointed out, various synthesis methods could introduce different native defects, which may be removed by post synthetic treatments.[81] Thus, by removing the native carbon and hydroxide layer, as was done in

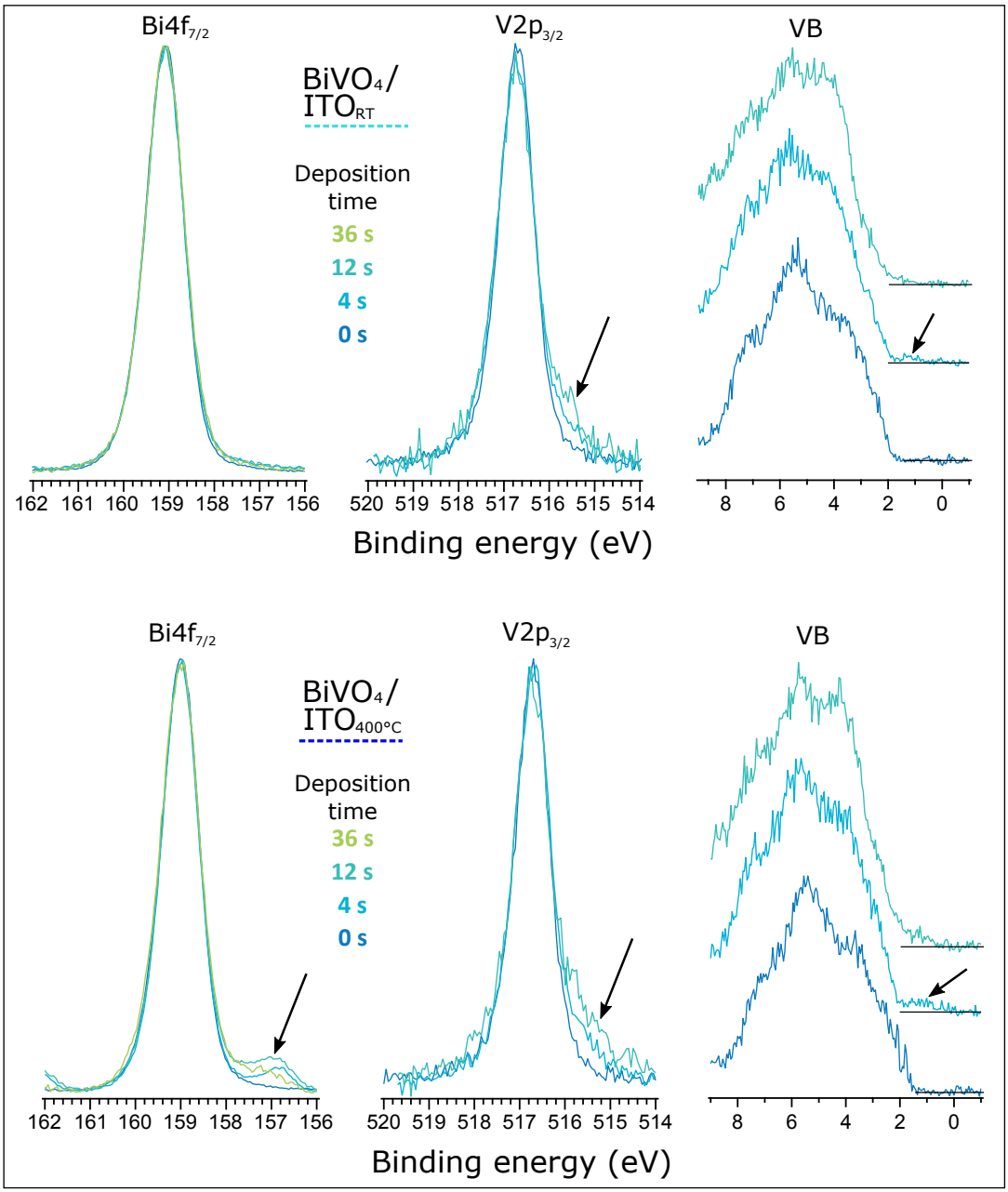

Figure 5.21: $Bi4f_{7/2}$, $V2p_{3/2}$ spectra and valence band spectra for the $BiVO_4$/ITO(RT) and $BiVO_4$/ITO(400 °C) interface experiments. For the core level spectra the background was subtracted using a Tougaard function for the Bi4f spectra and a Shirley function for the $V2p_{3/2}$ spectra. Then, the core level spectra were normalized and shifted along the x-axis to align the line maxima. The contact layer deposition times are denoted in the spectra.

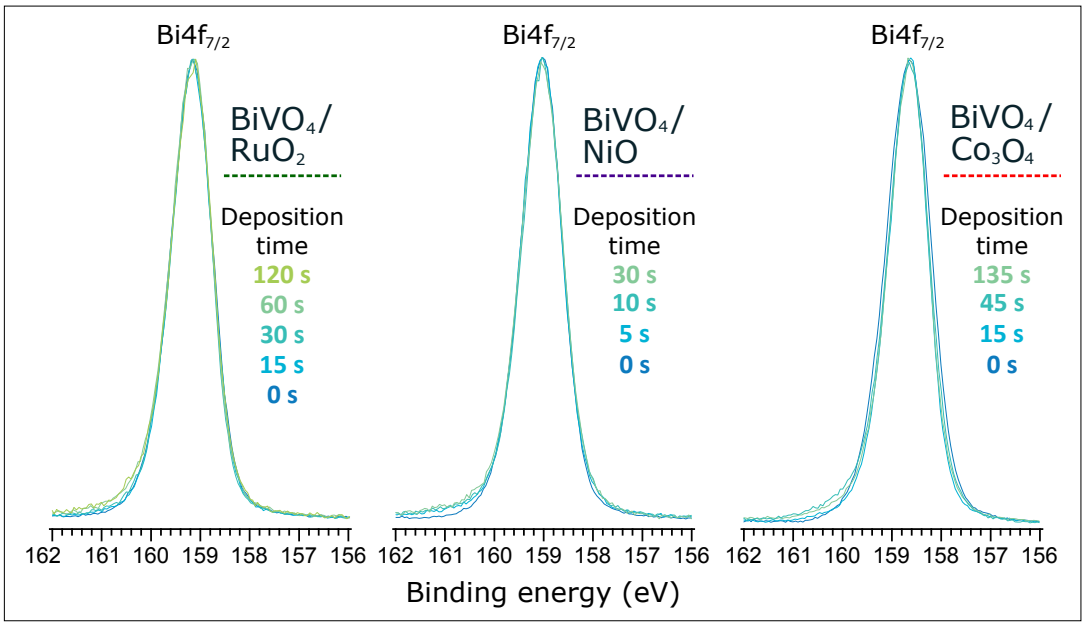

Figure 5.22: $Bi4f_{7/2}$ spectra for the $BiVO_4/RuO_2$, $BiVO_4/NiO$ and $BiVO_4/CoO_x$ interface. First, the background of the Bi4f core level spectra was subtracted using a Tougaard function. Then, the core level spectra were normalized and shifted along the x-axis to align the line maxima. The contact layer deposition times are denoted in the spectra.

this work through an oxygen plasma treatment, the $BiVO_4$ surface states, which previously have been identified as recombination centres and the cause of Fermi level pinning, may be removed.

Nevertheless, because of the differing work functions of CoO_x, NiO and RuO_2, the $BiVO_4$ Fermi level limit at -1.7 eV vs SHE may indicate intrinsic defect compensation, involving gap state (polaron) formation, whereby such states could still act as charge carrier recombination centres. The observed lower Fermi level limit at -1.7 eV vs SHE differs, however, strongly from the recently theoretically calculated $BiVO_4$ hole polaron level, situated at -2.5 eV vs SHE.[73] Alternatively, the hole defect compensation level can be estimated from the standard reduction potentials involving bismuth and vanadium. As presented in Figure 5.23, the Bi^{5+}/Bi^{3+}, redox couple at -1.59 eV vs SHE,[82] is close to the observed lower Fermi level limit. Hence, defect compensation by oxidation of Bi^{3+} to Bi^{5+} is still a possibility. Similarly, the Fermi level limit at -0.6 eV vs SHE can be due to the intrinsic defect compensation involving the reduction of Bi^{3+} and/or V^{5+}. Indeed, indications of Bi^{3+} and V^{5+} reduction were observed in the XP core level spectra of the $BiVO_4$/ITO interface experiment (Figure 5.21). The reduction of Bi^{3+} could be linked to the standard reduction potential of Bi^{3+}/Bi(s), at -0.31 eV vs SHE. Pinpointing the standard redox levels involving V^{5+} is more complicated since the V^{5+}/V^{4+} and V^{4+}/V^{3+} standard redox potentials do not formally exist, possibly due to V^{5+} and V^{4+} being unstable in aqueous electrolytes, wherein these ions form (hydr)oxide based compounds. Nevertheless, the V^{5+}/V^{4+} reduction can be represented by the V_2O_5/VO^{2+} standard redox potential at -1.0 eV vs SHE. The Bi^{3+}/Bi(s) and

V_2O_5/VO^{2+} standard reduction potentials differ, however, from the Fermi level limit at -0.6 eV vs SHE, which may be due to the solid state reduction potentials being different from the standard reduction potentials measured in an electrolyte, because of the different coordination of metal ions in an electrolyte compared to a crystal lattice. Additionally, the calculated V^{5+}/V^{4+} electron polaron level position[72,73] is about 0.3 eV lower than the observed upper Fermi level limit. Further reduction of V^{4+} to V^{3+} may be possible, but the reduction of V^{3+} to V^{2+} is unlikely due to its unsuitable standard reduction potential at 0.26 eV vs SHE.

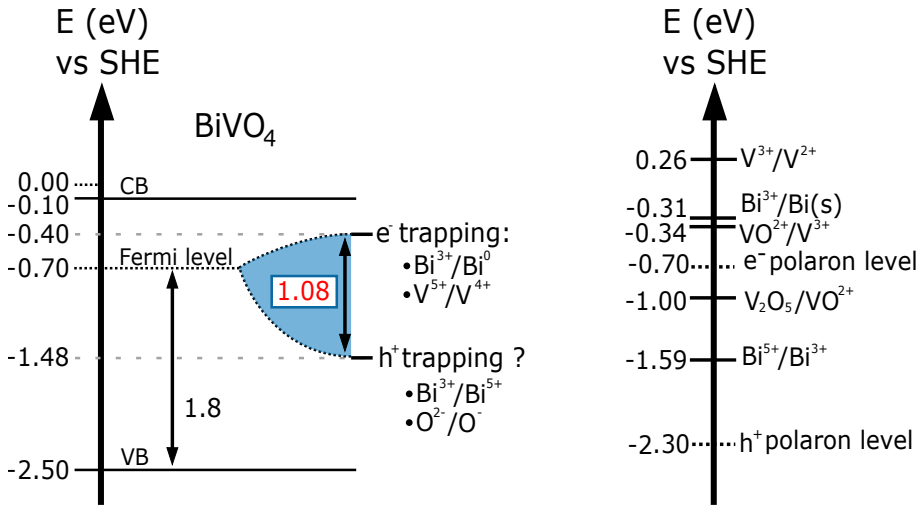

Figure 5.23: Left: diagram showing the Fermi level tunability in $BiVO_4$ and the limits based on the obtained information from the interface experiments. The $BiVO_4$ band positions are here taken from literature.[20,43,78] Right: a series of standard reduction potentials related to bismuth and vanadium species are shown on the standard hydrogen electrode scale.[82,83]

5.3.3 Solid state band alignment

Mostly, band alignment between two solid state compounds is not evaluated through interface experiments, but simply by observing how the bands of the individual compounds align before contact.[84–86] The band positions are in this approach most often experimentally derived through flat-band measurements. Indeed, capacitance-derived flat-band potential measurements from Mott-Schottky plots give, next to information on the kinetics and energetics of the semiconductor-liquid junctions, information on the location of the band positions with respect to the reference electrode. Such measurements were often performed in the early days of semiconductor electrochemistry (1970s – 1980s), mostly on defined surfaces of single crystals. These were used to align the commonly studied semiconductor electrodes relative to the H^+/H_2 redox potential.[26–28,87] By assuming transitivity of band alignment this provides a comparison of band edge energies of the different photoelectrodes. The energy band alignment of different oxides inferred from such studies is shown in Figure 5.24.

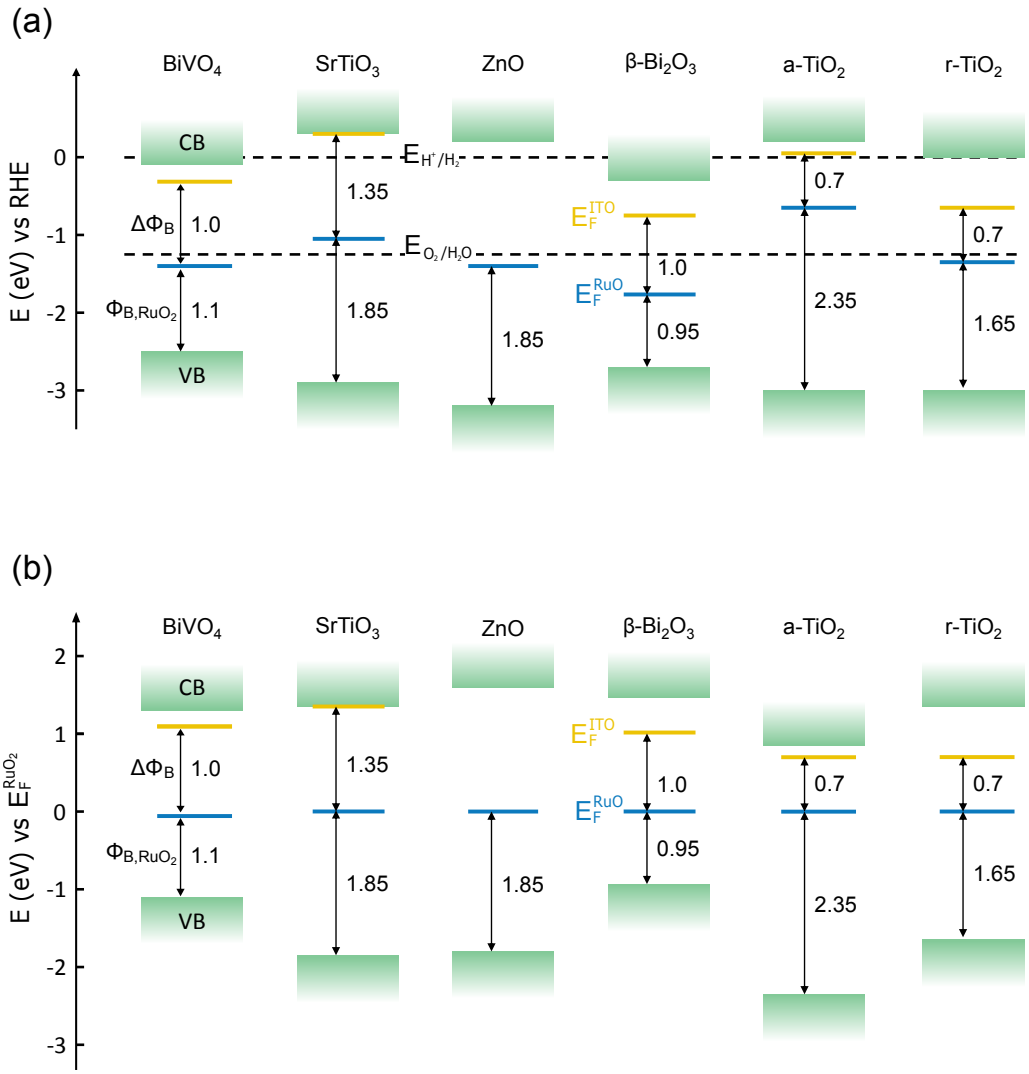

Figure 5.24: Conduction band and valence band alignment of a series of semiconductor oxides relative to the (a) H^+/H_2 standard redox potential and to the (b) RuO_2 Fermi level position. The barrier heights of these oxides at the interfaces with RuO_2 (blue) and ITO (yellow) were determined through interface experiments. a-TiO_2: anatase, r-TiO_2: rutile, Φ_{B,RuO_2}: barrier height between substrate and RuO_2, $\Delta\Phi_B$: barrier height difference between substrate/RuO_2 and substrate/ITO.

From the electrochemical alignment of the energy bands, which positions the valence and conduction band energies relative to the H^+/H_2 redox potential and which is established in literature,[26,28,88] the relative alignment between two semiconducting oxides can be directly extracted by assuming transitivity. In principle, the same can be achieved using the Fermi level position at the interfaces of the oxides with the same metal, also assuming transitivity.[89] The interface experiments with RuO_2 and ITO described in this Chapter can, in principle, both be used to compare the band edge energies.[90,91] Transitivity of band alignment is, however, not necessarily valid when Fermi level pinning is involved in interface formation, as this affects the measured Fermi level positions.[69,92–94] In the extreme case of pinning, known as Bardeen limit, the Fermi level at an interface becomes independent on metal work function. In such a case, the Fermi level at the interfaces with RuO_2 and ITO would be identical. This is definitely not the case, as evidenced by Figure 5.24. Additionally, the band edge positions or dipole layer at the interface may vary due to adsorbates as well as ionic surface terminations. Such offsets may be expected, especially for semiconductor/electrolyte interfaces, but they have hardly been studied yet in a systematic manner.[32]

For classical semiconductors, Fermi level pinning might be induced by virtual gap states[89,95] or by deposition-induced defects.[96] The latter are almost always observed during deposition of elementary metals on clean oxide surfaces,[69,97,98] but can be avoided by contact formation with conducting metal oxides, depending on the applied deposition parameters.[69] The Fermi levels observed at contacts of $BiVO_4$ (this work) and other oxides with RuO_2 (high work function) and ITO (low work function) are included in Figure 5.24. In the present case, the variation of Fermi level position at the interfaces of $BiVO_4$ with RuO_2 and ITO amounts to about 1.0 eV. This variation is higher than observed for rutile and anatase TiO_2,[52] lower than the variation observed for $SrTiO_3$[69,99,100] and about the same as the variation determined for β-Bi_2O_3.[35]

In the case of (Ba,Sr)TiO_3 and Pb(Zr,Ti)O_3, the alignment determined using transitivity with ITO or RuO_2 and the alignment extracted from direct interface formation all agree within 0.2 eV, giving substantial credit to this approach.[90] However, there is substantial deviation between the electrochemical alignment and those obtained by aligning the Fermi energies at interfaces with RuO_2 and ITO for the materials included in Figure 5.24. This difference is valid even if the different magnitude of Fermi level splitting for the different oxides is taken into account. An instructive example is given by anatase and rutile TiO_2, where it was shown recently using complementary approaches that the valence band of rutile is about 0.7 eV higher than that of anatase, which substantially differs from the alignment obtained using electrochemical studies.[52,101,102]

The valence band maximum of $BiVO_4$ and β-Bi_2O_3 is about 0.4 eV above that of $SrTiO_3$ according to the electrochemical alignment from flatband potential measurements.[78,103,104] Using the RuO_2 and ITO interfaces, the valence band of $BiVO_4$ would be 0.75/1.25 eV higher than that of $SrTiO_3$. The latter alignment would correspond well with the alignment of $SrTiO_3$ with other perovskites having Bi^{3+} or Pb^{2+} as A-site cations.[90,105,106] The higher valence band maximum of the latter perovskites is explained by the contribution of the occupied 6s orbitals of Bi or Pb.[107]

As higher valence band maxima are quite generally observed for such compounds, it seems reasonable to expect that the valence band maximum of $BiVO_4$ is also about 1 eV higher than that of $SrTiO_3$, which would better agree with the alignment obtained from transitivity of RuO_2 and ITO interfaces.

The deviation of the energy band alignment obtained using transitivity from electrochemical or solid-state interfaces may be explained either by the presence of Fermi level pinning or by a fundamental difference between solid/electrolyte and solid/solid interfaces. For solid/solid interfaces, the presence or the degree of Fermi level pinning can be obtained by comparing the variation of the Fermi energy using contact materials with different work functions. Such experiments should, however, take into account that Fermi level pinning might also be caused by lattice defects, which are frequently introduced on oxide surfaces by metal deposition.[69,108] However, even in the case of unreactive interfaces, such as those between two oxides used in the present study, bulk or surface defects may also result in a substantial variation of band alignment.[94,109–111] As a consequence, one may expect a substantial dependence of the band alignment on the preparation conditions. For instance, different concentrations of oxygen vacancies in ZnO and metallic precipitates in Cu_2O result in a variation of the band alignment by more than 1 eV at the interface between these materials.[94] In contrast, the effect of defects on the band alignment at oxide/liquid interfaces has been less extensively studied. In addition, specific surface interaction mechanisms must be considered for solid/electrolyte interfaces, which will be different in solid/solid interfaces. First of all, the substrate surface may be terminated in a different way due to specific adsorption of H^+, OH^-, or molecular H_2O species from the solution phase. Specific adsorption of supporting electrolyte species and solution contaminants may also play a role. The adsorption of ionic species results in the formation of a charged inner Helmholtz layer, which does not exist in similar form on solid surfaces. Additionally, an electrochemical double layer, the outer Helmholtz layer is formed due to electrostatic attraction of charged species or dipoles in the electrolyte to the (charged) solid surface. Due to thermal diffusion and dipolar interactions this layer can extend up to several hundreds of nm into the electrolyte solution (Gouy-Chapman or Stern layer). Finally, the different procedures in contact formation may lead to additional differing defect formation or passivation reactions at the interface. For solid/solid interfaces, defect passivation or surface reactions typically take place during contact formation, after which the contact properties show little or no further changes. In contrast, the properties of the solid/electrolyte interface can be easily and often reversibly modified afterwards by e.g. applying a potential, changing the pH of the solution, or by illumination in case of a semiconducting solid.

5.3.4 $BiVO_4/H_2O$

In addition to the solid state $BiVO_4$ interfaces studied in the previous Section through interface experiments, we studied the interaction of $BiVO_4$ with water through water exposure and water desorption experiments. In a water exposure experiment, a freshly calcined PLD $BiVO_4$ thin film

was exposed to several bursts of water in a chamber operated under high vacuum, in the absence of oxygen and light (see Section 3.4.4.2 for more experimental details). In a water desorption experiment a freshly calcined PLD $BiVO_4$ thin film substrate was first exposed to defined amounts of water at 77 K and high vacuum, after which the water was desorbed by allowing the sample to heat up again to room temperature (see Section 3.4.4.3 for more experimental details). Photoelectron spectroscopy was used to study the electronic and chemical changes after the water exposure/desorption.

Before the water exposure experiment was carried out, the PLD $BiVO_4$ thin film was calcined for 2 h at 400 °C in a pure oxygen atmosphere to remove the upper surface contamination layer. As can be seen in the survey spectra in Figure 5.25 all the carbonaceous surface species were evidently removed after the calcination, because no C1s photoelectrons could be detected any more. On this seemingly clean surface, the water exposure experiment was carried out. In the survey spectrum after the water exposure no additional photoelectrons besides those expected for $BiVO_4$ were detected. In Figure 5.26 the effect of water exposure on the Bi4f, $V2p_{3/2}$, O1s and valence band XP spectra of $BiVO_4$ is shown and in Table 5.3 a summary of the most important information obtained from this water exposure experiment is given. There are a few remarkable observations one can draw from the water exposure experiment on $BiVO_4$. First of all, an increase in binding energy of about 0.3 — 0.5 eV can be noticed for the Bi4f, V2p and VBM spectra between a cleaned sample (after calcination/oxygen plasma) and the same sample exposed to water. After the water exposure a $Bi4f_{7/2}$ and $V2p_{3/2}$ binding energy of 159.6 eV and 517.3 eV, respectively, is retrieved, which is slightly higher than the respective 159.2 eV and 517.0 eV binding energies, observed after ITO was sputtered onto $BiVO_4$. However, the cleaned $BiVO_4$ substrate, before water exposure, had already high $Bi4f_{7/2}$ and $V2p_{3/2}$ binding energies of 159.2 and 516.8 eV, respectively. These high core level binding energies are probably a consequence of a high Fermi level position, as an E_F-E_{VBM} of 2.0 eV could be determined from the valence band spectrum of the thermally cleaned $BiVO_4$ sample. Hence, the thermal cleaning step, used before the water exposure, probably maintains a higher amount of oxygen vacancies than a typical oxygen plasma treatment, which was used as cleaning method before the interface experiments.

Moreover, additional features in the $Bi4f_{7/2}$, $V2p_{3/2}$ and O1s spectra can be seen after the exposure of the $BiVO_4$ substrate to water. The features at lower binding energies in the Bi4f and $V2p_{3/2}$ spectra indicate the reduction of Bi^{3+} and V^{5+}, respectively.[44] The second feature in the $V2p_{3/2}$ spectrum after water exposure has also been seen before by Favaro et al. during near ambient pressure XPS measurements, which the authors also related to the reduction of V^{5+} to V^{4+}.[112] The feature at 157.4 eV in the $Bi4f_{7/2}$ spectrum most likely corresponds to metallic bismuth.[113] The feature at higher binding energy in the O1s spectrum is most likely due to the formation of hydroxides.[44,114] The $BiVO_4$ reduction could be partially reversed by exposing the sample to an oxygen atmosphere at room temperature, as the additional features in the O1s, $V2p_{3/2}$ and Bi4f seemingly decrease after the oxygen exposure. Furthermore, an oxygen plasma treatment, which is an even more oxidative treatment, led to a complete removal of the additional

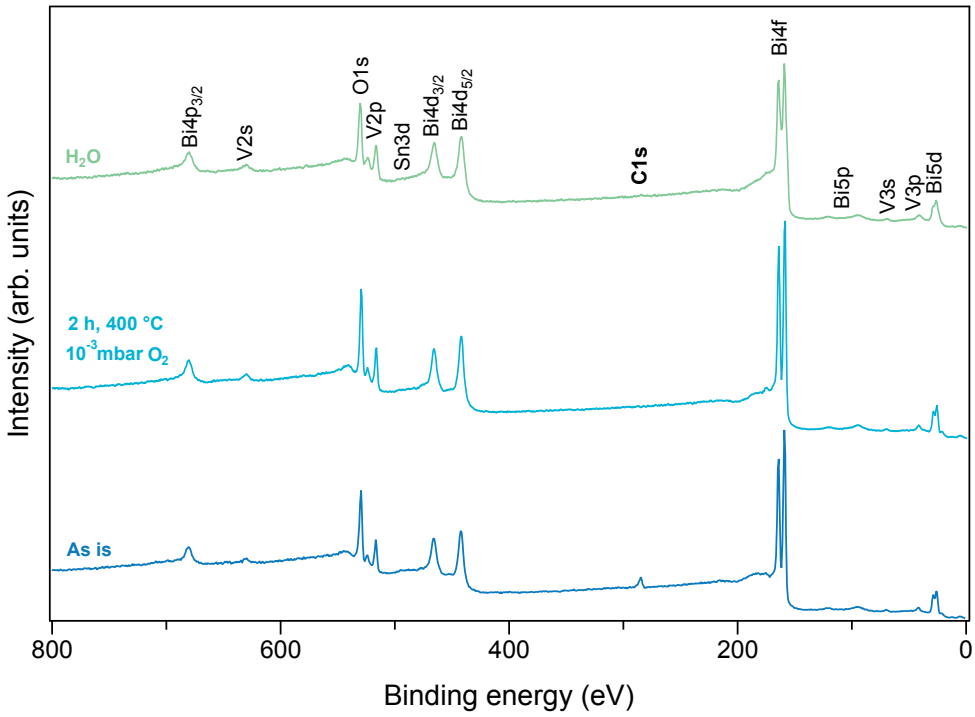

Figure 5.25: Survey XP spectra for the $BiVO_4$ water exposure experiment. O_2: oxygen flow (2 sccm, 1 x 10^{-3} mbar), H_2O: water exposure.

features. Exposing the oxygen plasma cleaned sample again to water, led again to the formation of hydroxy groups and the reduction of bismuth and vanadium.

The intensities of the core level spectra in Figure 5.26, determined through integration of the core level signals after background subtraction, were used to determine surface intensity ratios, which are denoted in Table 5.3. Surface treatments may change these intensity ratios through changes of the surface chemistry or through the formation/removal of an overlayer. The change of the surface intensity ratios after removal or formation of an overlayer is a consequence of the

Table 5.3: Summary of $BiVO_4$ water exposure experiment.

Treatment	as is	2 h, 400 °C, O_2	H_2O	30 min, RT, O_2	15 min O_2 plasma	H_2O
$BE_{Bi4f_{7/2}}$ (eV)	159.5	159.2	159.6	159.6	159.3	159.6
$BE_{V2p_{3/2}}$ (eV)	517.1	516.8	517.3	517.3	517.0	517.3
BE_{O1s} (eV)	530.2	529.9	530.5	530.4	530.1	530.5
$I_{V2p_{3/2}}/I_{Bi4f}$	0.78	0.90	0.94	0.89	0.94	0.99
$I_{O1s}/I_{V2p_{3/2}}$	4.4	**3.9**	**3.3**	3.7	**4.0**	**3.2**
$I_{O^{2-}}/I_{OH}$	—	—	1.96	4.10	—	1.91
$I_{V^{5+}}/I_{V^{4+}}$	—	—	0.39	0.61	—	0.38

BE: Binding energy, I_x: Integrated intensity of core level spectrum x, $I_{V^{5+}}/I_{V^{4+}}$: ratio of integerated intensities of fitted $V2p_{3/2}$ components, $I_{O^{2-}}/I_{OH}$: ratio of integerated intensities of fitted O1s components, O_2: oxygen flow (2 sccm, 1 x 10^{-3} mbar), H_2O: water exposure.

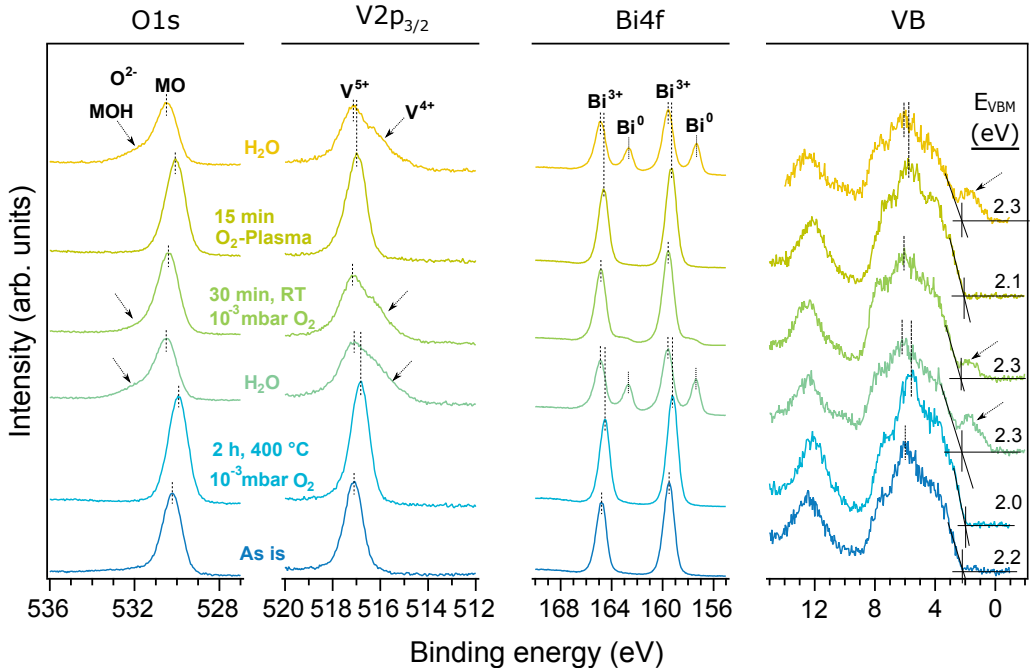

Figure 5.26: O1s, V2p$_{3/2}$, Bi4f core level and valence band XP spectra for the $BiVO_4$ water exposure experiment. The treatments are denoted in the O1s spectra. O_2: oxygen flow (2 sccm, 1 x 10^{-3} mbar), H_2O: water exposure.

kinetic energy dependent mean free path of photoelectrons and the different kinetic energies of photoelectrons removed from core levels with different characteristic binding energies. Due to the much lower binding energy and thus higher kinetic energy of the Bi4f electrons compared to the V2p$_{3/2}$ electrons, the formation/removal of an overlayer will lead to a weaker/stronger attenuation of the Bi4f core level intensity compared to the V2p$_{3/2}$ core level intensity. This can be clearly seen after the calcination step where the $I_{V2p_{3/2}}/I_{Bi4f}$ ratio increases after the removal of the extrinsic contamination layer. Due to the O1s and V2p$_{3/2}$ core levels having a very small difference in binding energy, overlayers play a much smaller role in the difference of $I_{O1s}/I_{V2p_{3/2}}$ ratios. Therefore, the decrease of $I_{O1s}/I_{V2p_{3/2}}$ from 4.4 to 3.9 after calcination, is most likely due to the removal of the (carbo)(hydr)oxide species in the extrinsic contamination layer and not due to the removal of the overlayer itself. After calcination, the 3.9 $I_{O1s}/I_{V2p_{3/2}}$ surface ratio suggest that the $BiVO_4$ sample surface is more or less stoichiometric in the amount of oxygen. The most remarkable result of the water exposure experiment on $BiVO_4$ is the reduction of $I_{O1s}/I_{V2p_{3/2}}$ from 3.9 to 3.3, because it indicates that the water reacts with the $BiVO_4$ surface, removes oxygen from the $BiVO_4$ surface and leaves behind a strongly reduced $BiVO_4$ surface. Possible mechanisms of the water reduction on $BiVO_4$ are discussed below.

Also, the extra features that appear in the Bi4f, O1s and V2p$_{3/2}$ spectra after water exposure indicate the reduction of the $BiVO_4$ surface. Peak fitting was performed to better assess the relative intensity of the different components in the O1s and V2p$_{3/2}$ spectra peak fitting. The

fitting parameters are denoted in Table 3.2 and the results of the fitting can be seen in Figure 5.27. The second component in the $V2p_{3/2}$ core level spectrum after water exposure is most likely due to the presence of V^{4+}, although the binding energy difference only amounts to 0.76 eV, where for vanadium oxides normally a binding energy difference of 1.2 eV is measured between V^{5+} and V^{4+}.[115] In the fitting, the strong reduction of the vanadium sample after water exposure is again apparent as the $I_{V^{5+}}/I_{V^{4+}}$ drops to 0.39. Simultaneously, a second feature appears in the O1s spectrum at a binding energy difference of 1.05 eV to the metal oxide O^{2-} species, which is close to the 1.2 eV binding energy difference normally noticed between metal oxide and metal hydroxide species.[44,114] Thus, also the fitted spectra of the water exposure experiment hint at a chemical reaction that leads to the formation of hydroxides and the reduction of V^{5+} and V^{4+}.

The valence band difference spectra in Figure 5.28 seemingly confirm the conclusions drawn from the core level binding energy shifts and the appearance of the additional features in the O1s, $V2p_{3/2}$ and Bi4f spectra. The features denoted in the valence band spectra correspond to that of pristine $BiVO_4$. In the difference trace a decrease in intensity after the water exposure at a binding energy of about 2.7 eV, 3.7 eV and 5.5 eV can be seen, which correspond to unhybridized $O2p_\pi$ mixed with Bi6s states, unhybridized $O2p_\pi$ states and hybridized Osp^2/V3d states.[43] The decrease in intensity of these three features is most likely correlated to the perceived decrease in the amount of surface oxygen, as determined from the reduced $I_{O1s}/I_{V2p_{3/2}}$ surface intensity ratio. The increase in signal intensity in the binding energy region from $8 - 10$ eV could possibly be due to the formation of hydroxides at the surface.[116] The appearance of the feature at a binding energy of 1.5 eV is most likely due to the filling of the V3d states and Bi6p states, as those feature have been linked before to V^{4+} for tungsten and molybdenum doped $BiVO_4$ samples[74] and to metallic bismuth,[117] respectively.

Also in the valence band region of the UP spectra (Figure 5.29) the effects of the water exposure on the $BiVO_4$ sample can be seen. Namely, the distinct signals at 3.6 eV, 5.4 eV and 7.2 eV characteristic to $BiVO_4$ cannot be seen any more after exposing $BiVO_4$ to water, but are restored after the oxygen plasma treatment. The SEC also moves to a higher binding energy after the water exposure, meaning that the work function is reduced.

The results of the water exposure experiment were cross-checked through the similar water desorption experiment, where a water layer was gradually deposited on top of a liquid nitrogen cooled $BiVO_4$ thin film substrate and, subsequently, desorbed by allowing the sample to heat up again to room temperature. First of all, the PLD $BiVO_4$ thin film was calcined under the same conditions as the thin film substrates used for the water exposure experiment. However, this surface cleaning step did not fully remove the carbon contamination layer here. As can be seen in Figure 5.30, the survey and C1s XP spectra still exhibit a signal related to extrinsic carbonaceous species. Most likely, the thermal contact between the heat source and the sample holder was not well established. The Bi4f, O1s, $V2p_{3/2}$ core level and valence band XP spectra recorded during the water desorption experiment are shown in Figure 5.31. The binding energies of $V2p_{3/2}$, Bi4f and valence band stay somewhat the same during the whole experiment. There is only a small 0.1 eV

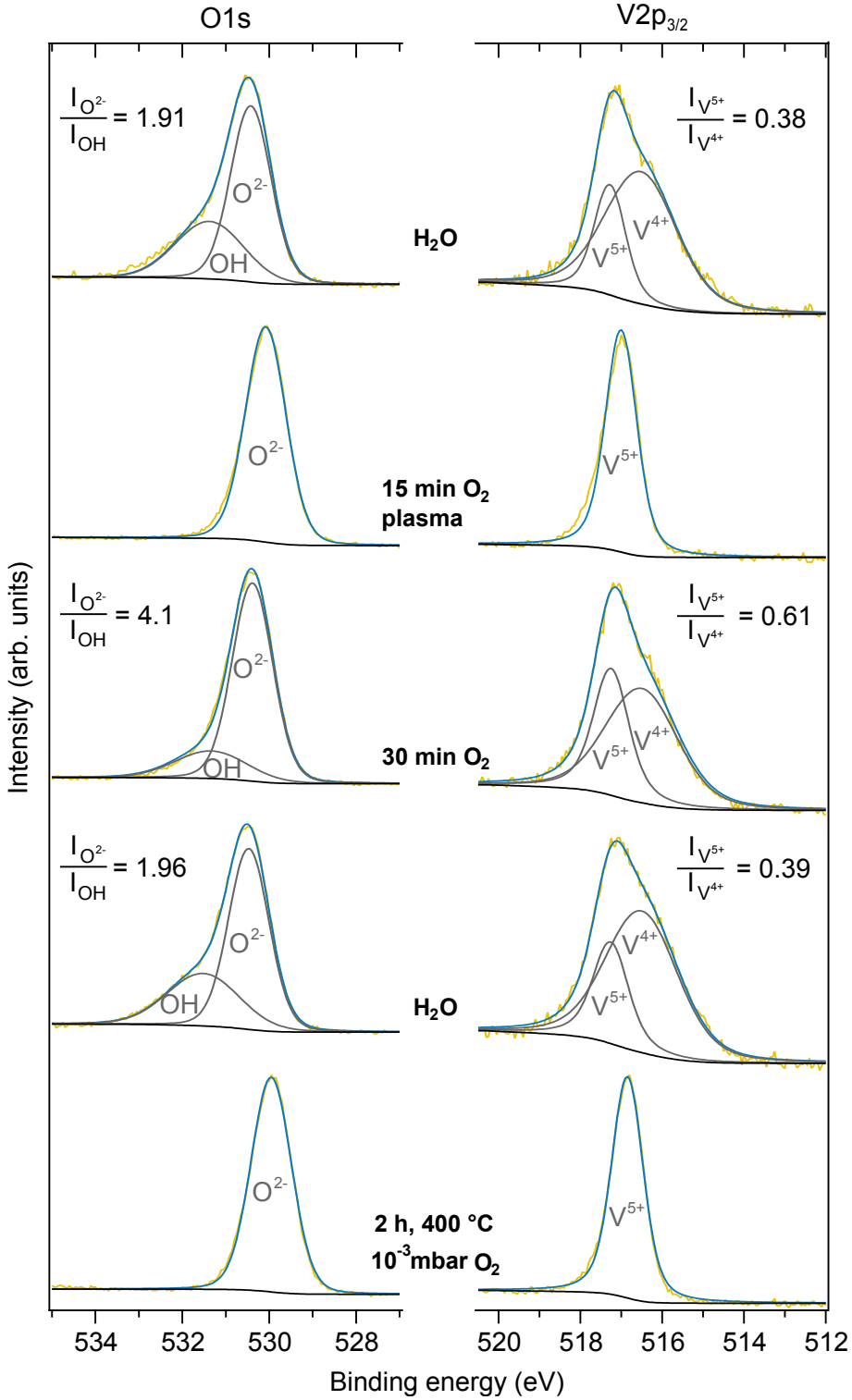

Figure 5.27: Fitting of the $V2p_{3/2}$ and O1s core level components from the water exposure experiment on $BiVO_4$. The treatments are denoted in the O1s spectra. The ratios of the integrated components are denoted as well.

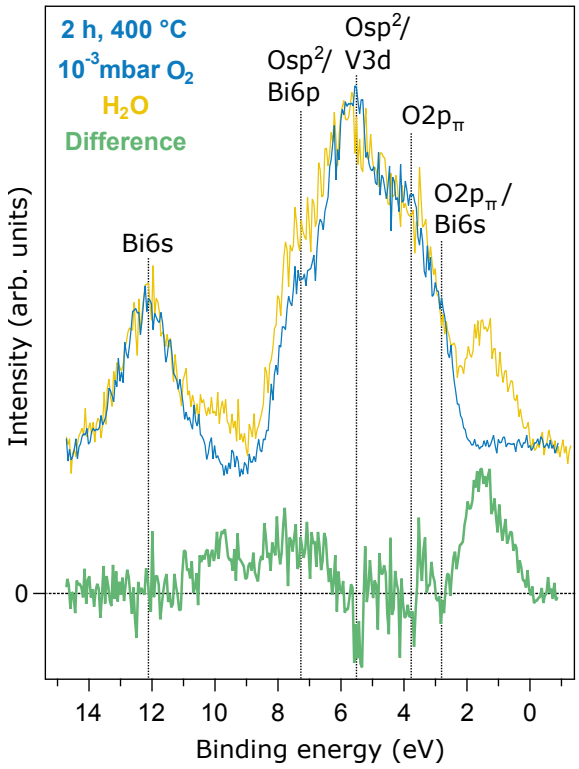

Figure 5.28: Difference spectra of valence band after calcination and after water exposure. The contributions of the $BiVO_4$ valence band orbitals to the valence band are indicated. The background was subtracted through the Shirley method, and the spectra were normalised on the intensity and the binding energy scale according to the Bi6s orbital.

shift towards a higher binding energy after cooling the calcined $BiVO_4$ sample to 77 K. Because part of the extrinsic contamination layer was still present on the $BiVO_4$ surface after calcination, a second feature in the O1s spectrum at higher binding energy can be seen. This feature can be more clearly observed after peak fitting (Figure 5.32). This additional O1s feature has a relatively high FWHM and originates likely from oxygen containing carbonaceous species and hydroxy groups at the surface.[44] During the water adsorption a third feature appears in the O1s spectrum, which shifts to higher binding energies with increasing amounts of adsorbed water. The binding energy of this feature after the deposition of 12.8 L of H_2O is situated at 534.1 eV, which is typical for water molecules in a multilayer film.[114,118–120] The binding energy shift of this feature has generally been explained by final state screening effects, whereby a core hole in water is screened more effectively by electrons at the surface than by electrons from adjacent water molecules in a multilayer.[120] The fitted O1s components in Figure 5.32 seemingly show that the intensity of the OH+CO component with respect to the intensity of the O^{2-} component increases during the water adsorption and decreases after water desorption. This could mean that water already dissociates into hydroxy groups during the water adsorption at 77 K and that these hydroxy

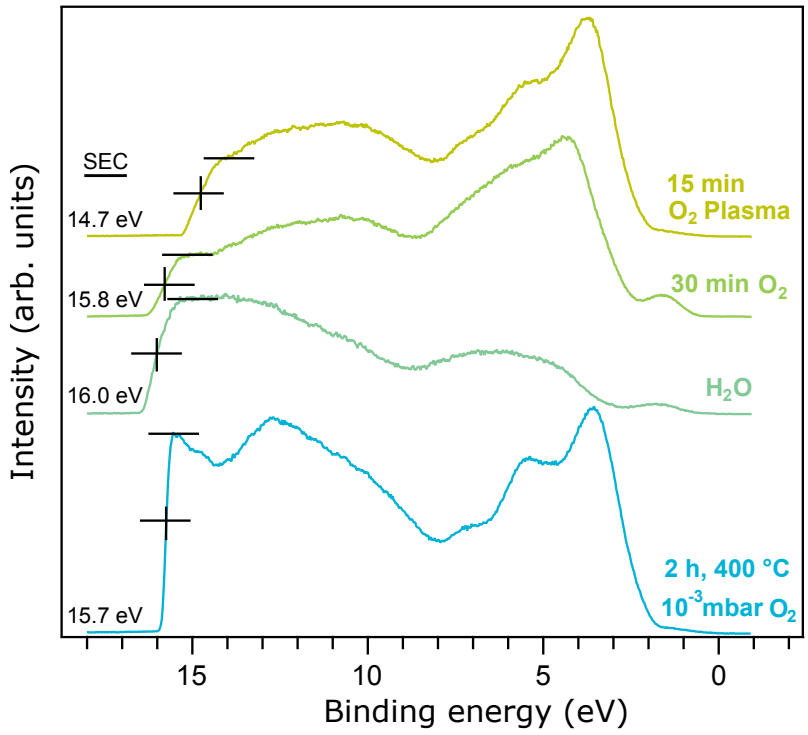

Figure 5.29: UP spectra (He I excitation) for the $BiVO_4$ water exposure experiment. Secondary electron cut-offs (SEC) are denoted in the graph. O_2: oxygen flow (2 sccm, 1 x 10^{-3} mbar), H_2O: water exposure.

groups react when the sample heats up to RT. During the water adsorption at 77 K no additional features appear in the Bi4f and $V2p_{3/2}$ spectra. However, after water desorption the same features as the ones observed after water exposure appear in the $V2p_{3/2}$ and Bi4f spectra, indicating the partial reduction of Bi^{3+} to Bi^0 and V^{5+} to V^{4+}. The features have, however, a lower intensity than those observed after the water exposure experiment, which could be due to the presence of the contamination layer which covered part of the $BiVO_4$ surface. Another possibility is that only the water layer closest to the $BiVO_4$ surface participated in a surface reaction. Thus, according to this hypothesis, a water desorption experiment where the $BiVO_4$ surface only interacts once with water would result in a less strong reduction of $BiVO_4$ in comparison to a water exposure experiment where a sample is exposed to water during 15 cycles of exposure-pumping down.

Thus, all results described above indicate that water dissociates at the $BiVO_4$ surface, forming hydroxy groups at the surface. These hydroxy groups then seem to react further with the oxygen atoms in the $BiVO_4$ lattice, generating a volatile oxygen-containing reaction product and an excess of electrons which reside on bismuth and vanadium atoms. There are several possible mechanisms for dissociative water adsorption, depending on the exact surface terminations.[120] Most commonly a distinction is made between defect, for example oxygen vacancies, and non-defect mediated dissociation. Both of these are a possibility for $BiVO_4$, because the high E_F-E_{VBM}

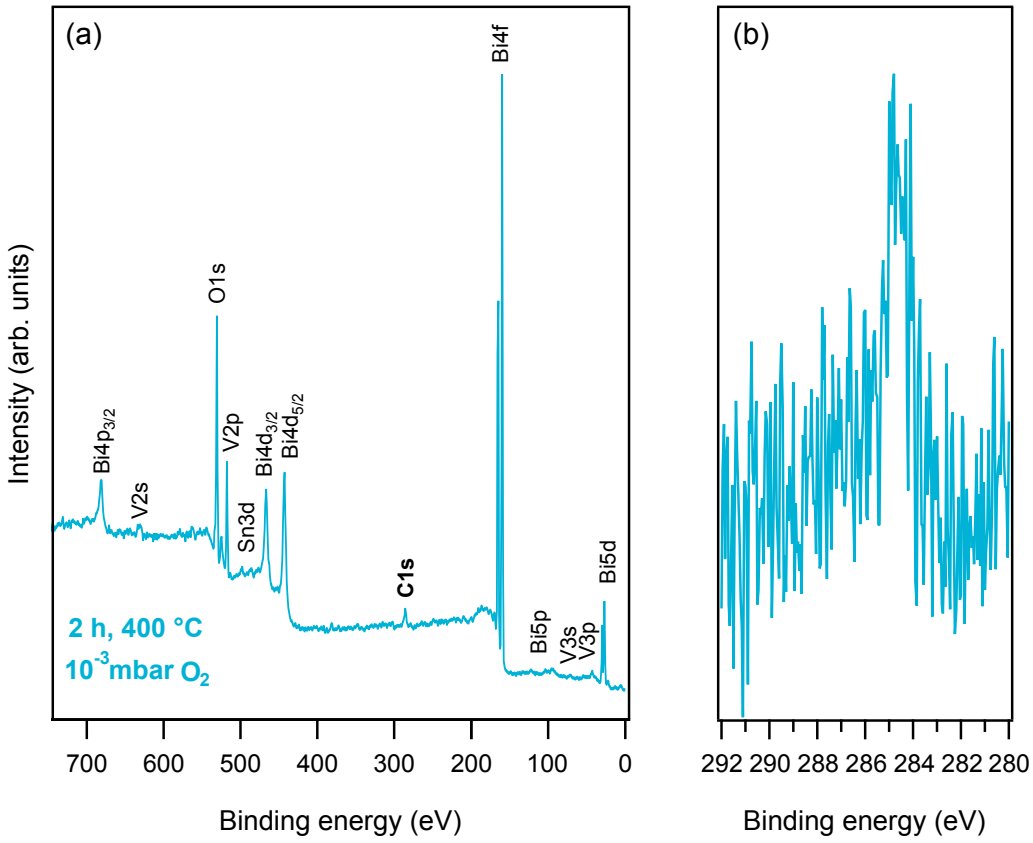

Figure 5.30: (a) Survey and (b) C1s XP spectra after calcination for the $BiVO_4$ water desorption experiment. O_2: oxygen flow (2 sccm, 1 x 10^{-3} mbar).

position obtained after calcination indicates that the $BiVO_4$ surface contains a reasonable amount of oxygen vacancies at which water dissociation could take place. To obtain more information on the water dissociation mechanism one may try to perform the water exposure experiment on a specific nearly defect free $BiVO_4$ surface.

After the water dissociation and the formation of hydroxy groups, these hydroxy groups somehow seemingly react with the lattice oxygen. This is a somewhat puzzling phenomenon because reductive water dissociation, to my knowledge, has only been described before for CeO_{2-x} by Berner et al.[121] The decrease in lattice oxygen should be due to the formation of a volatile oxygen containing compound, which is most likely oxygen or hydrogen peroxide. In Section 2.2.2 in Chapter 2 the electrochemical formation of oxygen and hydrogen peroxide from water is described. In both reaction pathways, hydroxy group intermediates are involved. However, the formation of oxygen and hydrogen peroxide from water under standard conditions is highly endothermic, being associated with standard reduction potentials of 1.23 V vs NHE and 1.78 V vs NHE, respectively. This means that at room temperature these reactions do not take place spontaneously. The conditions of the water exposure can, however, not be considered standard, as the pressure is situated at about $10^{-6} - 10^{-7}$ mbar and not the standard 1 bar. However, the deviation

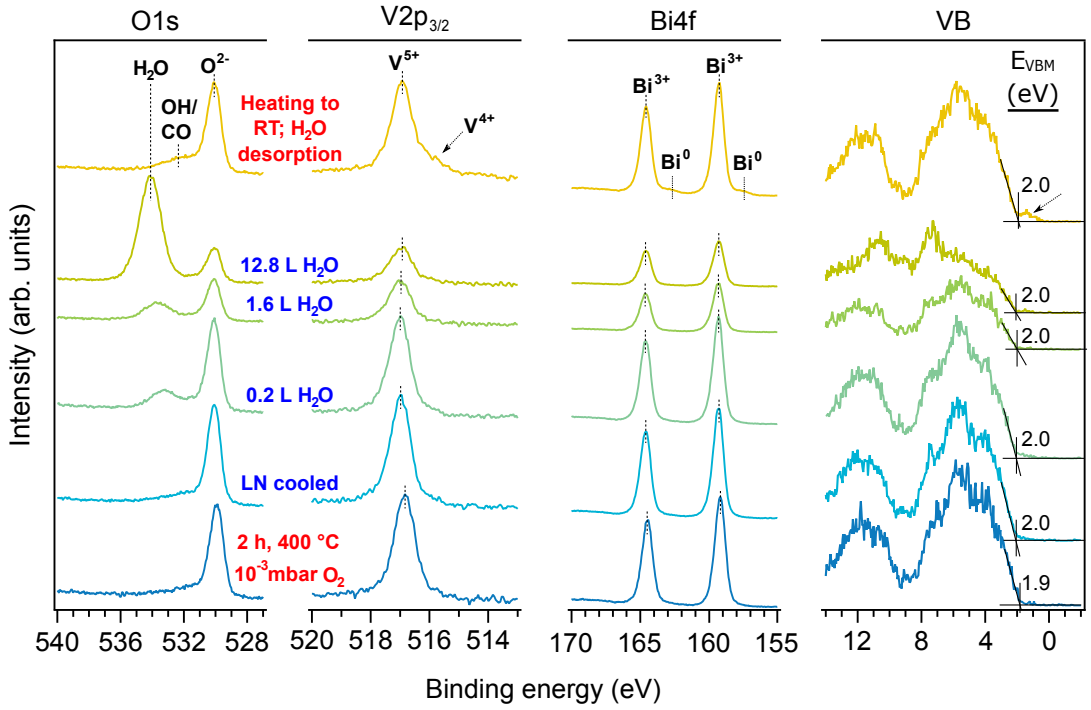

Figure 5.31: O1s, V2p$_{3/2}$, Bi4f core level and valence band XP spectra for the $BiVO_4$ water desorption experiment. The treatments and water coverage (in red: RT; in blue: 77 K) are denoted in the O1s spectra. O_2: oxygen flow (2 sccm, 1 x 10^{-3} mbar).

from the standard conditions will most likely not alter the spontaneity of either reaction. For example, for the oxygen evolution reaction which corresponds to a standard Gibbs energy ΔG^0 of 237.13 kJ/mol, an equilibrium constant K_{eq} of 10^{-46} can be calculated according to:

$$K_{eq} = 10^{\Delta G^0 / 2.303 RT} \tag{5.1}$$

$$K_{eq} = 10^{237130\ \text{J.K} \,/\, 2.303 * 8.31\ \text{J.K}^{-1}.\text{mol}^{-1} * 273.15\ \text{K}} \tag{5.2}$$

with R the gas constant and T the temperature. This means that the vacuum conditions are likely not sufficient to drive the reaction towards the formation of oxygen. Another important notice which has to be made is that hydrogen peroxide or oxygen are not formed with two surface hydroxy groups originating from water but that at least one oxygen in the reaction originates from the lattice, which may or may not be hydroxylated. This may alter the reaction mechanisms denoted in Section 2.2.2 and, thus, the standard Gibbs energy.

Due to the water oxidation reactions not being spontaneous, another source of energy may aid the transformation of surface hydroxy groups to oxygen or hydrogen peroxide. The only source of energy (besides thermal energy) are the X-rays photons used to measure the XP spectra.

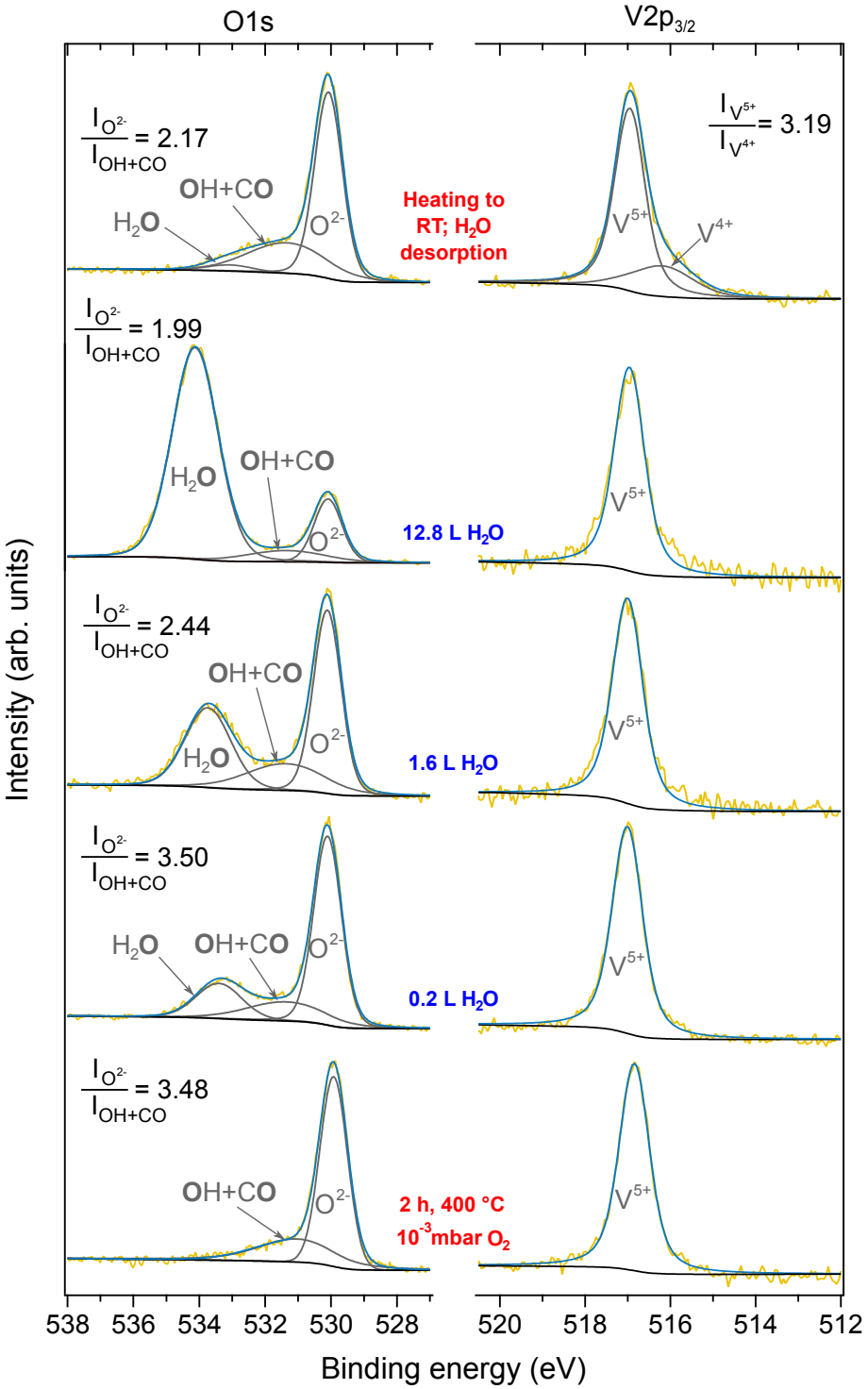

Figure 5.32: Fitting of the $V2p_{3/2}$ and O1s core level components from the water desorption experiment on $BiVO_4$. The treatments are denoted in the O1s spectra. The treatments in red and blue refer to the core level spectra measured at RT and at 77 K, respectively. Ratios of integrated components are denoted as well.

Herein, the photoelectric effect does not only create a core hole but also leads to a cascade of secondary electrons (and holes) in follow up processes. The holes created during these follow up processes should have enough energy to oxidise the surface hydroxy groups. To confirm this pathway one may try to perform the PES measurements at 77 K after having carried out the water exposure procedure at RT. The hydroxy groups may not be oxidised at these low temperatures. This experiment may give more information since the water desorption experiment did not lead to a reduction of vanadium or bismuth while being cooled to 77 K, meaning that neither water nor any formed hydroxy groups were oxidised at this low temperature.

Another unlikely possibility is that the upward Fermi level shift precedes the chemical reactions that involve the lattice oxygen. The Fermi level shift would lead to a higher amount of reduced bismuth and vanadium due to the reasons specified in Section 5.3.3. Namely, the Fermi level would cross the Bi^{3+}/Bi^{0} and V^{5+}/V^{4+} reduction potentials leading to the reduction of bismuth and vanadium. As a consequence of this reduction, the Bi-O-V bond may become unstable after which the lattice oxygen reacts with hydroxy groups at the surface. This mechanism is unlikely, because water normally does not donate electrons which would increase the Fermi level of the substrate. Hence, the source of injected electrons and, thus, the origin of the upward Fermi level shift, which forms the base of this hypothesis, is rather unclear.

All in all, the water exposure experiment on $BiVO_4$ is surprising, because it revealed that a cleaned $BiVO_4$ substrate is reduced after it makes contact with water. The exact reaction mechanisms which cause the $BiVO_4$ surface reduction upon contact with water are, however, still unclear.

5.4 Conclusion

In conclusion, we have demonstrated that the Fermi level position within $BiVO_4$ can be effectively tuned over a range of 1.1 eV through the formation of junctions with high and low work function materials. This remarkably high Fermi level tunability convincingly demonstrates that bulk Fermi level pinning is limited within $BiVO_4$ and explains why rather high photovoltages can be obtained with $BiVO_4$.

The high upwards band bending, 0.45 eV, 0.71 eV and 0.78 eV observed for the $BiVO_4/CoO_x$, $BiVO_4/RuO_2$ and $BiVO_4/NiO$ heterostructures, respectively, strongly indicates that high work function transition metal oxides very likely enhance the separation of charge carriers within $BiVO_4$ upon light absorption. Thus, the charge carrier separation effect of a contact material may absolutely not be disregarded when assessing the photo(electro)chemical water splitting efficiency of a heterostructure. It may even be the main reason for improved water splitting activities.

For increasing E_F-E_{VBM}, as probed by contacting $BiVO_4$ at elevated temperature with a low work function material, ITO, Fermi level pinning seems to take place at E_F-$E_{VBM} > 2.0 - 2.1$ eV

since a reduction of bismuth and vanadium was observed when the $BiVO_4$/ITO contact was established. This Fermi level pinning state has most probably no severe implications for reduction reactions in photoelectrochemical cells since $BiVO_4$ is usually not subjected to cathodic potentials. However, it may limit the effective n-type doping concentration which can be attained by incorporating donor impurities.

Furthermore, the assumed transitivity of the RuO_2 and ITO interface experiments allowed to align $BiVO_4$ relative to other oxides studied for photo(electro)chemical water splitting, showing that the alignment based on solid/electrolyte and solid/solid interfaces differ from each other. These findings clearly show that the alignment based on solid/electrolyte interfaces cannot be used to interpret the junctions of heterostructured materials. Thus, interface experiments, which allow the direct analysis of the contact properties of newly formed junctions, are needed to understand such heterojunctions and may help to design more efficient photoelectrodes.

One of the most noteworthy observations we made was during the $BiVO_4$ water exposure experiment, which clearly demonstrated that an oxidised $BiVO_4$ thin film was reduced upon contact with water. Namely, a reduction of Bi^{3+} to Bi^0, a reduction of V^{5+} to V^{4+} and a reduced amount of oxygen could be shown through photoelectron spectroscopy. Furthermore, this reduction proved to be reversible as the exposure of the reduced $BiVO_4$ substrate to oxygen at room temperature could partly reoxidise the surface and an oxygen plasma treatment led to a complete reoxidation of the $BiVO_4$ surface. The reduction of $BiVO_4$ upon contact with water is so remarkable, because it could provide insight in the $BiVO_4$ based photochemical water splitting mechanism, whereby the first step would not be the absorption of light but the reduction of the substrate and the oxidation of water.

References

(1) Abdi, F. F.; Firet, N.; VandeKrol, R. Efficient $BiVO_4$ Thin Film Photoanodes Modified with Cobalt Phosphate Catalyst and W-doping. *ChemCatChem* **2013**, *5*, 490–496.

(2) Li, R.; Han, H.; Zhang, F.; Wang, D.; Li, C. Highly efficient photocatalysts constructed by rational assembly of dual-cocatalysts separately on different facets of $BiVO_4$. *Energy Environ. Sci.* **2014**, *7*, 1369–1376.

(3) Kim, T. W.; Choi, K.-S. Nanoporous $BiVO_4$ Photoanodes with Dual-Layer Oxygen Evolution Catalysts for Solar Water Splitting. *Science (80-.).* **2014**, *343*, 990–994.

(4) He, Z.; Shi, Y.; Gao, C.; Wen, L.; Chen, J.; Song, S. BiOCl/$BiVO_4$ p–n Heterojunction with Enhanced Photocatalytic Activity under Visible-Light Irradiation. *J. Phys. Chem. C* **2014**, *118*, 389–398.

(5) Wang, J.; Osterloh, F. E. Limiting factors for photochemical charge separation in $BiVO_4$/Co_3O_4, a highly active photocatalyst for water oxidation in sunlight. *J. Mater. Chem. A* **2014**, *2*, 9405–9411.

(6) Pihosh, Y.; Turkevych, I.; Mawatari, K.; Uemura, J.; Kazoe, Y.; Kosar, S.; Makita, K.; Sugaya, T.; Matsui, T.; Fujita, D.; Tosa, M.; Kondo, M.; Kitamori, T. Photocatalytic generation of hydrogen by core-shell WO_3/$BiVO_4$ nanorods with ultimate water splitting efficiency. *Sci. Rep.* **2015**, *5*, 11141.

(7) Abdi, F. F.; Han, L.; Smets, A. H. M.; Zeman, M.; Dam, B.; van de Krol, R. Efficient solar water splitting by enhanced charge separation in a bismuth vanadate-silicon tandem photoelectrode. *Nat. Commun.* **2013**, *4*, 17594–17598.

(8) Qiu, Y.; Liu, W.; Chen, W.; Zhou, G.; Hsu, P. C.; Zhang, R.; Liang, Z.; Fan, S.; Zhang, Y.; Cui, Y. Efficient solar-driven water splitting by nanocone $BiVO_4$-perovskite tandem cells. *Sci. Adv.* **2016**, *2*, e1501764.

(9) Wang, D.; Li, R.; Zhu, J.; Shi, J.; Han, J.; Zong, X.; Li, C. Photocatalytic water oxidation on $BiVO_4$ with the electrocatalyst as an oxidation cocatalyst: Essential relations between electrocatalyst and photocatalyst. *J. Phys. Chem. C* **2012**, *116*, 5082–5089.

(10) Zhong, M.; Hisatomi, T.; Kuang, Y.; Zhao, J.; Liu, M.; Iwase, A.; Jia, Q.; Nishiyama, H.; Minegishi, T.; Nakabayashi, M.; Shibata, N.; Niishiro, R.; Katayama, C.; Shibano, H.; Katayama, M.; Kudo, A.; Yamada, T.; Domen, K. Surface modification of CoO_x loaded $BiVO_4$ photoanodes with ultrathin p-type NiO layers for improved solar water oxidation. *J. Am. Chem. Soc.* **2015**, *137*, 5053–5060.

(11) Wang, Q.; Hisatomi, T.; Jia, Q.; Tokudome, H.; Zhong, M.; Wang, C.; Pan, Z.; Takata, T.; Nakabayashi, M.; Shibata, N.; Li, Y.; Sharp, I. D.; Kudo, A.; Yamada, T.; Domen, K. Scalable water splitting on particulate photocatalyst sheets with a solar-to-hydrogen energy conversion efficiency exceeding 1%. *Nat. Mater.* **2016**, *15*, 611–615.

(12) Kanan, M. W.; Nocera, D. G. In situ formation of an oxygen-evolving catalyst in neutral water containing phosphate and Co^{2+}. *Science (80-.).* **2008**, *321*, 1072–1075.

(13) Man, I. C.; Su, H. Y.; Calle-Vallejo, F.; Hansen, H. A.; Martínez, J. I.; Inoglu, N. G.; Kitchin, J.; Jaramillo, T. F.; Nørskov, J. K.; Rossmeisl, J. Universality in Oxygen Evolution Electrocatalysis on Oxide Surfaces. *ChemCatChem* **2011**, *3*, 1159–1165.

(14) Zhong, D. K.; Choi, S.; Gamelin, D. R. Near-Complete Suppression of Surface Recombination in Solar Photoelectrolysis by "Co-Pi" Catalyst-Modified W:$BiVO_4$. *J. Am. Chem. Soc.* **2011**, *133*, 18370–18377.

(15) Zachäus, C.; Abdi, F. F.; Peter, L. M.; Van De Krol, R. Photocurrent of $BiVO_4$ is limited by surface recombination, not surface catalysis. *Chem. Sci.* **2017**, *8*, 3712–3719.

(16) Lin, F.; Boettcher, S. W. Adaptive semiconductor/electrocatalyst junctions in water-splitting photoanodes. *Nat. Mater.* **2014**, *13*, 81–86.

(17) Barroso, M.; Cowan, A. J.; Pendlebury, S. R.; Grätzel, M.; Klug, D. R.; Durrant, J. R. The role of cobalt phosphate in enhancing the photocatalytic activity of α-Fe_2O_3 toward water oxidation. *J. Am. Chem. Soc.* **2011**, *133*, 14868–14871.

(18) Melo, M. A.; Wu, Z.; Nail, B. A.; De Denko, A. T.; Nogueira, A. F.; Osterloh, F. E. Surface Photovoltage Measurements on a Particle Tandem Photocatalyst for Overall Water Splitting. *Nano Lett.* **2018**, *18*, 805–810.

(19) Nellist, M. R.; Laskowski, F. A. L.; Lin, F.; Mills, T. J.; Boettcher, S. W. Semiconductor–Electrocatalyst Interfaces: Theory, Experiment, and Applications in Photoelectrochemical Water Splitting. *Acc. Chem. Res.* **2016**, *49*, 733–740.

(20) Resasco, J.; Zhang, H.; Kornienko, N.; Becknell, N.; Lee, H.; Guo, J.; Briseno, A. L.; Yang, P. TiO_2/$BiVO_4$ Nanowire Heterostructure Photoanodes Based on Type II Band Alignment. *ACS Cent. Sci.* **2016**, *2*, 80–88.

(21) Yuan, Q.; Chen, L.; Xiong, M.; He, J.; Luo, S. L.; Au, C. T.; Yin, S. F. Cu_2O/$BiVO_4$ heterostructures: Synthesis and application in simultaneous photocatalytic oxidation of organic dyes and reduction of Cr(VI) under visible light. *Chem. Eng. J.* **2014**, *255*, 394–402.

(22) Mahadik, M. A.; Chung, H.-S.; Lee, S.-Y.; Cho, M.; Jang, J. S. In-Situ Noble Fabrication of Bi_2S_3/$BiVO_4$ Hybrid Nanostructure through a Photoelectrochemical Transformation Process for Solar Hydrogen Production. *ACS Sustain. Chem. Eng.* **2018**, *6*, 12489–12501.

(23) Qiao, R.; Mao, M.; Hu, E.; Zhong, Y.; Ning, J.; Hu, Y. Facile Formation of Mesoporous $BiVO_4$/Ag/AgCl Heterostructured Microspheres with Enhanced Visible-Light Photoactivity. *Inorg. Chem.* **2015**, *54*, 9033–9039.

(24) Gleria, M.; Memming, R. Charge transfer processes at large band gap semiconductor electrodes: reactions at SiC-electrodes. *J. Electroanal. Chem.* **1975**, *65*, 163–175.

(25) Gelderman, K.; Lee, L.; Donne, S. W. Flat-Band Potential of a Semiconductor: Using the Mott–Schottky Equation. *J. Chem. Educ.* **2007**, *84*, 685.

(26) Gerischer, H. Electrolytic decomposition and photodecomposition of compound semiconductors in contact with electrolytes. *J. Vac. Sci. Technol.* **1978**, *15*, 1422–1428.

(27) Serpone, N.; Pelizzetti, E., *Photocatalysis : fundamentals and applications*; Wiley: New York, 1989, p 650.

(28) Sakata, T.; Kawai, T. In *Energy Resour. Through Photochem. Catal.* Academic Press: 1983, pp 331–358.

(29) Cardon, F.; Gomes, W. P. On the determination of the flat-band potential of a semiconductor in contact with a metal or an electrolyte from the Mott-Schottky plot. *J. Phys. D. Appl. Phys.* **1978**, *11*, L63–L67.

(30) Butler, M. A. Prediction of Flatband Potentials at Semiconductor-Electrolyte Interfaces from Atomic Electronegativities. *J. Electrochem. Soc.* **1978**, *125*, 228.

(31) Xu, Y.; Schoonen, M. A. A. The Absolute Energy Positions of Conduction and Valence Bands of Selected Semiconducting Minerals. *Am. Mineral.* **2000**, *85*, 543–556.

(32) Jaegermann, W. In *Photoelectrochem. Photovoltaics Layer. Semicond.* Kluwer Academic Publishers: Dordrecht, the Netherlands, 1992, pp 195–295.

(33) Waldrop, J. R.; Kraut, E. A.; Kowalczyk, S. P.; Grant, R. W. Valence-band discontinuities for abrupt (110), (100), and (111) oriented Ge-GaAs heterojunctions. *Surf. Sci.* **1983**, *132*, 513–518.

(34) Greiner, M. T.; Chai, L.; Helander, M. G.; Tang, W. M.; Lu, Z. H. Transition metal oxide work functions: The influence of cation oxidation state and oxygen vacancies. *Adv. Funct. Mater.* **2012**, *22*, 4557–4568.

(35) Morasch, J.; Li, S.; Brötz, J.; Jaegermann, W.; Klein, A. Reactively magnetron sputtered Bi_2O_3 thin films: Analysis of structure, optoelectronic, interface, and photovoltaic properties. *Phys. Status Solidi Appl. Mater. Sci.* **2014**, *211*, 93–100.

(36) Gassenbauer, Y.; Schafranek, R.; Klein, A.; Zafeiratos, S.; Hävecker, M.; Knop-Gericke, A.; Schlögl, R. Surface states, surface potentials, and segregation at surfaces of tin-doped In_2O_3. *Phys. Rev. B - Condens. Matter Mater. Phys.* **2006**, *73*, 245312.

(37) McCrory, C. C. L.; Jung, S.; Ferrer, I. M.; Chatman, S. M.; Peters, J. C.; Jaramillo, T. F. Benchmarking Hydrogen Evolving Reaction and Oxygen Evolving Reaction Electrocatalysts for Solar Water Splitting Devices. *J. Am. Chem. Soc.* **2015**, *137*, 4347–4357.

(38) Zhou, M.; Bao, J.; Bi, W.; Zeng, Y.; Zhu, R.; Tao, M.; Xie, Y. Efficient Water Splitting via a Heteroepitaxial $BiVO_4$ Photoelectrode Decorated with Co-Pi Catalysts. *ChemSusChem* **2012**, *5*, 1420–1425.

(39) Chen, L.; Alarcón-Lladó, E.; Hettick, M.; Sharp, I. D.; Lin, Y.; Javey, A.; Ager, J. W. Reactive sputtering of bismuth vanadate photoanodes for solar Water splitting. *J. Phys. Chem. C* **2013**, *117*, 21635–21642.

(40) Liang, Y.; Tsubota, T.; Mooij, L. P. A.; Van De Krol, R. Highly improved quantum efficiencies for thin film $BiVO_4$ photoanodes. *J. Phys. Chem. C* **2011**, *115*, 17594–17598.

(41) Yu, J.; Kudo, A. Effects of structural variation on the photocatalytic performance of hydrothermally synthesized $BiVO_4$. *Adv. Funct. Mater.* **2006**, *16*, 2163–2169.

(42) Su, J.; Zou, X.-X.; Li, G.-D.; Wei, X.; Yan, C.; Wang, Y.-N.; Zhao, J.; Zhou, L.-J.; Chen, J.-S. Macroporous V_2O_5—$BiVO_4$ Composites: Effect of Heterojunction on the Behavior of Photogenerated Charges. *J. Phys. Chem. C* **2011**, *115*, 8064–8071.

(43) Cooper, J. K.; Gul, S.; Toma, F. M.; Chen, L.; Glans, P. A.; Guo, J.; Ager, J. W.; Yano, J.; Sharp, I. D. Electronic structure of monoclinic $BiVO_4$. *Chem. Mater.* **2014**, *26*, 5365–5373.

(44) Moulder, J. F.; Stickle, W. F.; Sobol, P. E.; Bomben, K. D., *Handbook of X-ray photoelectron spectroscopy: a reference book of standard spectra for identification and interpretation of XPS data*; Physical Electronics: Eden Prairie MN, 1992, p 261.

(45) Fritsche, J.; Schulmeyer, T.; Thißen, A.; Klein, A.; Jaegermann, W. Interface modification of CdTe thin film solar cells by $CdCl_2$-activation. *Thin Solid Films* **2003**, *431-432*, 267–271.

(46) Murcia-López, S.; Fàbrega, C.; Monllor-Satoca, D.; Hernández-Alonso, M. D.; Penelas-Pérez, G.; Morata, A.; Morante, J. R.; Andreu, T. Tailoring Multilayered $BiVO_4$ Photoanodes by Pulsed Laser Deposition for Water Splitting. *ACS Appl. Mater. Interfaces* **2016**, *8*, 4076–4085.

(47) Wang, G.; Ling, Y.; Lu, X.; Qian, F.; Tong, Y.; Zhang, J. Z.; Lordi, V.; Rocha Leao, C.; Li, Y. Computational and Photoelectrochemical Study of Hydrogenated Bismuth Vanadate. *J. Phys. Chem. C* **2013**, *117*, 10957–10964.

(48) Yin, W.-J.; Wei, S.-H.; Al-Jassim, M. M.; Turner, J.; Yan, Y. Doping properties of monoclinic $BiVO_4$ studied by first-principles density-functional theory. *Phys. Rev. B* **2011**, *83*, 155102.

(49) Fan, J. C. C.; Goodenough, J. B. X-ray photoemission spectroscopy studies of Sn-doped indium-oxide films. *J. Appl. Phys.* **1977**, *48*, 3524–3531.

(50) Jeong, S.; Ha, Y.-G.; Moon, J.; Facchetti, A.; Marks, T. J. Role of Gallium Doping in Dramatically Lowering Amorphous-Oxide Processing Temperatures for Solution-Derived Indium Zinc Oxide Thin-Film Transistors. *Adv. Mater.* **2010**, *22*, 1346–1350.

(51) Dupin, J.-C.; Gonbeau, D.; Vinatier, P.; Levasseur, A. Systematic XPS studies of metal oxides, hydroxides and peroxides. *Phys. Chem. Chem. Phys.* **2000**, *2*, 1319–1324.

(52) Pfeifer, V.; Erhart, P.; Li, S.; Rachut, K.; Morasch, J.; Brötz, J.; Reckers, P.; Mayer, T.; Rühle, S.; Zaban, A.; Mora Seró, I.; Bisquert, J.; Jaegermann, W.; Klein, A. Energy band alignment between anatase and rutile TiO_2. *J. Phys. Chem. Lett.* **2013**, *4*, 4182–4187.

(53) Kachouane, A.; Addou, M.; Bougrine, A.; El idrissi, B.; Messoussi, R.; Regragui, M.; Bérnede, J. Preparation and characterisation of tin-doped indium oxide films. *Mater. Chem. Phys.* **2001**, *70*, 285–289.

(54) Gassenbauer, Y.; Wachau, A.; Klein, A. Chemical and electronic properties of the ITO/Al_2O_3 interface. *Phys. Chem. Chem. Phys.* **2009**, *11*, 3049.

(55) Walsh, A.; Da Silva, J. L.; Wei, S. H.; Körber, C.; Klein, A.; Piper, L. F.; Demasi, A.; Smith, K. E.; Panaccione, G.; Torelli, P.; Payne, D. J.; Bourlange, A.; Egdell, R. G. Nature of the band gap of In_2O_3 revealed by first-principles calculations and X-ray spectroscopy. *Phys. Rev. Lett.* **2008**, *100*, 167402.

(56) Grosvenor, A. P.; Biesinger, M. C.; Smart, R. S. C.; McIntyre, N. S. New interpretations of XPS spectra of nickel metal and oxides. *Surf. Sci.* **2006**, *600*, 1771–1779.

(57) Weidler, N.; Paulus, S.; Schuch, J.; Klett, J.; Hoch, S.; Stenner, P.; Maljusch, A.; Brötz, J.; Wittich, C.; Kaiser, B.; Jaegermann, W. CoO_x thin film deposited by CVD as efficient water oxidation catalyst: change of oxidation state in XPS and its correlation to electrochemical activity. *Phys. Chem. Chem. Phys.* **2016**, *18*, 10708–10718.

(58) Qiao, L.; Xiao, H. Y.; Meyer, H. M.; Sun, J. N.; Rouleau, C. M.; Puretzky, A. A.; Geohegan, D. B.; Ivanov, I. N.; Yoon, M.; Weber, W. J.; Biegalski, M. D. Nature of the band gap and origin of the electro-/photo-activity of Co_3O_4. *J. Mater. Chem. C* **2013**, *1*, 4628.

(59) Uddin, M. T.; Nicolas, Y.; Olivier, C.; Toupance, T.; Müller, M. M.; Kleebe, H.-J.; Rachut, K.; Ziegler, J.; Klein, A.; Jaegermann, W. Preparation of RuO_2/TiO_2 Mesoporous Heterostructures and Rationalization of Their Enhanced Photocatalytic Properties by Band Alignment Investigations. *J. Phys. Chem. C* **2013**, *117*, 22098–22110.

(60) Schafranek, R.; Schaffner, J.; Klein, A. In situ photoelectron study of the (Ba,Sr)TiO_3/RuO_2 contact formation. *J. Eur. Ceram. Soc.* **2010**, *30*, 187–192.

(61) Tengeler, S.; Fingerle, M.; Calvet, W.; Steinert, C.; Kaiser, B.; Mayer, T.; Jaegermann, W. The Impact of Different Si Surface Terminations in the (001) n-Si/NiO_x Heterojunction on the Oxygen Evolution Reaction (OER) by XPS and Electrochemical Methods. *J. Electrochem. Soc.* **2018**, *165*, H3122–H3130.

(62) Lohaus, C.; Morasch, J.; Brötz, J.; Klein, A.; Jaegermann, W. Investigations on RF-magnetron sputtered Co_3O_4 thin films regarding the solar energy conversion properties. *J. Phys. D. Appl. Phys.* **2016**, *49*, 155306.

(63) Greiner, M. T.; Helander, M. G.; Wang, Z. B.; Tang, W. M.; Lu, Z. H. Effects of processing conditions on the work function and energy-level alignment of NiO thin films. *J. Phys. Chem. C* **2010**, *114*, 19777–19781.

(64) Klein, A.; Körber, C.; Wachau, A.; Säuberlich, F.; Gassenbauer, Y.; Harvey, S. P.; Proffit, D. E.; Mason, T. O. Transparent conducting oxides for photovoltaics: Manipulation of fermi level,work function and energy band alignment. *Materials (Basel).* **2010**, *3*, 4892–4914.

(65) Tokunaga, S.; Kato, H.; Kudo, A. Selective preparation of monoclinic and tetragonal $BiVO_4$ with scheelite structure and their photocatalytic properties. *Chem. Mater.* **2001**, *13*, 4624–4628.

(66) Irwin, M. D.; Buchholz, D. B.; Hains, A. W.; Chang, R. P. H.; Marks, T. J. p-Type semiconducting nickel oxide as an efficiency-enhancing anode interfacial layer in polymer bulk-heterojunction solar cells. *Proc. Natl. Acad. Sci.* **2008**, *105*, 2783–2787.

(67) Barreca, D.; Massignan, C.; Daolio, S.; Fabrizio, M.; Piccirillo, C.; Armelao, L.; Tondello, E. Composition and Microstructure of Cobalt Oxide Thin Films Obtained from a Novel Cobalt(II) Precursor by Chemical Vapor Deposition. *Chem. Mater.* **2001**, *13*, 588–593.

(68) Xu, J. M.; Cheng, J. P. The advances of Co_3O_4 as gas sensing materials: A review. *J. Alloys Compd.* **2016**, *686*, 753–768.

(69) Klein, A. Interface Properties of Dielectric Oxides. *J. Am. Ceram. Soc.* **2016**, *99*, 369–387.

(70) Lee, K. H.; Jang, H. W.; Kim, K.-B.; Tak, Y.-H.; Lee, J.-L. Mechanism for the increase of indium-tin-oxide work function by O_2 inductively coupled plasma treatment. *J. Appl. Phys.* **2004**, *95*, 586–590.

(71) Hagleitner, D. R.; Menhart, M.; Jacobson, P.; Blomberg, S.; Schulte, K.; Lundgren, E.; Kubicek, M.; Fleig, J.; Kubel, F.; Puls, C.; Limbeck, A.; Hutter, H.; Boatner, L. A.; Schmid, M.; Diebold, U. Bulk and surface characterization of In_2O_3(001) single crystals. *Phys. Rev. B* **2012**, *85*, 115441.

(72) Kweon, K. E.; Hwang, G. S.; Kim, J.; Kim, S.; Kim, S. Electron small polarons and their transport in bismuth vanadate: A first principles study. *Phys. Chem. Chem. Phys.* **2015**, *17*, 256–260.

(73) Wiktor, J.; Ambrosio, F.; Pasquarello, A. Role of Polarons in Water Splitting: The Case of $BiVO_4$. *ACS Energy Lett.* **2018**, *3*, 1693–1697.

(74) Jovic, V.; Laverock, J.; Rettie, A. J. E.; Zhou, J.-S.; Mullins, C. B.; Singh, V. R.; Lamoureux, B.; Wilson, D.; Su, T.-Y.; Jovic, B.; Bluhm, H.; Söhnel, T.; Smith, K. E. Soft X-ray spectroscopic studies of the electronic structure of M:$BiVO_4$ (M = Mo, W) single crystals. *J. Mater. Chem. A* **2015**, *3*, 23743–23753.

(75) Winiarski, A.; Wübbeler, G.; Scharfschwerdt, C.; Clausing, E.; Neumann, M. Photoemission studies of $BaPb_{1-x}Bi_xO_3$ and $Ba_{1-y}K_yBiO_3$ crystals. *Fresenius. J. Anal. Chem.* **1991**, *341*, 296–300.

(76) Nagoshi, M.; Suzuki, T.; Fukuda, Y.; Ueki, K.; Tokiwa, A.; Kiruchi, M.; Syono, Y.; Tachiki, M. Electronic states of $BaBiO_{3\text{-delta}}$ and K-doping effects studied by photoelectron spectroscopy. *J. Phys. Condens. Matter* **1992**, *4*, 5769–5781.

(77) Chouhan, A. S.; Athresh, E.; Ranjan, R.; Raghavan, S.; Avasthi, S. $BaBiO_3$: A potential absorber for all-oxide photovoltaics. *Mater. Lett.* **2018**, *210*, 218–222.

(78) Hong, S. J.; Lee, S.; Jang, J. S.; Lee, J. S. Heterojunction $BiVO_4/WO_3$ electrodes for enhanced photoactivity of water oxidation. *Energy Environ. Sci.* **2011**, *4*, 1781.

(79) Shi, Q.; Murcia-López, S.; Tang, P.; Flox, C.; Morante, J. R.; Bian, Z.; Wang, H.; Andreu, T. Role of Tungsten Doping on the Surface States in $BiVO_4$ Photoanodes for Water Oxidation: Tuning the Electron Trapping Process. *ACS Catal.* **2018**, *8*, 3331–3342.

(80) Pattengale, B.; Huang, J. Implicating the contributions of surface and bulk states on carrier trapping and photocurrent performance of $BiVO_4$ photoanodes. *Phys. Chem. Chem. Phys.* **2017**, *19*, 6831–6837.

(81) Lamm, B.; Trześniewski, B. J.; Döscher, H.; Smith, W. A.; Stefik, M. Emerging Post-synthetic Improvements of $BiVO_4$ Photoanodes for Solar Water Splitting. *ACS Energy Lett.* **2018**, *3*, 112–124.

(82) Milazzo, G.; Caroli, S.; Sharma, V. K.; International Union of Pure and Applied Chemistry. Electrochemistry Commission., *Tables of standard electrode potentials*; Wiley: London, 1978, p 421.

(83) Bard, A. J.; Parsons, R.; Jordan, J.; International Union of Pure and Applied Chemistry., *Standard potentials in aqueous solution*; Dekker: New York, 1985, p 834.

(84) Zhang, J.; Ren, F.; Deng, M.; Wang, Y. Enhanced visible-light photocatalytic activity of a g-$C_3N_4/BiVO_4$ nanocomposite: a first-principles study. *Phys. Chem. Chem. Phys.* **2015**, *17*, 10218–10226.

(85) Qiu, W.; Huang, Y.; Tang, S.; Ji, H.; Tong, Y. Thin-Layer Indium Oxide and Cobalt Oxyhydroxide Cobalt-Modified $BiVO_4$ Photoanode for Solar-Assisted Water Electrolysis. *J. Phys. Chem. C* **2017**, *121*, 17150–17159.

(86) Cao, J.; Zhou, C.; Lin, H.; Xu, B.; Chen, S. Surface modification of m-$BiVO_4$ with wide band-gap semiconductor BiOCl to largely improve the visible light induced photocatalytic activity. *Appl. Surf. Sci.* **2013**, *284*, 263–269.

(87) Kudo, A.; Miseki, Y. Heterogeneous photocatalyst materials for water splitting. *Chem. Soc. Rev.* **2009**, *38*, 253–278.

(88) Pelizzetti, E.; Visca, M. In *Energy Resour. Through Photochem. Catal.* Academic Press: 1983, pp 261–296.

(89) Mönch, W., *Electronic properties of semiconductor interfaces*; Springer: 2004, p 263.

(90) Schafranek, R.; Li, S.; Chen, F.; Wu, W.; Klein, A. $PbTiO_3$/$SrTiO_3$ interface: Energy band alignment and its relation. *Phys. Rev. B* **2011**, *84*, 045317.

(91) Klein, A.; Lohaus, C.; Reiser, P.; Dimesso, L.; Wang, X.; Yang, T. Energy band alignment of antiferroelectric (Pb,La)(Zr,Sn,Ti)O_3. *Appl. Surf. Sci.* **2017**, *407*, 99–104.

(92) Klein, A. Energy band alignment in chalcogenide thin film solar cells from photoelectron spectroscopy. *J. Phys. Condens. Matter* **2015**, *27*, 134201.

(93) Klein, A. Transparent conducting oxides: Electronic structure-property relationship from photoelectron spectroscopy with in situ sample preparation. *J. Am. Ceram. Soc.* **2013**, *96*, ed. by Green, D. J., 331–345.

(94) Siol, S.; Hellmann, J. C.; Tilley, S. D.; Graetzel, M.; Morasch, J.; Deuermeier, J.; Jaegermann, W.; Klein, A. Band Alignment Engineering at Cu_2O/ZnO Heterointerfaces. *ACS Appl. Mater. Interfaces* **2016**, *8*, 21824–21831.

(95) Tersoff, J. Schottky barrier heights and the continuum of gap states. *Phys. Rev. Lett.* **1984**, *52*, 465–468.

(96) Spicer, W. E.; Kendelewicz, T.; Newman, N.; Cao, R.; McCants, C.; Miyano, K.; Lindau, I.; Liliental-Weber, Z.; Weber, E. R. The advanced unified defect model and its applications. *Appl. Surf. Sci.* **1988**, *33-34*, 1009–1029.

(97) Chen, F.; Schafranek, R.; Wu, W.; Klein, A. Reduction-induced Fermi level pinning at the interfaces between Pb(Zr,Ti)O_3 and Pt, Cu and Ag metal electrodes. *J. Phys. D. Appl. Phys.* **2011**, *44*, 255301.

(98) Körber, C.; Harvey, S. P.; Mason, T. O.; Klein, A. Barrier heights at the SnO_2/Pt interface: In situ photoemission and electrical properties. *Surf. Sci.* **2008**, *602*, 3246–3252.

(99) Giesecke, R.; Hertwig, R.; Bayer, T. J.; Randall, C. A.; Klein, A. Modification of the Schottky barrier height at the RuO_2 cathode during resistance degradation of Fe-doped $SrTiO_3$. *J. Am. Ceram. Soc.* **2017**, *100*, 4590–4601.

(100) Li, S.; Ghinea, C.; Bayer, T. J. M.; Motzko, M.; Schafranek, R.; Klein, A. Electrical properties of (Ba, Sr)TiO_3 thin films with Pt and ITO electrodes: Dielectric and rectifying behaviour. *J. Phys. Condens. Matter* **2011**, *23*, 334202.

(101) Deák, P.; Aradi, B.; Frauenheim, T. Band lineup and charge carrier separation in mixed rutile-anatase systems. *J. Phys. Chem. C* **2011**, *115*, 3443–3446.

(102) Scanlon, D. O.; Dunnill, C. W.; Buckeridge, J.; Shevlin, S. A.; Logsdail, A. J.; Woodley, S. M.; Catlow, C. R. A.; Powell, M. J.; Palgrave, R. G.; Parkin, I. P.; Watson, G. W.; Keal, T. W.; Sherwood, P.; Walsh, A.; Sokol, A. A. Band alignment of rutile and anatase TiO_2. *Nat. Mater.* **2013**, *12*, 798–801.

(103) Nozik, A. J. Photoelectrochemistry: Applications to Solar Energy Conversion. *Annu. Rev. Phys. Chem.* **1978**, *29*, 189–222.

(104) Hoyos, L. J.; Rivera, D. F.; Gualdrón-Reyes, A. F.; Ospina, R.; Rodríguez-Pereira, J.; Ropero-Vega, J. L.; Niño-Gómez, M. E. Influence of immersion cycles during n—β—Bi_2O_3 sensitization on the photoelectrochemical behaviour of N—F—codoped TiO_2 nanotubes. *Appl. Surf. Sci.* **2017**, *423*, 917–926.

(105) Li, S. et al. Intrinsic energy band alignment of functional oxides. *Phys. Status Solidi - Rapid Res. Lett.* **2014**, *8*, 571–576.

(106) Li, S.; Morasch, J.; Klein, A.; Chirila, C.; Pintilie, L.; Jia, L.; Ellmer, K.; Naderer, M.; Reichmann, K.; Gröting, M.; Albe, K. Influence of orbital contributions to the valence band alignment of Bi_2O_3, Fe_2O_3, $BiFeO_3$, and $Bi_{0.5}Na_{0.5}TiO_3$. *Phys. Rev. B - Condens. Matter Mater. Phys.* **2013**, *88*, 045428.

(107) Walsh, A.; Payne, D. J.; Egdell, R. G.; Watson, G. W. Stereochemistry of post-transition metal oxides: Revision of the classical lone pair model. *Chem. Soc. Rev.* **2011**, *40*, 4455–4463.

(108) Brillson, L. J. In *Phys. Rev. Lett.* 4; Springer, Dordrecht: 1978; Vol. 40, pp 260–263.

(109) Brillson, L. J.; Dong, Y.; Tuomisto, F.; Svensson, B. G.; Kuznetsov, A. Y.; Doutt, D.; Mosbacker, H. L.; Cantwell, G.; Zhang, J.; Song, J. J.; Fang, Z.-Q.; Look, D. C. Interplay of native point defects with ZnO Schottky barriers and doping. *J. Vac. Sci. Technol. B, Nanotechnol. Microelectron. Mater. Process. Meas. Phenom.* **2012**, *30*, 050801.

(110) Brillson, L. J.; Lu, Y. ZnO Schottky barriers and Ohmic contacts. *J. Appl. Phys.* **2011**, *109*, 121301.

(111) Allen, M. W.; Durbin, S. M. Influence of oxygen vacancies on Schottky contacts to ZnO. *Appl. Phys. Lett.* **2008**, *92*, 122110.

(112) Favaro, M.; Abdi, F. F.; Lamers, M.; Crumlin, E. J.; Liu, Z.; van de Krol, R.; Starr, D. E. Light-Induced Surface Reactions at the Bismuth Vanadate/Potassium Phosphate Interface. *J. Phys. Chem. B* **2018**, *122*, 801–809.

(113) Dharmadhikari, V. S.; Sainkar, S.; Badrinarayan, S.; Goswami, A. Characterisation of thin films of bismuth oxide by X-ray photoelectron spectroscopy. *J. Electron Spectros. Relat. Phenomena* **1982**, *25*, 181–189.

(114) Fingerle, M.; Tengeler, S.; Calvet, W.; Mayer, T.; Jaegermann, W. Water Interaction with Sputter-Deposited Nickel Oxide on n-Si Photoanode: Cryo Photoelectron Spectroscopy on Adsorbed Water in the Frozen Electrolyte Approach. *J. Electrochem. Soc.* **2018**, *165*, H3148–H3153.

(115) Silversmit, G.; Depla, D.; Poelman, H.; Marin, G. B.; De Gryse, R. Determination of the V2p XPS binding energies for different vanadium oxidation states (V^{5+} to V^{0+}). *J. Electron Spectros. Relat. Phenomena* **2004**, *135*, 167–175.

(116) Brookes, I. M.; Muryn, C. A.; Thornton, G. Imaging Water Dissociation on TiO_2(110). *Phys. Rev. Lett.* **2001**, *87*, 266103.

(117) Baer, Y.; Myers, H. An XPS study of the valence bands in solid and liquid bismuth. *Solid State Commun.* **1977**, *21*, 833–835.

(118) Thiel, P. A.; Madey, T. E. The interaction of water with solid surfaces: Fundamental aspects. *Surf. Sci. Rep.* **1987**, *7*, 211–385.

(119) Motzko, M.; Carrillo Solano, M. A.; Jaegermann, W.; Hausbrand, R. Photoemission Study on the Interaction Between LiCoO ¡sub¿2¡/sub¿ Thin Films and Adsorbed Water. *J. Phys. Chem. C* **2015**, *119*, 23407–23412.

(120) Henderson, M. A. The interaction of water with solid surfaces: fundamental aspects revisited. *Surf. Sci. Rep.* **2002**, *46*, 1–308.

(121) Berner, U.; Schierbaum, K.; Jones, G.; Wincott, P.; Haq, S.; Thornton, G. Ultrathin ordered CeO_2 overlayers on Pt(111): interaction with NO_2, NO, H_2O and CO. *Surf. Sci.* **2000**, *467*, 201–213.

Chapter 6

Heterostructured $CuFeO_2$

6.1 Introduction

All the information that was gathered on how to prepare anisotropic $BiVO_4$ heterostructures (Chapter 4) and how to analyse the interfaces of $BiVO_4$ heterostructures through photoelectron spectroscopy (Chapter 5) was used to develop and analyse heterostructures of a promising photocathode material, delafossite copper iron oxide or $CuFeO_2$.

As described in the main Introduction (Chapter 2) there is an immediate need to study and develop new efficient visible light active photocathode materials. Few oxides have proven to be suitable for hydrogen production through photochemical water splitting.[1] Photochemical water splitting has been demonstrated with TiO_2 and $SrTiO_3$, which, however, have an intrinsically low water splitting efficiency due to their relatively wide band gap ($E_g > 3$ eV).[2] The main problem is that oxides generally have a low VBM, owing to the O2p character of their valence band. Strategies to enhance visible light absorption, such as impurity doping or mixing in nitrogen to form oxynitrides, only led to a small improvement of the (sacrificial) hydrogen evolution efficiency.[3,4] Some oxides, however, exhibit a higher VBM due to the hybridization of metal valence states with the O2p states, as is the case for copper based oxides.[5–7] Indeed, due to its narrow band gap of 2.0 — 2.2 eV, Cu_2O based photocathodes have been able to reach state-of-the-art cathodic photocurrents, up to -7.6 mA cm^{-2} at 0 V_{RHE},[8] admittedly, using TiO_2 protection layers to protect Cu_2O against photocorrosion.[8,9] A promising alternative to cuprous oxide could be the delafossite copper iron oxide due to its even lower band gap of about 1.5 eV,[10,11] good carrier mobility of about 0.2 cm^2 V^{-1} s^{-1},[12] and its suitable CBM, at -0.1 — -0.5 eV vs RHE.[1,10,12,13]

However, only poor to mediocre hydrogen evolution efficiencies have been measured so far with $CuFeO_2$. Jin et al. showed that a thin film of dropcasted 2H-$CuFeO_2$ nanoplatelets only exhibited a photocurrent of 8.8 μA cm^{-2} at 0 V_{RHE},[11] which is far below the efficiency which can be expected from the absorption spectrum, which should allow to reach photocurrents up to 15 mA cm^{-2}.[12] Prévot et al. demonstrated photocurrents of up to 2.4 mA cm^{-2} for a host-guest

$CuAlO_2$/$CuFeO_2$ system, whereby however oxygen had to be used as an electron scavenger, so that water splitting could not be assumed any more.[14] Jang et al. found a fairly reasonable photocurrent of 2.4 mA cm^{-2} at 0.4 V_{RHE}, here in the absence of oxygen, for a $CuFeO_2$ photocathode, which was modified through hybrid microwave annealing and a NiFe-layered double hydroxide/reduced graphene oxide electrocatalyst.[15] To the best of my knowledge, no higher photocurrents or hydrogen evolution efficiencies have been reported up to now. Another remarkable conclusion is that unbiased hydrogen evolution with $CuFeO_2$ has also not yet been achieved. Several reasons have been suggested to explain why $CuFeO_2$ have showed low hydrogen evolution efficiencies so far, which include Fermi level pinning at inter band gap states in the bulk,[16] Fermi level pinning at surface states,[12] photocorrosion[10] and poor catalytic activity.[15]

In this Chapter the development of anisotropic $CuFeO_2$ heterostructures will be described as a strategy to improve the hydrogen evolution efficiency through optimization of the charge carrier separation and by including more performant hydrogen evolution electrocatalysts in contact with the electrolyte. Specifically, the 2H-$CuFeO_2$ polytype was chosen, because its hexagonal lattice system allows the preparation of hexagonal $CuFeO_2$ nanoplatelets with different exposed facets.[11] The upscaling of the $CuFeO_2$ nanoplatelet synthesis procedure will be detailed in this Chapter, as well as the exploration of regioselectivity of the photodeposition of platinum, silver and nickel(hydroxide). In the second part of the Chapter, the tunability of the Fermi level position in $CuFeO_2$ is explored by contacting water and ITO in individual interface experiments with 2H-$CuFeO_2$ pellets.

6.2 Synthesis hexagonal $CuFeO_2$ nanoplatelets

2H-$CuFeO_2$ nanoplatelets were synthesized according to a recently published synthesis procedure (See Section 3.1.3 for a thorough description).[11] Considering that the original synthesis procedure only yielded about 75 mg per synthesis, we tested whether the reaction parameters could be upscaled by a factor of 4 and a factor of 8, so that a batch of 6 g could be produced in a more timely manner. First, the hydrothermal treatment of the reaction mixture was tried in a one-way sealed glass vessel, which was however not a good option, because the glass vessel exploded, in the protective container where it was put in, due to pressure built-up and the very basic conditions of the reaction mixture, that probably led to glass corrosion. In the next try, the glass vessel was replaced by a Teflon lined stainless steel pressure reactor, capable of handling elevated pressures and possessing a high chemical inertness due to the Teflon lining. As can be seen in the secondary electron images in Figure 6.1a, the 4x an 8x upscaling of the reaction parameters led to a powder of which the particles still look hexagonally shaped. Furthermore, the powder X-ray diffractograms (Figure 6.1b) show that the powder almost completely consists of 2H-$CuFeO_2$ with 3R-$CuFeO_2$ being detected in only a minor amount. Another noticeable feature in the diffractograms is the higher than normal background, which was caused by X-ray fluorescence. The energy of the X-rays emitted by the copper anode (Cu Kα: 8046 eV) of our

lab diffractometer can be absorbed by the iron atoms (Fe K-edge: 7112 eV) of the $CuFeO_2$ sample, which leads to fluorescence after radiative de-excitation. X-ray fluorescence can be easily overcome by using another X-ray anode with lower characteristic emission energies (such as Fe or Cr) or by installing a second monochromator before the detector. As such, the 4x upscaled powder was measured again with another PXRD apparatus that had a monochromator before the detector (Figure 6.2). In this diffractogram the background is greatly reduced and the presence of 3R-$CuFeO_2$ is more pronounced.

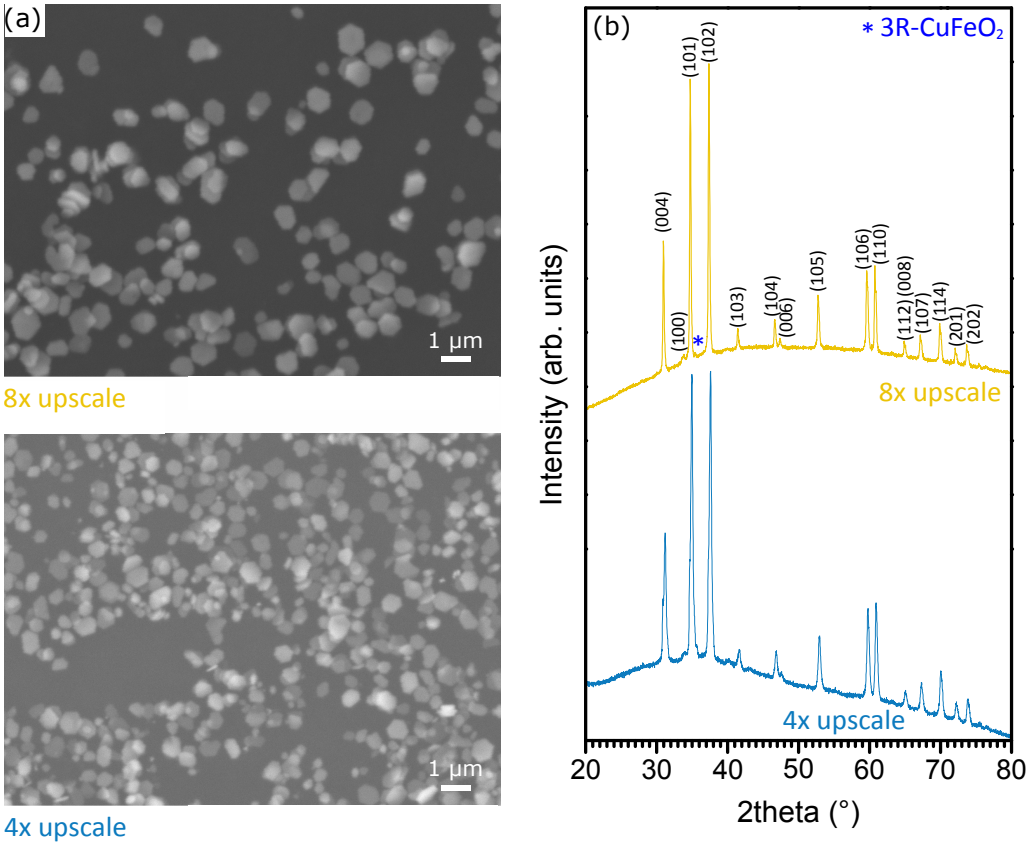

Figure 6.1: (a) Secondary electron images and (b) powder X-ray diffractograms for 4x and 8x upscaled $CuFeO_2$ powder with the (hkl) reflections of 2H-$CuFeO_2$ indicated in the graph.

The FESEM images of the 4x upscaled $CuFeO_2$ powder in Figure 6.3 show the hexagonal nanoplatelet morphology more clearly. The short diagonal length is ± 600 nm and the thickness lies in the range of 100 — 200 nm. However, the exposed faces appear to be much rougher than those of the truncated bipyramidal $BiVO_4$ microcrystals, which can complicate the introduction and detection of fine deposits.

At first glance, the overall characteristics of the upscaled $CuFeO_2$ powder were quite satisfactory, so that the $CuFeO_2$ production with the 8x upscaled reaction parameters was continued.

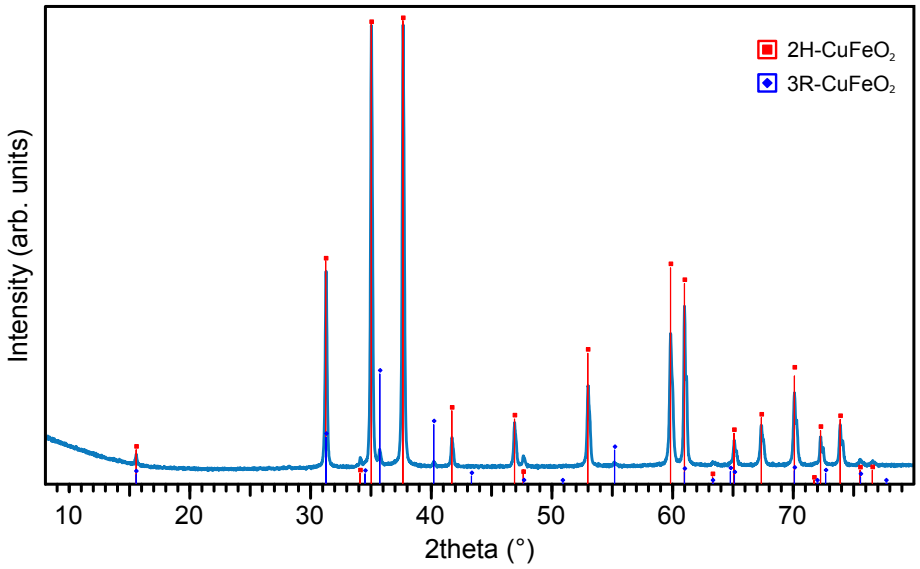

Figure 6.2: High resolution powder X-ray diffractogram of 4x upscaled $CuFeO_2$ powder, whereby the 2H-$CuFeO_2$ (red, ICSD: 01-079-1546) and 3R-$CuFeO_2$ (blue, ICSD: 01-075-2146) phases are indicated.

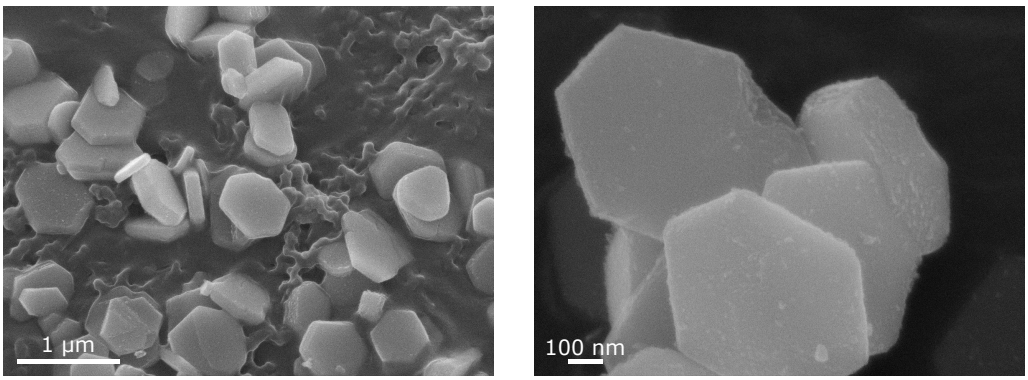

Figure 6.3: FESEM images of 4x upscaled $CuFeO_2$ powder.

Further upscaling was not considered, because the 125 mL stainless steel pressure reactor had reached its filling limit.

With the 8x upscaled parameters, each synthesis yielded about 600 mg $CuFeO_2$, so that in principle the reaction had to be carried out 10 times to create a batch of 6 g. However, due to problems with reproducibility the synthesis had to be performed 25 times. In all cases monodisperse hexagonal $CuFeO_2$ particles were obtained. However, some samples seemingly exhibited stronger particle aggregation/agglomeration, which could hinder studying the regioselectivity of the photodeposition of additional materials, because of increased concealing of certain particle surfaces. Furthermore, particle aggregation may increase the chance of charge carrier recombination, which would have a negative impact on water splitting efficiencies. Figure 6.4 shows the SEM images of three $CuFeO_2$ samples, one where the powder is almost not aggregated/agglomerated, one where the particles are slightly aggregated/agglomerated and one where strong aggregation/agglomeration is observed. The majority of the $CuFeO_2$ powder samples were slightly aggregated/agglomerated. In the batch for the photodeposition tests only the samples which exhibited no to slight particle aggregation/agglomeration were included. The powders which were strongly aggregated were used to prepare pellets (See Section 6.5.1).

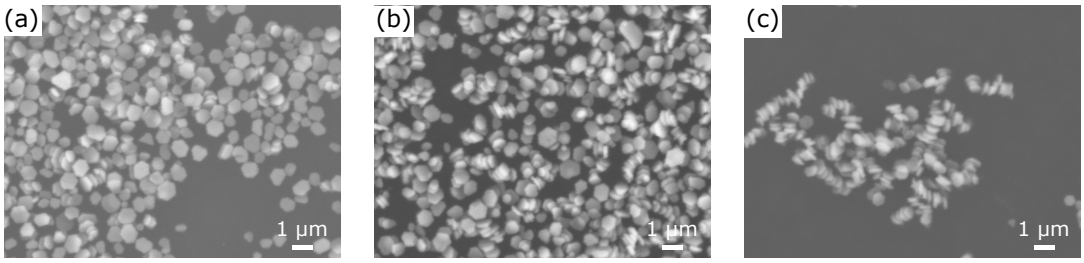

Figure 6.4: SEM images of (a) almost not aggregated, (b) slightly aggregated and (c) strongly aggregated $CuFeO_2$ powder.

Another problem was that not all samples were composed of pure 2H-$CuFeO_2$, as high to low amounts of 3R-$CuFeO_2$ were observed in the powder X-ray diffractograms of several samples (Figure 6.5). Hence, diffractograms were taken of each synthesized $CuFeO_2$ powder and only the $CuFeO_2$ samples, for which almost none or a very little amount of 3R-$CuFeO_2$ was detected, were included in the batch used for the photodeposition experiments. The powders which contained a little 3R-$CuFeO_2$ were used to prepare pellets (See Section 6.5.1).

After all the suitable $CuFeO_2$ powders were homogeneously mixed into one large batch of ± 800 mg, the whole batch was characterized again. The high resolution powder X-ray diffractogram in Figure 6.6 surprisingly shows that only a minimal amount of 3R-$CuFeO_2$ seems to be present in the batch. Furthermore, the FESEM images in Figure 6.7, taken from a sample of the $CuFeO_2$ batch, again show the hexagonal nanoplatelet morphology and, more remarkably, demonstrate a much lower surface roughness of the exposed $CuFeO_2$ nanoplatelet faces com-

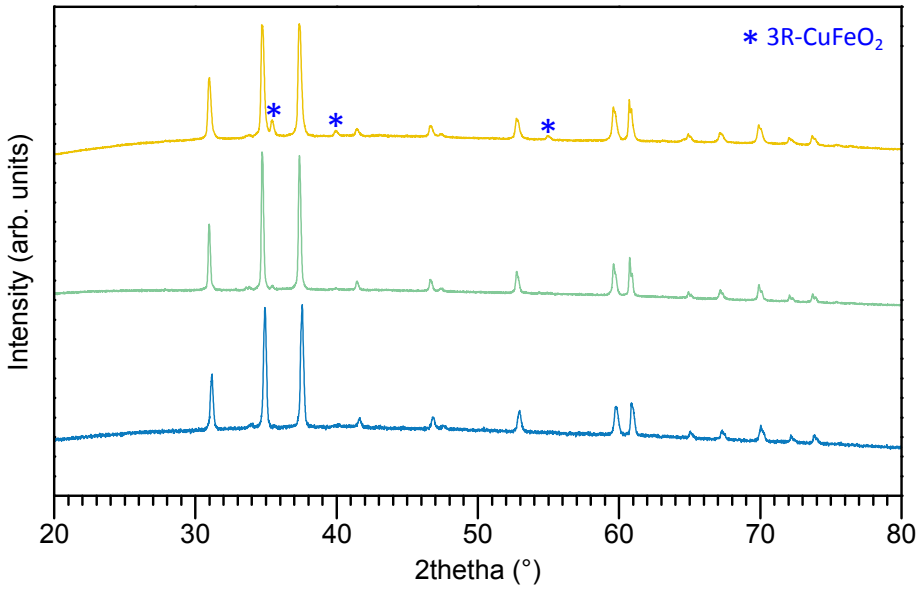

Figure 6.5: Powder X-ray diffractograms of $CuFeO_2$ powders with almost no (blue), a very little amount of (green) and a little amount (yellow) of 3R-$CuFeO_2$.

pared to the sample that was upscaled 8x times (Figure 6.3). However, there seems to be still a deposit present with a particular morphology on some of the nanoplatelets. Auger electron spectroscopy (AES) was performed on these samples to figure out if the additional deposits had another composition, but no differences could be found.

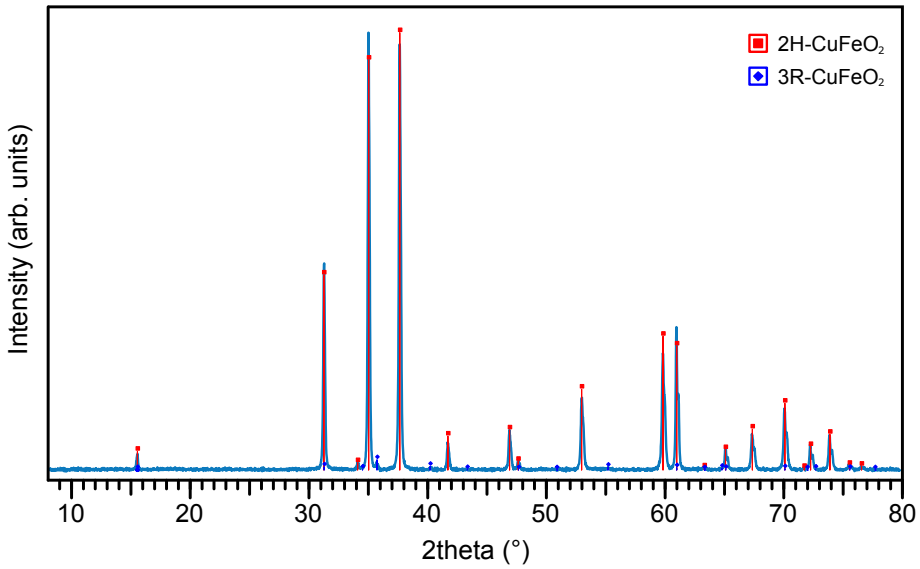

Figure 6.6: High resolution powder X-ray diffractogram of the batch of $CuFeO_2$ powder used for the photodeposition experiments, whereby the 2H-$CuFeO_2$ (red, ICSD: 01-079-1546) and 3R-$CuFeO_2$ (blue, ICSD: 01-075-2146) phases are indicated.

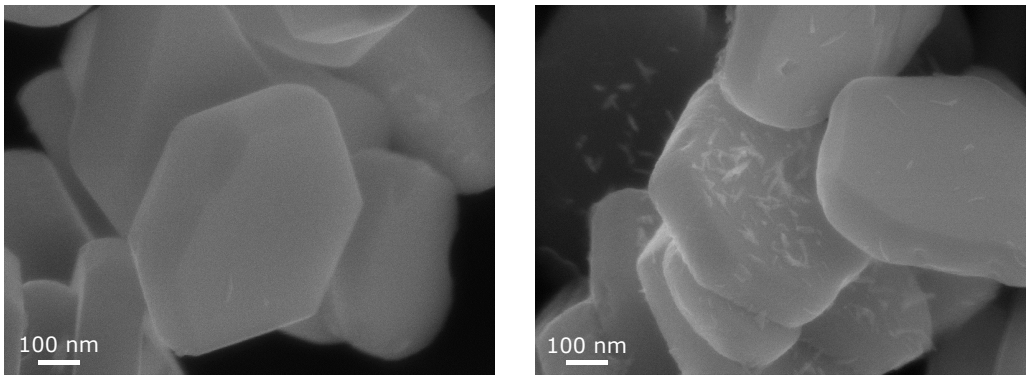

Figure 6.7: FESEM images of the batch of $CuFeO_2$ powder used for the photodeposition experiments.

To study the regioselectivity of the photodeposition process it would be good to know which crystalline facets can be associated with the exposed faces of the hexagonal $CuFeO_2$ nanoplatelets. Considering that the hexagonal nanoplatelets belong to the hexagonal 2H-$CuFeO_2$ crystalline phase, the basal planes of the hexagonal nanoplatelets can be confidently indexed as the {0001} facets. The indexing of the side faces of the nanoplatelets is more complicated because the sides of the nanoplatelets appear to be rounded, as can be seen in Figure 6.8a. In Figure 6.8b the most common facets of the hexagonal crystal family are shown. Depending on the relative size of the facets, particles, belonging to the hexagonal crystal family, exhibit different morphologies including rods,[17] prisms,[18] bipyramids,[19] truncated bipyramids[20] and discs/platelets.[11,21] The hexagonal $CuFeO_2$ nanoplatelets synthesized in this work most likely don't have a prism morphology, because the sides would then have to be flat and correspond solely to {10-10} facets. Instead, the hexagonal truncated bipyramidal morphology (Figure 6.8c) would be more likely, where the nanoplatelet sides certainly consist of {10-11} facets and possibly {10-10} facets. The presence and relative size of {10-10} facets could, however, not be proven and, possibly, the relative size of {10-10} facets varies within the batch of $CuFeO_2$ powder. Therefore, no specific index is associated with the sides of the hexagonal $CuFeO_2$ nanoplatelets in the remainder of the work.

XPS was performed on the $CuFeO_2$ batch to figure out whether the main oxidation state of the copper and iron atoms was actually Cu^+ and Fe^{3+}, respectively (Figure 6.9). The oxidation state of copper cannot be solely determined from the $Cu2p_{3/2}$ core level spectrum since the $Cu2p_{3/2}$ binding energy for the different oxidation states is quite similar and the whole $Cu2p_{3/2}$ spectrum for metallic copper and copper(I) oxide is indistinguishable.[22] However, Cu^{2+} does not seem to be present in large amounts since that would have given rise to a strong satellite signal in the range of 940 — 945 eV. To distinguish metallic copper from copper(I) oxide, the CuLMM Auger spectrum should be inspected, whereby the CuLMM binding energy here is found at 569.8 eV, typical for Cu^+.[22] No signal is present at a binding energy of 568.0 eV, the CuLMM binding energy characteristic for metallic copper, thus excluding the presence of metallic copper. Determining

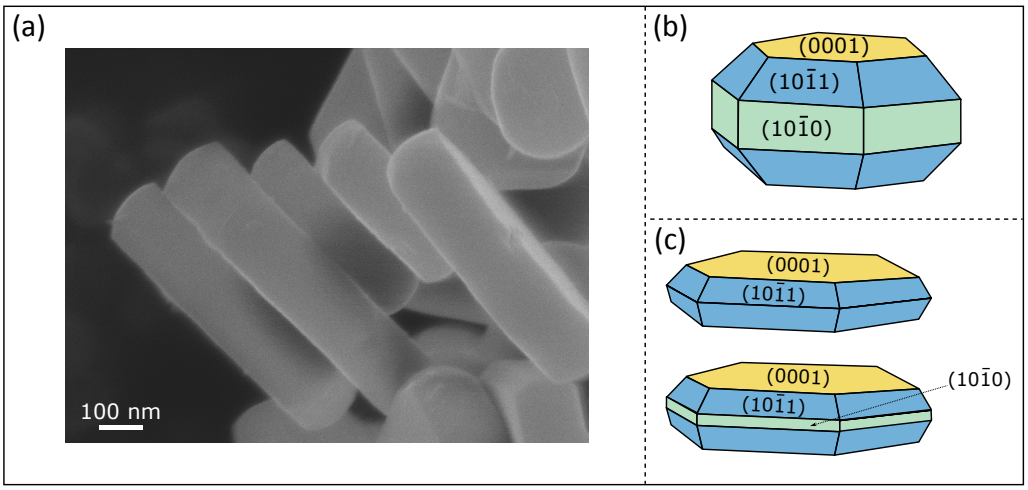

Figure 6.8: (a) FESEM image showing sides of hexagonal $CuFeO_2$ nanoplatelets, (b) common low-index facets of particles in the hexagonal crystal class and (c) possible indexing of exposed sides of the hexagonal $CuFeO_2$ nanoplatelets.

the oxidation state of iron from the main $Fe2p_{3/2}$ binding energy is difficult as well. However, in the satellite structure, Fe^{2+} gives rise to a signal at about 716 eV, whereas Fe^{3+} give rise to a signal at about 719 eV.[23] In the Fe2p spectrum in Figure 6.9 no satellite signal can be seen around 716 eV only a shoulder at about 720 eV is present, thus indicating that Fe^{3+} is the main oxidation state in the analysed $CuFeO_2$ sample. Peak fitting of the Fe2p spectrum would be the ideal way to assign the iron oxidation state, however the noise and the possibility of surface charging does not allow proper peak fitting. In the Fe2p spectrum a signal can be seen at a binding energy of 705 eV. This signal corresponds to $In3p_{1/2}$[24] and originates from the indium foil used to glue the powder sample to the substrate holder. In the O1s spectrum signals belonging to oxide (530 eV) and hydroxide/carbonyl (532 eV) can be seen.[24] The hydroxide/carbonyl signal is most likely due to the sample having been prepared ex situ.

6.3 Anisotropic photodeposition on $CuFeO_2$

Once the $CuFeO_2$ batch was fully analysed, samples were taken of this batch to perform photodeposition experiments to test whether certain metal(oxide)s could be selectively deposited on certain regions (regioselectivity) of the anisotropic hexagonal $CuFeO_2$ nanoplatelets. The photodeposition procedure is extensively explained in Section 3.1.4 and specific experimental parameters of the $CuFeO_2$ photodeposition experiments can be found in Table 6.1.

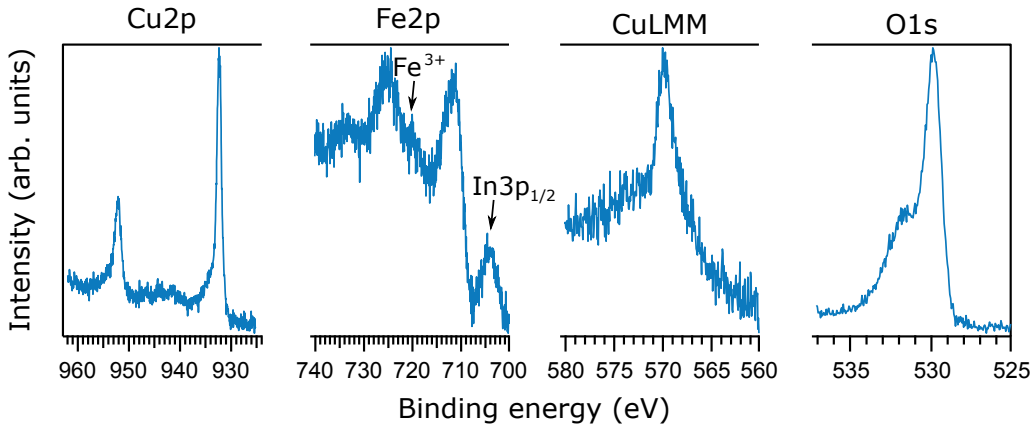

Figure 6.9: Cu2p, Fe2p and O1s core level XP spectra and CuLMM Auger spectrum of the batch of $CuFeO_2$ powder used for the photodeposition experiments.

Table 6.1: Experimental details for the $CuFeO_2$ based heterostructured powders fabricated through photodeposition.

Heterostructure	m_{CuFeO_2} (mg)	Precursor	Hole/electron scavenger	pH	V (mL)	$t_{illum.}$ (h)
$CuFeO_2$/Ag	100	$AgNO_3$	MeOH (25 vol%)	7	20	5
$CuFeO_2$/Pt	100	H_2PtCl_6	MeOH (40 vol%)	2.9	20	5
$CuFeO_2/NiO_xOH_y$	100	$NiCl_2$	-	9.2 (KBi buffer)	20	2

$t_{illum.}$: solar simulator illumination time

6.3.1 $CuFeO_2$/Ag

Silver has been effectively deposited onto the $CuFeO_2$ nanoplatelets following the photodeposition process, as can be perceived in Figure 6.10. Evidently, more silver is present on the {0001} facets than on the sides, which is however difficult to conclude with high certainty because the silver coverage appears to be quite low despite a 10 wt% Ag solution being used in the photodeposition process. The low silver coverage can be related to the rather large size (50 — 200 nm) of the deposited silver particles, indicating that growth instead of nucleation was preferred during the photodeposition process. The low coverage and particle size of the silver deposit agree quite well with what was found for the silver photodeposition experiments on $BiVO_4$ (Section 4.3.1).

AES was carried out to see whether more information on the regioselectivity of the silver deposit could be obtained. Due to the previously observed problems with AES mapping on $BiVO_4$ samples (Section 4.3.2), i.e. sample degradation and long measurement times, we opted to not perform any mapping and instead did several rapid point measurements on certain positions on the $CuFeO_2$/Ag (10 wt%) sample (Figure 6.11). On positions, where in the FESEM images

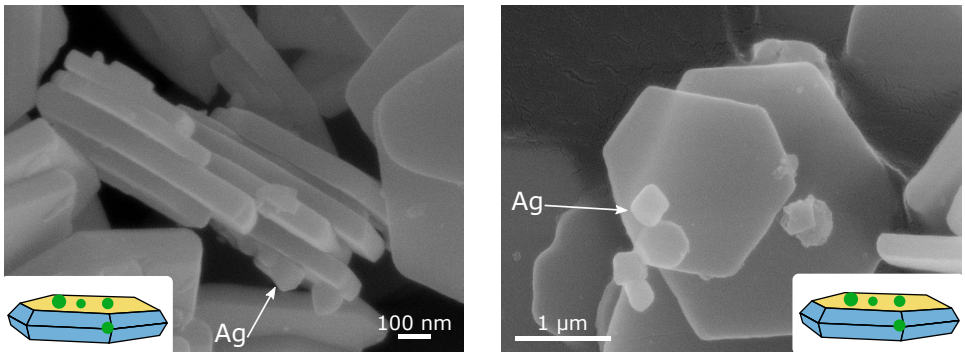

Figure 6.10: FESEM images of $CuFeO_2$/Ag (10 wt%).

a Ag deposit seems to be present (more brilliant spots), silver Auger electrons were detected, confirming that silver was effectively deposited onto the $CuFeO_2$ nanoplatelets. The number of silver deposits is, however, so sparse that the regioselectivity of the deposit could not be verified with high certainty from these AES point measurements.

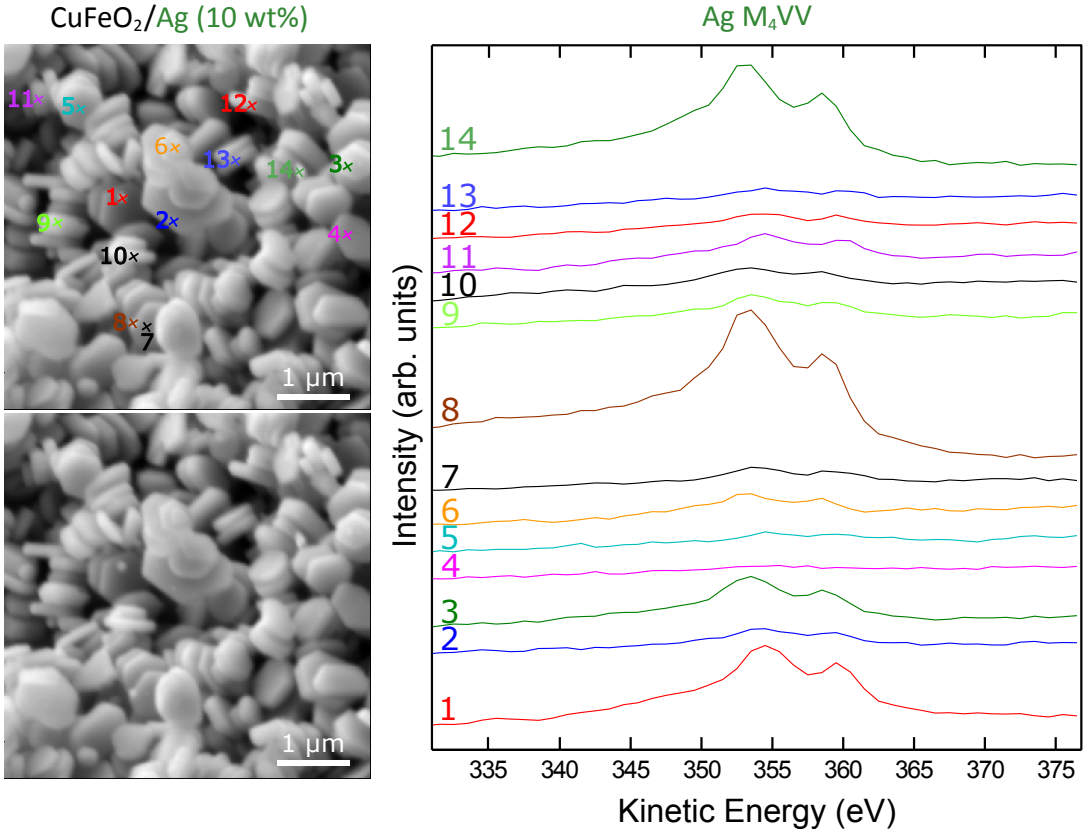

Figure 6.11: Left: FESEM images of $CuFeO_2$/Ag (10 wt%) sample with the AES measurement points indicated in the top image. Right: Ag M_4VV Auger electron spectra for the different measurement points.

The silver oxidation state of the $CuFeO_2$/Ag (10 wt%) sample was determined through XPS (Figure 6.12). First, the Fe2p, Cu2p and CuLMM core level spectra were checked for inhomogeneous sample charging, as this phenomenon made the oxidation state analysis for some $BiVO_4$ based powder samples (see Chapter 4) more complicated. However, the charge carrier mobility of $CuFeO_2$, 10^{-1} cm^2 V^{-1} s^{-1}, is one order of magnitude higher than for $BiVO_4$,[12,25] so that inhomogeneous sample charging during XPS measurements on $CuFeO_2$ should be less prevalent. Indeed, in the $CuFeO_2$/Ag core level spectra no indications of inhomogeneous sample charging can be found, so that the recorded Ag3d spectrum can be reliably used to define the silver species. The Ag3d spectrum here consists of two symmetric signals at 368.2 eV and 374.3 eV which belong to the characteristic binding energies of $Ag3d_{5/2}$ and $Ag3d_{3/2}$, respectively, of metallic silver,[24] thus proving that the silver photodeposition involves the reduction of Ag^+ to Ag(0).

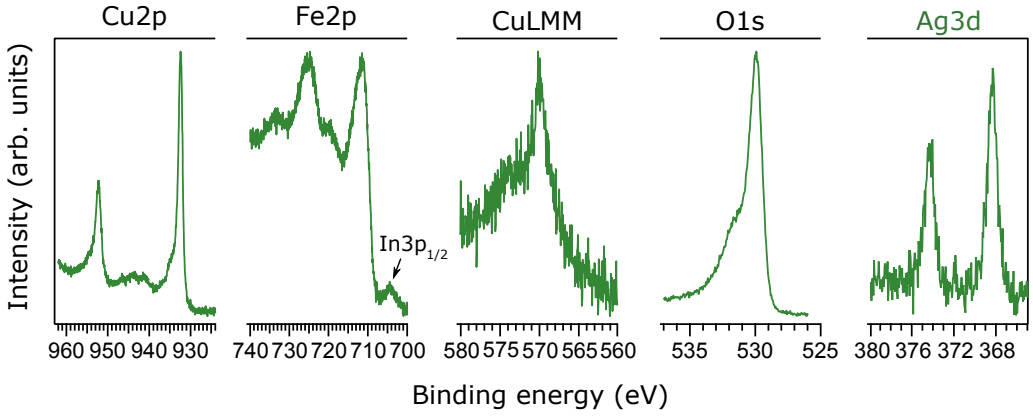

Figure 6.12: Cu2p, Fe2p, O1s and Ag3d core level XP spectra and CuLMM Auger spectrum of the $CuFeO_2$/Ag (10 wt%) sample.

6.3.2 $CuFeO_2$/Pt

The photodeposition of platinum was next in line. For $BiVO_4$, the acidic H_2PtCl_6 precursor was found to change the pH of the photodeposition reaction mixture (Section 4.3.2). Moreover, the pH and platinum precursor concentration had a strong effect on the Pt distribution and oxidation state. In particular, a reaction mixture pH of 2.5 — 3 resulted predominantly in metallic platinum deposits, whereas at higher pHs oxidized platinum species were preferentially deposited. Hence, for the photodeposition of platinum on $CuFeO_2$ the pH was not altered with sodium hydroxide and was preferentially held between 2.5 — 3. After making a 10 wt% platinum solution a pH of 2.9 was obtained. As can be seen in Figure 6.13 the size of the platinum deposits after the photodeposition process are in the range of 10 — 50 nm. Furthermore, the platinum coverage is also much higher than what was obtained for the silver photodeposition on $CuFeO_2$.

Even more remarkably, the Pt deposit seems to be highly selectively deposited onto the {0001} facets, which constitutes a strong proof that the anisotropic shape of the $CuFeO_2$ nanoplatelets

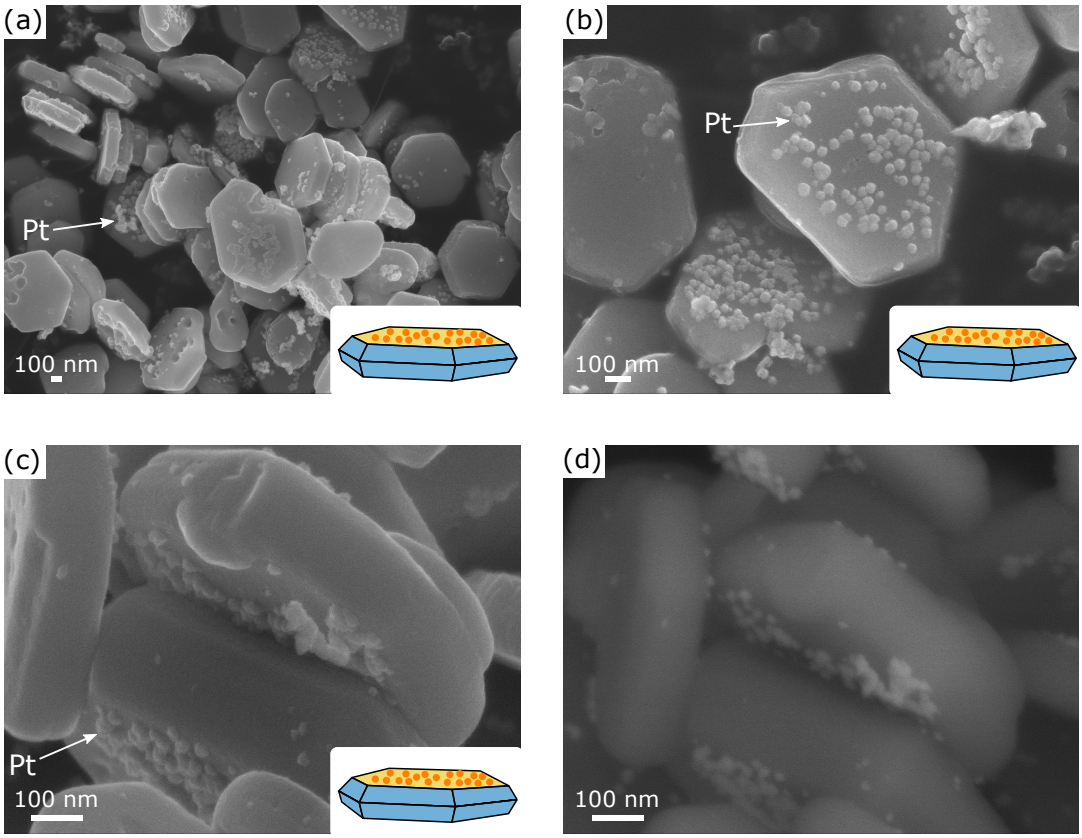

Figure 6.13: (a-c) FESEM and (d) BSE images of $CuFeO_2$/Pt (10 wt%)—pH 2.9.

leads to anisotropic charge accumulation upon light absorption. Herein, the electrons would then preferentially accumulate on the {0001} facets. Previously, Li et al. showed through extensive experimental investigation that for truncated bipyramidal $BiVO_4$, upon light absorption, electrons and holes accumulate on the {010} and {110} crystalline facets, respectively, making that reduction and oxidation reactions are spatially separated and take place on different crystalline facets.[26–28] Since then, the light-induced charge migration has also been demonstrated for anisotropically shaped $SrTiO_3$ and TiO_2.[29,30] The particular crystal structure of $CuFeO_2$ and the proposed small polaron hopping charge carrier conduction mechanism[25,31] could be the reasons for regioselective charge accumulation. The $CuFeO_2$ crystal structure consists of alternating layers of $[FeO_2^-]$ and $[Cu^+]$ which are stacked perpendicular to the c-axis. When assuming that charge carriers follow the small polaron hopping mechanism, hole hopping occurs presumingly between copper sites (forming Cu^{2+} ions) and electron hopping between iron sites (forming Fe^{2+} ions).[25] In a simplistic electrostatic model, electrons must hop from iron to iron site over a saddle type configuration of oxygen anions, due to the iron ions being octahedrally coordinated by oxygen ions. In contrast, the copper cations are, in line with the c-axis, coordinated by two oxygen anions, whereas no oxygen anions, and thus no barrier, are present in the $[Cu^+]$ layers perpendicular to the c-axis, so that a higher hole mobility perpendicular to the c-axis would be expected.

Indeed, electrical conductivity measurements on p-type $CuFeO_2$ single crystals demonstrated that the resistivity along the c-axis, 3 x 10^1 Ωm, was several orders of magnitude higher than perpendicular to the c-axis, 5 x 10^{-3} Ωm.[32]

Besides anisotropic charge accumulation, the reason for regioselective deposition of platinum on the $CuFeO_2$ nanoplatelets can possibly be due to a difference in surface polarity between the {0001} facets and the sides of the nanoplatelets. The {0001} facets should then be more positively charged than the sides, so that the $[PtCl_6]^{2-}$ precursor species preferentially adsorb onto the {0001} facets, followed by reduction of the precursor to Pt(0). This alternative pathway of anisotropic deposition has already been documented by Wenderich et al., who showed that $[PtCl_6]^{2-}$ preferentially adsorbed onto the small subordinate facets of platelike WO_3 through a comparison of dark impregnation and photodeposition experiments, and aqueous-phase atomic force microscopy (AFM) measurements.[33] Thus, in principle, dark impregnation experiments could be performed to determine whether platinum was selectively deposited onto the {0001} facets through light-induced charge carrier migration or through facet-preferential $[PtCl_6]^{2-}$ adsorption. However, the impregnation of platinum on the 2H-$CuFeO_2$ nanoplatelets could not be performed, because the impregnation process requires a heating step in a controlled atmosphere to convert the precursor to the desired deposit with the desired oxidation state and, unfortunately, the 2H-$CuFeO_2$ phase and hexagonal nanoplatelet morphology was not stable at the elevated temperature, i.e. 400 °C, that is required for metal(oxide) impregnation (which will be shown in Section 6.5.1). Nonetheless, the observation that the positively charged Ag^+ precursor is also selectively reduced and deposited onto the {0001} facets of 2H-$CuFeO_2$ hexagonal nanoplatelets speaks against the sorption-determined platinum deposition hypothesis.

The deposit, found on the $CuFeO_2$ particles, is indeed platinum, because Pt M_5VV Auger electrons were detected when an AES point measurement was performed on a point which was assumed to be a deposit in the recorded secondary electron image (Figure 6.14).

XP core level spectra were measured to verify the platinum species (Figure 6.15). No signs of inhomogeneous sample charging were observed, so that the Pt4f spectrum could be used to analyse the oxidation state of the platinum deposit. Two intense signals at 71.0 eV and 74.4 eV can be seen which are characteristic for the binding energies of $Pt4f_{7/2}$ and $Pt4f_{5/2}$, respectively, of metallic platinum.[24] Additionally, a shoulder can be seen at a binding energy of 77.4 eV, which is indicative of $Pt4f_{5/2}$ of platinum oxide[24] As was discussed for the photodeposition of platinum onto $BiVO_4$ (Section 4.3.2), platinum oxide can be formed when $[PtCl_6]^{2-}$ is only partially reduced.

6.3.3 $CuFeO_2/NiO_xOH_y$

Next, the photodeposition of nickel was investigated. The FESEM images (Figure 6.16) show that the deposited nickel particles have a distinct morphology, yielding sizes of just a few nanometer and with part of the particles being seemingly elongated. Nonetheless, the nickel deposit is slightly more difficult to identify due to the strong similarity with the deposit that was found on

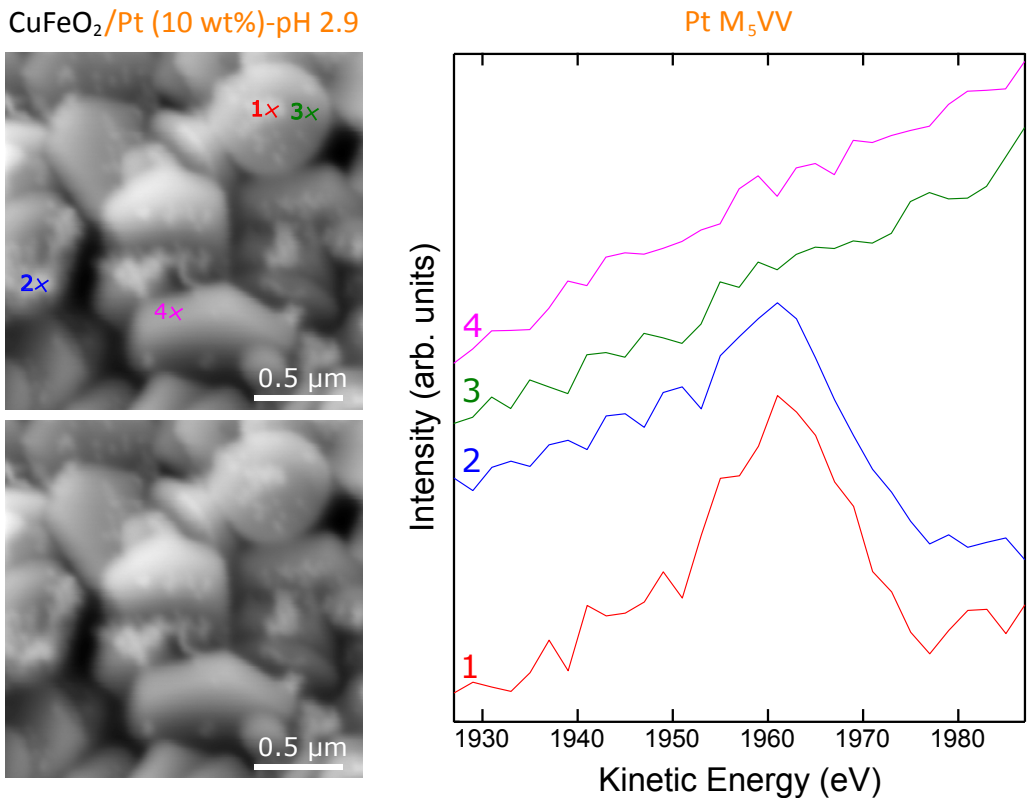

Figure 6.14: Left: FESEM images of $CuFeO_2$/Pt (10 wt%)—pH 2.9 sample with the AES measurement points indicated in the top image. Right: Pt M_5VV Auger electron spectra for the different measurement points.

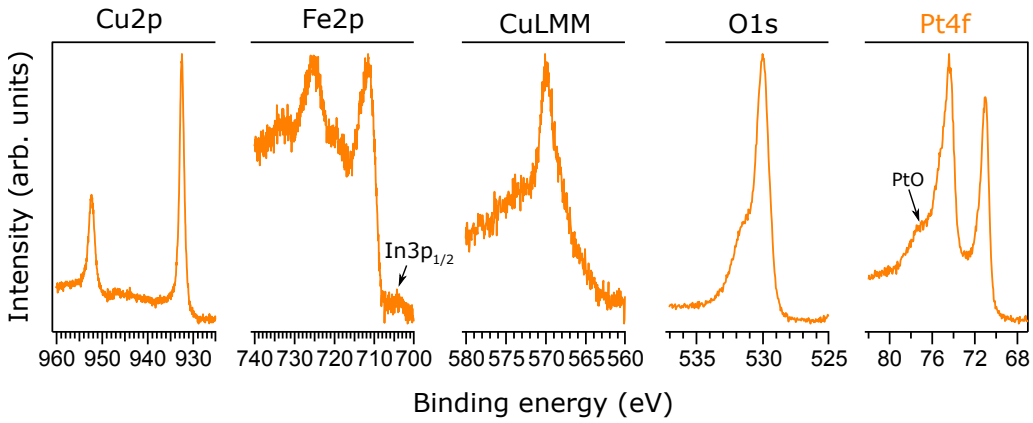

Figure 6.15: Cu2p, Fe2p, O1s and Pt4f core level XP spectra and CuLMM Auger spectrum of the $CuFeO_2$/Pt (10 wt%)—pH 2.9 sample.

some of the nanoplatelets of the batch of bare $CuFeO_2$ (Figure 6.7). The nickel deposit seems to be distributed all over the $CuFeO_2$ nanoplatelets, just as was seen for the $BiVO_4/NiO_xOH_y$ (10 wt%) and $BiVO_4/NiO_xOH_y$ (1 wt%) sample.

AES was performed to determine whether all of the supposed deposits were containing nickel. However, the most intense nickel Auger lines overlap with either the Auger signals of iron or copper, and the less intense nickel Auger lines do not have a high enough signal-to-noise ratio. Hence, nickel could not be detected through AES. EDS was not considered due to the small size of the deposits.

The reason that $BiVO_4$ and $CuFeO_2$ are evidently completely covered by photodeposited nickel could be that, at a pH of 9.2, regioselective deposition of nickel is inhibited, due to the surface polarity being the same on every exposed facet at that pH, suggesting that the deposition of nickel is sorption-determined. Another possibility is that Ni^{2+} reduction and oxidation takes place simultaneously. In Section 4.3.4 the reduction potentials of the possible Ni^{2+} redox reactions, i.e Ni^{2+}/Ni and $NiOOH/Ni^{2+}$, were calculated according to the Nernst equations for the 1 wt% and 0.1 wt% nickel solutions at a pH of 9.2. By considering these reduction potentials and the valence band maximum (VBM) and conduction band minimum (CBM) of $CuFeO_2$, commonly positioned at 1.2 V and -0.3 V, respectively,[1] the spontaneity of the light-induced reduction and/or oxidation of Ni^{2+} by $CuFeO_2$ can be evaluated. For the Ni^{2+}/Ni reduction reaction, reduction potentials of 0.13 V and 0.07 V were calculated for a 1 wt% and 0.1 wt% nickel solution, respectively. Since the CBM of $CuFeO_2$ is more negative than these reduction potentials, the Ni^{2+}/Ni reduction reaction is thermodynamically allowed. In contrast, the VBM of $CuFeO_2$ has a similar potential as the standard reduction potentials, of the $NiOOH/Ni^{2+}$ reduction reaction, 1.33 V and 1.44 V for a 1 wt% and 0.1 wt% nickel solution, respectively. Hence, light-induced Ni^{2+} reduction could already be limited for a 1 wt% nickel solution and would be impossible for a 0.1 wt% nickel solution. Thus, if the regioselectivity of the nickel deposit could be more straightforwardly detected through FESEM imaging or AES, the regioselective photo-oxidation of Ni^{2+}

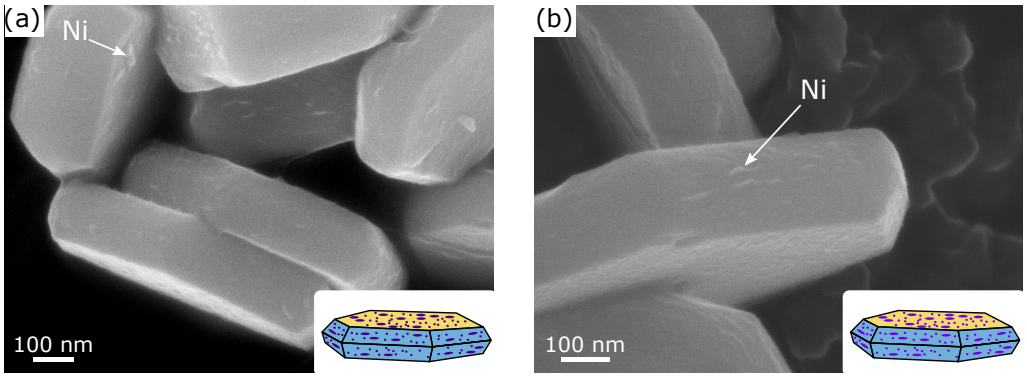

Figure 6.16: FESEM images of $CuFeO_2/NiO_xOH_y$ samples with (a) ± 10 wt% and (b) 1 wt% NiO_xOH_y.

using a 0.1 wt% nickel solution would be able to be determined. Due to the similarity of the nickel deposit for both $CuFeO_2$ and $BiVO_4$, an alternative reaction mechanism which does not involve light can not be excluded, despite no alternative mechanisms having been mentioned in literature, as far as we know.

XPS measurements were performed to investigate the oxidation state of the deposited nickel species (Figure 6.17). Again, no signs of inhomogeneous surface charging can be found in the core level spectra, so that the deposited nickel species can be evaluated from the Ni2p spectrum. The Ni2p spectrum is quite similar to the Ni2p spectrum measured for $BiVO_4/NiO_xOH_y$ (Figure 4.30 in Section 4.3.4), indicating that the nickel species consists of oxides and hydroxides, which is why the nickel deposit herein is denoted as NiO_xOH_y. Despite the presumed photoreduction of Ni^{2+} to metallic nickel, no sign of metallic nickel, which has a characteristic Ni $2p_{3/2}$ binding energy of 852.6 eV, can be seen in the Ni2p spectrum. The reason is that metallic nickel would readily oxidise to $Ni(OH)_2$, as explained in Section 4.3.4.

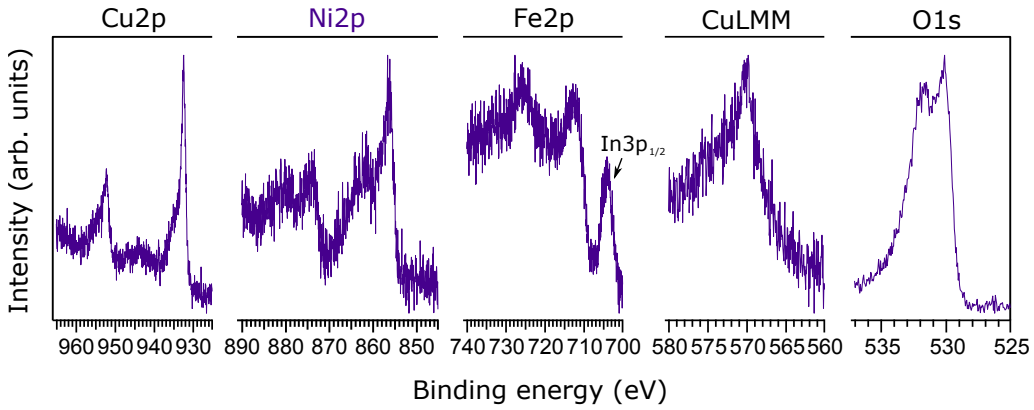

Figure 6.17: Cu2p, Ni2p, Fe2p and O1s core level XP spectra and CuLMM Auger spectrum of the $CuFeO_2/NiO_xOH_y$ (± 10 wt%) sample.

6.3.4 UV-Vis-NIR diffuse reflectance spectroscopy

For all heterostructured $CuFeO_2$ powders, UV-Vis-NIR diffuse reflectance spectra were recorded (Figure 6.18a). Subsequently, the diffuse reflectance data were transformed into Tauc plots to determine the indirect and direct optical band gaps of the different heterostructures (Figure 6.18b). The indirect and direct optical band gaps of the heterostructured $CuFeO_2$ powders are similar to bare $CuFeO_2$ and apparently lie within a range of 1.22 — 1.26 eV and 1.43 — 1.45 eV, respectively. The direct band gap values are close to the previously determined direct optical band gap of 2H-$CuFeO_2$.[11] Thus, eventual deviations in sacrificial water splitting between the different $CuFeO_2$ powders will not be caused by differences in light absorption. Furthermore, due to the 0.2 eV difference between the direct and the indirect band gap, radiative charge carrier recombination will be less likely.

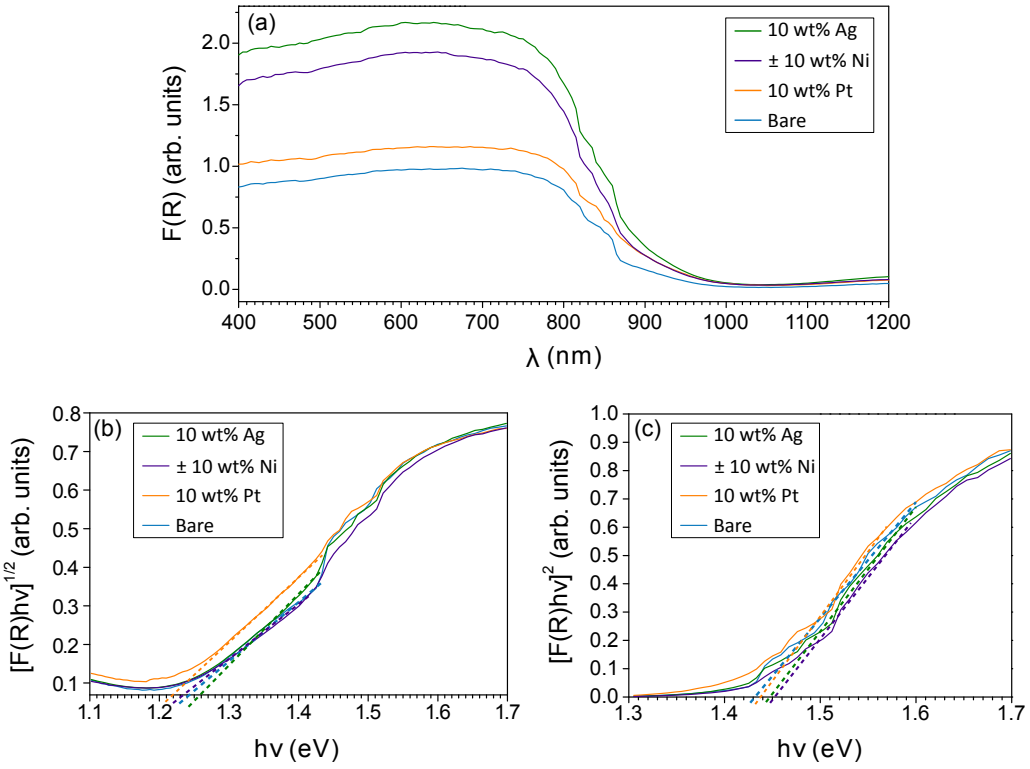

Figure 6.18: (a) UV-Vis-NIR diffuse reflectance spectra and (b) Tauc plots for bare and heterostructured $CuFeO_2$ powder samples.

6.4 Water reduction

All the $CuFeO_2$ heterostructures were tested for their sacrificial photochemical water splitting performance. The complete testing procedure is explained in detail in Section 3.4.5.2. The heterostructured $CuFeO_2$ nanoplatelets were expected to act as good sacrificial water splitting systems, because of the straightforward photodeposition of silver and platinum, the apparent spatial separation of photogenerated charge carriers, and the good electrocatalytic properties of the deposited cocatalysts; platinum for hydrogen evolution[34] and nickel based species for oxygen evolution.[35]

However, none of the heterostructured $CuFeO_2$ powders showed any significant water splitting performance, even though two different sacrificial agents, methanol and triethanolamine, and two different weight percentages for every heterostructure were tested. Even when the reaction times were extended to 72 hours or when UV lamps were used instead of Xenon lamps, no gas evolution could be noticed by the automatic burette of the closed batch reactor. Nonetheless, gas samples were taken from the reactor for GC analysis after the hydrogen evolution experiments were terminated. Hydrogen could be detected for the $CuFeO_2$/Ag and $CuFeO_2$/Pt powders. However, the hydrogen GC signal was so low that it did not reach the calibration range of the GC apparatus, so that the amount of evolved hydrogen was considered to be below 1 μmol/h. This

unsatisfactory water splitting efficiency is in accordance with the previously determined poor photocurrent, 8.8 μA cm^{-2} at 0 V_{RHE}, for a thin film of dropcasted 2H-$CuFeO_2$ nanoplatelets.[11] According to Prévot et al. Fermi level pinning at surface states, due to formation of metal hydroxides at the semiconductor electrolyte junction, impairs the PEC water splitting performance of $CuFeO_2$.[12] In the following Section additional reasons for the bad hydrogen evolution efficiency of $CuFeO_2$ are explored through interface experiments of $CuFeO_2$ with the low work function material ITO and through water exposure experiments.

6.5 Interfacial band alignment of heterostructured $CuFeO_2$

6.5.1 $CuFeO_2$ pellet fabrication

Before any interface experiments could be performed, suitable $CuFeO_2$ substrates had to be prepared onto which ITO could be sputtered and for which X-ray photoelectron spectra could be measured. To our knowledge, no experimental procedures have been published for the fabrication of 2H-$CuFeO_2$ thin films so far, only some examples of 3R-$CuFeO_2$ thin films could be found in literature.[16,36–38] Exploring the preparation of 2H-$CuFeO_2$ thin films ourselves seemed too complex due to the stringent conditions, high temperature and specific atmosphere, required to produce phase pure delafossite $CuFeO_2$ thin films[36,37] and because of the privileged growth of the 3R-$CuFeO_2$ phase when fusing copper and iron precursors. Thus, rather than preparing thin films, 2H-$CuFeO_2$ substrates were prepared by pressing a certain amount of previously prepared 2H-$CuFeO_2$ powder into pellets. The pellets were pressed with the 2H-$CuFeO_2$ powder that was discarded earlier because of its unsuitable properties for photodeposition and water splitting experiments (See Section 6.2). Obviously, pellets are a few order of magnitudes thicker than thin films, but inhomogeneous surface charging during XPS measurements was not expected due to the good electrical conductivity of $CuFeO_2$ and because the top surface of the pellets is grounded through a mask, which keeps the pellet in place. 2H-$CuFeO_2$ pellets were prepared through a combination of uniaxial and isostatic pressing. The complete synthesis procedure can be found in Section 3.3. Normally, to obtain compact $CuFeO_2$ pellets, sintering at temperatures above 1000 °C is required.[39,40] However, fully compacted pellets did not seem imperative for the execution of interface experiments and, more importantly, the 2H-$CuFeO_2$ crystalline phase was found to be not stable at temperatures > 400 °C. As can be seen in Figure 6.19, the 2H-$CuFeO_2$ crystalline phase completely changed into Fe_3O_4 and CuO after heating for 2 h in air at 400 °C. Moreover, the hexagonal nanoplatelets seem to fragment into smaller particles during the calcination (Figure 6.20), which is most likely due to the phase change that takes place.

Since the pellets were made ex situ, the surface had to be cleaned before interface experiments could be performed. The survey XP spectra in Figure 6.21 demonstrate the effects of a few cleaning procedures on the surface chemistry of the $CuFeO_2$ pellets. Both, thermally cleaning at 200 °C in an oxygen atmosphere and oxygen plasma, led to a complete removal of the adventitious

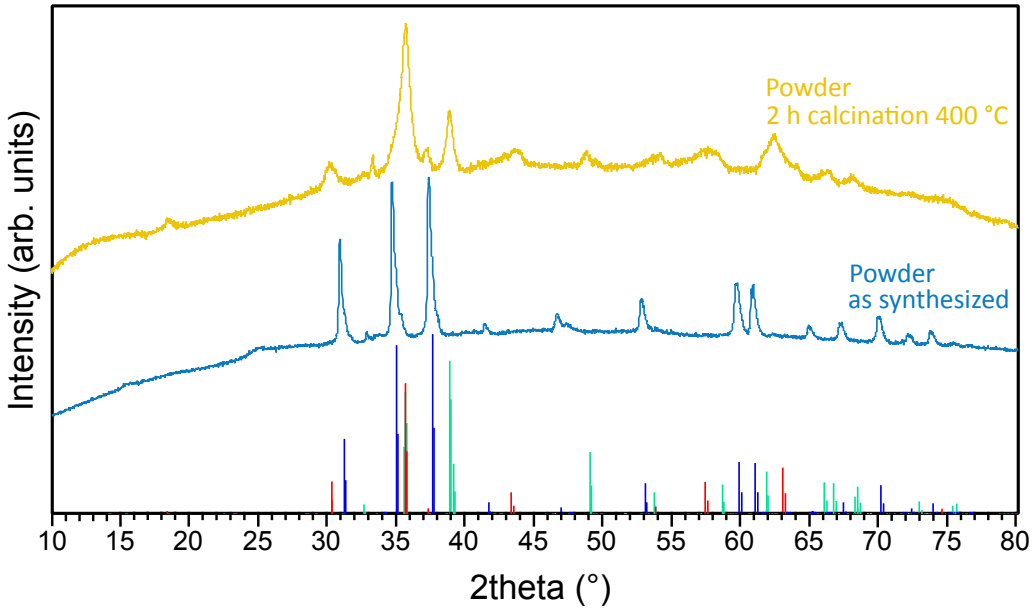

Figure 6.19: Powder X-ray diffractograms for $CuFeO_2$ powder before (blue) and after calcination at 400 °C in air for 2 h (yellow). The crystalline phases 2H-$CuFeO_2$ (blue, JCPDS: 96-202-0231), Fe_3O_4 (red, JCPDS: 96-900-6319) and CuO (light green, JCPDS: 96-101-1149) are indicated.

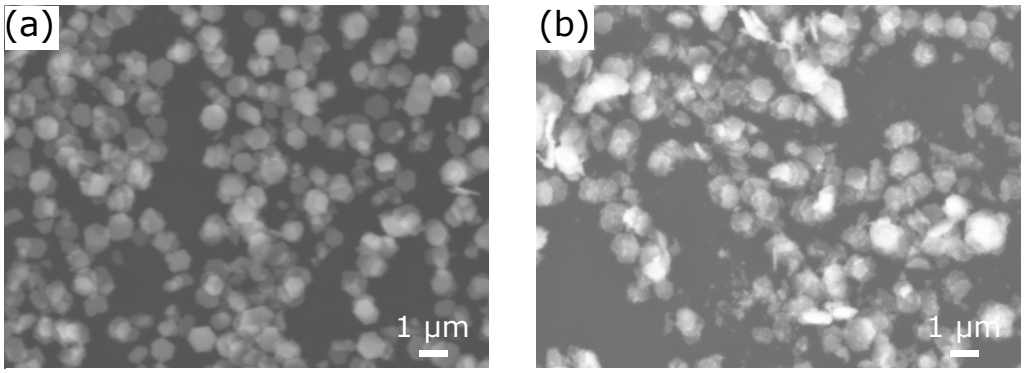

Figure 6.20: SEM images on $CuFeO_2$ powder (a) before and (b) after calcination at 400 °C in air for 2 h.

carbon species. However, after the oxygen plasma treatment extra signals in the Cu2p region of the survey spectrum can be seen, which indicate a change in the $CuFeO_2$ surface chemistry. Additionally, an extra signal at 1071.2 eV can be identified, which is characteristic for the Na1s core level electrons of sodium. Thus, sodium seems to segregate to the pellet surface after the heat treatment. Most likely, the small amount of sodium is a leftover from the sodium hydroxide that was used in the 2H-$CuFeO_2$ powder synthesis. The presence of sodium was unexpected, because no sodium was detected while measuring the XP spectra of the heterostructured $CuFeO_2$ powders. Possibly, sodium is incorporated into the bulk of the $CuFeO_2$ particles and may explain the bad hydrogen evolution efficiencies, since bulk incorporated impurities can act as charge carrier recombination centres. However, photodeposition of Ag, Pt and NiO_xOH_y took place readily, despite those light-induced reactions being negatively influenced by charge carrier recombination as well. The small amount of sodium at the surface was not expected to interfere with the interface experiments.

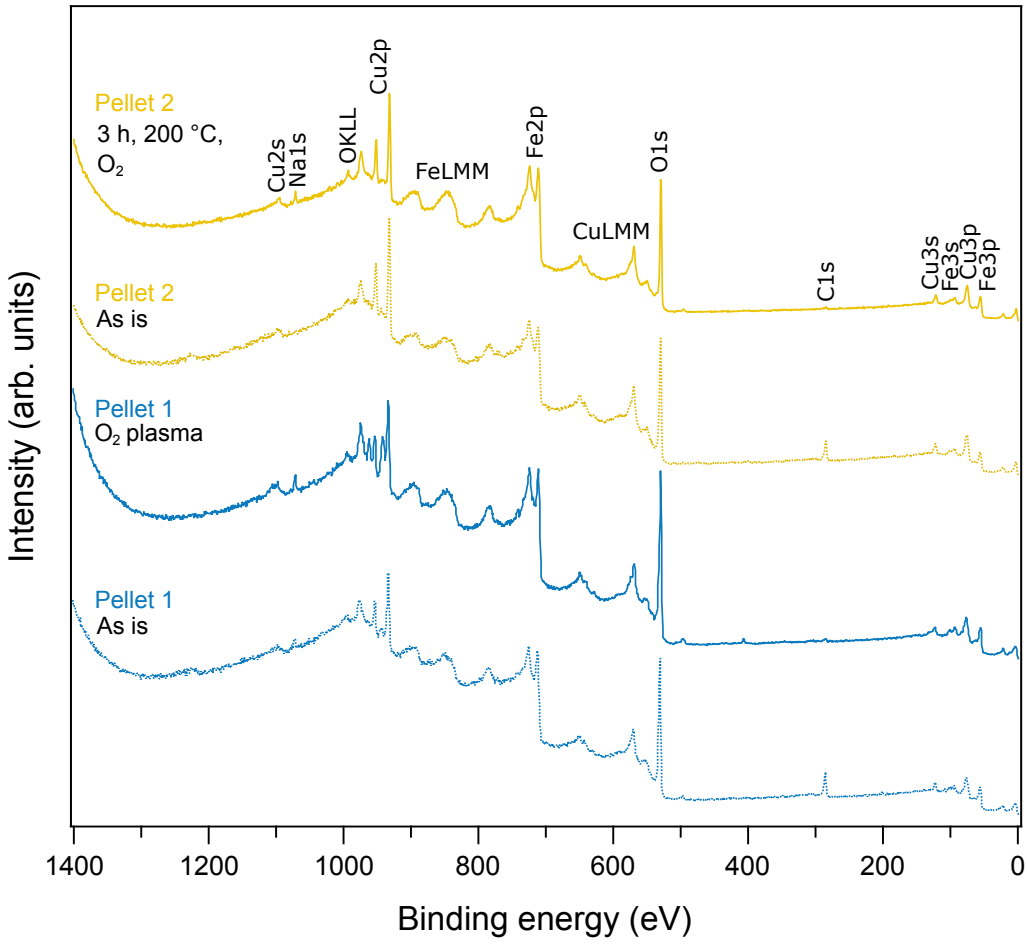

Figure 6.21: Survey XP spectra of $CuFeO_2$ pellets subjected to different surface cleaning procedures: oxygen plasma (blue) and 3 h thermally cleaning at 200 °C in oxygen atmosphere (2 x 10^{-3} mbar) (yellow).

Additionally, Cu2p, Fe2p, O1s and VB XP core level spectra and CuLMM Auger spectra were recorded for the different $CuFeO_2$ cleaning procedures (Figure 6.22). These measurements indeed confirm that the oxygen plasma was a too oxidative treatment, because in the Cu2p spectrum a broadening of the main $Cu2p_{3/2}$ line and an intensity increase in the satellite area around 940 — 945 eV can be observed, which are both typical features for copper in the Cu^{2+} oxidation state.[22] Furthermore, in the CuLMM spectrum a broadening of the main line can be noticed, which is most likely related to the presence of Cu^{2+}, because the Cu^{2+} CuLMM spectrum is usually shifted towards a lower binding energy compared to the CuLMM spectrum of Cu^{+}.[22] In the Fe2p spectrum no noticeable change can be seen, mainly because the oxidation of Fe^{3+} to Fe^{4+} is unlikely, due to Fe^{3+} being a more stable oxidation state for iron containing solid state compounds. For the heat treatment in oxygen atmosphere, the formation of Cu^{2+} could not be observed and also the Fe2p region remains largely the same. However, the $CuFeO_2$ pellet, before treatment, exhibited a bump at a binding energy of 935 eV in the Cu2p spectrum, which disappears after the thermally cleaning step at 200 °C Furthermore, in the O1s region the shoulder at 531.6 eV, characteristic for hydroxyl and carbonyl groups, disappears after the thermally cleaning step, indicating that the oxygen heat treatment completely oxidises the surface, removing all hydroxides and carbonaceous species. Another observation is that, after the heat treatment, the valence band maximum shift from 0.41 eV to 0.19 eV, indicating that $CuFeO_2$ becomes more p-type.

As mentioned above, the 2H-$CuFeO_2$ pellets were made from the $CuFeO_2$ powder which was not appropriate for the photodeposition experiments, i.e. the powder which was more aggregated and which contained more 3R-$CuFeO_2$. In Figure 6.23 the X-ray diffractograms of the powder, used to prepare the pellets, and the pellet after the 200 °C thermally cleaning step are shown. Surprisingly, not much 3R-$CuFeO_2$ seems to be present in the powder. Moreover, 3R-$CuFeO_2$ could not be detected any more after pressing the powder into a pellet and cleaning it through the oxygen heat treatment, which may indicate that the 3R-$CuFeO_2$ phase converts into the 2H-$CuFeO_2$ at the used cleaning conditions. Another remarkable feature is the relatively higher intensity of the $\{001\}$ reflections for the pellet, which most likely originate from the stacking of the nanoplatelets according to the [0001] direction during uniaxial pressing. This preferential stacking could also be the reason that 3R-$CuFeO_2$ cannot be observed any more in the θ-2θ scan of the pellet. Additionally, the [0001] orientation of the grains in the pellets means that the interface experiments on these pellets mostly yields information on how the $\{0001\}$ surfaces of 2H-$CuFeO_2$ align with the contact material.

6.5.2 $CuFeO_2$/ITO

As the 2H-$CuFeO_2$ pellets already showed a low E_F-E_{VBM} value of 0.19 eV after the thermally cleaning step, interface experiments with high work function materials, to lower E_F-E_{VBM} further, were not expected to give any new information, so that only interface experiments with a low work function material, ITO, were performed. Testing by how much E_F-E_{VBM} in 2H-$CuFeO_2$

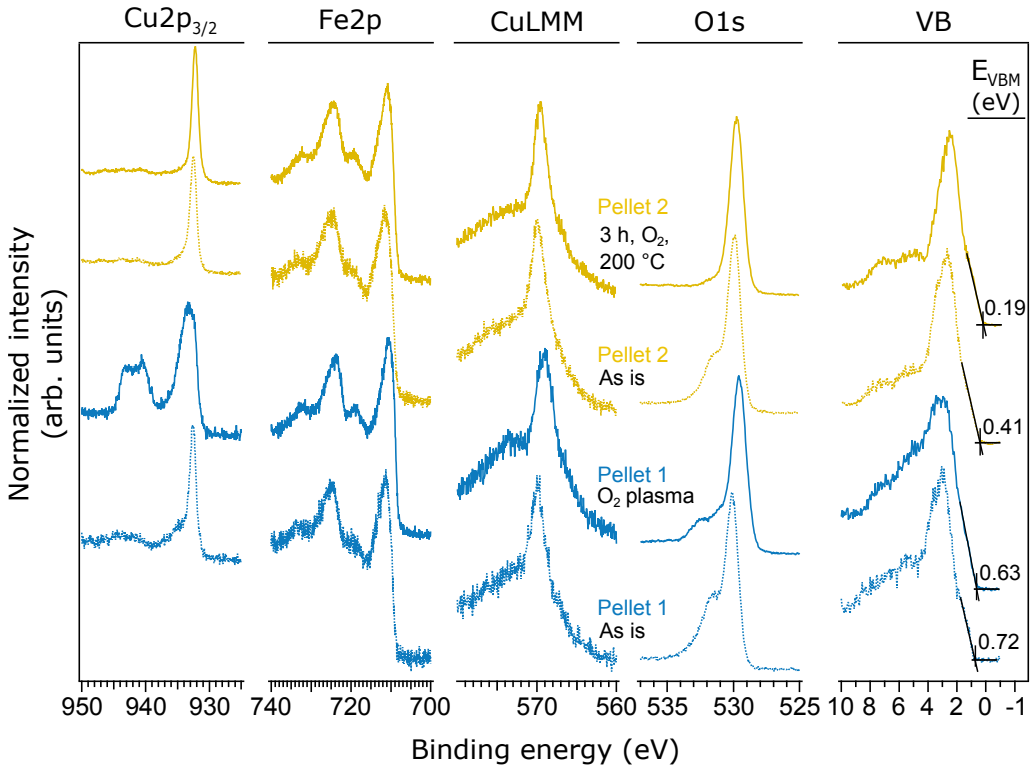

Figure 6.22: $Cu2p_{3/2}$, Fe2p, O1s core level and valence band XP spectra and CuLMM Auger spectrum of $CuFeO_2$ pellets subjected to different surface cleaning procedures: oxygen plasma (blue) and 3 h thermally cleaning at 200 °C in an oxygen atmosphere (2 x 10^{-3} mbar) (yellow).

can be raised is also more relevant for $CuFeO_2$ based hydrogen evolution compounds, because then information can be gained on the extent of feasible downwards band bending and an idea can be conceived on whether photovoltage will be limited due to bulk electronic processes. The sputtering parameters of ITO can be found in Section 3.2.2. The details of an interface experiment are described in Section 3.4.4.1. Figure 6.24 shows how the Cu2p, Fe2p, CuLMM, O1s and VB spectra evolve with increasing ITO coverage. The developing $CuFeO_2$/ITO interface can be clearly followed, as the Cu2p, Fe2p and CuLMM spectra decrease and the $In3d_{5/2}$ intensity increases with increased ITO sputtering time. Meanwhile, the O1s intensity remains constant.

The shift of the Cu2p, CuLMM, Fe2p and valence band spectra towards higher binding energies can be noticed with increased ITO coverage, which indicates an electronic, rather than a chemical, shift. As E_F-E_{VBM} of bare $CuFeO_2$ is quite low, the ITO valence band spectrum does not overlap with that of $CuFeO_2$, so that the shift in the $CuFeO_2$ VBM can be used to quantify the electronic shift. Quantifying the shift by following the shift in the CuLMM and $Fe2p_{3/2}$ is more complicated, because of the asymmetric line shape in both spectra and, additionally, the large number of satellites and mixing in of $In3p_{1/2}$ and $Sn3p_{3/2}$ in the $Fe2p_{3/2}$ spectra. The $Cu2p_{3/2}$ binding energy shift can be followed with ease due to its relatively strong intensity and well-

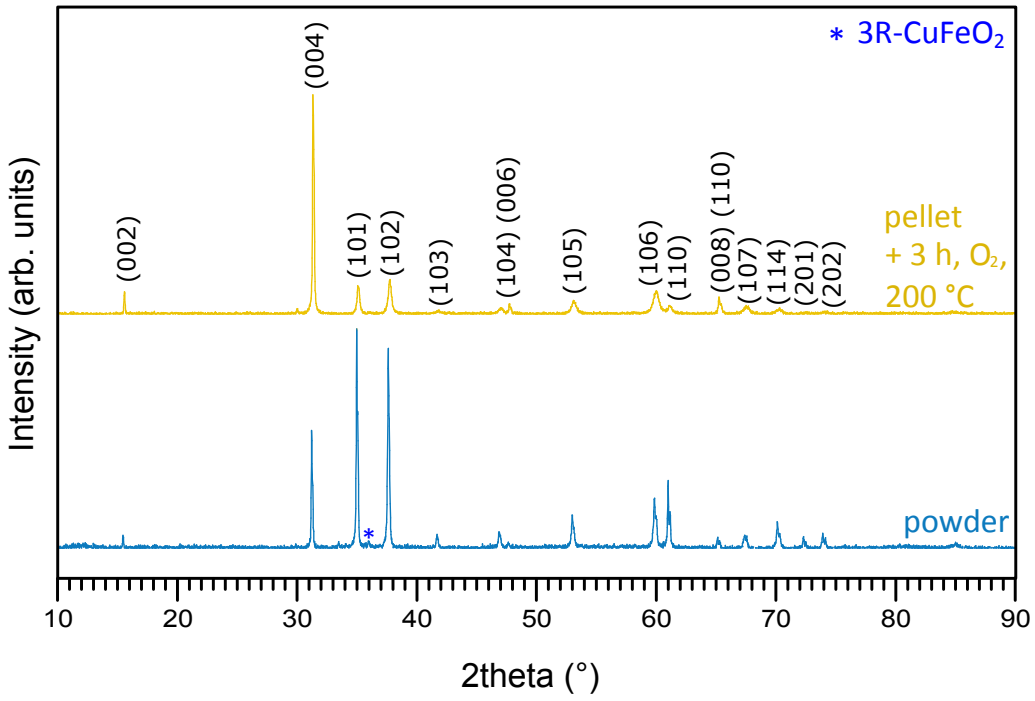

Figure 6.23: High resolution powder X-ray diffractograms for the $CuFeO_2$ powder used to prepare the pellets (blue) and a pellet after the thermally cleaning step at 200 °C (yellow). The (hkl) reflections of 2H-$CuFeO_2$ are indicated in the graph.

defined line shape. For the VBM and $Cu2p_{3/2}$ a complete upwards binding energy shift of 0.32 eV and 0.37 eV, respectively, is obtained. A second interface experiment showed very similar shifts of 0.37 eV and 0.44 eV for VBM and $Cu2p_{3/2}$, respectively.

From the secondary electron cut-offs of the measured UP spectra (Figure 6.25), work functions of 5.2 eV and 4.3 eV were determined for the $CuFeO_2$ pellet and the ITO film, respectively. The ITO work function, here, is similar to the ITO work functions measured earlier for the $BiVO_4$/ITO interface experiments (Section 5.3.1). When combining the 5.2 eV $CuFeO_2$ work function with the value of 0.2 eV for E_F-E_{VBM}, an ionization potential of 5.4 eV is retrieved for the $CuFeO_2$ pellet. Contrarily, Benko et al. calculated an ionization potential of 4.95 eV from the flatband potential, derived from photocurrent onset potential measurements at pH_{ZPC}, of a polycrystalline $CuFeO_2$ pellet, which was prepared through conventional solid-state synthesis.[25] However, the authors report optical band gaps, 1.15 eV (indirect) and 2.03 eV (direct), which differ strongly from the optical band gaps, 1.24 eV (indirect) and 1.43 eV (direct), determined for our 2H-$CuFeO_2$ powder. This band gap dissimilarity could be due to structural and electronic differences, which can explain the difference in ionization potentials. Another way of estimating the ionization potential is through a semi-empirical calculation developed by Butler and Ginley,[41] which involves the Mulliken electronegativity of $CuFeO_2$, calculated from the absolute electronegativities χ of copper (4.48 eV), oxygen (7.54 eV) and iron (4.06 eV):[42]

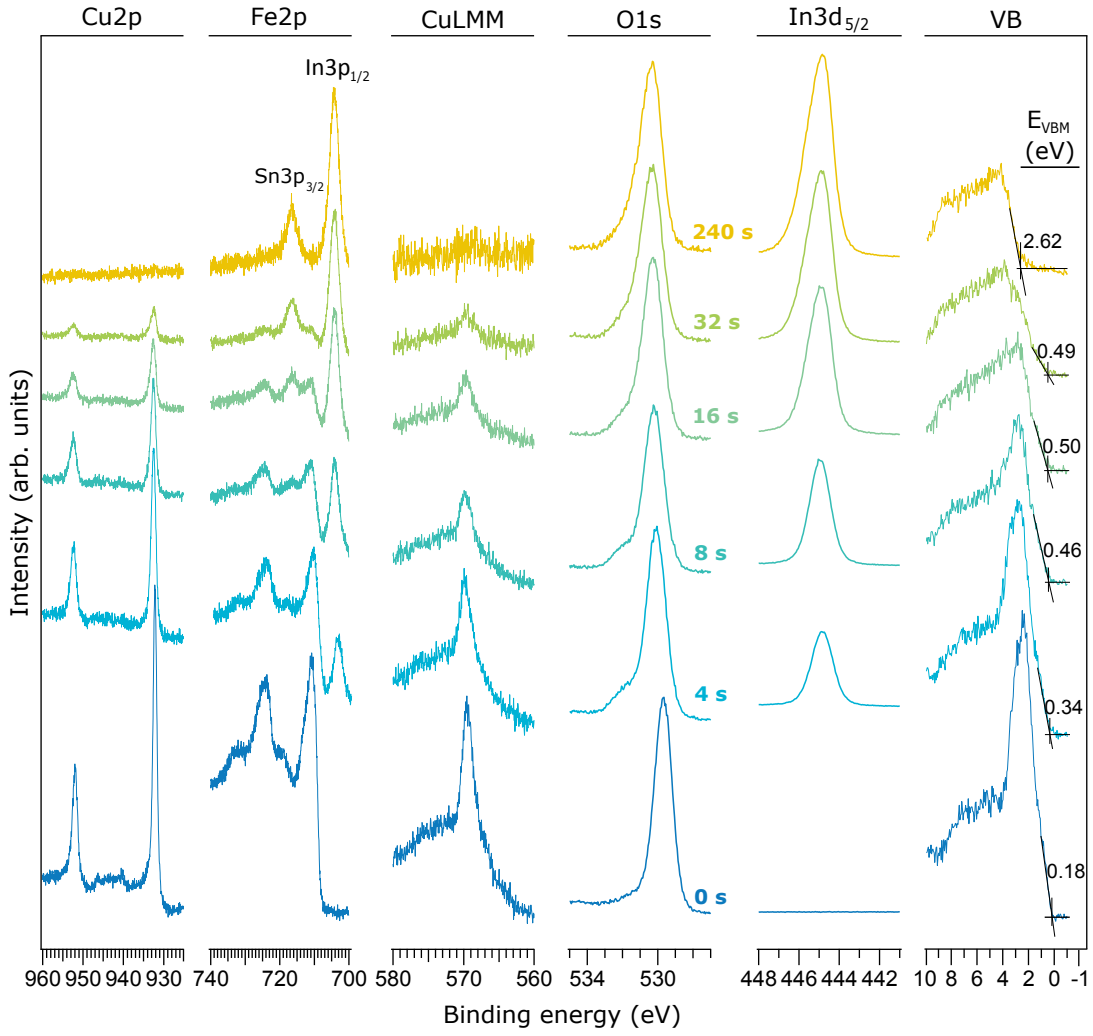

Figure 6.24: Cu2p, Fe2p, O1s, $In3d_{5/2}$ core level and valence band XP spectra, and CuLMM Auger spectra for $CuFeO_2$/ITO(RT) interface. ITO deposition times are denoted in the O1s spectra.

$$I_P = (\chi(Cu) * \chi(Fe) * \chi(O)^2)^{\frac{1}{6}} + \frac{1}{2}E_g \tag{6.1}$$

with E_g being the electronic band gap, herein given by the 1.24 eV indirect optical band gap:

$$I_P = (4.48 * 4.06 * 7.54^2)^{\frac{1}{6}} + \frac{1}{2}1.24 = 6.29 \tag{6.2}$$

This calculated ionization potential differs largely from what we obtained using photoelectron spectroscopy and from the $CuFeO_2$ valence band positions mentioned in literature.[1,10] Koffyberg et al. found out that the ionization potentials of metal oxides calculated with the semi-empirical Butler-Ginley equation correlate well with experimental values when the valence band consists

mainly of O2p character, but not when the valence band has mainly metal 3d character, as is the case for example for CuO and NiO.[43] Hence, the strong discrepancy in calculated and experimentally determined ionization potentials most likely has to do with the Cu3d character of the $CuFeO_2$ valence band. More recently, Omeiri et al. determined through Mott-Schottky flat band measurements that the ionization potential of the (001) surface of a 3R-$CuFeO_2$ single crystal amounts to 5.4 eV,[13] which is quite similar to the 5.2 eV ionization potential determined here for the [001] oriented $CuFeO_2$ pellet. Due to the Mott-Schottky measurements being performed at the point of zero charge, the similarity of the $CuFeO_2$ surfaces and the similarity of the ionization potentials, the presence of a strong surface dipole at the 2H-$CuFeO_2$ pellet surface is regarded as being highly unlikely.

Difference spectra of $Cu2p_{3/2}$, CuLMM and $Fe2p_{3/2}$ were made (Figure 6.26) to verify whether the ITO interface experiment led to any chemical changes in $CuFeO_2$. In the $Cu2p_{3/2}$ core level spectrum a broadening of the main $Cu2p_{3/2}$ line can be seen, which is at first glance a somewhat strange phenomenon, because oxidation state changes normally lead to the appearance of new signals with a shifted binding energy. Anyway, the different copper oxidation states cannot be easily recognized by analysing the main $Cu2p_3$ line, as the Cu2p spectrum of Cu^+ only differs

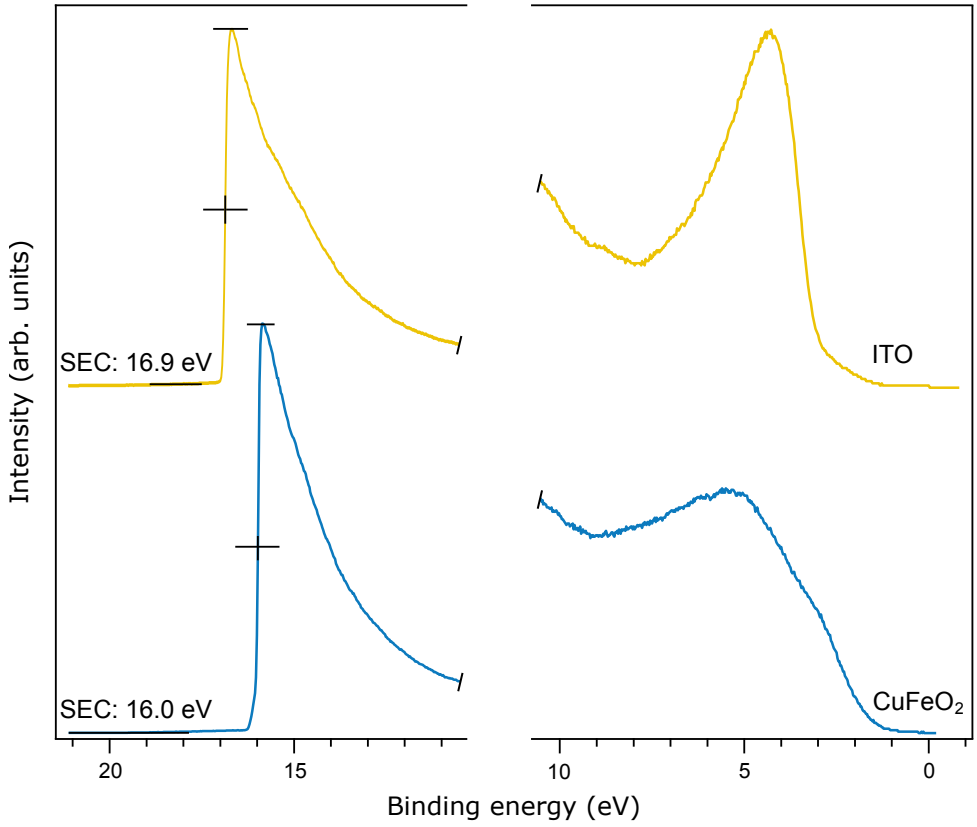

Figure 6.25: UP spectra (He I excitation) of the $CuFeO_2$ substrate (blue) and the ITO film (yellow) after 240 s deposition time.

marginally from that of metallic copper, and the $Cu2p_{3/2}$ line of Cu^{2+} yields only a slight shift and broadening compared to Cu^{+}.[22] However, the broadening of the principal $Cu2p_{3/2}$ line, seen here, most likely does not correspond to an oxidation of Cu^{+} to Cu^{2+}, because then an increase in intensity in the satellite region between 940 eV and 945 eV, characteristic for Cu^{2+}, should be seen as well.[22] Furthermore, the CuLMM Auger spectrum after 4 s of ITO deposition does not show any sign of Cu^{2+} either, as then a signal should appear at a 0.9 eV lower binding energy than the main Cu^{+} CuLMM line.[44] In addition, a change from Cu^{2+} to Cu^{+} is not consistent with the observed increase in binding energies. Hence, the broadening of the main $Cu2p_{3/2}$ line is not likely due to a change in copper oxidation state. Another possible reason for the increased broadening of the main $Cu2p_{3/2}$ line is inhomogeneous ITO coverage due to the large substrate surface roughness, which is plausible for a powder pressed pellet. In this case, the $Cu2p_{3/2}$ line at 4 s ITO coverage would then be a composite signal consisting of $Cu2p_{3/2}$ signals with different binding energy shifts, originating from positions with differing ITO thickness. Indeed, surface profiles show that the 2H-$CuFeO_2$ pellet surface roughness appears to be an order of magnitude higher compared to that of a $BiVO_4$ thin film (Figure 6.27). Thus, surface roughness seems to be a possible explanation for the observed $Cu2p_{3/2}$ broadening. However, the CuLMM and $Fe2p_{3/2}$ spectrum apparently do not suffer from line broadening, which would be expected if surface roughness was the cause of $Cu2p_{3/2}$ line broadening. Therefore, the exact cause of $Cu2p_{3/2}$ line broadening could not be confidently determined.

Furthermore, an extra signal at lower binding energy, i.e. around 709 eV, appears in the $Fe2p_{3/2}$ difference spectra after 4 s of ITO deposition (Figure 6.26). Since this binding energy position is characteristic for Fe^{2+},[45] Fe^{3+} is likely partly reduced to Fe^{2+}, as effect of the ITO coverage. Moreover, in our group the appearance of Fe^{2+} in the $Fe2p_{3/2}$ spectrum has been observed before for hematite,[46] lanthanum ferrite (unpublished results) and bismuth ferrite (unpublished results), while increasing the Fermi level position in these materials through ITO deposition.

The results of the $CuFeO_2$/ITO interface experiment are summarized in Figure 6.28. The band diagram shows that there is a staggered type II alignment between ITO and $CuFeO_2$, where, upon light absorption, electrons would flow towards ITO due to the downward band bending. A vacuum level offset of 0.58 eV can be seen, which can be caused by a surface dipole or by Fermi level pinning. The possibility of a surface dipole at the $CuFeO_2$ surface can be cautiously neglected, because (as discussed above) the 2H-$CuFeO_2$ pellet ionization potential corresponds well to that of an $\{001\}$ exposed 3R-$CuFeO_2$ single crystal determined at the point of zero charge under flat band conditions.[13] Contrarily, the 4.3 eV ITO work function is quite low, considering the value of 2.6 eV for E_F-E_{VBM} (Figure 6.24). However, this work function agrees well with what other people in our group have found for ITO films deposited at room temperature. Another possible reason for the observed vacuum level offset could be Fermi level pinning. Figure 6.28b shows the band positions of $CuFeO_2$ as they are commonly depicted, VBM at -1.0 — -1.4 eV vs RHE and CBM at 0.1 — 0.5 eV.[1,10,12,13] Additionally, the apparent 0.32 eV Fermi level shift, as determined from the ITO interface experiment is shown. In Figure 6.28c a series of standard reduction potentials are

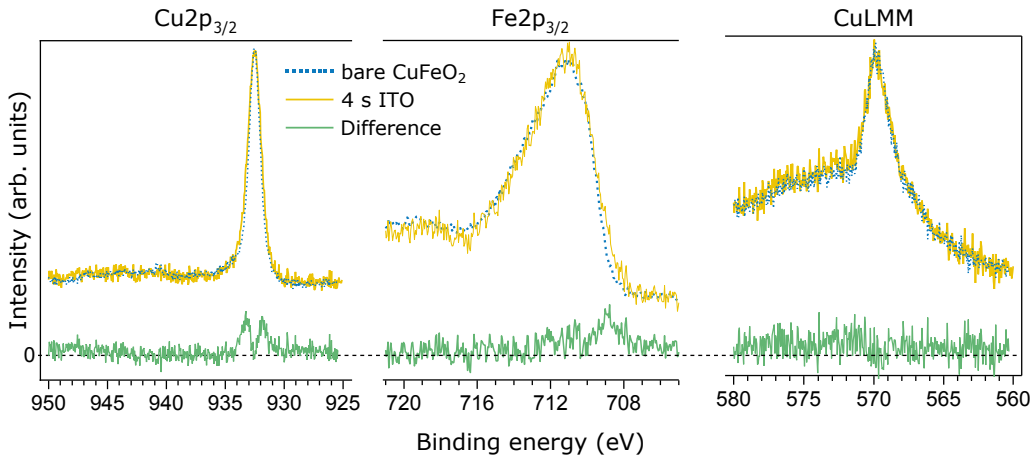

Figure 6.26: Difference spectra of $Cu2p_{3/2}$, CuLMM and $Fe2p_{3/2}$ between bare $CuFeO_2$ and $CuFeO_2$/ITO (4 s). Shirley background subtraction was done for Cu2p and Tougaard background subtraction for Fe2p. The spectra were normalized and shifted towards the same binding energy.

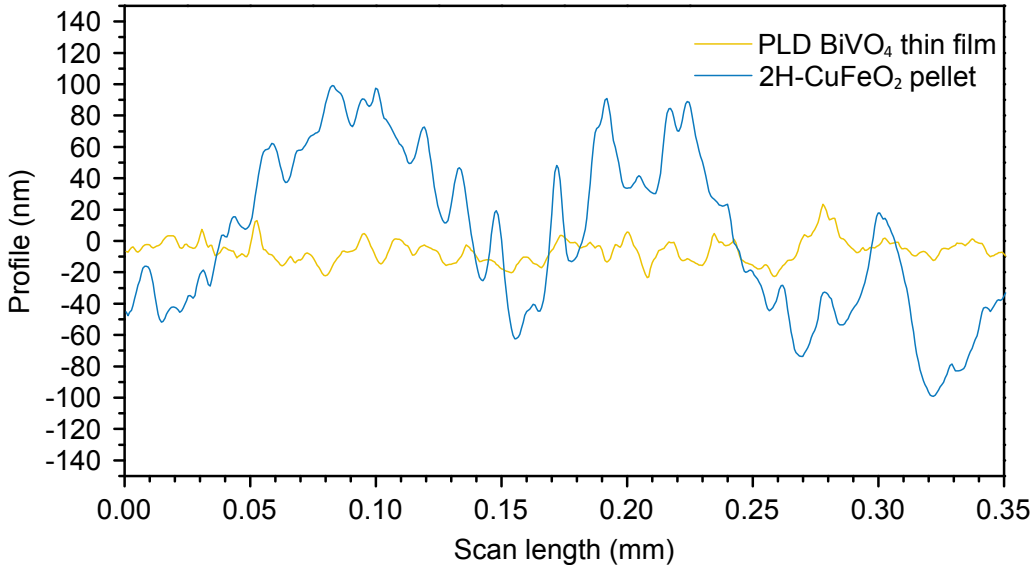

Figure 6.27: Roughness profile of PLD $BiVO_4$ thin film and 2H-$CuFeO_2$ pellet, measured with a Dektak XT Advanced System profilometer

shown on the RHE scale.[i] As was shown above, Fe^{3+} is evidently partly reduced to Fe^{2+} after establishing the $CuFeO_2$/ITO interface. The Fe^{3+}/Fe^{2+} (pH 7) reduction potential, at about -1.18 eV vs RHE, cannot explain the induced Fe^{3+} reduction at the $CuFeO_2$/ITO contact, as this reduction potential would mean that the iron would already be in the Fe^{2+} state for bare $CuFeO_2$, with a Fermi level position at about -1.02 eV vs RHE. However, the Fe^{3+} coordination in solution and in the 2H-$CuFeO_2$ crystal lattice differs from one another, meaning that the actual Fe^{3+}/Fe^{2+} charge transfer level in 2H-$CuFeO_2$ probably does not correspond to the Fe^{3+}/Fe^{2+} aqueous reduction potential. Recently, Lohaus et al. demonstrated that the Fe^{3+}/Fe^{2+} polaron level for hematite, lies at -0.3 eV vs NHE,[46] which on the RHE scale will be -0.7 eV vs RHE (pH 7). Now, for hematite the iron sites are octahedrally coordinated by oxygen just like the iron sites in $CuFeO_2$. Therefore, the Fe^{3+}/Fe^{2+} polaron level in $CuFeO_2$ can expected to be situated around -0.7 eV vs RHE (pH 7) as well, a position which would agree nicely with the Fermi level shift feasible by ITO deposition. Furthermore, Prévot et al. also observed Fermi level pinning in 3R-$CuFeO_2$ at ± -0.7 eV vs RHE (pH 7), which the authors assumed to be caused by surface states.[12] However, as our results suggest Fermi level pinning does not take place because of surface states, but due to the bulk Fe^{3+}/Fe^{2+} polaron level at -0.7 eV vs RHE. Bulk Fermi level pinning can, thus, strongly impair the potential water reduction capacity of $CuFeO_2$, because then not enough photovoltage can be created to achieve water reduction and no solution could be engineered because the photovoltage limit would be intrinsic to $CuFeO_2$. The -0.7 eV vs RHE Fermi level limit could also explain why $PtCl_6^{2-}$, with a reduction potential of -0.75 eV vs RHE, and Ag^+, with a reduction potential of -1.02 eV vs RHE, could be reduced, upon light absorption, whereas water, with a reduction potential of 0 eV vs RHE, could not. Only the nickel photodeposition could disprove the hypothesis of bulk Fermi level pinning at the Fe^{3+}/Fe^{2+} polaron level, as the Ni^{2+}/Ni reduction potential is situated at about -0.13 eV vs RHE. However, due to the absence of regioselectivity in the nickel deposition (Figure 6.16), a dark nickel impregnation mechanism could not be excluded. Fermi level tuning was further investigated through water exposure experiments, which will be discussed in the next Section.

[i]The RHE scale is chosen because the $CuFeO_2$ band positions and, the H^+/H_2 and O_2/H_2O reduction potentials are then independent of pH (See also Figure 2.18). However, the reduction potentials of the other listed reactions, although they do not involve any hydroxide anions or hydrogen cations, shift with pH on the RHE scale, due to the pH dependence of the reversible hydrogen electrode with respect to the standard hydrogen electrode. These reduction potentials are then calculated according to the modified Nernst equation: $E_{RHE} = E^0{}_{SHE} + 0.059pH + \frac{0.059}{n} log(Q_{ini})$; with the $E^0{}_{SHE}$ taken from literature,[47] n the number of electrons involved in the reduction reaction and Q_{ini} the initial reaction quotient. The standard reduction potentials of $PtCl_6^{2-}/PtCl_4^{2-}$ and $Ag^+/Ag(s)$ are calculated for pH 3 and pH 7, respectively, because the photodeposition of platinum and silver were performed at pH 3 and pH 7, respectively. The Fe^{3+}/Fe^{2+} polaron level, situated at -0.29 eV vs SHE as was recently proven by Lohaus et al.,[46] and reduction potentials of $Cu^+/Cu(s)$ and Fe^{3+}/Fe^{2+} are calculated at pH 7, because the bare $CuFeO_2$ pellet, in the absence of a surface dipole (see above) and under flat band conditions, is regarded as being at the pH of zero point charge, which is around pH 7.[13]

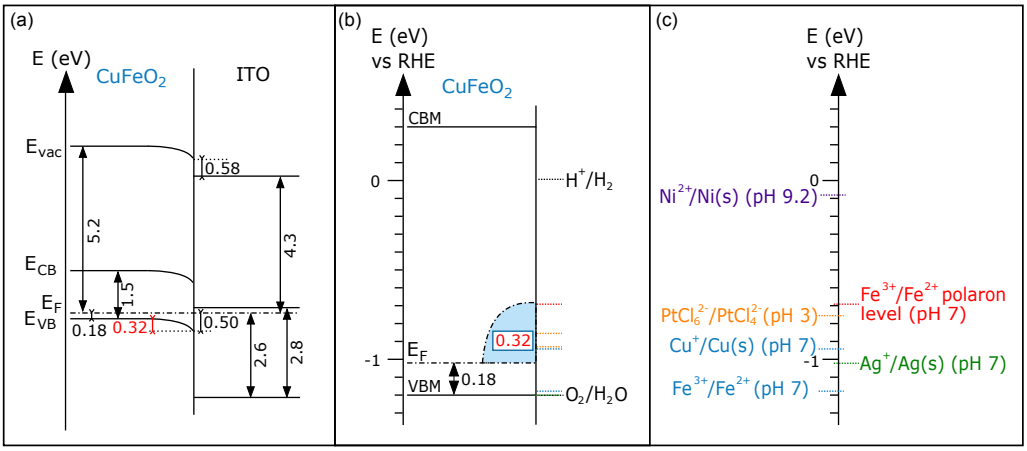

Figure 6.28: (a) Energy band diagram of $CuFeO_2$/ITO with all energy values denoted in eV and the band gap of ITO taken from literature.[48] (b) Diagram showing the Fermi level tunability in $CuFeO_2$ based on the $CuFeO_2$/ITO interface experiment. (c) A series of reduction potentials calculated at particular pH values on the RHE scale.[i]

6.5.3 $CuFeO_2/H_2O$

The experimental procedure of a water exposure experiment can be found in Section 3.4.4.2. Before exposing the $CuFeO_2$ samples to water, they were calcined in a pure oxygen atmosphere to remove the extrinsic contamination layer. However, the calcination was not effective at removing the upper contamination layer, since the intensity of the C1s signal in the survey spectrum (Figure 6.29) does not decrease after the calcination procedure. The incomplete removal of the extrinsic carbonaceous species could be due to the low temperature that had to be used in the calcination procedure or due to the porosity of the pellets. In Figure 6.30 the effect of water exposure on the $Cu2p_{3/2}$, Fe2p, O1s and valence band XP and CuLMM Auger spectra of $CuFeO_2$ is shown. All spectra shift towards higher binding energies, as can be expected from the contact with a low work function material.[49] The determined valence band maxima show that water exposure had a stronger effect than ITO as here the VBM is pushed towards 0.7 — 0.8 eV. Admittedly, the VBM of pellet 1 before water exposure was already positioned at a quite high position. In the O1s spectra an additional feature at a binding energy of 532 eV can be seen, which is characteristic for carbonyl bonds and hydroxides.[24] After water exposure this signal at 532 eV increases, indicating that hydroxides were formed during water exposure.

Figure 6.31 displays the UP spectra of $CuFeO_2$ before and after water exposure. First of all, the upward binding energy shift induced by the water exposure can also be noticed in the VB region of the UP spectra. Secondly, the work function of the $CuFeO_2$ pellets before water exposure, 5.2 eV, corresponds to what was found earlier and after water exposure the work function shifts towards 4.3 — 4.4 eV We did not see this high work function shift for the $BiVO_4$ substrates. Most likely this is due to the $CuFeO_2$ substrate being a pellet, which has a higher porosity and is thus

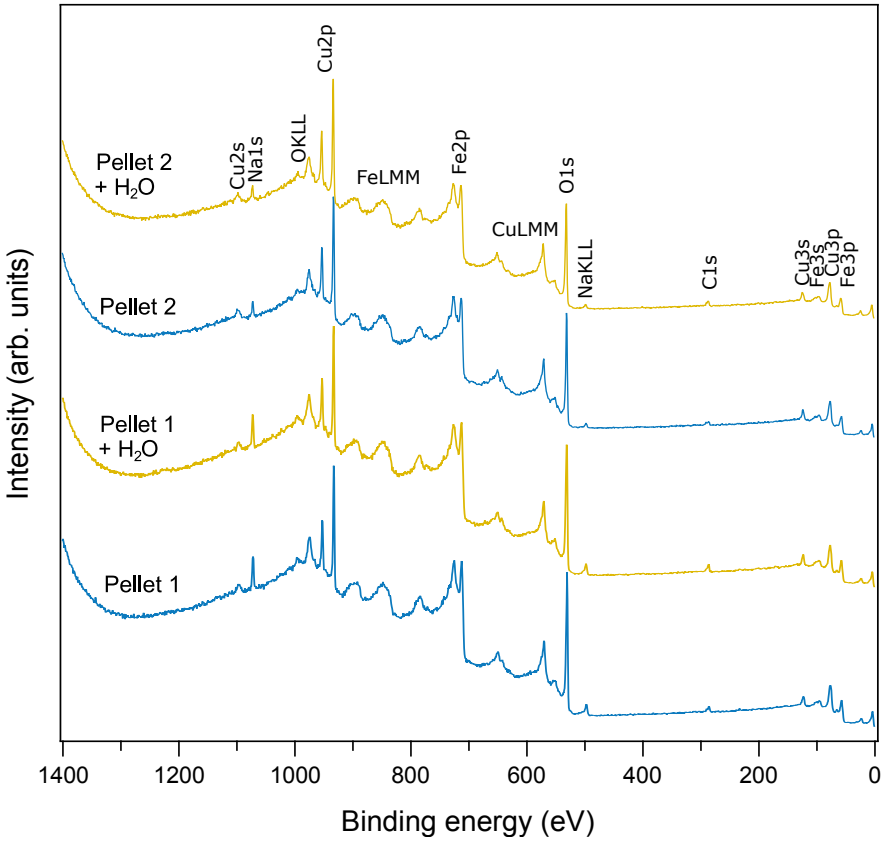

Figure 6.29: Survey XP spectra of two thermally cleaned (200 °C, O_2, 3 h) $CuFeO_2$ pellets before (blue) and after (yellow) water exposure.

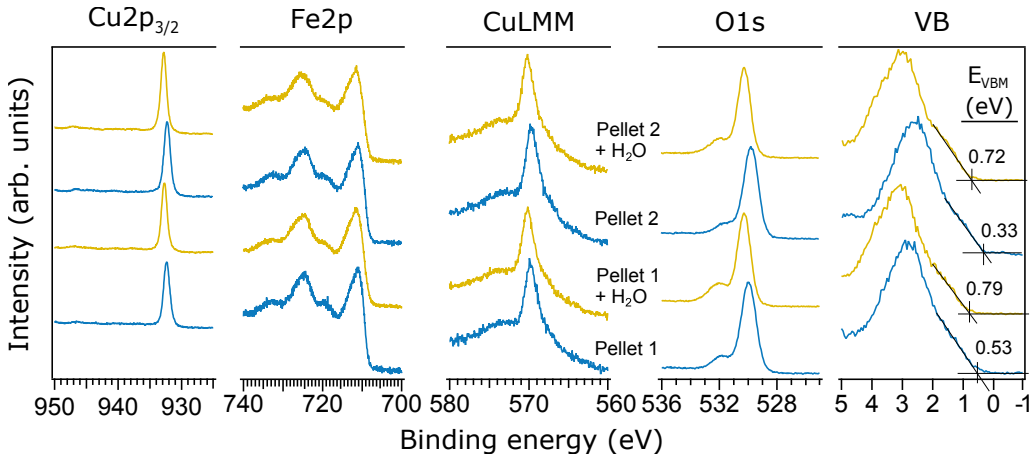

Figure 6.30: $Cu2p_{3/2}$, Fe2p, O1s core level and valence band XP spectra and CuLMM Auger spectrum of two thermally cleaned (200 °C, O_2, 3 h) $CuFeO_2$ pellets before (blue) and after (yellow) water exposure.

more prone to retain water after a water exposure experiment compared to a $BiVO_4$ thin film. This hypothesis is also seemingly confirmed by the valence band region in the UPS spectra. After water exposure, features at 5.3 eV, 7.4 eV and 11.2 eV can be seen, which are characteristic to the $1b_1$, $3a_1$ and $1b_2$ orbitals, respectively, of water, only shifted by about 2 eV.[50] The shift is likely due to the water being physisorbed to the $CuFeO_2$ substrate, as a 1 eV shift with respect to molecular water was seen earlier for physisorbed water on NiO.[51]

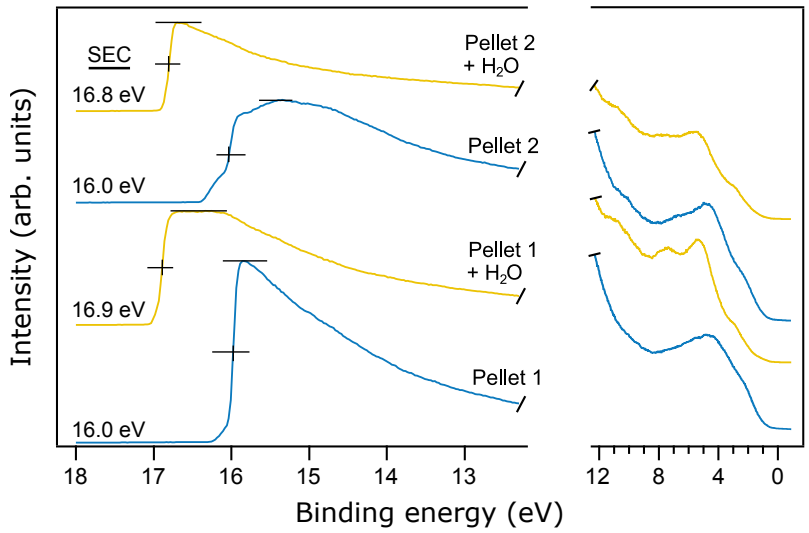

Figure 6.31: UP spectra (He I excitation) of two thermally cleaned (200 °C, O_2, 3 h) $CuFeO_2$ pellets before (blue) and after (yellow) water exposure.

Difference spectra of $Cu2p_{3/2}$, $Fe2p_{3/2}$, CuLMM and Fe3p (Figure 6.32) were generated to verify whether the exposure of $CuFeO_2$ to water led to any chemical changes. In the difference trace of the main $Cu2p_{3/2}$ signal an apparent line narrowing can be seen. Possibly, copper may get reduced from Cu^{2+}, which could be present in small amounts, to Cu^+, which is however unlikely as no changes are noticed in the $Cu2p_{3/2}$ satellite region.[22] Another possibility is the reduction from Cu^+ to Cu(0), which is also unlikely since then an extra signal at lower binding energy in the CuLMM spectra should appear.[22] Hence, just like for the line broadening observed after ITO deposition no clear explanation can be deduced for the main $Cu2p_{3/2}$ line width change. Both $Fe2p_{3/2}$ and Fe3p show that an extra signal appears at lower binding energy, which indicates the presence of Fe^{2+}.[45,52] The Fe^{2+} signal is also somewhat more intense than what was seen for the $CuFeO_2$/ITO interface.

Again, the upwards Fermi level shift and coinciding reduction of Fe^{3+} to Fe^{2+} support the hypothesis of Fermi level pinning at the formation and occupation of the Fe^{3+}/Fe^{2+} polaron level at 0.7 eV vs RHE, which was introduced after the results of the $BiVO_4$/ITO experiment were analysed.

It is surprising that Fermi level pinning seems to take place and Fe^{2+} appears at an E_F-E_{VB} of 0.5 eV during ITO deposition and at 0.7 — 0.8 eV after water exposure. For Fermi level pinning

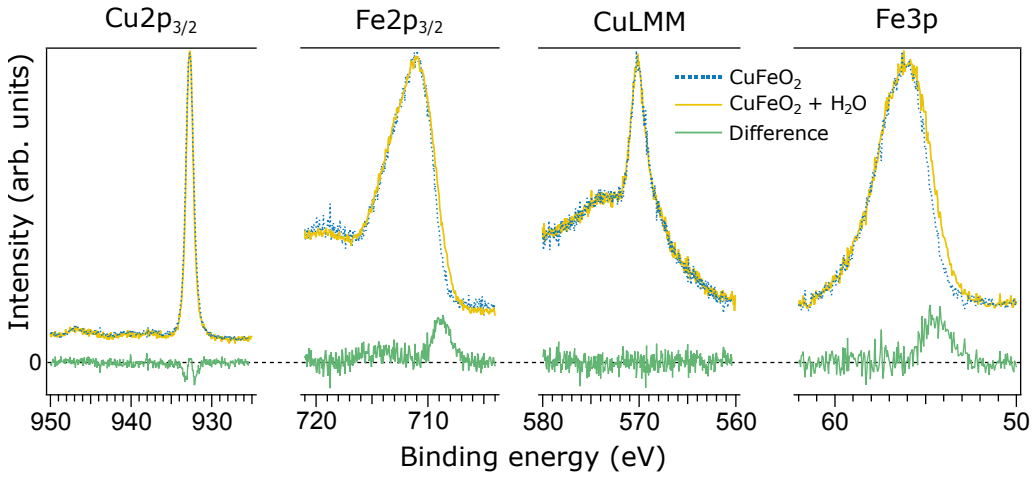

Figure 6.32: Difference spectra (green) of $Cu2p_{3/2}$, $Fe2p_{3/2}$, CuLMM and Fe3p between thermally cleaned (200 °C, O_2, 3 h) $CuFeO_2$ pellet 1 before (blue) and after (yellow) water exposure. Shirley background subtraction was performed for Cu2p and Fe3p, and Tougaard background subtraction for Fe2p. The spectra were normalized and shifted towards the same binding energy.

at the Fe^{3+}/Fe^{2+} polaron formation level, the E_F-E_{VB} positions should normally be the same for both experiments.

6.6 Conclusion

2H-$CuFeO_2$ hexagonal nanoplatelet heterostructures were effectively created through photodeposition. Specifically, silver, platinum and nickel(hydroxide) were deposited, whereby, silver and platinum were selectively found on the $\{0001\}$ facets of the 2H-$CuFeO_2$ nanoplatelets. No selectivity was found for the nickel(hydroxide) deposits.

Despite the creation of anisotropic heterostructures with performant hydrogen evolution electrocatalysts, i.e. $CuFeO_2$/Pt, only trace amounts of hydrogen were detected for the heterostructured $CuFeO_2$ powders after testing the photochemical sacrificial water splitting activity of the powders in a closed batch reactor coupled to an automatic burette.

$CuFeO_2$ substrates were prepared, by pressing $CuFeO_2$ powder into pellets, to perform interface experiments with ITO and water to elucidate why the $CuFeO_2$ powders showed a poor hydrogen evolution efficiency, while still being active for the photodeposition of Ag, Pt and NiO_xOH_y. The interface experiments showed that the Fermi level tunability was limited, with Schottky type barriers amounting to 0.5 and 0.8 for the $CuFeO_2$/ITO interface experiment and the $CuFeO_2/H_2O$ water exposure experiments, respectively. Additionally, for both type of experiments, the reduction of Fe^{3+} to Fe^{2+} could be observed in the Fe2p and Fe3p core level XP spectra. These results indicate that for $CuFeO_2$ bulk Fermi level pinning takes place at the Fe^{3+}/Fe^{2+} elec-

tron polaron level. Therefore, the photovoltage achievable with $CuFeO_2$ seems to be limited, inhibiting unbiased photochemical hydrogen evolution. Should this be true, no optimization would allow $CuFeO_2$ based photocathodes to even come close to its theoretically allowed photocurrent of 15 mA cm^{-2} in the absence of a bias, due to the intrinsic nature of the bulk Fermi level pinning phenomenon.

The results obtained in this Chapter also suggest that, when selecting future promising photocathode materials, the energetic positions of polaron levels have to be taken into account.

References

(1) Sivula, K.; Van De Krol, R. Semiconducting materials for photoelectrochemical energy conversion. *Nat. Rev. Mater.* **2016**, *1*, 15010.

(2) Kudo, A.; Miseki, Y. Heterogeneous photocatalyst materials for water splitting. *Chem. Soc. Rev.* **2009**, *38*, 253–278.

(3) Iwashina, K.; Kudo, A. Rh-Doped $SrTiO_3$ Photocatalyst Electrode Showing Cathodic Photocurrent for Water Splitting under Visible-Light Irradiation. *J. Am. Chem. Soc.* **2011**, *133*, 13272–13275.

(4) Abe, R. Recent progress on photocatalytic and photoelectrochemical water splitting under visible light irradiation. *J. Photochem. Photobiol. C Photochem. Rev.* **2010**, *11*, 179–209.

(5) Kormányos, A.; Thomas, A.; Huda, M. N.; Sarker, P.; Liu, J. P.; Poudyal, N.; Janáky, C.; Rajeshwar, K. Solution Combustion Synthesis, Characterization, and Photoelectrochemistry of $CuNb_2O_6$ and $ZnNb_2O_6$ Nanoparticles. *J. Phys. Chem. C* **2016**, *120*, 16024–16034.

(6) Önsten, A.; Månsson, M.; Claesson, T.; Muro, T.; Matsushita, T.; Nakamura, T.; Kinoshita, T.; Karlsson, U. O.; Tjernberg, O. Probing the valence band structure of Cu_2O using high-energy angle-resolved photoelectron spectroscopy. *Phys. Rev. B* **2007**, *76*, 115127.

(7) Yourey, J. E.; Bartlett, B. M. Electrochemical deposition and photoelectrochemistry of $CuWO_4$, a promising photoanode for water oxidation. *J. Mater. Chem.* **2011**, *21*, 7651.

(8) Paracchino, A.; Laporte, V.; Sivula, K.; Grätzel, M.; Thimsen, E. Highly active oxide photocathode for photoelectrochemical water reduction. *Nat. Mater.* **2011**, *10*, 456–461.

(9) Huang, L.; Peng, F.; Yu, H.; Wang, H. Preparation of cuprous oxides with different sizes and their behaviors of adsorption, visible-light driven photocatalysis and photocorrosion. *Solid State Sci.* **2009**, *11*, 129–138.

(10) Read, C. G.; Park, Y.; Choi, K.-S. Electrochemical Synthesis of p-Type $CuFeO_2$ Electrodes for Use in a Photoelectrochemical Cell. *J. Phys. Chem. Lett.* **2012**, *3*, 1872–1876.

(11) Jin, Y.; Chumanov, G. Solution synthesis of pure 2H $CuFeO_2$ at low temperatures. *RSC Adv.* **2016**, *6*, 26392–26397.

(12) Prévot, M. S.; Jeanbourquin, X. A.; Bourée, W. S.; Abdi, F.; Friedrich, D.; van de Krol, R.; Guijarro, N.; Le Formal, F.; Sivula, K. Evaluating Charge Carrier Transport and Surface States in $CuFeO_2$ Photocathodes. *Chem. Mater.* **2017**, *29*, 4952–4962.

(13) Omeiri, S.; Bellal, B.; Bouguelia, A.; Bessekhouad, Y.; Trari, M. Electrochemical and photoelectrochemical characterization of $CuFeO_2$ single crystal. *J. Solid State Electrochem.* **2009**, *13*, 1395–1401.

(14) Prévot, M. S.; Li, Y.; Guijarro, N.; Sivula, K. Improving charge collection with delafossite photocathodes: a host–guest $CuAlO_2$/$CuFeO_2$ approach. *J. Mater. Chem. A* **2016**, *4*, 3018–3026.

(15) Jang, Y. J.; Park, Y. B.; Kim, H. E.; Choi, Y. H.; Choi, S. H.; Lee, J. S. Oxygen-Intercalated $CuFeO_2$ Photocathode Fabricated by Hybrid Microwave Annealing for Efficient Solar Hydrogen Production. *Chem. Mater.* **2016**, *28*, 6054–6061.

(16) Prévot, M. S.; Guijarro, N.; Sivula, K. Enhancing the Performance of a Robust Sol-Gel-Processed p-Type Delafossite $CuFeO_2$ Photocathode for Solar Water Reduction. *ChemSusChem* **2015**, *8*, 1359–1367.

(17) Panigrahy, B.; Aslam, M.; Misra, D. S.; Bahadur, D. Polymer-mediated shape-selective synthesis of ZnO nanostructures using a single-step aqueous approach. *CrystEngComm* **2009**, *11*, 1920.

(18) Wang, H.; Wang, C.; Cui, X.; Qin, L.; Ding, R.; Wang, L.; Liu, Z.; Zheng, Z.; Lv, B. Design and facile one-step synthesis of $FeWO_4$/Fe_2O_3 di-modified WO_3 with super high photocatalytic activity toward degradation of quasi-phenothiazine dyes. *Appl. Catal. B Environ.* **2018**, *221*, 169–178.

(19) Lin, M.; Tng, L.; Lim, T.; Choo, M.; Zhang, J.; Tan, H. R.; Bai, S. Hydrothermal Synthesis of Octadecahedral Hematite (α-Fe_2O_3) Nanoparticles: An Epitaxial Growth from Goethite (α-FeOOH). *J. Phys. Chem. C* **2014**, *118*, 10903–10910.

(20) Mishra, M.; Mukherjee, I.; Mall, A. K.; Mitra, A.; Dash, S.; Chatterjee, S.; Mukherjee, S.; Roy, A. Truncated hexagonal bi-pyramidal gallium ferrite nanocrystals: integration of structural details with visible-light photo-activity and self-cleaning properties. *J. Mater. Chem. A* **2018**, *6*, 13031–13040.

(21) Peng, D.; Beysen, S.; Li, Q.; Sun, Y.; Yang, L. Hydrothermal synthesis of monodisperse α-Fe_2O_3 hexagonal platelets. *Particuology* **2010**, *8*, 386–389.

(22) Biesinger, M. C.; Lau, L. W.; Gerson, A. R.; Smart, R. S. Resolving surface chemical states in XPS analysis of first row transition metals, oxides and hydroxides: Sc, Ti, V, Cu and Zn. *Appl. Surf. Sci.* **2010**, *257*, 887–898.

(23) Yamashita, T.; Hayes, P. Analysis of XPS spectra of Fe^{2+} and Fe^{3+} ions in oxide materials. *Appl. Surf. Sci.* **2008**, *254*, 2441–2449.

(24) Moulder, J. F.; Stickle, W. F.; Sobol, P. E.; Bomben, K. D., *Handbook of X-ray photoelectron spectroscopy: a reference book of standard spectra for identification and interpretation of XPS data*; Physical Electronics: Eden Prairie MN, 1992, p 261.

(25) Benko, F.; Koffyberg, F. Opto-electronic properties of p- and n-type delafossite, $CuFeO_2$. *J. Phys. Chem. Solids* **1987**, *48*, 431–434.

(26) Zhu, J.; Fan, F.; Chen, R.; An, H.; Feng, Z.; Li, C. Direct Imaging of Highly Anisotropic Photogenerated Charge Separations on Different Facets of a Single $BiVO_4$ Photocatalyst. *Angew. Chemie - Int. Ed.* **2015**, *54*, 9111–9114.

(27) Li, R.; Zhang, F.; Wang, D.; Yang, J.; Li, M.; Zhu, J.; Zhou, X.; Han, H.; Li, C. Spatial separation of photogenerated electrons and holes among $\{010\}$ and $\{110\}$ crystal facets of $BiVO_4$. *Nat. Commun.* **2013**, *4*, 1432.

(28) Li, R.; Han, H.; Zhang, F.; Wang, D.; Li, C. Highly efficient photocatalysts constructed by rational assembly of dual-cocatalysts separately on different facets of $BiVO_4$. *Energy Environ. Sci.* **2014**, *7*, 1369–1376.

(29) Mu, L.; Zhao, Y.; Li, A.; Wang, S.; Wang, Z.; Yang, J.; Wang, Y.; Liu, T.; Chen, R.; Zhu, J.; Fan, F.; Li, R.; Li, C. Enhancing charge separation on high symmetry $SrTiO_3$ exposed with anisotropic facets for photocatalytic water splitting. *Energy Environ. Sci.* **2016**, *9*, 2463–2469.

(30) Liu, X.; Dong, G.; Li, S.; Lu, G.; Bi, Y. Direct Observation of Charge Separation on Anatase TiO_2 Crystals with Selectively Etched $\{001\}$ Facets. *J. Am. Chem. Soc.* **2016**, *138*, 2917–2920.

(31) Rettie, A. J. E.; Chemelewski, W. D.; Emin, D.; Mullins, C. B. Unravelling Small-Polaron Transport in Metal Oxide Photoelectrodes. *J. Phys. Chem. Lett.* **2016**, *7*, 471–479.

(32) Shannon, R. D.; Prewitt, C. T.; Rogers, D. B. Chemistry of noble metal oxides. II. Crystal structures of platinum cobalt dioxide, palladium cobalt dioxide, coppper iron dioxide, and silver iron dioxide. *Inorg. Chem.* **1971**, *10*, 719–723.

(33) Wenderich, K.; Klaassen, A.; Siretanu, I.; Mugele, F.; Mul, G. Sorption-determined deposition of platinum on well-defined platelike platelike WO_3. *Angew. Chemie - Int. Ed.* **2014**, *53*, 12476–12479.

(34) McCrory, C. C. L.; Jung, S.; Ferrer, I. M.; Chatman, S. M.; Peters, J. C.; Jaramillo, T. F. Benchmarking Hydrogen Evolving Reaction and Oxygen Evolving Reaction Electrocatalysts for Solar Water Splitting Devices. *J. Am. Chem. Soc.* **2015**, *137*, 4347–4357.

(35) McCrory, C. C. L.; Jung, S.; Peters, J. C.; Jaramillo, T. F. Benchmarking Heterogeneous Electrocatalysts for the Oxygen Evolution Reaction. *J. Am. Chem. Soc.* **2013**, *135*, 16977–16987.

(36) Joshi, T.; Senty, T. R.; Trappen, R.; Zhou, J.; Chen, S.; Ferrari, P.; Borisov, P.; Song, X.; Holcomb, M. B.; Bristow, A. D.; Cabrera, A. L.; Lederman, D. Structural and magnetic properties of epitaxial delafossite $CuFeO_2$ thin films grown by pulsed laser deposition. *J. Appl. Phys.* **2015**, *117*, 013908.

(37) Barnabé, A.; Mugnier, E.; Presmanes, L.; Tailhades, P. Preparation of delafossite $CuFeO_2$ thin films by rf-sputtering on conventional glass substrate. *Mater. Lett.* **2006**, *60*, 3468–3470.

(38) Abdelwahab, H.; Ratep, A.; Abo Elsoud, A.; Boshta, M.; Osman, M. Influences of annealing temperature on sprayed $CuFeO_2$ thin films. *Results Phys.* **2018**, *9*, 1112–1115.

(39) Stöcker, T.; Exner, J.; Schubert, M.; Streibl, M.; Moos, R.; Stöcker, T.; Exner, J.; Schubert, M.; Streibl, M.; Moos, R. Influence of Oxygen Partial Pressure during Processing on the Thermoelectric Properties of Aerosol-Deposited $CuFeO_2$. *Materials (Basel).* **2016**, *9*, 227.

(40) Bassaid, S.; Chaib, M.; Omeiri, S.; Bouguelia, A.; Trari, M. Photocatalytic reduction of cadmium over $CuFeO_2$ synthesized by sol-gel. *J. Photochem. Photobiol. A Chem.* **2009**, *201*, 62–68.

(41) Butler, M. A. Prediction of Flatband Potentials at Semiconductor-Electrolyte Interfaces from Atomic Electronegativities. *J. Electrochem. Soc.* **1978**, *125*, 228.

(42) Pearson, R. G. Absolute electronegativity and hardness: application to inorganic chemistry. *Inorg. Chem.* **1988**, *27*, 734–740.

(43) Koffyberg, F. P.; Benko, F. A. A photoelectrochemical determination of the position of the conduction and valence band edges of p-type CuO. *J. Appl. Phys.* **1982**, *53*, 1173–1177.

(44) Poulston, S.; Parlett, P. M.; Stone, P.; Bowker, M. Surface Oxidation and Reduction of CuO and Cu_2O Studied Using XPS and XAES. *Surf. Interface Anal.* **1996**, *24*, 811–820.

(45) Biesinger, M. C.; Payne, B. P.; Grosvenor, A. P.; Lau, L. W.; Gerson, A. R.; Smart, R. S. C. Resolving surface chemical states in XPS analysis of first row transition metals, oxides and hydroxides: Cr, Mn, Fe, Co and Ni. *Appl. Surf. Sci.* **2011**, *257*, 2717–2730.

(46) Lohaus, C.; Klein, A.; Jaegermann, W. Limitation of Fermi level shifts by polaron defect states in hematite photoelectrodes. *Nat. Commun.* **2018**, *9*, 4309.

(47) Harris, D. C., *Quantitative Chemical Analysis*; W.H. Freeman: New York, 2015, p 928.

(48) Walsh, A.; Da Silva, J. L.; Wei, S. H.; Körber, C.; Klein, A.; Piper, L. F.; Demasi, A.; Smith, K. E.; Panaccione, G.; Torelli, P.; Payne, D. J.; Bourlange, A.; Egdell, R. G. Nature of the band gap of In_2O_3 revealed by first-principles calculations and X-ray spectroscopy. *Phys. Rev. Lett.* **2008**, *100*, 167402.

(49) Trasatti, S. The absolute electrode potential: an explanatory note (Recommendations 1986). *Pure Appl. Chem.* **1986**, *58*, 955–966.

(50) Thiel, P. A.; Madey, T. E. The interaction of water with solid surfaces: Fundamental aspects. *Surf. Sci. Rep.* **1987**, *7*, 211–385.

(51) Fingerle, M.; Tengeler, S.; Calvet, W.; Mayer, T.; Jaegermann, W. Water Interaction with Sputter-Deposited Nickel Oxide on n-Si Photoanode: Cryo Photoelectron Spectroscopy on Adsorbed Water in the Frozen Electrolyte Approach. *J. Electrochem. Soc.* **2018**, *165*, H3148–H3153.

(52) Grosvenor, A. P.; Kobe, B. A.; Biesinger, M. C.; McIntyre, N. S. Investigation of multiplet splitting of Fe 2p XPS spectra and bonding in iron compounds. *Surf. Interface Anal.* **2004**, *36*, 1564–1574.

Conclusions and Perspectives

6.7 Concluding statements

In the broad context of the development of efficient materials for the renewable production of solar fuels, this work deals with the synthesis and interface analysis of heterostructured oxide photoabsorbers for the purpose of photochemical water splitting. We used bismuth vanadate ($BiVO_4$) and copper iron oxide ($CuFeO_2$) as main photoabsorbers for the water oxidation and water reduction, respectively.

We have shown, using a combination of electron microscopy techniques (SAM, TEM, (FE)SEM), that photodeposition was a reliable ways of creating anisotropic heterostructures. Namely, metallic silver (Ag) and cobalt (oxy)(hydr)oxide (CoO_xOH_y) could be selectively deposited onto the $\{010\}$ and $\{110\}$ facets, respectively, of a $\{010\}/\{110\}$ dual facet exposed $BiVO_4$ microcrystalline powder. Metallic platinum (Pt) could evidently be deposited as well on the $\{010\}$ facets, under the condition that the right pH, $2.5 - 3$, was used during the photodeposition procedure. Furthermore, the regioselectivity of the nickel (oxy)(hydr)oxide photodeposition was investigated for the first time. For the photodeposition of $\pm$ 10 wt% and 1 wt% NiO_xOH_y no selectivity could be obtained, whereas a 0.1 wt% NiO_xOH_y has apparently been deposited onto the $\{010\}$ facets and the edges between the $\{110\}$ facets in a preferential manner.

Another novelty in this work was the creation of heterostructured $CuFeO_2$ powders through the photodeposition method. Here, we successfully demonstrated that Ag and Pt could be selectively deposited onto the $\{0001\}$ facets of the 2H-$CuFeO_2$ hexagonal nanoplatelets. Also, NiO_xOH_y could be effectively deposited onto the $CuFeO_2$ powder, however NiO_xOH_y seemed to be present over the entire $CuFeO_2$ particles, thus showing no particular regioselectivity. A possible reason for the non-selective NiO_xOH_y photodeposition on the $CuFeO_2$ nanoplatelets could be the simultaneous oxidation and reduction of the Ni^{2+} ion.

The photocatalytic performance of the (heterostructured) powders was tested through sacrificial water splitting for which a closed batch reactor coupled to an automatic burette was used. In addition, the dye degradation performance of the (heterostructured) $BiVO_4$ powders was tested. The results showed that a $BiVO_4$ heterostructured photocatalyst which performs well at dye degradation does not necessarily exhibit a good photochemical oxygen evolution rate. Quali-

tatively, the photochemical water photo-oxidation performance of the heterostructured $BiVO_4$ powders are similar to the results of other researchers. However, with respect to those previously published results, we found a 21x higher absolute oxygen evolution rate with bare $BiVO_4$, which could be due to our $BiVO_4$ powder having a higher quality. Unfortunately, the NiO_xOH_y contact material that we introduced for the first time on particulate $BiVO_4$ only yielded a 2x higher oxygen evolution rate compared to bare $BiVO_4$, whereas Pt and CoO_xOH_y exhibited a 5x and 10x higher water photo-oxidation rate, respectively. The low oxygen evolution rate with NiO_xOH_y as contact material is surprising, because NiO_xOH_y contact layers previously showed to have a positive effect on the water oxidation performance of $BiVO_4$ thin films. The low regioselectivity of the NiO_xOH_y deposit with respect to the other investigated contact materials, is the likely reason why we did not observe a high oxygen evolution rate with NiO_xOH_y as contact material.

The most disappointing result was obtained when testing the sacrificial water reduction performance of the heterostructured $CuFeO_2$ powders, because only trace amounts of hydrogen were found, even after prolonged reaction times and the use of highly intense UV light. Based on previous literature results, we assumed that the rather poor photochemical hydrogen evolution was due to Fermi level pinning which limits the photovoltage that can be generated with $CuFeO_2$.

Through so-called interface experiments, whereby a thin film contact was stepwise deposited onto a photoabsorber substrate, the Fermi level tunability within $CuFeO_2$ and $BiVO_4$ was determined as well as the electronic and chemical structure of the in situ formed heterojunctions. For $BiVO_4$ we showed that the Fermi level could be tuned over a wide range of 1.1 eV, which may explain why high photovoltages have been reached previously with $BiVO_4$ based photoanodes. Especially, by contacting $BiVO_4$ with CoO_x, RuO_2 and NiO, which are materials with high work functions, values as low as 1.0 eV could be obtained for E_F-E_{VBM}. Thus, by contacting $BiVO_4$ with high work function materials, high upwards band bending can be reached. As a consequence enhanced charge carrier separation can be expected for these heterostructures. In contrast, when $BiVO_4$ thin films were contacted with ITO, a low work function material, a limited increase in E_F-E_{VBM}, up to 2.1 eV, was found, together with a reduction of vanadium and also bismuth when ITO was deposited at 400 °C. These results indicate that Fermi level pinning occurs, which may be due to polaron formation.

To perform interface experiments with $CuFeO_2$, the synthesized $CuFeO_2$ powder was pressed into pellets. These $CuFeO_2$ pellets were only applied for interface experiments with ITO, because the already very low 0.2 eV value of E_F-E_{VBM}, obtained for the p-type pellets, was not expected to change through contacts with high work function materials. Remarkably, only a rather low E_F-E_{VBM} increase, up to 0.5 eV, could be obtained during the ITO interface experiments, which suggests that Fermi level pinning likely occurs. Indeed, by taking a closer look to the Fe2p core level spectrum, indications of the formation of Fe^{2+} were found. Furthermore the position of the Fe^{3+}/Fe^{2+} transition corresponds well to what others found in our group for other iron containing compounds. Thus, the reason why we did not observe any significant water splitting with

any of the heterostructured $CuFeO_2$ powders is very likely because $CuFeO_2$ cannot reach high photovoltages due to bulk Fermi level pinning at the Fe^{3+}/Fe^{2+} electron polaron level.

The most remarkable results in this work were obtained through water exposure experiments, whereby surface cleaned $CuFeO_2$ and $BiVO_4$ substrates were exposed to water and analysed through photoelectron spectroscopy. Unexpectedly, the $BiVO_4$ surface was highly reduced after the contact with water was established, since features typical of V^{4+} and Bi^0 could be detected. Moreover, a decreased amount of lattice oxygen could be noticed. The reduction of the $BiVO_4$ surface could be partly reversed by introducing the sample into an oxygen atmosphere or completely reoxidised by subjecting the sample to an oxygen plasma treatment. For $CuFeO_2$, the water exposure experiment demonstrated a similar behaviour as for the $CuFeO_2$/ITO interface experiment. Namely, the E_F-E_{VBM} of $CuFeO_2$ only increased by a limited amount, which does not allow for water reduction, and Fe^{3+} was partly reduced to Fe^{2+}. Cu^+ was neither reduced nor oxidised. Furthermore, the UPS measurements, recorded after the $CuFeO_2$ pellets had been exposed to water, showed a UPS valence band structure typical for physisorbed water and a relatively low work function of 4.4 eV. Therefore, the $CuFeO_2$ water exposure experiment can possibly be seen as an interface experiment. Indeed, physisorption of water may be feasible with the porous $CuFeO_2$ samples.

6.8 Perspectives

This dissertation has considered a few fundamental aspects regarding photochemical water splitting and, thus, contains a broad range of information, which may be used to guide future research.

First of all, it has been shown that the photodeposition technique is a versatile technique allowing the deposition of metals and metal(hydr)oxides on different kinds of photoabsorbers. Additionally, deposits may exhibit a certain regioselectivity for powders wherein the particles have defined anisotropic shapes. The photodeposition method certainly has to be studied further to increase understanding why certain deposits show a particular regioselectivity, as well as to develop new anisotropic heterostructures.

Secondly, the interface experiments performed in this work have shown to give detailed information, not only on the in situ formed junction between substrate and contact material but also on the substrate itself. The interface experiments have shown that heterostructures may not only lead to the previously proposed benefits of improved reaction kinetics, enhanced surface passivation or corrosion protection, but may also yield increased band bending and, thus, better charge carrier separation. Future interface experiments could focus on the band alignment of contact materials with specific crystalline facets of $BiVO_4$ to elucidate whether other surface structures have a strong influence on the contact properties. Additionally, other promising photoabsorbers may be coated as well with high and low work function materials to investigate to what extent the Fermi level may be tuned in those compounds.

Third, the remarkable water exposure experiment on $BiVO_4$ suggests two things: 1) that the water reacts at the surface to form a volatile oxygen containing compound, leaving the surface reduced and 2) that the surface reduction could be reversed through oxidative treatments. These astonishing observations may indicate that the photochemical water oxidation mechanism at the $BiVO_4$ surface, follows a completely different path than what common knowledge dictates. Namely, that in photocatalysis first light is absorbed, then charge carrier separation takes place and finally the surface redox reactions happen with the surface accumulated electrons and holes. Instead, it may very well be that the surface reactions happen first after which the charge carriers at the surface need to be replenished through the absorption of light. This mechanism would also strongly agree with our assumptions on the role of a contact material in heterostructured $BiVO_4$. Namely, that a contact material primary helps to increase charge carrier separation and has little to no additional effect on the water oxidation reaction kinetics. We think that the research community should investigate these remarkable findings further in more detail. One should also check that the high energy holes generated during photoelectron spectroscopy measurements do not initiate the oxidation of the hydroxy groups at the water exposed $BiVO_4$ sample.

Furthermore, new photoabsorbers able to perform water oxidation and/or water reduction have to be identified, because $BiVO_4$ is a suboptimal light absorber and $CuFeO_2$ seems to have inherent limits, which inhibit its water reduction capacity. Off course, the GaInP/GaInAs combination has shown to have the ideal light absorption complementarity and demonstrated the state of the art 16.2% photoelectrochemical STH efficiency. However, their high cost and the insecurity about their long term stability in an electrolyte likely prevent III-V semiconductors in becoming the solution for particulate water splitting systems. Instead, new combinations of metal oxides have to be searched for, potentially partly mixing in nitrogen or sulphur to increase the valence band position, since now only binary, ternary and occasionally quaternary materials have been considered along the chemical space. Herein, computational studies could play a primary role. Preferably, iron should be excluded in the search towards photochemical water reducing compounds, due to the seemingly universal Fe^{3+}/Fe^{2+} polaron formation level which limits the potential photovoltage of iron containing compounds.

Although, strong doubts exist regarding the ability of photoelectrochemical water splitting with thin film stacks to be a viable alternative to steam methane reforming or photovoltaic-electrolysis in the near future, research should still be performed on these systems, because the information obtained may be transferred to the inherently cheaper but more difficult to study particulate systems. A particulate system which can achieve a 5% STH efficiency and has a stability of at least five years may be economically competitive to photovoltaic-electrolysis and even to steam methane reforming

All in all, we can conclude that there is still a long road ahead to establish an efficient and stable particulate photochemical water splitting system that would yield economical parity to conventional hydrogen production methods.

Appendix A

Appendix A

A.1 Linear regression data water oxidation $BiVO_4$

		Linear regression						
		slope (ml/min)	std error	intercept	R^2	ml/h O2	std error	umol/h O2
bare BiVO4	1	0.00355	4E-05	1.10	0.967	0.21	2E-03	8.7
	2	0.00269	3E-05	0.80	0.959	0.16	2E-03	6.6
	mean	**0.00312**	3E-05	0.95	0.963	**0.19**	2E-03	**7.7**
NiOxOHy (0.1 wt%) dark	1	-6.80E-04	3E-05	0.32	0.633	-	-	-
NiOxOHy (0.1 wt%)	1	0.00683	5E-05	0.87	0.986	0.41	3E-03	16.8
	2	0.00511	2E-05	1.25	0.993	0.31	1E-03	12.5
	mean	**0.00597**	4E-05	1.06	0.989	**0.36**	2E-03	**14.6**
NiOxOHy (1 wt%)	1	0.00722	3E-05	0.50	0.993	0.43	2E-03	17.7
	2	0.00671	6E-05	0.76	0.976	0.40	4E-03	16.5
	3	0.00471	2E-05	0.86	0.995	0.28	1E-03	11.6
	mean	**0.00621**	4E-05	0.81	0.985	**0.37**	2E-03	**15.2**
CoOxOHy (0.08 wt%)	1	0.0278	9E-05	1.31	0.997	1.67	5E-03	68.2
	2	0.026	8E-05	1.41	0.997	1.56	5E-03	63.8
	mean	**0.0269**	8E-05	1.36	0.997	**1.61**	5E-03	**66.0**
CoOxOHy (0.2 wt%)	1	0.0318	3E-05	0.96	1.000	1.91	2E-03	78.0
	2	0.0309	7E-05	1.15	0.998	1.85	4E-03	75.8
	mean	**0.03135**	5E-05	1.06	0.999	**1.88**	3E-03	**76.9**
Pt (0.5 wt%)	1	0.0173	5E-05	0.70	0.997	1.04	3E-03	42.4
	2	0.0195	8E-05	0.98	0.995	1.17	5E-03	47.8
	mean	**0.0184**	7E-05	0.84	0.996	**1.10**	4E-03	**45.1**

Figure A.1: Raw data obtained from the linear regression of the oxygen evolution curves and calculation of oxygen evolution for the sacrificial water oxidation experiments on the (heterostructured) $BiVO_4$ powders.